COK-U014.72-1-G10[illegible]

ANNUAL OF THE CHINESE SOCIETY OF NAVAL ARCHITECTURE AND MARINE ENGINEERING

Vol. 1 1982

1

CHINA ACADEMIC PUBLISHERS
BEIJING CHINA

First Edition 1982

The Copyright is owned by China Academic Publishers. No part of this publication may be reproduced, stored in a retrieval system, or transmitted in any form or by any means, electronic, mechanical, photocopying or otherwise, without the prior permission of the Copyright owner.

CSBN W15262 · 002 China Academic publishers

G 10.104

Edited by
THE EDITORIAL OFFICE OF SHIPBUILDING OF CHINA
P. O. Box 4116, Shanghai, China

Published by
CHINA ACADEMIC PUBLISHERS
137 Chaonei Street, Beijing, China

Printed by
SHANGHAI THE THIRD PRINTING FACTORY
665 Kongjiang Road, Shanghai, China

Distributed by
CHINA PUBLICATIONS CENTRE (GUOJI SHUDIAN)
P. O. Box 399, Beijing, China

Printed in the People's Republic of China

PREFACE

Since its founding in 1943, the Chinese Society of Naval Architecture and Marine Engineering has edited and published many series of books and certain technical journals to stimulate technical exchange and to promote the development of China's shipbuilding technology and scientific research. At present, the Society publishes several technical journals and other such publications.

In recent years, with the development of China's shipbuilding and its increasingly frequent technical contacts with foreign countries, overseas experts have a keen desire to keep abreast of current development in China's shipbuilding technology through the vehicle of English, the commonly-used universal language in international shipbuilding circles, so that international academic exchange can be further extended. To meet these requirements, the Society has decided to publish annual in English and has instructed the Editorial Office of the Journal of "Shipbuilding of China" to be in charge of the editing and publishing.

During the preparatory period for this present volume of annual, the various academic committees and technical subcommittees of the Society have all helped, especially by recommending excellent papers in their specific, professional areas. The Editorial Office reviewed all the papers submitted and has selected 16 papers for inclusion in this annual publication. These papers embody the most recent developments in all the various fields of China's shipbuilding research.

It is the first time we have published this kind of annual collection. We expect there are many areas in which subsequent collections can be changed and improved and, therefore, request our readers, both at home and abroad, to let us know fully their response to this volume.

The Chinese Society of Naval Architecture
and Marine Engineering

CONTENTS

Numerical Solution of the Hydrofoil of Finite Span by the Horseshoe Vortex Lattice Method .... Li Baiqi (李百齐) and He Yousheng (何友声) (1)

A-Function—a Special Function Used in Naval Hydrodynamics...Chen Caikan (陈材侃) (18)

A Streamline-Iteration Method for Calculating Turbulent Flow around the Stern of a Body of Revolution and Its Wake.......................... Zhou Liandi (周连弟) (3[illegible])

Calculation of Hydrodynamic Coefficients for Bulbous Sections and Twin-body Sections Using the Multi-pole Expansion Method ....
Dai Yishan (戴遗山), Jiang Xiaoxiong (蒋小雄) and Min Meisong (闵美松) (53)

Approximate Method for Calculation of Hydrodynamic Derivatives of an Intersecting Tail Fin on a Body of Revolution .... Zhang Zhonglai (张中骒) (63)

An Exact Solution for Axisymmetrically Loaded Thick Annular Plates ....
.... Sun Quanxin (孙全新) and Luo Zudao (罗祖道) (77)

Strength in Opening with Various Reinforcements in Spherical and Cylindrical Structures .... Xu Binghan (徐秉汉) and Pei Junhou (裴俊厚) (91)

Superelement Method of Modal Synthesis and Its Application to Dynamic Calculation of Ship Structure ....
Yun Weijun (恽伟君), Duan Genbao (段根宝) and Hu Zhonggen (胡仲根) (1[illegible])

SFFJ Method and Application in Optimum Design of Structures..........................
.... Cui Chengxian (崔承宪) (1[illegible])

Experience of Adopting Circular-Arc-Profile Reduction Gear Onboard Ship and Its Related Problems... Hua Jiashou (花家寿) (13[illegible])

Determination of the Maximum Heat Flux of Evaporating Tubes in Marine Boilers and the Film Coefficient of Heat Transfer at the Inner Surface of the Tube ...
....Gong Sansheng (龚三省) (1[illegible])

Damping Method of Fitting Silicone Fluid Dampers to Transmission Shafts ....
.... Nie Deyao (聂德耀) (1[illegible])

Experimental Investigation on Cylinder Head of E390V Marine Diesel Engine ......
.... Jiang Rongpei (蒋荣培), Zhang Xiaoling (张晓泠), Li Changhan (李昌汉), Li Fuxing (李福兴) and Wu Jinyuan (吴金源) ([illegible])

The Reliability Analysis of the Ship's Navigation System .... Li Zigang (李滋刚) ([illegible]3)

Ship End Launching without Fore Poppet..
.... Zhu Chongxian (朱崇贤) and Lu Weidong (陆伟东) ([illegible])

The Mechanism of Fisheye Formation in Welded Seam and Its Influence on the Fracture Process..Cai Zegao (蔡泽高), Chen Yazhen (陈雅珍), Zeng Zhenpeng (曾振鹏) and Shui Cheng (水 澄) (21[illegible])

Annual of the CSNAME, Vol. 1, 1982

NUMERICAL SOLUTION OF THE HYDROFOIL OF FINITE SPAN BY THE HORSESHOE VORTEX LATTICE METHOD

Li Baiqi (李百齐)

China Ship Scientific Research Center

He Yousheng (何友声)

Shanghai Jiao Tong University

SUMMARY

Applying the lifting surface theory which considers both spanwise and chordwise vortex distribution, a numerical method for calculating the hydrodynamic characteristics of fully submerged hydrofoil of finite span is presented in this paper. In order to improve Wu's and Nishiyama's work an appropriate technique treating the singular integrand is introduced.

The planform of the hydrofoil are divided into $M \times N$ plane rectangular elements, each of which is replaced by a horseshoe vortex with unknown circulation strength. Taking the normal components of fluid velocity zero on the control points, we obtain a set of linear algebraic equations solving the circulation strength on the rectangular elements. Thus the lift as well as the drag can be computed.

As an example, numerical computations of a flat plate hydrofoil of aspect ratio 4, 6 and 10 at various depth of submergence are carried out. The comparison of theory with experiment shows that the method described in this study is satisfying for predicting the hydrodynamic properties of a hydrofoil in the extended range of Froude number and submergence chord ratio. It also provides the possibility to predict accurately the flow velocity and pressure distribution.

I. Introduction

The prediction of the hydrodynamic characteristics of a hydrofoil with finite span has bee one of the basic problems to the hydrofoil-supported craft. In an earlier paper[1], Wu presente a theory for hydrofoils of finite span by means of lifting line approximation. The difficult risen from the intractable evaluation of the downwash which is turned out of the velocity potential of wave formation due to its singularity has been dodged through considering the downwash on the location of the bound vortex only in Wu's work. Nishiyama has given some contributions in this area. He[2] treated the hydrofoil of finite span as a simplified lifting surface which was still represented by a concentrated horseshoe vortex through an averaging procedure taking account of the chordwise load distribution. Strictly speaking, it was a lifting line theory yet. In addition, the aforementioned difficulty was evaded under the assumption of that three dimensional local disturbance can be represented approximately by two dimensional one in his paper. Their theories are expected to be valid when the aspect ratio of the hydrofoil and the depth of immersion below the water surface are large enough.

The study in present paper is undertaken as an extension of attempts to solve a similar problem by applying really a lifting surface model which considers both spanwise and chordwise vortex distribution. The planform of a hydrofoil is to be divided into many rectangular elements, each of that is to be replaced by a discrete horseshoe vortex with constant circulation strength and then a numerical method utilized to evaluate the hydrodynamic properties such as circulation strength, lift, induced drag, velocity and pressure distribution is given.

The difficulty connected with singularity is overcome through a refined quadrature. From numerical results comparied with the experimental data of a plate hydrofoil, conclusions are drawn that the method provided in this paper are expected to be valid in a wide range of the depth of immersion, Froude number and aspect ratio.

II. Formulation of the Perturbation Velocity Potentials and Induced Velocities of a Horseshoe Vortex Moving Beneath the Water Surface

Fig. 1 shows the steady flow which is to be studied. Consider a horseshoe vortex of span $2b$ with constant circulation strength Γ_0, advancing forward with constant velocity U at fixed depth of submergence h beneath the undisturbed water surface. We choose a coordinate system fixed with respect to the horseshoe vortex. The origin of the coordinate $OXYZ$ is situated at the middle point of bound vortex as shown in Fig. 1. Let the X-axis be parallel to the direc-

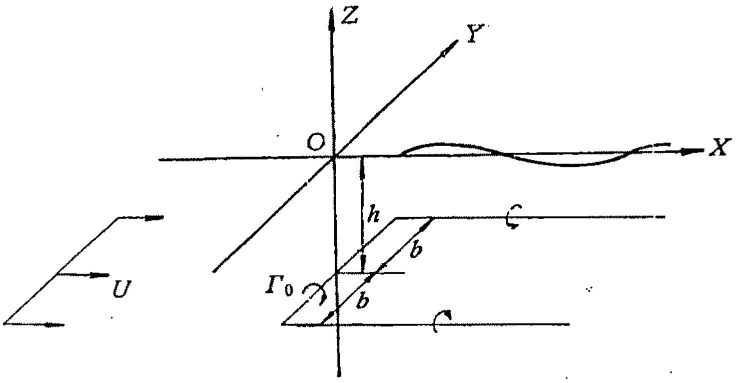

Fig. 1

tion of the free stream, Y-axis be parallel to the spanwise direction and Z-axis point upward, with $z=0$ representing the undisturbed free surface.

The fluid is assumed to be incompressible and inviscid or ideal. According to the condition of irrotationality and continuity, the perturbation velocity potential ϕ satisfies the Laplace equation

$$\nabla^2\phi = 0 \tag{1}$$

Under the assumption of infinitesimal wave, the corresponding linearized boundary condition are given.

$$\begin{gathered}\left(\frac{\partial^2\phi}{\partial x^2}+k\frac{\partial\phi}{\partial z}\right)_{z=0}=0\\ \lim_{z\to-\infty}\operatorname{grad}\phi=0\\ \lim_{x\to-\infty}\operatorname{grad}\phi=0\end{gathered} \tag{2}$$

where $k=\frac{g}{U^2}$.

The perturbation velocity potential ϕ, which satisfies the linearized boundary conditions (2), caused by the vortex sheet with circulation distribution $\Gamma(y)$ has been shown to have the following integral representation[1]:

$$\phi=\phi_1+\phi_2+\phi_3+\phi_4 \tag{3}$$

where $$\phi_1=\frac{z+h}{4\pi}\int_{-b}^{b}\frac{\Gamma(\eta)}{(y-\eta)^2+(z+h)^2}\left\{1+\frac{x}{\sqrt{x^2+(y-\eta)^2+(z+h)^2}}\right\}d\eta \tag{4}$$

$$\phi_2=\frac{z-h}{4\pi}\int_{-b}^{b}\frac{\Gamma(\eta)}{(y-\eta)^2+(z-h)^2}\left\{1+\frac{x}{\sqrt{x^2+(y-\eta)^2+(z-h)^2}}\right\}d\eta \tag{5}$$

$$\begin{aligned}\phi_3=&-\frac{k}{\pi^2}\int_{-b}^{b}\Gamma(\eta)\,d\eta\int_0^{\pi/2}\sec^3\theta d\theta\int_0^{\infty}e^{K(z-h)}\sin(Kx\cos\theta)\frac{\cos[K(y-\eta)\sin\theta]}{K-k\sec^2\theta}dK\\&+\frac{1}{2\pi}\int_{-b}^{b}\Gamma(\eta)\,d\eta\int_0^{\infty}e^{K(z-h)}\cos K(y-\eta)\,dK\end{aligned} \tag{6}$$

$$\phi_4=-\frac{k}{\pi}\int_{-b}^{b}\Gamma(\eta)\,d\eta\int_0^{\pi/2}e^{k(z-h)\sec^2\theta}\cos(kx\sec\theta)\cos[k(y-\eta)\sec^2\theta\sin\theta]\sec^3\theta\,d\theta \tag{7}$$

ϕ_1 represents the velocity potential of vortex sheet in unbounded fluid, ϕ_2 is equivalent to the potential of image part of a biplane system, ϕ_3 represents the potential due to wave formation, and ϕ_4 is representative of the potential due to free wave system.

Let $\Gamma(\eta)=\Gamma_0$, (4) to (7) can be integrated.

$$\begin{aligned}\phi_1=&\frac{\Gamma_0}{4\pi}\operatorname{tg}^{-1}\frac{2b(z+h)}{(z+h)^2+y^2-b^2}\\&+\frac{\Gamma_0}{4\pi}\operatorname{tg}^{-1}\frac{x(z+h)[(y+b)\sqrt{x^2+(y-b)^2+(z+h)^2}-(y-b)\sqrt{x^2+(y+b)^2+(z+h)^2}]}{(z+h)^2\sqrt{[x^2+y^2+b^2+(z+h)^2]^2-4y^2b^2}+x^2(y^2-b^2)}\end{aligned} \tag{8}$$

$$\phi_2=\frac{\Gamma_0}{4\pi}\mathrm{tg}^{-1}\frac{2b(z-h)}{(z-h)^2+y^2-b^2}$$

$$+\frac{\Gamma_0}{4\pi}\mathrm{tg}^{-1}\frac{x(z-h)[(y+b)\sqrt{x^2+(y-b)^2+(z-h)^2}-(y-b)\sqrt{x^2+(y+b)^2+(z-h)^2}]}{(z-h)^2\sqrt{[x^2+y^2+b^2+(z-h)^2]^2-4y^2b^2}+x^2(y^2-b^2)} \tag{9}$$

$$\phi_3=\frac{k\Gamma_0}{\pi^2}\int_0^{\pi/2}\frac{\sec^3\theta}{\sin\theta}d\theta\int_0^\infty e^{K(z-h)}\frac{\sin(Kx\cos\theta)}{K(K-k\sec^2\theta)}\{\sin[K(y-b)\sin\theta]$$

$$-\sin[K(y+b)\sin\theta]\}\,dK-\frac{\Gamma_0}{2\pi}\int_0^\infty e^{K(z-h)}\frac{1}{K}[\sin K(y-b)-\sin K(y+b)]dK \tag{10}$$

$$\phi_4=\frac{\Gamma_0}{\pi}\int_0^{\pi/2}\exp[k(z-h)\sec^2\theta]\cos(kx\sec\theta)\frac{\sec\theta}{\sin\theta}\{\sin[k(y-b)\sec^2\theta\sin\theta]$$

$$-\sin[k(y+b)\sec^2\theta\sin\theta]\}d\theta \tag{11}$$

Thus it follows that,

$$\bar{w}_1=\frac{w_1}{U}=-\left(\frac{\partial\phi_1}{\partial z}\right)_{z=-h}\Big/U=\frac{\bar{\Gamma}_0}{4\pi}\left\{\frac{\bar{x}(\bar{y}+\bar{b})}{\sqrt{\bar{x}^2+(\bar{y}+\bar{b})^2}}\left[\frac{1}{\bar{x}^2}+\frac{1}{(\bar{y}+\bar{b})^2}\right]\right.$$

$$\left.-\frac{\bar{x}(\bar{y}-\bar{b})}{\sqrt{\bar{x}^2+(\bar{y}-\bar{b})^2}}\left[\frac{1}{\bar{x}^2}+\frac{1}{(\bar{y}-\bar{b})^2}\right]-\left[\frac{1}{\bar{y}-\bar{b}}-\frac{1}{\bar{y}+\bar{b}}\right]\right\} \tag{12}$$

$$\bar{w}_2=\frac{w_2}{U}=-\left(\frac{\partial\phi_2}{\partial z}\right)_{z=-h}\Big/U=\frac{\bar{\Gamma}_0}{4\pi}\left\{\frac{\bar{x}(\bar{y}+\bar{b})}{\sqrt{\bar{x}^2+(\bar{y}+\bar{b})^2+4\bar{h}^2}}\left[\frac{1}{\bar{x}^2+4\bar{h}^2}+\frac{1}{(\bar{y}+\bar{b})^2+4\bar{h}^2}\right]\right.$$

$$-\frac{\bar{x}(\bar{y}-\bar{b})}{\sqrt{\bar{x}^2+(\bar{y}-\bar{b})^2+4\bar{h}^2}}\left[\frac{1}{\bar{x}^2+4\bar{h}^2}+\frac{1}{(\bar{y}-\bar{b})^2+4\bar{h}^2}\right]$$

$$\left.-\left[\frac{\bar{y}-\bar{b}}{(\bar{y}-\bar{b})^2+4\bar{h}^2}-\frac{\bar{y}+\bar{b}}{(\bar{y}+\bar{b})^2+4\bar{h}^2}\right]\right\} \tag{13}$$

$$\bar{w}_3=\frac{w_3}{U}=-\left(\frac{\partial\phi_3}{\partial z}\right)_{z=-h}\Big/U=\frac{\bar{\Gamma}_0}{\pi^2F_{rc}^2}\int_0^{\pi/2}\frac{\sec^3\theta}{\sin\theta}d\theta\int_0^\infty e^{-2K\bar{h}}\frac{\sin(K\bar{x}\cos\theta)}{K-\frac{1}{F_{rc}^2}\sec^2\theta}$$

$$\times\{\sin[K(\bar{y}+\bar{b})\sin\theta]-\sin[K(\bar{y}-\bar{b})\sin\theta]\}dK$$

$$+\frac{\bar{\Gamma}_0}{2\pi}\int_0^\infty e^{-2K\bar{h}}[\sin K(\bar{y}-\bar{b})-\sin K(\bar{y}+\bar{b})]dK \tag{14}$$

$$\bar{w}_4=\frac{w_4}{U}=-\left(\frac{\partial\phi_4}{\partial z}\right)_{z=-h}\Big/U=\frac{\bar{\Gamma}_0}{\pi F_{rc}^2}\int_0^{\pi/2}\exp\left(-\frac{2\bar{h}}{F_{rc}^2}\sec^2\theta\right)\cos\left(\frac{\bar{x}}{F_{rc}^2}\sec\theta\right)$$

$$\times\left\{\sin\left[\frac{\bar{y}+\bar{b}}{F_{rc}^2}\sec^2\theta\sin\theta\right]-\sin\left[\frac{\bar{y}-\bar{b}}{F_{rc}^2}\sec^2\theta\sin\theta\right]\right\}\frac{\sec^3\theta}{\sin\theta}d\theta \tag{15}$$

Here w_i and $\bar{w}_i$ (i = 1, 2, 3, 4) are the corresponding downwashs and its non-dimensional quantities, $\bar{\Gamma}_0=\frac{\Gamma_0}{Uc}$, $F_{rc}=\frac{U}{\sqrt{gc}}=\frac{1}{\sqrt{kc}}$, $\bar{x}=\frac{x}{c}$, $\bar{y}=\frac{y}{c}$, $\bar{b}=\frac{b}{c}$, $\bar{h}=\frac{h}{c}$ and c is a characteristic length which will be taken as the chord length of each element henceforth. The expressions of $\bar{w}_i$ (i=1, 2, 3, 4) are discussed as follow. It is easy to evaluate $\bar{w}_1$ and $\bar{w}_2$ by virtue of (12) and (13) being algebraic relations. The integrand in (15) will trend to $\frac{2\bar{b}}{F_{rc}^2}\times\exp\left(-2\frac{\bar{h}}{F_{rc}^2}\right)\cos\left(\frac{\bar{x}}{F_{rc}^2}\right)$ by using L'Hospital rule when $\theta=0$ and vanish when $\theta=\frac{\pi}{2}$

because of that the term with factor $\sec^3\theta \exp\left(-\frac{2\bar{h}}{F_{rc}^2}\sec^2\theta\right)$ in Eq. (15) will diminish rapidly as θ approaching $\frac{\pi}{2}$. Thus (15) is integrable as a result of the integrand being definite everywhere in the interval $\left(0, \frac{\pi}{2}\right)$.

The expression (14) of $\bar{w}_3$ which is intractable one may be split into two terms. One of them represents the first integral and the other represents the second integral in (14), namely

$$\bar{w}_3 = \bar{w}_{3AB} + \bar{w}_{3C} \tag{16}$$

Using some trigonometrical relations, it follows that,

$$\bar{w}_{3AB} = \frac{\bar{\Gamma}_0}{\pi^2 F_{rc}^2}\int_0^{\pi/2}\frac{\sec^3\theta}{\sin\theta}d\theta\left\{-\frac{1}{2}\int_0^\infty e^{-2K\bar{h}}\frac{\cos(K\bar{\omega}_{1+})}{K-\frac{1}{F_{rc}^2}\sec^2\theta}dK\right.$$
$$+\frac{1}{2}\int_0^\infty e^{-2K\bar{h}}\frac{\cos(K\bar{\omega}_{1-})}{K-\frac{1}{F_{rc}^2}\sec^2\theta}dK + \frac{1}{2}\int_0^\infty e^{-2K\bar{h}}\frac{\cos(K\bar{\omega}_{2+})}{K-\frac{1}{F_{rc}^2}\sec^2\theta}dK$$
$$\left.-\frac{1}{2}\int_0^\infty e^{-2K\bar{h}}\frac{\cos(K\bar{\omega}_{2-})}{K-\frac{1}{F_{rc}^2}\sec^2\theta}dK\right\} \tag{17}$$

where $\bar{\omega}_{1\pm} = \bar{x}\cos\theta \pm (\bar{y}+\bar{b})\sin\theta$

$\bar{\omega}_{2\pm} = \bar{x}\cos\theta \pm (\bar{y}-\bar{b})\sin\theta.$

Typical form of generalized integrals in (17) is given by

$$\int_0^\infty \mathrm{e}^{-PK}\frac{\cos(QK)}{K-K_0}dK$$

It will be noticed that the integrand has a pole at the point $K=K_0$. Using a contour integral procedure, we obtain:

$$\int_0^\infty e^{-PK}\frac{\cos(QK)}{K-K_0}dK = -\operatorname{sign}(Q)\pi e^{-K_0P}\sin(K_0Q) + \int_0^\infty e^{-|Q|K}\frac{K\cos PK - K_0\sin PK}{K^2+K_0^2}dK \tag{18}$$

and then

$$\bar{w}_{3AB} = \bar{w}_{3A} + \bar{w}_{3B} \tag{19}$$

where

$$\bar{w}_{3A} = \frac{\bar{\Gamma}_0}{2\pi F_{rc}^2}\int_0^{\pi/2}\exp\left(-\frac{2\bar{h}}{F_{rc}^2}\sec^2\theta\right)\frac{\sec^3\theta}{\sin\theta}\left\{\left[\operatorname{sign}(\bar{\omega}_{1+})\sin\left(\frac{1}{F_{rc}^2}\bar{\omega}_{1+}\sec^2\theta\right)\right.\right.$$
$$\left.-\operatorname{sign}(\bar{\omega}_{1-})\sin\left(\frac{1}{F_{rc}^2}\bar{\omega}_{1-}\sec^2\theta\right)\right]-\left[\operatorname{sign}(\bar{\omega}_{2+})\sin\left(\frac{1}{F_{rc}^2}\bar{\omega}_{2+}\sec^2\theta\right)\right.$$
$$\left.\left.-\operatorname{sign}(\bar{\omega}_{2-})\sin\left(\frac{1}{F_{rc}^2}\bar{\omega}_{2-}\sec^2\theta\right)\right]\right\}d\theta \tag{20}$$

$$\bar{w}_{3B} = \frac{\bar{\Gamma}_0}{2\pi^2 F_{rc}^2}\int_0^{\pi/2}\int_0^\infty \frac{K\cos 2\bar{h}K - \frac{1}{F_{rc}^2}\sec^2\theta\sin 2\bar{h}K}{K^2+\frac{1}{F_{rc}^4}\sec^4\theta}\left[-e^{-|\bar{\omega}_{1+}|K}\right.$$
$$\left.+e^{-|\bar{\omega}_{1-}|K}\right]\frac{\sec^3\theta}{\sin\theta}dK\,d\theta - \frac{\bar{\Gamma}_0}{2\pi^2 F_{rc}^2}\int_0^{\pi/2}\int_0^\infty \frac{K\cos 2\bar{h}K - \frac{1}{F_{rc}^2}\sec^2\theta\sin 2\bar{h}K}{K^2+\frac{1}{F_{rc}^4}\sec^4\theta}$$
$$\times\left[-e^{-|\bar{\omega}_{2+}|K} + e^{-|\bar{\omega}_{2-}|K}\right]\frac{\sec^3\theta}{\sin\theta}dK\,d\theta \tag{2\ }$$

The integrand in (20) is equal to $\operatorname{sign}(\bar{x}) \cdot \frac{4\bar{b}}{F_{rc}^2} \exp\left(-\frac{2\bar{h}}{F_{rc}^2}\right) \cos\left(\frac{\bar{x}}{F_{rc}^2}\right)$, when $\theta = 0$ and zero when $\theta = \frac{\pi}{2}$. Thus this integral can be calculated directly by numerical method without any difficulty.

The expression (21) of $\bar{w}_{3B}$ consists of two double integral with similar type. Consider first one as an example. There is no pole in its integrand with respect to variable K and the integrand vanishes as K becomes infinite. Similarly the integrand which becomes sign($\bar{x}$)$\cdot$ $\times 2(\bar{y}+\bar{b}) \exp(-|\bar{x}|K) \dfrac{K\left(K\cos 2\bar{h}K - \frac{1}{F_{rc}^2}\sin 2\bar{h}K\right)}{K^2+\frac{1}{F_{rc}^4}}$ when $\theta=0$ and $-\operatorname{sign}(\bar{y}+\bar{b})\cdot 2F_{rc}^2 K\bar{x}$ $\times \exp(-|\bar{y}+\bar{b}|K) \sin 2\bar{h}K$ when $\theta = \frac{\pi}{2}$ will be definite with respect to variable θ. Thus, this double integral is convergent. The integration can be made with respect to K prior to θ. The computing time will depend on the convergence of the process which is concerned with the magnitudes of $|\bar{\omega}_{1+}|$ and $|\bar{\omega}_{1-}|$ by virtue of that the integrand displays a behavior of oscillatory function with damping amplitute during the integration with respect to K. It will be rapidly convergent for larger value of $|\bar{\omega}_{1+}|$ as well as $|\bar{\omega}_{1-}|$, and vice versa. Hence it is hard to carry out on numerical computation provided either $|\bar{\omega}_{1-}|$ or $|\bar{\omega}_{1-}|$ approaches to zero. It is obvious that there is only just one null point θ_0 for all $|\bar{\omega}_{1+}|$ and $|\bar{\omega}_{1-}|$ in range of $\theta=0$ to $\frac{\pi}{2}$, where $\theta_0 = \mathrm{tg}^{-1}\left|\frac{\bar{x}}{\bar{y}+\bar{b}}\right|$. Now, if $\bar{\omega}_{1+}$ has a null point, in case of $\theta=\theta_0$ the integral with respect to K can be reduced to

$$\int_0^\infty \frac{K\cos 2\bar{h}K - \frac{1}{F_{rc}^2}\sec^2\theta_0 \sin 2\bar{h}K}{K^2+\frac{1}{F_{rc}^4}\sec^4\theta_0}\left[-1+e^{-|(\bar{\omega}_{1-})_{\theta=\theta_0}|K}\right]\frac{\sec^3\theta_0}{\sin\theta_0}\,dK$$

$$= \exp\left(-\frac{2\bar{h}}{F_{rc}^2}\sec^2\theta_0\right) E_i\left(\frac{2\bar{h}}{F_{rc}^2}\sec^2\theta_0\right)\frac{\sec^3\theta_0}{\sin\theta_0}$$

$$+\int_0^\infty \frac{K\cos 2\bar{h}K - \frac{1}{F_{rc}^2}\sec^2\theta_0 \sin 2\bar{h}K}{K^2+\frac{1}{F_{rc}^4}\sec^4\theta_0}\, e^{-|(\bar{\omega}_{1-})_{\theta=\theta_0}|K}\,\frac{\sec^3\theta_0}{\sin\theta_0}\,dK \tag{22}$$

Here $E_i(z)$ is a modified integral exponential function which may be expressed by the following series:

$$E_i(z) = \gamma + \ln z + \frac{z}{1\cdot 1!} + \frac{z^2}{2\cdot 2!} + \cdots \tag{23}$$

where γ is Euler number. An asymptotic expansion can be used for large values of z,

$$E_i(z) \approx \frac{e^z}{z}\left[1 + \frac{1!}{z} + \frac{2!}{z^2} + \cdots\right] \tag{24}$$

Noting the above mentioned case, the intractable difficulty during calculation can be avoided.

It is stipulated that the integral with respect to K will be carried out according to (21) for $0\leqslant\theta\leqslant\theta_0-\Delta\theta$ or $\theta_0+\Delta\theta\leqslant\theta\leqslant\frac{\pi}{2}$ and according to three-point interpolation method for $\theta_0-\Delta\theta<\theta<\theta_0+\Delta\theta$, using the results of integration at $\theta\doteq\theta_0-\Delta\theta$ as well as $\theta=\theta_0+\Delta\theta$ by (21) and $\theta=\theta_0$ by (22) respectively. The magnitude of $\Delta\theta$ may be determined in accordance with the required accuracy and the savings in computing time.

It must be pointed out that the terms consisting of $\bar\omega_{1+}$ and $\bar\omega_{1-}$ or $\bar\omega_{2+}$ and $\bar\omega_{2-}$ in brackets of (20) and (21) should be computed in pairs in order to make the integral convergent. Otherwise, each separated integral will be divergent owing to its infinity at $\theta=0$ or $\theta=\frac{\pi}{2}$.

The expression of $\bar w_{3C}$ can be integrated directly. Thus we obtain:

$$\bar w_{3C}=\frac{\bar\Gamma_0}{2\pi}\left[\frac{\bar y-\bar b}{(\bar y-\bar b)^2+4\bar h^2}-\frac{\bar y+\bar b}{(\bar y+\bar b)^2+4\bar h^2}\right] \tag{25}$$

Total non-dimensional downwash $\bar w$ is

$$\bar w=\bar w_1+\bar w_2+\bar w_{3A}+\bar w_{3B}+\bar w_{3C}+\bar w_4 \tag{26}$$

From (12), (13), (15), (20), (21) and (25), it is easy to show that each components of (26) are even function of y. In addition, $\bar w_{3A}$ and $\bar w_{3B}$ are odd functions of $\bar x$ and $\bar w_4$ is even function of $\bar x$. Using these properties, the savings in computing time can be achieved. The influence coefficients which correspond to respective components of non-dimensional downwash caused by a horseshoe vortex with unit non-dimensional circulation strength are

$$\frac{\bar w_1}{\bar\Gamma_0}=F_1(\bar x,\ \bar y),\quad \frac{\bar w_2}{\bar\Gamma_0}=F_2(\bar x,\ \bar y),\quad \frac{\bar w_{3A}}{\bar\Gamma_0}=F_{3A}(\bar x,\ \bar y),\quad \frac{\bar w_{3B}}{\bar\Gamma_0}=F_{3B}(\bar x,\ \bar y),$$

$$\frac{\bar w_{3C}}{\bar\Gamma_0}=F_{3C}(\bar y),\quad \frac{\bar w_4}{\bar\Gamma_0}=F_4(\bar x,\ \bar y),\quad \frac{\bar w}{\bar\Gamma_0}=F(\bar x,\ \bar y) \tag{27}$$

It is obvious that these influence coefficients are independent from $\bar\Gamma_0$ and we have:

$$F=F_1+F_2+F_{3A}+F_{3B}+F_{3C}+F_4 \tag{28}$$

III. Solution of a Hydrofoil with Rectangular Planform by Using the Horseshoe Vortex Lattice Method

Consider a hydrofoil with rectangular planform of span $2B$ and chord C, moving with constant forward velocity U beneath the water surface at fixed depth of immersion h and attack angle α. We choose a coordinate system $O_fX_fY_fZ_f$ fixed with respect to the hydrofoil. The plane $X_fO_fY_f$ coincides with undisturbed water surface. Let the X_f-axis be parallel to the direction of the uniform flow and Z_f-axis vertically upward as well as through the middle point of leading edge as shown in Fig. 2.

Apart from the assumption of ideal fluid and infinitesimal wave, here we focus our attention on the flow past the mean-camber surface of zero thickness with both camber and attack angle small, on where a normal velocity distribution is specified,

$$\overline{W}|_{z_f=-h} = -\frac{\partial\beta(x_f, y_f)}{\partial x_f} \tag{29}$$

Here $\overline{W}=\frac{W}{U}$ denotes the non-dimensional downwash induced by the vortex system of hydrofoil and β (x_f, y_f) denotes a given mean-camber surface of zero thickness.

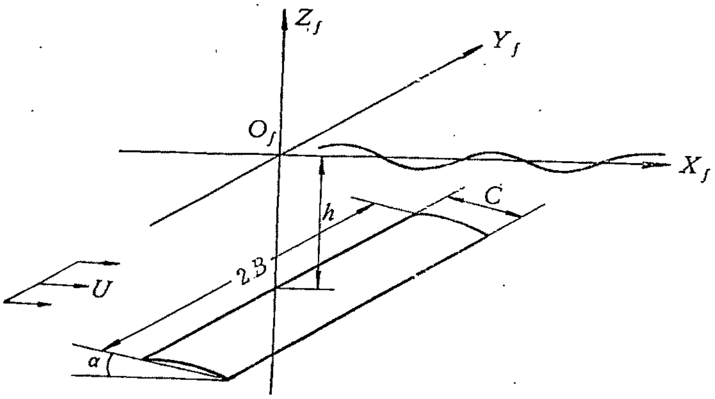

Fig. 2

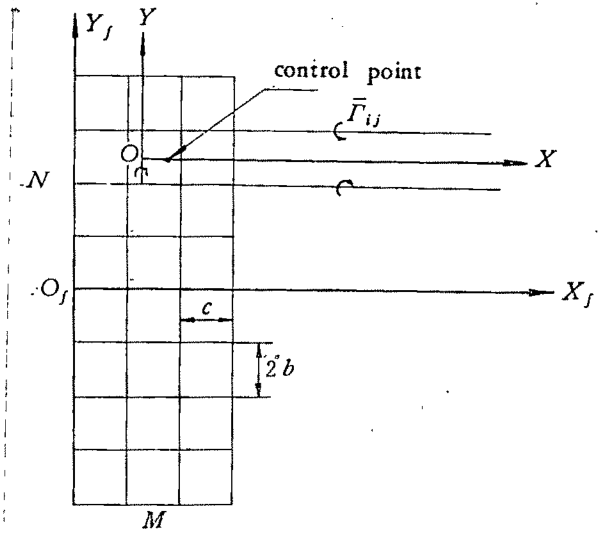

Fig. 3

Divide equidistantly the chord C into M segments and the span $2B$ into N segments. Thus the planform of the rectangular hydrofoil is represented by $M\times N$ planar rectangular elements with its magnitude $c=\frac{C}{M}$ chordwise and $2b=\frac{2B}{N}$ spanwise respectively, each of which is replaced by a horseshoe vortex of span $2b$ situated at quarter chord c of the element with unknown circulation strength, as shown in Fig. 3.

The control points situated at 3/4 chord of symmetric axis of each element are selected, on which the boundary condition (29) is satisfied.

Assuming that i denotes the order of the segments chordwise, j denotes the order of the segments spanwise and ij denotes the index of corresponding element, we take $OXYZ$ as a local Cartesian coordinate system situated over an element with ij just as shown in Fig. 1.

The non-dimensional coordinates of the control point on an element with index kl are expressed in terms of a coordinate system situated over the element with index ij in following form:

$$\begin{aligned} \bar{x} &= k-i+\tfrac{1}{2} \\ \bar{y} &= 2(l-j)\bar{b} \end{aligned} \tag{30}$$

Adopting the results derived from above paragraph, we obtain the non-dimensional downwash $\overline{W}_{ij}^{kl}$ induced at the control point of the element with index kl by the horseshoe vortex situated at the element with index ij,

$$\overline{W}_{ij}^{kl}=\overline{\Gamma}_{ij}\cdot F[k-i+\tfrac{1}{2},\ 2(l-j)\overline{b}] \tag{31}$$

where $\overline{\Gamma}_{ij}=\dfrac{\Gamma_{ij}}{UC}$ is the non-dimensional circulation strength of the horseshoe vortex situated at the element with index ij. The total non-dimensional downwash induced by all horseshoe vortices are expressed as the sum:

$$\overline{W}^{kl}=\sum_{i=1}^{M}\sum_{j=1}^{N}\overline{\Gamma}_{ij}\cdot F[k-i+\tfrac{1}{2},\ 2(l-j)\overline{b}] \tag{32}$$

Substituting (32) into the boundary condition (29) and taking $k=1,2,\cdots,M$, $l=1,2,\cdots,N$, give a set of linear algebraic equations

$$\sum_{i=1}^{M}\sum_{j=1}^{N}\overline{\Gamma}_{ij}\cdot F[k-i+\tfrac{1}{2},\ 2(l-j)\overline{b}]=-\beta_x^{kl} \tag{33}$$

Here $\beta_x^{kl}=\dfrac{\partial}{\partial x_f}\beta(x_f,\ y_f)\,|_{x_f=(k-\frac{1}{4})c,\ y_f=(2l-N-1)b}$. Thus the equations can be used to determine $\overline{\Gamma}_{ij}$, where $i=1,2,\cdots,M$ and $j=1,2,\cdots,N$.

Applying Kutta–Joukowski theorem gives

$$C_{Lkl}=2\overline{\Gamma}_{kl} \tag{34}$$

$$C_{Dkl}=2\overline{W}_v^{kl}\overline{\Gamma}_{kl} \tag{35}$$

where C_{Lkl} and C_{Dkl} are the local lift coefficient as well as the local induced drag coefficient based on the area of each element respectively, and $\overline{W}_v^{kl}$ is the non-dimensional downwash induced at the middle point of vortex of the element with index kl, deducting the contribution of k th bound vortex, namely

$$\begin{aligned}\overline{W}_v^{kl}=&\sum_{i=1}^{M}\sum_{j=1}^{N}\overline{\Gamma}_{ij}\{F[k-i,\ 2(l-j)\overline{b}]-F_1[k-i,\ 2(l-j)\overline{b}]\}\\&+\sum_{\substack{i=1\\i\neq k}}^{M}\sum_{j=1}^{N}\overline{\Gamma}_{ij}\cdot F_1[k-i,\ 2(l-j)\overline{b}]+\sum_{j=1}^{N}\overline{\Gamma}_{kj}F_{1f}[0,\ 2(l-j)\overline{b}]\end{aligned} \tag{36}$$

where F_{1f} is the influence coefficient corresponding to the part of free vortex in F_1. Thus the lift coefficient C_L and induced drag coefficient C_D based on total area of the planform are given.

$$C_L=\frac{1}{M\times N}\sum_{k=1}^{M}\sum_{l=1}^{N}C_{Lkl} \tag{37}$$

$$C_D=\frac{1}{M\times N}\sum_{k=1}^{M}\sum_{l=1}^{N}C_{Dkl} \tag{38}$$

IV. Numerical Results and Comparison with Experimental Data

The above method of numerical computation has been programmed according to ALGOL–

60 Systematic calculations for a rectangular plate hydrofoil with the aspect ratio $AR = 4,6,10$ have been carried out as an example. Here the set of linear algebraic equations solving the circulation strength are reduced to

$$\sum_{i=1}^{M}\sum_{j=1}^{N}\overline{\Gamma}_{ij}\cdot F[k-i+\tfrac{1}{2},\ 2(l-j)\overline{b}]=\alpha=\text{const.} \tag{39}$$

where $k = 1,2,\cdots, M$, $l = 1,2,\cdots, N$. Assuming $\alpha=1°$ does not lose its generality due to $\overline{\Gamma}_{ij}$ in proportion to α.

Numerical results are shown in Fig. 4 and Fig. 5 with $M = 1, 4$ and $N = 11$ for comparison. The ordinates are C_L and $\frac{C_D}{C_L^2}$ respectively and the abscissas are Froude number F_{RC} based on total chord length C. Taking the submergence chord ratio $\widetilde{h} = \frac{h}{C}$ as a para-

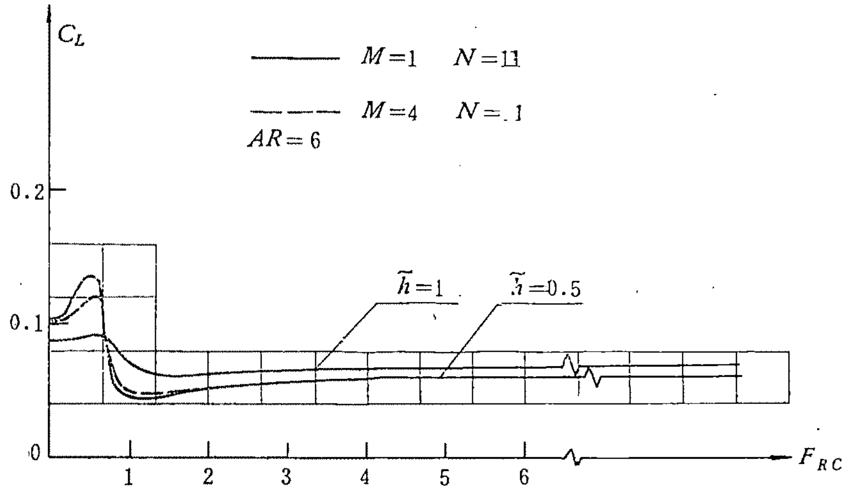

Fig. 4

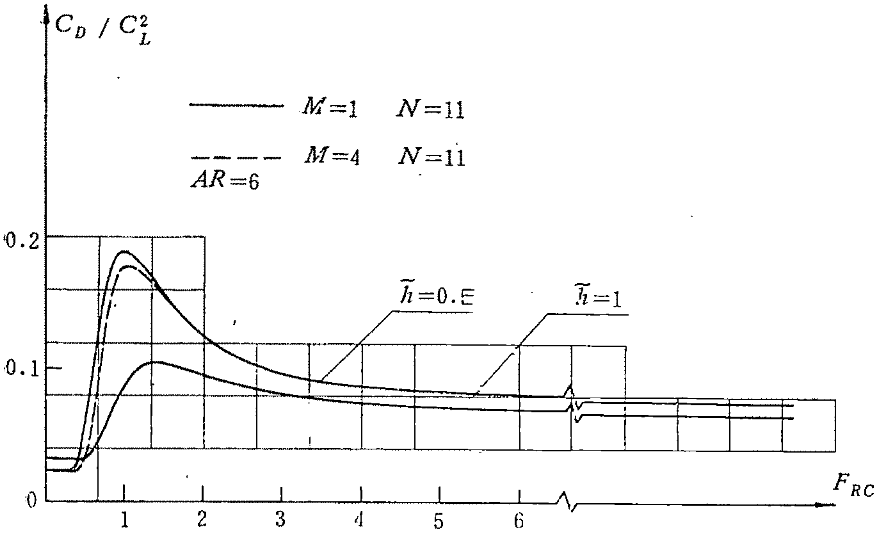

Fig. -

meter, we find that the value of C_L slowly increases with increasing F_{RC} as $F_{RC}>4$ and approaches to the corresponding value of a biplane as $F_{RC}\rightarrow\infty$. However, the value of $\frac{C_D}{C_L^2}$ slowly decreases with increasing F_{RC} as $F_{RC}>4$ and approaches to a limiting value also.

It may be pointed out that the curves of C_L and $\frac{C_D}{C_L^2}$ versus F_{RC} are quite consistent for $M=1$ and $M=4$ when $\tilde{h}\geqslant 1$. It implies that the hydrodynamic properties of a plate hydrofoil can be predicted precisely by using one lifting line instead of the whole hydrofoil when $\tilde{h}\geqslant 1$.

In addition, it is found that some irregular oscillating characters appear on the curves of lift and drag coefficients versus Froude number when $F_{RC}<1$ and $\tilde{h}=0.25$ for $M=1$ and $N=11$. This phenomenen will be vanished as soon as $M=4$ and $N=11$. It means that treating the hydrofoil as a lifting surface is essential at low Froude number and shallow submergence chord ratio.

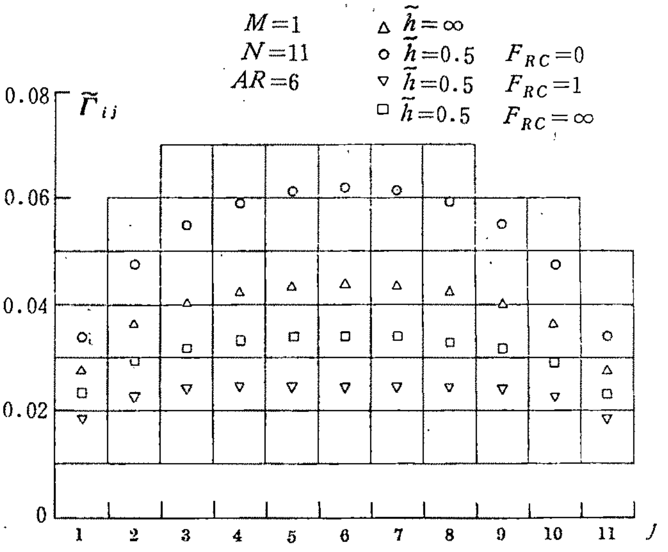

Fig. 6

The results of the distribution of spanwise non-dimensional circulation strength $\tilde{\Gamma}_{1j}=\frac{\Gamma_{1j}}{UC}$ are plotted in Fig. 6 with various submergence chord ratio and Froude number for the case of $M=1$, $N=11$.

The relation between C_L and N also C_D/C_L^2 and N are given in Fig. 7 and Fig. 8. It

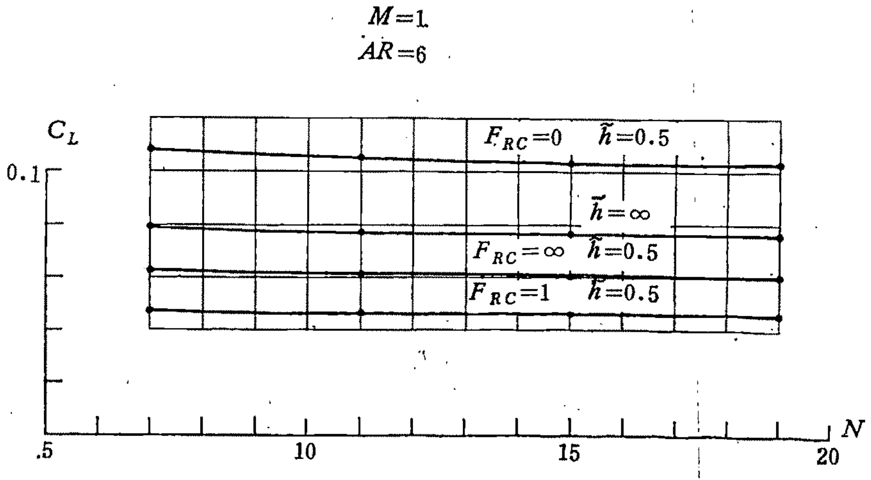

Fig. 7

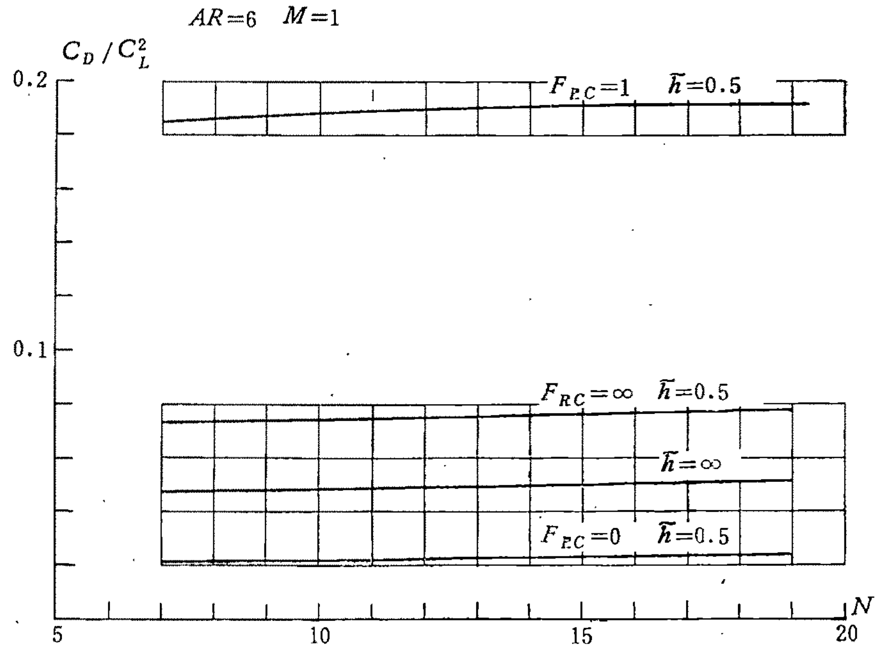

Fig. 8

is shown that the values of C_L as well as C_D/C_L^2 will be approximately independent of the amounts of spanwise segments in case of $N \geqslant 15$.

Fig. 9 compares the present numerical results with some experimental data extracted from [3]. Fig. 10 gives a contrast at lower Froude number, where the results of test are quoted from [4]. The agreement between numerical result and experimental data is, in general, quite good. It is indicated that the numerical technique presented in this paper gives adequate accuracy to predict the hydrodynamic characteristics of a hydrofoil.

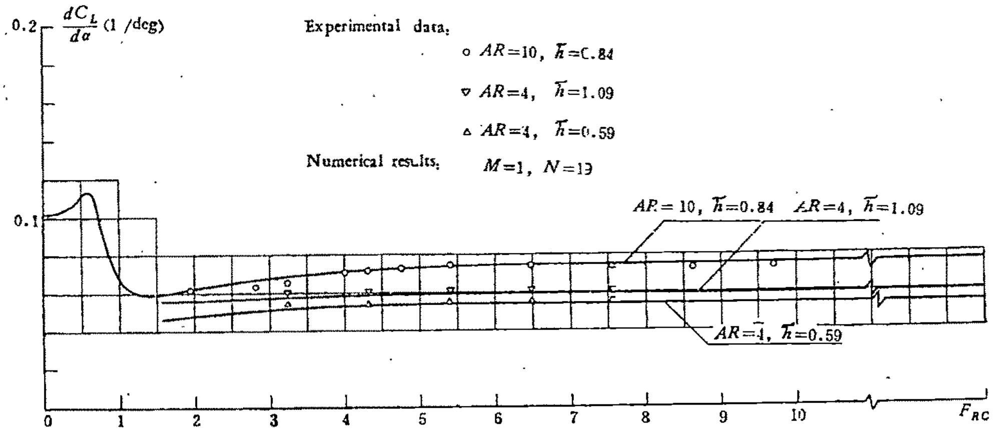

Fig. 9

A rough estimate of pressure difference distribution ΔC_{pij} on both surface of a plate hydrofoil is given in Fig. 11. Of course, it is known that the pressure function has a jump on the mean-camber surface and is odd with respect to z on the upper and lower surface of foil.

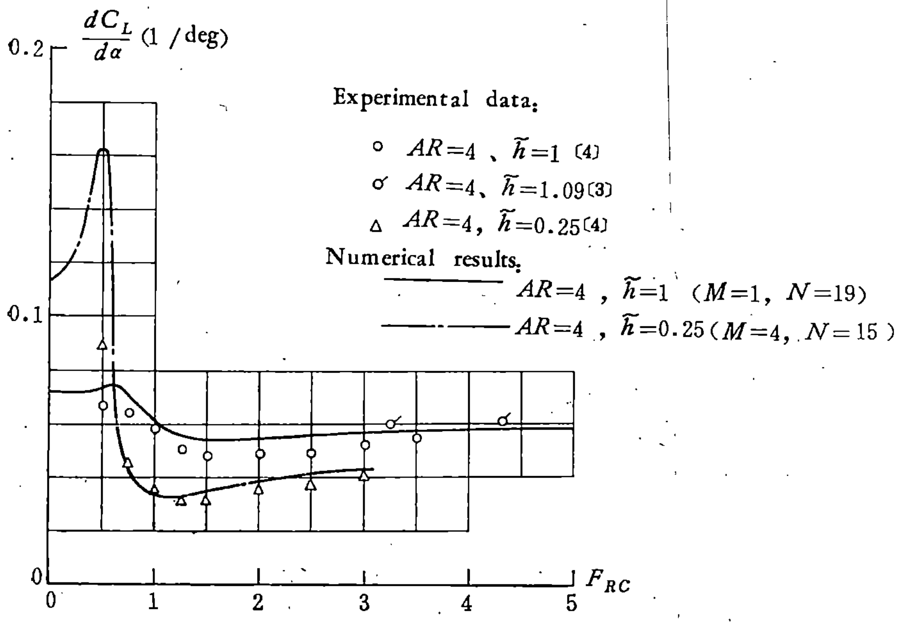

Fig. 10

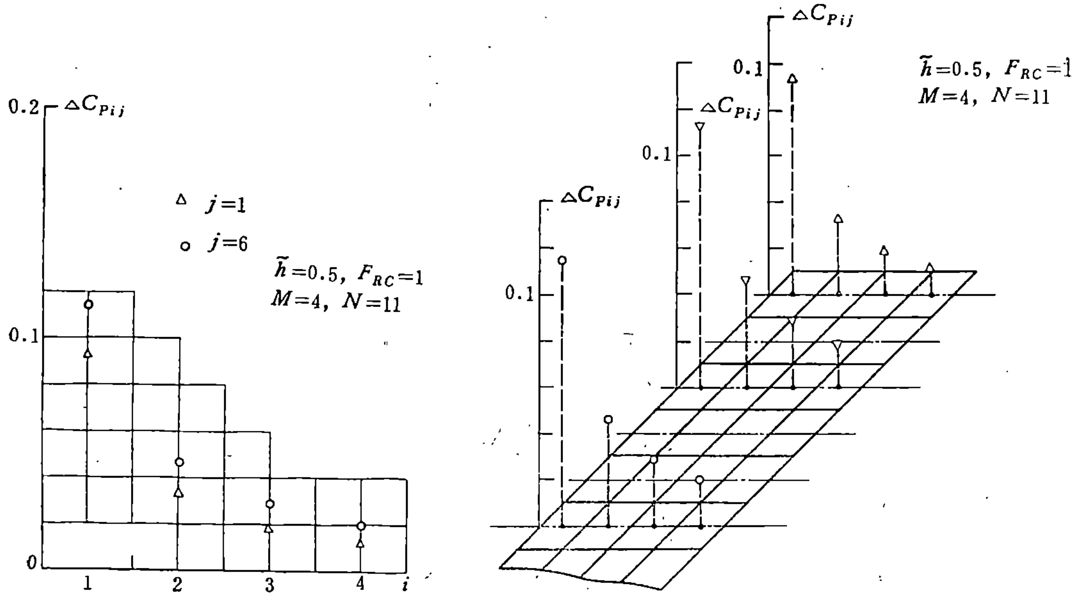

Fig. 11

V. Conclusions

1. The comparison of theory and experiment shows that the numerical technique described in this study is proved to be a good prediction method for the hydrodynamic properties of a hydrofoil in a wide range of Froude number and submergence chord ratio.

2. In order to improve the computational results, a lifting surface approximation introduced

is essential in case of lower Froude number and shallower submergence.

3. The possibility to predict accurately the flow velocity and pressure distribution on the hydrofoil surface is provided for estimation of cavitation inception, boundary layer development and so on.

References

[1] Y. T. Wu: *A Theory for Hydrofoils of Finite Span.* **Journal of Math. and Phys.** Vol. 33, No. 3, 1954.

[2] T. Nishiyama: *Lifting-Surface Theory of a Fully Submerged Hydrofoil.* **J. S. R.** Vol. 8, No.4, 1965.

[3] K. L. Wadlin: *A Theoretical and Experimental Investigation of the Lift and Drag Characteristics of Hydrofoils at Subcritical and Supercritical Speeds,* **NACA**, TR–1232, 1955.

[4] M. B. Wilson and D. L. Gregory: *Large Flat Plate Hydrofoil Experiments at Low Froude Numbers.* **NSRDC SPD-706-01, AD-A029023, 1976.**

Annual of the CSNAME, Vol. 1, 1982

A-FUNCTION——A SPECIAL FUNCTION USED IN NAVAL HYDRODYNAMICS

Chen Caikan (陈材侃)

Huazhong Institute of Technology

SUMMARY

In this paper, a special function is defined and given the name of *A*-Function.

$$A_r^s(z) = (-1)^k \int_0^{\pi/2} \sin^s\theta \cos^r\theta \, e^{iz\sec\theta} d\theta$$

A-Function is divided into 4 groups, *C*, *D*, *E* and *F* which not only contain Euler's first integral, i.e. *B*-Function, Havelock-Function and some kernel functions given by J. N. Newman, F. C. Michelson and Chuan Lee widely used in naval hydrodynamics. These functions have been expanded immensely. The differential circular relationship and the circular formulae of *A*-Function are established. For each group of functions, we give 9 functions respectively as examples. Their series expansions, asymptotic expansions for large $|z|$ and general formulae of their coefficients are derived. The differential equations satisfied for each group of functions are described. For real z, the values of these functions are calculated and they are functions decreasing alternately.

I. Introduction

Swiss mathematician Euler once discussed an integral including two parameters over two hundred years ago. It is named Euler's first integral (i.e. *B*–Function). From 1923 to 1925, when studying wave resistance, J. H. Havelock discussed a special function named Havelock-function which was republished in [1] and [2]. In 1963 J. N. Newman presented his paper "The determination of wave resistance from the wave pattern" at the International Seminar on theoretical wave resistance [3]. A kernel function $K(z)$ was defined and its series expansion and asymptotic expansion for large $|z|$ was also given in his paper. In 1971 F. C. Michelsen and S. B. S. Uberoi also discussed the kernel function $K(z)$[4], and in 1974 Chuan Lee gave several other kernel functions when studying wave resistance of a point dipole[5].

Prior to this paper I have published another one entitled "Program for the Analysis of the longitudinal wave profile and calculation of the kernel function $K(z)$" in the Journal of Shipbuilding of China, No. 2. 1981 [6]. $K(z)$ was discussed and the correct formulas of the coefficients were derived in that paper.

Since then, I have made further investigations on these special functions, which have resulted in the present paper.

In this paper, a new special function is defined and named *A*-Function, denoted $A_r^s(z)$ for short. It is an integral including three parameters and divided into 4 groups, *C*,*D*,*E* and *F*.

When $z=0$, $A_r^s(0)$ becomes *B*-Function and when $s=0$, $C_r^0(z)$ becomes Havelock-Function. And $C_r^2(z)$ is the kernel function $K(z)$ given by Newman, $F_1^1(z)$ and $F_2^1(z)$ are other two kernel functions given by Chuan Lee. They are widely used in naval hydrodynamics. The *A*-Function not only contains these functions, they have been expanded immensely. The properties of *A*-Function are studied in a systematic way in this paper.

It is expected that the *A*-Function will be applied more extensively in naval hydrodynamics.

II. Definitions and Theorems

1. Definitions

Definition 1: A special function defined with formula (2.1) is called *A*-Function:

$$A_r^s(z)=(-1)^k\int_0^{\pi/2}\sin^s\theta\cos^r\theta\, e^{iz\sec\theta}\,d\theta=(-1)^k\int_0^{\pi/2}\sin^s\theta\cos^r\theta\cos(z\sec\theta)\,d\theta$$

$$+i(-1)^k\int_0^{\pi/2}\sin^s\theta\cos^r\theta\sin(z\sec\theta)\,d\theta \qquad (2.1)$$

$$\mathrm{Im}(z)\geqslant 0$$

where z=complex variable

θ=real variable

s=row-mark

=$2l$ or $2l+1$

r=column-mark

=$2k$ or $2k-1$

l or k=0, 1, 2, 3......

It can be proved when $\mathrm{Im}(z)>0$, $A_r^s(z)$ is analytical function and when $\mathrm{Im}(z)=0$, the integral given by (2.1) is convergent. Thus, (2.1) is defined when $\mathrm{Im}(z)\geqslant 0$ and denoted by A_r^s.

As the row-mark and the column-mark take an even or odd number, we can get four formulas, as follows:

$$\left.\begin{aligned}A_{2k-1}^{2l}&=C_{2k-1}^{2l}+iD_{2k-1}^{2l}\\A_{2k}^{2l}&=D_{2k}^{2l}+iC_{2k}^{2l}\\A_{2k-1}^{2l+1}&=E_{2k-1}^{2l+1}+iF_{2k-1}^{2l+1}\\A_{2k}^{2l+1}&=F_{2k}^{2l+1}+iE_{2k}^{2l+1}\end{aligned}\right\}\qquad (2.2)$$

Thus, we have obtained four groups of functions in *A*-Function. They are defined as follows:

Definition 2: *C*-Function

$$\left.\begin{aligned} C_{2k-1}^{2l}(z) &= (-1)^k \int_0^{\pi/2} \sin^{2l}\theta \cos^{2k-1}\theta \cos(z\cdot\sec\theta)\,d\theta \\ C_{2k}^{2l}(z) &= (-1)^k \int_0^{\pi/2} \sin^{2l}\theta \cos^{2k}\theta \sin(z\cdot\sec\theta)\,d\theta, \quad \mathrm{Im}(z)\geqslant 0 \end{aligned}\right\} \tag{2.3}$$

Definition 3: *D*–Function

$$\left.\begin{aligned} D_{2k-1}^{2l}(z) &= (-1)^k \int_0^{\pi/2} \sin^{2l}\theta \cos^{2k-1}\theta \sin(z\cdot\sec\theta)\,d\theta \\ D_{2k}^{2l}(z) &= (-1)^k \int_0^{\pi/2} \sin^{2l}\theta \cos^{2k}\theta \cos(z\cdot\sec\theta)\,d\theta, \quad \mathrm{Im}(z)\geqslant 0 \end{aligned}\right\} \tag{2.4}$$

Definition 4: *E*–Function

$$\left.\begin{aligned} E_{2k-1}^{2l+1}(z) &= (-1)^k \int_0^{\pi/2} \sin^{2l+1}\theta \cos^{2k-1}\theta \cos(z\cdot\sec\theta)\,d\theta \\ E_{2k}^{2l+1}(z) &= (-1)^k \int_0^{\pi/2} \sin^{2l+1}\theta \cos^{2k}\theta \sin(z\cdot\sec\theta)\,d\theta, \quad \mathrm{Im}(z)\geqslant 0 \end{aligned}\right\} \tag{2.5}$$

Definition 5: *F*–Function

$$\left.\begin{aligned} F_{2k-1}^{2l+1}(z) &= (-1)^k \int_0^{\pi/2} \sin^{2l+1}\theta \cos^{2k-1}\theta \sin(z\cdot\sec\theta)\,d\theta \\ F_{2k}^{2l+1}(z) &= (-1)^k \int_0^{\pi/2} \sin^{2l+1}\theta \cos^{2k}\theta \cos(z\cdot\sec\theta)\,d\theta, \quad \mathrm{Im}(z)\geqslant 0 \end{aligned}\right\} \tag{2.6}$$

C–, *D*–, *E*– and *F*–Functions are related to Bessel Functions[7], Sine Integral and Cosine Integral respectively. As we shall see later, it is necessary and convenient to divide *A*–Function into four groups.

2. Theorems

Theorem 1: The differential circular relationship of *A*–Function is

$$\left.\begin{aligned} \frac{d}{dz}A_{2k}^{s} &= iA_{2k-1}^{s} \\ \frac{d}{dz}A_{2k-1}^{s} &= -iA_{2k-2}^{s} \end{aligned}\right\} \tag{2.7}$$

Differentiating (2.1), we can prove this theorem. And we can deduce following formulas for each group of function from (2.7).

$$\frac{d^n}{dz^n}C_r^{2l} = C_{r-n}^{2l} \tag{2.8}$$

$$\frac{d^n}{dz^n}D_r^{2l} = (-1)^n D_{r-n}^{2l} \tag{2.9}$$

$$\frac{d^n}{dz^n}E_r^{2l+1} = E_{r-n}^{2l+1} \tag{2.10}$$

$$\frac{d^n}{dz^n}F_r^{2l+1} = (-1)^n F_{r-n}^{2l+1} \tag{2.11}$$

Theorem 2: The circular formula of the functions with different row–marks is

$$A_r^s = A_r^{s-2} + A_{r+2}^{s-2} \tag{2.12}$$

By deducing, we have:

$$C_r^{2l} = C_r^{2l-2} + C_{r+2}^{2l-2} \tag{2.13}$$

$$D_r^{2l} = D_r^{2l-2} + D_{r-2}^{2l-2} \tag{2.14}$$

$$E_r^{2l+1} = E_r^{2l-1} + E_{r-2}^{2l-1} \tag{2.15}$$

$$F_r^{2l+1} = F_r^{2l-1} + F_{r+2}^{2l-1} \tag{2.16}$$

Theorem 3: When $r \geqslant 2$ the circular formula of the functions with the same row–mark is

$$\left.\begin{aligned} (2k+s)A_{2k}^{s} &= iz(A_{2k-1}^{s} + A_{2k-3}^{s}) - (2k-1)A_{2k-2}^{s} \\ [(2k-1)+s]A_{2k-1}^{s} &= -iz(A_{2k-2}^{s} + A_{2k-4}^{s}) - [(2k-1)-1]A_{2k-3}^{s} \end{aligned}\right\} \tag{2.17}$$

By deducing, we have:

$$(r+2l)C_r^{2l} = z(C_{r-1}^{2l} + C_{r-3}^{2l}) - (r-1)C_{r-2}^{2l} \tag{2.18}$$

$$(r+2l)D_r^{2l} = -z(D_{r-1}^{2l} + D_{r-3}^{2l}) - (r-1)D_{r-2}^{2l} \tag{2.19}$$

$$(r+2l+1)E_r^{2l+1} = z(E_{r-1}^{2l+1} + E_{r-3}^{2l+1}) - (r-1)E_{r-2}^{2l+1} \tag{2.20}$$

$$(r+2l+1)F_r^{2l+1} = -z(F_{r-1}^{2l+1} + F_{r-3}^{2l+1}) - (r-1)F_{r-2}^{2l+1} \tag{2.21}$$

3. The relationships between *A*–Function and *B*–Function, Bessel Function, Si(*z*), Ci(*z*)

From the definition of Euler's first integral and (2.1), we have:

$$A_r^s(0) = (-1)^k \int_0^{\pi/2} \sin^s\theta \cos^r\theta \, d\theta = (-1)^k \frac{\Gamma\left(\frac{s+1}{2}\right) \cdot \Gamma\left(\frac{r+1}{2}\right)}{2\Gamma\left(\frac{s+r}{2}+1\right)}$$

$$= \frac{(-1)^k}{2} B\left(\frac{s+1}{2}, \frac{r+1}{2}\right) \tag{2.22}$$

From the integral representations of Bessel Functions and (2.1), (2.2), we have:

$$A_{-1}^0(z) = \frac{\pi i}{2} H_0^{(1)}(z) = \frac{\pi i}{2}[J_0(z) + iY_0(z)] \tag{2.23}$$

Similarly, from the definitions of *Si*(*z*) and *Ci*(*z*) and (2.1), (2.2), we obtain:

$$A_{-1}^1(z) = -Ei(iz) = -Ci(z) + i\left[\frac{\pi}{2} - Si(z)\right] \tag{2.24}$$

III C-Function

We can see that if we know the formulae of three fundamental functions in the same row, it is possible to derive the formula of each function in this row by (2.18). By using (2.13), from the functions in this row we can derive those in the adjacent row. That is to say, the whole group of *C*–Function can be derived from the three functions. Therefore, we first establish the formulas of C_{-1}^0, C_0^0 and C_1^0.

From the integral representations of Bessel Functions and (2.3), we get:

$$C_{-1}^0(z) = -\frac{\pi}{2} Y_0(z) \tag{3.1}$$

$$C_0^0(z) = -\frac{\pi}{2} \int_0^z Y_0(z) \, dz \tag{3.2}$$

$$C_1^0(z) = z\frac{\pi}{2}\left[Y_1(z) - \int_0^z Y_0(z)\,dz\right] \tag{3.3}$$

Putting the series expansions of Bessel Functions and those of the integrals of Bessel Functions into (3.1), (3.2) and (3.3), we get:

$$C_{-1}^0(z) = \sum_{r=0}^{\infty}\frac{(-1)^{r+1}(z/2)^{2r}}{(r!)^2}[\ln(z/2)-\psi(r+1)], \qquad |\arg z|<\pi \tag{3.4}$$

$$C_0^0(z) = 2\sum_{r=0}^{\infty}\frac{(-1)^{r+1}(z/2)^{2r+1}}{(r!)^2(2r+1)}\left[\ln(z/2)-\psi(r+1)-\frac{1}{2r+1}\right], \quad |\arg z|<\pi \tag{3.5}$$

$$C_1^0(z) = 2\sum_{r=0}^{\infty}\frac{(-1)^{r+1}(z/2)^{2r+2}}{(r!)^2(2r+1)(r+1)}\left[\ln(z/2)-\psi(r+1)-\frac{4r+3}{2(r+1)(2r+1)}\right]-1$$
$$|\arg z|<\pi \tag{3.6}$$

By using (2.13) and (2.18), we can derive the series expansion of each function in C–Function. We give formulas of another six functions as examples:

$$C_{-1}^2(z) = \sum_{r=0}^{\infty}\frac{(-1)^{r}(z/2)^{2r}}{(r!)^2(2r-1)}\left[\ln(z/2)-\psi(r+1)-\frac{1}{2r-1}\right] \tag{3.7}$$

$$C_2^0(z) = 4\sum_{r=0}^{\infty}\frac{(-1)^{r}(z/2)^{2r+1\cdot r}}{(r!)^2(2r+1)(2r-1)}\left[\ln(z/2)-\psi(r+1)-\frac{4r^2+1}{2r(2r+1)(2r-1)}\right] \tag{3.8}$$

$$C_0^2(z) = 2\sum_{r=0}^{\infty}\frac{(-1)^{r}(z/2)^{2r+1}}{(r!)^2(2r+1)(2r-1)}\left[\ln(z/2)-\psi(r+1)-\frac{4r}{(2r+1)(2r-1)}\right] \tag{3.9}$$

$$C_3^0(z) = 4\sum_{r=0}^{\infty}\frac{(-1)^{r}(z/2)^{2r+2\cdot r}}{(r!)^2(2r+1)(2r-1)(r+1)}\left[\ln(z/2)-\psi(r+1)\right.$$
$$\left.-\frac{8r^3+4r^2+1}{2r(2r+1)(2r-1)(r+1)}\right]+\frac{2}{3} \tag{3.10}$$

$$C_1^2(z) = 2\sum_{r=0}^{\infty}\frac{(-1)^{r}(z/2)^{2r+2}}{(r!)^2(2r+1)(2r-1)(r+1)}\left[\ln(z/2)-\psi(r+1)\right.$$
$$\left.-\frac{12r^2+8r-1}{2(r+1)(2r+1)(2r-1)}\right]-\frac{1}{3} \tag{3.11}$$

$$C_{-1}^4(z) = 3\sum_{r=0}^{\infty}\frac{(-1)^{r+1}(z/2)^{2r}}{(r!)^2(2r-1)(2r-3)}\left[\ln(z/2)-\psi(r+1)-\frac{4(r-1)}{(2r-1)(2r-3)}\right] \tag{3.12}$$

It ought to be pointed out that C–Function expressed by these serieses can be extended analytically to the whole plane, save cut $(-\infty, 0)$.

Putting the asymptotic expansions of Bessel Functions and the asymptotic expansions of their integrals into (3.1), (3.2) and (3.3), we obtain asymptotic expansions of C_{-1}^0, C_0^0 and C_1^0. It is convenient to derive the asymptotic expansion of each function in C–Function by theorem 4.

Theorem 4: When $/z/\gg 1$ and $\mathrm{Im}(z)\geqslant 0$, if the general form of the asymptotic expansion of C–Function is

$$\left.\begin{aligned}
C_{2k-1}^{2l}(z)&\sim\sqrt{\frac{\pi}{2z}}\Bigg[\sum_{m=0}^{\infty} A_m^{\binom{2l}{2k-1}}\left(\frac{1}{z}\right)^{2m+1}\cos\left(z-\frac{\pi}{4}\right)\\
&\quad+\sum_{m=0}^{\infty} B_m^{\binom{2l}{2k-1}}\left(\frac{1}{z}\right)^{2m}\sin\left(z-\frac{\pi}{4}\right)\Bigg]\\
C_{2k}^{2l}(z)&\sim\sqrt{\frac{\pi}{2z}}\Bigg[\sum_{m=0}^{\infty} A_m^{\binom{2l}{2k}}\left(\frac{1}{z}\right)^{2m}\cos\left(z-\frac{\pi}{4}\right)\\
&\quad+\sum_{m=0}^{\infty} B_m^{\binom{2l}{2k}}\left(\frac{1}{z}\right)^{2m+1}\sin\left(z-\frac{\pi}{4}\right)\Bigg]
\end{aligned}\right\}\qquad(3.13)$$

then, their coefficients satisfy the following circular formulae:

$$\left.\begin{aligned}
A_m^{\binom{2l}{2k}}&=\frac{1}{2k+2l}\left[\left(A_m^{\binom{2l}{2k-1}}+A_m^{\binom{2l}{2k-3}}\right)-(2k-1)\,A_m^{\binom{2l}{2k-2}}\right]\\
B_m^{\binom{2l}{2k}}&=\frac{1}{2k+2l}\left[\left(B_{m+1}^{\binom{2l}{2k-1}}+B_{m+1}^{\binom{2l}{2k-3}}\right)-(2k-1)B_m^{\binom{2l}{2k-2}}\right]
\end{aligned}\right\}\qquad(3.14)$$

$$\left.\begin{aligned}
A_m^{\binom{2l}{2k-1}}&=\frac{1}{2k+2l-1}\left[\left(A_{m+1}^{\binom{2l}{2k-2}}+A_{m+1}^{\binom{2l}{2k-4}}\right)-(2k-2)\,A_m^{\binom{2l}{2k-3}}\right]\\
B_m^{\binom{2l}{2k-1}}&=\frac{1}{2k+2l-1}\left[\left(B_m^{\binom{2l}{2k-2}}+B_m^{\binom{2l}{2k-4}}\right)-(2k-2)\,B_m^{\binom{2l}{2k-3}}\right]
\end{aligned}\right\}\qquad(3.15)$$

$$\left.\begin{aligned}
A_m^{\binom{2l}{r}}&=A_m^{\binom{2l-2}{r}}+A_m^{\binom{2l-2}{r+2}}\\
B_m^{\binom{2l}{r}}&=B_m^{\binom{2l-2}{r}}+B_m^{\binom{2l-2}{r+2}}
\end{aligned}\right\}\qquad(3.16)$$

Substituting (3.13) into (2.13) and (2.18), we can prove this theorem. We give the formulas of the coefficients of 9 functions, as follows:

$$\left.\begin{aligned}
A_m^{\binom{0}{-1}}&=\frac{(-1)^m\Gamma^2(2m+1\frac{1}{2})}{\pi(2m+1)!\,2^{2m+1}}\\
B_m^{\binom{0}{-1}}&=\frac{(-1)^{m+1}\Gamma^2(2m+\frac{1}{2})}{\pi(2m)!\,2^{2m}}
\end{aligned}\right\}\qquad(3.17)$$

$$\left.\begin{aligned}
A_m^{\binom{0}{0}}&=\frac{(-1)^m\Gamma(2m+\frac{1}{2})}{\pi}\sum_{n=0}^{2m}\frac{\Gamma(n+\frac{1}{2})}{2^n n!}\\
B_m^{\binom{0}{0}}&=\frac{(-1)^m\Gamma(2m+1\frac{1}{2})}{\pi}\sum_{n=0}^{2m+1}\frac{\Gamma(n+\frac{1}{2})}{2^n n!}
\end{aligned}\right\}\qquad(3.18)$$

$$\left.\begin{aligned}
A_m^{\binom{0}{1}}&=\frac{(-1)^{m+1}\Gamma(2m+2\frac{1}{2})}{\pi}\sum_{n=0}^{2m+1}\frac{\Gamma(n+\frac{1}{2})}{n!\,2^n}+\frac{(-1)^{m+1}\Gamma^2(2m+1\frac{1}{2})}{\pi(2m+1)!\,2^{2m+1}}(2m+1\tfrac{1}{2})\\
B_m^{\binom{0}{1}}&=\frac{(-1)^m\Gamma(2m+1\frac{1}{2})}{\pi}\sum_{n=0}^{2m}\frac{\Gamma(n+\frac{1}{2})}{n!\,2^n}+\frac{(-1)^m\Gamma^2(2m+\frac{1}{2})}{\pi(2m)!\,2^{2m}}(2m+\tfrac{1}{2})
\end{aligned}\right\}\qquad(3.19)$$

$$\left.\begin{aligned}
A_m^{\binom{2}{-1}} &= \frac{(-1)^{m+1}\Gamma(2m+2\frac{1}{2})}{\pi}\sum_{n=0}^{2m+1}\frac{\Gamma(n+\frac{1}{2})}{n!\,2^n}+\frac{(-1)^{m+1}\Gamma^2(2m+1\frac{1}{2})}{\pi(2m+1)!\,2^{2m+1}}(2m+\tfrac{1}{2})\\
B_m^{\binom{2}{-1}} &= \frac{(-1)^{m}\Gamma(2m+1\frac{1}{2})}{\pi}\sum_{n=0}^{2m}\frac{\Gamma(n+\frac{1}{2})}{n!\,2^n}+\frac{(-1)^{m}\Gamma^2(2m+\frac{1}{2})}{\pi(2m)!\,2^{2m}}(2\mathrm{m}-\tfrac{1}{2})
\end{aligned}\right\}\quad(3.20)$$

$$\left.\begin{aligned}
A_m^{\binom{0}{2}} &= \frac{(-1)^{m+1}\Gamma(2m+\frac{1}{2})}{2\pi}\left[\left(2m+\frac{1}{2}\right)\left(2m+\frac{3}{2}\right)+1\right]\sum_{n=0}^{2m}\frac{\Gamma(n+\frac{1}{2})}{n!\,2^n}\\
&\quad+\frac{(-1)^{m+1}\Gamma^2(2m+1\frac{1}{2})}{\pi(2m)!\,2^{2m+1}}\\
B_m^{\binom{0}{2}} &= \frac{(-1)^{m+1}\Gamma(2\mathrm{m}+1\frac{1}{2})}{2\pi}\left[\left(2m+\frac{3}{2}\right)\left(2m+\frac{5}{2}\right)+1\right]\sum_{n=0}^{2m+1}\frac{\Gamma(n+\frac{1}{2})}{n!\,2^n}\\
&\quad+\frac{(-1)^{m+1}\Gamma^2(2m+2\frac{1}{2})}{\pi(2m+1)!\,2^{2m+2}}
\end{aligned}\right\}\quad(3.21)$$

$$\left.\begin{aligned}
A_m^{\binom{2}{0}} &= \frac{(-1)^{m+1}\Gamma(2m+\frac{1}{2})}{2\pi}\left[\left(2m+\frac{1}{2}\right)\left(2m+\frac{3}{2}\right)-1\right]\sum_{n=0}^{2m}\frac{\Gamma(n+\frac{1}{2})}{n!\,2^n}\\
&\quad+\frac{(-1)^{m+1}\Gamma^2(2\mathrm{m}+1\frac{1}{2})}{\pi(2m)!\,2^{2m+1}}\\
B_m^{\binom{2}{0}} &= \frac{(-1)^{m+1}\Gamma(2m+1\frac{1}{2})}{2\pi}\left[\left(2m+\frac{3}{2}\right)\left(2m+\frac{5}{2}\right)-1\right]\sum_{n=0}^{2m+1}\frac{\Gamma(n+\frac{1}{2})}{n!\,2^n}\\
&\quad+\frac{(-1)^{m+1}\Gamma^2(2m+2\frac{1}{2})}{\pi(2m+1)!\,2^{2m+2}}
\end{aligned}\right\}\quad(3.22)$$

$$\left.\begin{aligned}
A_m^{\binom{0}{3}} &= \frac{1}{3}\left\{\frac{(-1)^{m}\Gamma(2m+2\frac{1}{2})}{2\pi}\left[\left(2m+\frac{5}{2}\right)\left(2m+\frac{7}{2}\right)+3\right]\sum_{n=0}^{2m+1}\frac{\Gamma(n+\frac{1}{2})}{n!\,2^n}\right.\\
&\quad\left.+\frac{(-1)^{m}\Gamma^2(2m+2\frac{1}{2})}{\pi(2m+2)!\,2^{2m+2}}\left[\left(2\mathrm{m}+\frac{5}{2}\right)\left(2m+3\right)+\frac{4}{4m+3}+\frac{7}{2}\right]\right\}\\
B_m^{\binom{0}{3}} &= \frac{1}{3}\left\{\frac{(-1)^{m+1}\Gamma(2m+1\frac{1}{2})}{2\pi}\left[\left(2m+\frac{3}{2}\right)\left(2m+\frac{5}{2}\right)+3\right]\sum_{n=0}^{2m}\frac{\Gamma(n+\frac{1}{2})}{n!\,2^n}\right.\\
&\quad\left.+\frac{(-1)^{m+1}\Gamma^2(2m+1\frac{1}{2})}{\pi(2m+1)!\,2^{2m+1}}\left[\left(2m+\frac{3}{2}\right)(2m+2)+\frac{4}{4m+1}+\frac{7}{2}\right]\right\}
\end{aligned}\right\}\quad(3.23)$$

$$\left.\begin{aligned}
A_m^{\binom{2}{1}} &= \frac{(-1)^{m}\Gamma(2m+2\frac{1}{2})}{\pi}\left[\left(2m+\frac{5}{2}\right)\left(2m+\frac{7}{2}\right)\Big/6-\frac{1}{2}\right]\sum_{n=0}^{2m+1}\frac{\Gamma(n+\frac{1}{2})}{n!\,2^n}\\
&\quad+\frac{(-1)^{m}\Gamma^2(2m+2\frac{1}{2})}{3\pi(2m+2)!\,2^{2m+2}}\left[\left(2m+\frac{5}{2}\right)(2m+3)-\frac{2}{4m+3}-\frac{5}{2}\right]\\
B_m^{\binom{2}{1}} &= \frac{(-1)^{m+1}\Gamma(2m+1\frac{1}{2})}{\pi}\left[\left(2m+\frac{3}{2}\right)\left(2m+\frac{5}{2}\right)\Big/6-\frac{1}{2}\right]\sum_{n=0}^{2m}\frac{\Gamma(n+\frac{1}{2})}{n!\,2^n}\\
&\quad+\frac{(-1)^{m+1}\Gamma^2(2m+1\frac{1}{2})}{3\pi(2m+1)!\,2^{2m+1}}\left[\left(2m+\frac{3}{2}\right)(2m+2)-\frac{2}{4m+1}-\frac{5}{2}\right]
\end{aligned}\right\}\quad(3.24)$$

G 10,104

$$\left.\begin{aligned} A_m^{\binom{4}{-1}} &= \frac{(-1)^m \Gamma(2m+2\frac{1}{2})}{\pi}\left[\left(2m+\frac{5}{2}\right)\left(2m+\frac{7}{2}\right)\Big/6-\frac{3}{2}\right]\sum_{n=0}^{2m-1}\frac{\Gamma(n+\frac{1}{2})}{n!\,2^n} \\ &\quad+\frac{(-1)^m \Gamma^2(2m+2\frac{1}{2})}{3\pi(2m+2)!2^{2m+2}}\left[\left(2m+\frac{5}{2}\right)(2m+3)+\frac{2(2m+3)}{(2m+3/2)^2}-\frac{17}{2}\right] \\ B_m^{\binom{4}{-1}} &= \frac{(-1)^{m+1} \Gamma(2m+1\frac{1}{2})}{\pi}\left[\left(2m+\frac{3}{2}\right)\left(2m+\frac{5}{2}\right)\Big/6-\frac{3}{2}\right]\sum_{n=0}^{2m}\frac{\Gamma(n+\frac{1}{2})}{n!\,2^n} \\ &\quad+\frac{(-1)^{m+1} \Gamma^2(2m+1\frac{1}{2})}{3\pi(2m+1)!2^{2m+1}}\left[\left(2m+\frac{3}{2}\right)(2m+2)+\frac{4(m+1)}{(2m+\frac{1}{2})^2}-\frac{17}{2}\right] \end{aligned}\right\} \quad (3.25)$$

The values of the first nine coefficients are listed in table 1 in the appendix. Formula (3.20) is in accord with that of the kernel function $K(z)$ given in [2].

When calculating the values of C–Function for a real variable we can see that if we use (2.18) directly there will be a large error for large z. And the factor z isn't included in (3.14), (3.15) and (3.16). Therefore, the calculation of the coefficients is not influenced by z.

When $s=0$, C_r^0 is the famous Havelock function. As (3.1), C_{-1}^0 is a particular solution satisfying the following linear homogeneous differential equation of the second order having variable coefficient $1/z$.

$$u''+\frac{1}{z}u'+u=0 \quad (3.26)$$

We can see from (2.8) that the $C_r^0(z)$ satisfies a differential equation of the $(r+3)$ order,

$$u^{(r+3)}+\frac{1}{z}u^{(r+2)}+u^{(r+1)}=0 \quad (3.27)$$

And when $s=2l$, $C_r^{2l}(z)$ satisfies a non–homogeneous differential equation,

$$u^{(r+3)}+\frac{1}{z}u^{(r+2)}+u^{(r+1)}=\sum_{i=0}^{l-1}\left[C_{-1}^{2i}(z)+\frac{1}{z}C_0^{2i}(z)+C_1^{2i}(z)\right] \quad (3.28)$$

The right side of the equation consists of non–homogeneous terms including the sum of the functions having column-mark $r=-1, 0, 1$ and row–mark $s=0\sim 2(l-1)$. According to the principle of mathematical induction and by using (2.13) and (2.18), we can prove (3.28).

IV. *D*-Function

We can study D–Function with the same method as C–Function and give the following results:

$$D_{-1}^0(z)=\frac{\pi}{2}J_0(z) \quad (4.1)$$

$$D_0^0(z)=\frac{\pi}{2}\left(1-\int_0^z J_0(z)\,dz\right) \quad (4.2)$$

$$D_1^0(z)=-z\left(\frac{\pi}{2}J_1(z)+D_0^0(z)\right) \quad (4.3)$$

The series expansions of D–Function are

$$D_{-1}^0(z)=\frac{\pi}{2}\sum_{r=0}^{\infty}\frac{(-1)^r(z/2)^{2r}}{(r!)^2} \quad (4.4)$$

$$D_0^0(z)=\frac{\pi}{2}\left[1-2\sum_{r=0}^{\infty}\frac{(-1)^r(z/2)^{2r+1}}{(r!)^2(2r+1)}\right] \tag{4.5}$$

$$D_1^0(z)=-\frac{\pi z}{2}\left[1-\sum_{r=0}^{\infty}\frac{(-1)^r(z/2)^{2r+1}}{(r!)^2(2r+1)(r+1)}\right] \tag{4.6}$$

$$D_{-1}^2(z)=\frac{\pi}{2}\left[1-z+\sum_{r=0}^{\infty}\frac{(-1)^r(z/2)^{2r+2}}{[(r+1)!]^2(2r+1)}\right] \tag{4.7}$$

$$D_2^0(z)=-\frac{\pi}{4}\left[1-z^2+8\sum_{r=0}^{\infty}\frac{(-1)^{r+1}(z/2)^{2r+1}\cdot r}{(r!)^2(2r+1)(2r-1)}\right] \tag{4.8}$$

$$D_0^2(z)=\frac{\pi}{4}\left[1+z^2+4\sum_{r=0}^{\infty}\frac{(-1)^r(z/2)^{2r+1}}{(r!)^2(2r+1)(2r-1)}\right] \tag{4.9}$$

$$D_3^0(z)=\frac{\pi z}{4}\left[1-\frac{z^2}{3}-4\sum_{r=0}^{\infty}\frac{(-1)^r(z/2)^{2r+1}\cdot r}{(r!)^2(2r+1)(2r-1)(r+1)}\right] \tag{4.10}$$

$$D_1^2(z)=\frac{-\pi z}{4}\left[1+\frac{z^2}{3}+2\sum_{r=0}^{\infty}\frac{(-1)^r(z/2)^{2r+1}}{(r!)^2(2r+1)(2r-1)(r+1)}\right] \tag{4.11}$$

$$D_{-1}^4(z)=\frac{\pi}{4}\left[2-3z-\frac{z^3}{3}-6\sum_{r=0}^{\infty}\frac{(-1)^r(z/2)^{2r+2}}{[(r+1)!]^2(2r+1)(2r-1)}\right] \tag{4.12}$$

These series of *D*–Function are convergent on the whole plane, so *D*–Function expressed by the series is an entire function. Theorem 5 expresses the relationships between the coefficients of the asymptotic expansion of *D*–Function and those of *C*–Function.

Theorem 5: When $|z|\gg 1$ and $\mathrm{Im}(z)\geqslant 0$, suppose the general form of the asymptotic expansion of *D*–Function is

$$\left.\begin{aligned}
D_{2k-1}^{2l}(z) &\backsim \sqrt{\frac{\pi}{2z}}\left[\sum_{m=0}^{\infty} a_m^{\binom{2l}{2k-1}}\left(\frac{1}{z}\right)^{2m}\cos\left(z-\frac{\pi}{4}\right)\right.\\
&\qquad \left.-\sum_{m=0}^{\infty} b_m^{\binom{2l}{2k-1}}\left(\frac{1}{z}\right)^{2m+1}\sin\left(z-\frac{\pi}{4}\right)\right]\\
D_{2k}^{2l}(z) &\backsim \sqrt{\frac{\pi}{2z}}\left[\sum_{m=0}^{\infty} a_m^{\binom{2l}{2k}}\left(\frac{1}{z}\right)^{2m+1}\cos\left(z-\frac{\pi}{4}\right)\right.\\
&\qquad \left.-\sum_{m=0}^{\infty} b_m^{\binom{2l}{2k}}\left(\frac{1}{z}\right)^{2m}\sin\left(z-\frac{\pi}{4}\right)\right]
\end{aligned}\right\} \tag{4.13}$$

Then, we have:

$$\left.\begin{aligned}
a_m^{\binom{2l}{2k-1}} &= -B_m^{\binom{2l}{2k-1}}\\
b_m^{\binom{2l}{2k-1}} &= -A_m^{\binom{2l}{2k-1}}
\end{aligned}\right\} \tag{4.14}$$

$$\left.\begin{aligned}
a_m^{\binom{2l}{2k}} &= B_m^{\binom{2l}{2k}}\\
b_m^{\binom{2l}{2k}} &= A_m^{\binom{2l}{2k}}
\end{aligned}\right\} \tag{4.15}$$

According to theorem 5, we can obtain the coefficients of D–Function from the formulas of the coefficients of C–Function, and the values in table 1 can be used directly.

Like C–Function, $D^0_{-1}(z)$ satisfies the differential equation (3.26) and $D^0_r(z)$ satisfies (3.27). $D^{2l}_r(z)$ satisfies the following non–homogeneous differential equation

$$u^{(r+3)}+\frac{1}{z}\,u^{(r+2)}+u^{(r+1)}=\sum_{i=0}^{l-1}\left[(-1)^{r+3}D^{2i}_{-1}(z)+(-1)^{r+2}\cdot\frac{1}{z}\,D^{2i}_{0}(z)+(-1)^{r+1}D^{2i}_{1}(z)\right] \tag{4.16}$$

V. *E*-Function

From the definition of Cosine Integral and (2.5), we can find the relationships between E–Function and $Ci(z)$, as follows:

$$E^1_{-1}(z)=-Ci(z) \tag{5.1}$$

$$E^1_0(z)=\sin z-zCi(z) \tag{5.2}$$

$$E^1_1(z)=\frac{1}{2}[z\sin z-\cos z-z^2Ci(z)] \tag{5.3}$$

$$E^1_2(z)=\frac{1}{6}[(z^2-2)\sin z-z\cos z-z^3Ci(z)] \tag{5.4}$$

$$E^1_3(z)=\frac{1}{24}[z(z^2-2)\sin z+(6-z^2)\cos z-z^4Ci(z)] \tag{5.5}$$

$$E^3_{-1}(z)=\frac{1}{2}[z\sin z-\cos z-(2+z^2)Ci(z)] \tag{5.6}$$

$$E^3_0(z)=\frac{1}{6}[(z^2+4)\sin z-z\cos z-z(6+z^2)Ci(z)] \tag{5.7}$$

$$E^3_1(z)=\frac{1}{24}[z(z^2+10)\sin z-(6+z^2)\cos z-z^2(12+z^2)Ci(z)] \tag{5.8}$$

$$E^5_{-1}(z)=\frac{1}{24}[z(z^2+22)\sin z-(18+z^2)\cos z-(24+24z^2+z^4)Ci(z)] \tag{5.9}$$

These E–Functions expressed by above 9 formulae are analytic on the whole plane save cut $(-\infty,\ 0)$, because $Ci(z)$ is analytic in same region.

$E^{2l+1}_r(z)$ satisfies a non–homogeneous differential equation of $(r+2)$ order.

$$u^{(r+2)}=-\cos z/z+\sum_{i=0}^{l-1}E^{2i+1}_0(z) \tag{5.10}$$

VI. *F*-Function

From the definition of sine integral and (2.6), we give the relationship between F–Function and $Si(z)$, as follows:

$$F^1_{-1}(z)=\frac{\pi}{2}-Si(z) \tag{6.1}$$

$$F_0^1(z)=\cos z-zF_{-1}^1(z) \tag{6.2}$$

$$F_1^1(z)=\frac{1}{2}[-z\cos z-\sin z+z^2F_{-1}^1(z)] \tag{6.3}$$

$$F_2^1(z)=\frac{1}{6}[(z^2-2)\cos z+z\sin z-z^3F_{-1}^1(z)] \tag{6.4}$$

$$F_3^1(z)=\frac{1}{24}[(6-z^2)\sin z+z(2-z^2)\cos z+z^4F_{-1}^1(z)] \tag{6.5}$$

$$F_{-1}^3(z)=\frac{1}{2}[-\sin z-z\cos z+(2+z^2)F_{-1}^1(z)] \tag{6.6}$$

$$F_0^3(z)=\frac{1}{6}[z\sin z+(4+z^2)\cos z-z(6+z^2)F_{-1}^1(z)] \tag{6.7}$$

$$F_1^3(z)=\frac{1}{24}[-(6+z^2)\sin z-z(10+z^2)\cos z+z^2(12+z^2)F_{-1}^1(z)] \tag{6.8}$$

$$F_{-1}^5(z)=\frac{1}{24}[-(18+z^2)\sin z-z(22+z^2)\cos z+(24+24z^2+z^4)F_{-1}^1(z)] \tag{6.9}$$

These F–Functions expressed by above 9 formulae are entire functions because $Si(z)$ is analytic on the whole plane.

$F_r^{2l+1}(z)$ satisfies a non–homogeneous differential equation of $(r+2)$ order.

$$u^{(r+2)}=(-1)^r\sin z/z+(-1)^r\sum_{i=0}^{l-1}F_0^{2i+1}(z) \tag{6.10}$$

VII. Results of Calculation and Discussion

We have calculated the values of 36 functions for real variable $x=0.1$, 0.2, 0.3,......50. The results are expressed in the tables and graphs in the appendix. The error of calculation, $\delta<10^{-6}$. The region usable for the asymptotic expansions of C–Function and that of D–Function is listed in the last row in Table 1.

They are all functions decreasing alternately which vanish when x approaches infinity. The greater the values of s or r, the more rapidly the values of the functions are decreased. These functions have an infinite number of real zero points which appear aperiodically. The limits of C_{-1}^{2l} and E_{-1}^{2l+1} approach infinity as x approaches zero. The absolute values of all functions except C_{-1}^{2l} and E_{-1}^{2l+1} are no larger than $\pi/2$. Under A–Function the real axis in the z–plane maps onto many helices that converge to an origin gradually.

References

[1] Milton Abramowitz and Irene A. Stegun: *Handbook of Mathematical Functions with Formulas Graphs, and Mathematical Tables*, U. S. Depart. of Commerce and National Bureau of Standards, Washington, June 1964.

[2] Yudell L. Luke: Integrals of Bessel Function, McGraw-Hill Book Company, New York, Toronto, London, 1962.

[3] J. N. Newman: *The determination of wave resistance from wave measurements along a parallel cut*, **Proc. International Seminar on Theoretical Wave Resistance**, Ann. Arbor. Mich. Aug. 1963.

[4] F. C. Michelsen and S. B. S. Uberoi: *A study of wave resistance characteristics through the analysis of wave height and slope along a longitudinal track*, Hydro-and Aerodynamics Laboratory Report, No. Hy-15, Denmark, Aug. 1971.

[5] Chuan Lee: *Some numerical results on wave resistance of a point dipole*, **Journal of Ship Research**, Vol. 19, No. 3, 1975.

[6] Chen Caikan: *Program for the analysis of the longitudinal wave profile and calculation of the kernel function $K(z)$*, **Journal of Shipbuilding of China**, No. 2, 1981.

[7] N. W. Mclachlan: Bessel Function for engineers, Oxford at the clarendon press, 1955.

Appendix

Table and Graphs

Table 1 Values of the Coefficients

	$C^0_{-1}(z)$	$C^0_0(z)$	$C^0_1(z)$	$C^2_{-1}(z)$	$C^0_2(z)$	$C^2_0(z)$		$C^0_3(z)$	$C^2_1(z)$	$C^4_{-1}(z)$
m	$A_m^{\binom{0}{-1}}$	$A_m^{\binom{0}{0}}$	$A_m^{\binom{0}{1}}$	$A_m^{\binom{2}{-1}}$	$A_m^{\binom{0}{2}}$	$A_m^{\binom{2}{0}}$	m	$A_m^{\binom{0}{3}}$	$A_m^{\binom{2}{1}}$	$A_m^{\binom{4}{-1}}$
0	0.125	1.0	−1.125	−1.0	−1.0	0	0	2.125	1.0	0
1	−0.073242187	−1.0078125	9.3310546	9.2578125	5.1328125	4.125	1	−42.963867	−33.632812	−24.375
2	0.22710800	9.1868591	$-2.2987295\ 10^{2}$	$-2.2964584\ 10^{2}$	$-1.1941635\ 10^{2}$	$-1.1022949\ 10^{2}$	2	$1.9813010\ 10^{3}$	$1.751428\ 10^{3}$	$1.5217822\ 10^{3}$
3	−1.7277275	$-2.2919635\ 10^{2}$	$1.1199238\ 10^{4}$	$1.119751\ 10^{4}$	$5.7133535\ 10^{3}$	$5.4841571\ 10^{3}$	3	$-1.5630434\ 10^{5}$	$-1.451051\ 10^{5}$	$-1.3390759\ 10^{5}$
4	24.380529	$1.1192354\ 10^{4}$	$-9.0424585\ 10^{6}$	$-9.0422147\ 10^{6}$	$-4.5770691\ 10^{5}$	$-4.4651456\ 10^{5}$	4	$1.8649665\ 10^{7}$	$1.7745419\ 10^{7}$	$1.6841198\ 10^{7}$
5	−551.33589	$-9.0412425\ 10^{6}$	$1.0918568\ 10^{8}$	$1.0918513\ 10^{8}$	$5.5044628\ 10^{7}$	$5.4140504\ 10^{7}$	5	$-3.125427\ 10^{9}$	$-3.0162413\ 10^{9}$	$-2.9070562\ 10^{9}$
6	18257.755	$1.0918238\ 10^{8}$	$-1.842502\ 10^{10}$	$-1.8425001\ 10^{10}$	$-9.267092\ 10^{9}$	$-9.1579096\ 10^{9}$	6	$6.9938245\ 10^{11}$	$6.8095743\ 10^{11}$	$6.6253243\ 10^{11}$
7	−832859.30	$-1.8424892\ 10^{10}$	$4.1410203\ 10^{12}$	$4.1410195\ 10^{12}$	$2.0797222\ 10^{14}$	$2.0612973\ 10^{12}$	7	$-2.0135708\ 10^{14}$	$-1.9721606\ 10^{14}$	$-1.9307504\ 10^{14}$
8	50069589	$4.1410137\ 10^{12}$	$-1.1957194\ 10^{15}$	$-1.1957194\ 10^{15}$	$-5.9993021\ 10^{14}$	$-5.957892\ 10^{14}$	8	$7.2490489\ 10^{16}$	$7.129477\ 10^{16}$	$7.009905\ 10^{16}$
m	$B_m^{\binom{0}{-1}}$	$B_m^{\binom{0}{0}}$	$B_m^{\binom{0}{1}}$	$B_m^{\binom{2}{-1}}$	$B_m^{\binom{0}{2}}$	$B_m^{\binom{2}{0}}$	m	$B_m^{\binom{0}{3}}$	$B_m^{\binom{2}{1}}$	$B_m^{\binom{4}{-1}}$
0	−1.0	0.625	1.0	0	−1.625	−1.0	0	−1.0	0	0
1	0.0703125	−2.5927734	−2.6953125	−2.625	22.163085	19.570312	1	8.3203125	5.625	3.0
2	−0.11215209	41.567974	41.84555	41.733398	$-7.6724653\ 10^{2}$	$-7.2567855\ 10^{2}$	2	$-2.6978988\ 10^{2}$	$-2.2794433\ 10^{2}$	$-1.8621093\ 10^{2}$
3	0.57250142	$-1.4915040\ 10^{3}$	$-1.4934975\ 10^{3}$	$-1.492925\ 10^{3}$	$4.8336036\ 10^{4}$	$4.6844532\ 10^{4}$	3	$1.6610509\ 10^{4}$	$1.5117011\ 10^{4}$	$1.3624086\ 10^{4}$
4	−6.0740420	$9.5159393\ 10^{4}$	$9.5186642\ 10^{4}$	$9.5180568\ 10^{4}$	$-4.7947546\ 10^{6}$	$-4.6995952\ 10^{6}$	4	$-1.6299895\ 10^{6}$	$-1.5348028\ 10^{6}$	$-1.4396222\ 10^{6}$
5	110.017414	$-9.493856\ 10^{6}$	$-9.4944598\ 10^{6}$	$-9.4943498\ 10^{6}$	$6.9815428\ 10^{8}$	$6.7766043\ 10^{8}$	5	$2.3221645\ 10^{8}$	$2.2272199\ 10^{8}$	$2.1322764\ 10^{8}$
6	−3038.0905	$1.3647980\ 10^{9}$	$1.3648177\ 10^{9}$	$1.3048147\ 10^{9}$	$-1.3426367\ 10^{11}$	$-1.3289887\ 10^{11}$	6	$-4.5209502\ 10^{10}$	$-4.3844685\ 10^{10}$	$-4.247987\ 10^{10}$
7	118838.42	$-2.6716177\ 10^{11}$	$-2.6716266\ 10^{11}$	$-2.6716254\ 10^{11}$	$3.4296992\ 10^{13}$	$3.4029830\ 10^{13}$	7	$1.1521385\ 10^{13}$	$1.1254222\ 10^{13}$	$1.098706\ 10^{13}$
8	−6252951.4	$6.8326776\ 10^{13}$	$6.8326829\ 10^{13}$	$6.8326823\ 10^{13}$	$-1.1094568\ 10^{16}$	$-1.1026241\ 10^{16}$	8	$-3.7209649\ 10^{15}$	$-3.6526381\ 10^{15}$	$-3.5843113\ 10^{15}$
	$\|z\|>10$	$\|z\|>13$	$\|z\|>15$	$\|z\|>16$	$\|z\|>16$	$\|z\|>17$		$\|z\|>17$	$\|z\|>18$	$\|z\|>18$

Table 2 Values of $C_r^s(x)$

x \ $C_r^s(x)$	$C_{-1}^0(x)$	$C_0^0(x)$	$C_1^0(x)$	$C_2^0(x)$	$C_3^0(x)$
0	∞	0	−1	0	0.666667
0.1	2.409976	0.341539	−0.980415	−0.099292	0.661685
1.0	−0.138634	1.000700	−0.226420	−0.682880	0.256889
5.0	0.484618	−0.313718	−0.407277	0.350210	0.332338
10.0	−0.087448	−0.379018	0.121346	0.358997	−0.147633
20.0	−0.098396	0.264233	0.084960	−0.266472	−0.071568
50.0	0.154040	0.086102	−0.155634	−0.082905	0.157031

x \ $C_r^s(x)$	$C_{-1}^2(x)$	$C_0^2(x)$	$C_1^2(x)$	$C_{-1}^4(x)$	
0	∞	0	−0.333333	∞	
0.1	1.429561	0.242247	−0.318730	1.110830	
1.0	−0.365053	0.317826	0.030469	−0.334585	
5.0	0.077340	0.036492	−0.074940	0.002401	
10.0	0.033898	−0.020021	−0.026287	0.007611	
20.0	−0.013436	−0.002239	0.013396	−0.000043	
50.0	−0.001594	0.003197	0.001397	−0.000197	

Table 3 Values of $D_r^s(x)$

x \ $D_r^s(x)$	$D_{-1}^0(x)$	$D_0^0(x)$	$D_1^0(x)$	$D_2^0(x)$	$D_3^0(x)$
0	1.570796	1.570796	0	−0.785398	0
0.1	1.566872	1.413848	−0.149229	−0.777806	0.078285
1.0	1.201969	0.126087	−0.817317	−0.255370	0.587972
5.0	−0.278968	0.447187	0.336866	−0.363337	−0.355995
10.0	−0.386315	−0.105261	0.359743	0.135492	−0.347263
20.0	0.262362	−0.091701	−0.255600	0.073246	0.266870
50.0	0.087670	0.154861	−0.034513	−0.155358	0.081282

x \ $D_r^s(x)$	$D_{-1}^2(x)$	$D_0^2(x)$	$D_1^2(x)$	$D_{-1}^4(x)$	
0	1.570796	0.785398	0	1.570796	
0.1	1.417643	0.636042	−0.070944	1.346699	
1.0	0.384653	−0.129283	−0.229344	0.155308	
5.0	0.057897	0.078850	−0.019129	0.038768	
10.0	−0.016572	0.030230	0.022479	0.005907	
20.0	−0.003238	−0.013470	0.001270	−0.001968	
50.0	0.003157	−0.001496	−0.003231	0.000074	

Table 4 Values of $E_r^s(x)$

x \ $E_r^s(x)$	$E_{-1}^1(x)$	$E_0^1(x)$	$E_1^1(x)$	$E_2^1(x)$	$E_3^1(x)$
0	∞	0	−0.5	0	0.25
0.1	1.727868	0.272620	−0.483871	−0.049407	0.247516
1.0	−0.337404	0.504067	−0.018118	−0.286529	0.0634432
5.0	0.190030	−0.008776	−0.163770	0.046692	0.129280
10.0	0.045456	−0.089457	−0.027748	0.088846	0.012347
20.0	−0.044420	0.024549	0.041447	−0.027999	−0.037978
50.0	0.005628	0.019044	−0.006371	−0.018733	0.007084

x \ $E_r^s(x)$	$E_{-1}^3(x)$	$E_0^3(x)$	$E_1^3(x)$	$E_{-1}^5(x)$	
0	∞	0	−0.25	∞	
0.1	1.243997	0.223213	−0.236355	1.007642	
1.0	−0.355522	0.217538	0.045326	−0.310196	
5.0	0.026260	0.037916	−0.034490	−0.008230	
10.0	0.017708	−0.000611	−0.015401	0.002307	
20.0	−0.002973	−0.003451	0.003469	0.000497	
50.0	−0.000743	0.000312	0.000713	−0.000030	

Table 5 Values of $F_r^s(x)$

x \ $F_r^s(x)$	$F_{-1}^1(x)$	$F_0^1(x)$	$F_1^1(x)$	$F_2^1(x)$	$F_3^1(x)$
0	1.570796	1	0	−0.333333	0
0.1	1.470852	0.847919	−0.092313	−0.328591	0.033173
1.0	0.624713	−0.084411	−0.378530	−0.053924	0.223849
5.0	0.020865	0.179337	0.031120	−0.146421	−0.056705
10.0	−0.087551	0.036441	0.089805	−0.019659	−0.086858
20.0	0.022555	−0.043010	—0.026368	0.039760	0.029436
50.0	0.019179	0.006003	—0.018895	−0.006732	0.018553

x \ $F_r^s(x)$	$F_{-1}^3(x)$	$F_0^3(x)$	$F_1^3(x)$	$F_{-1}^5(x)$	
0	1.570796	0.666667	0	1.570796	
0.1	1.378539	0.519328	−0.059140	1.319400	
1.0	0.246183	−0.138335	−0.154681	0.091502	
5.0	0.051985	0.032916	−0.025585	0.026401	
10.0	0.002254	0.016782	0.002947	0.005200	
20.0	−0.003813	−0.003250	0.003068	−0.000745	
50.0	0.000284	−0.000728	−0.000342	−0.000057	

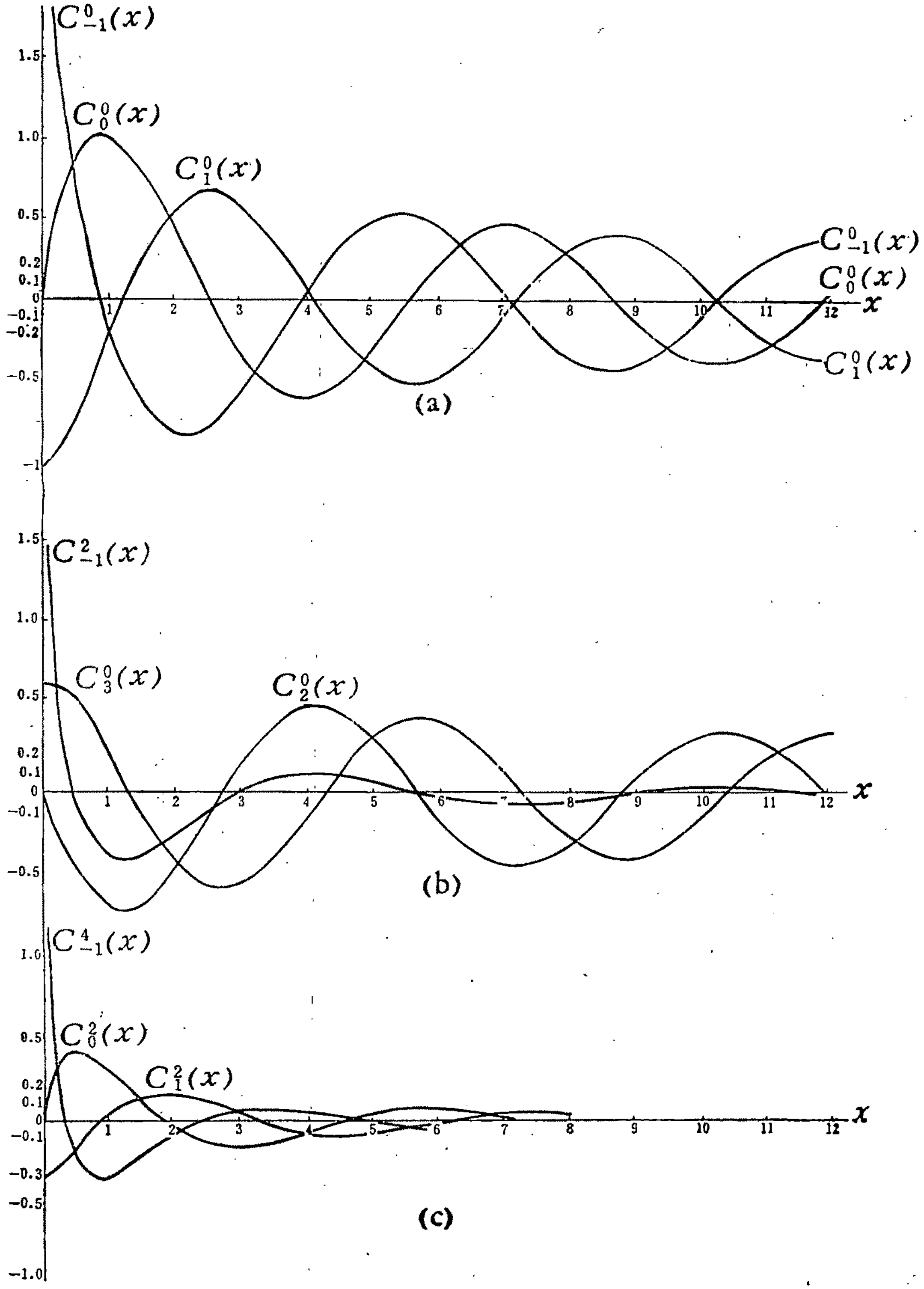

Fig. 1 Curves of C-Function

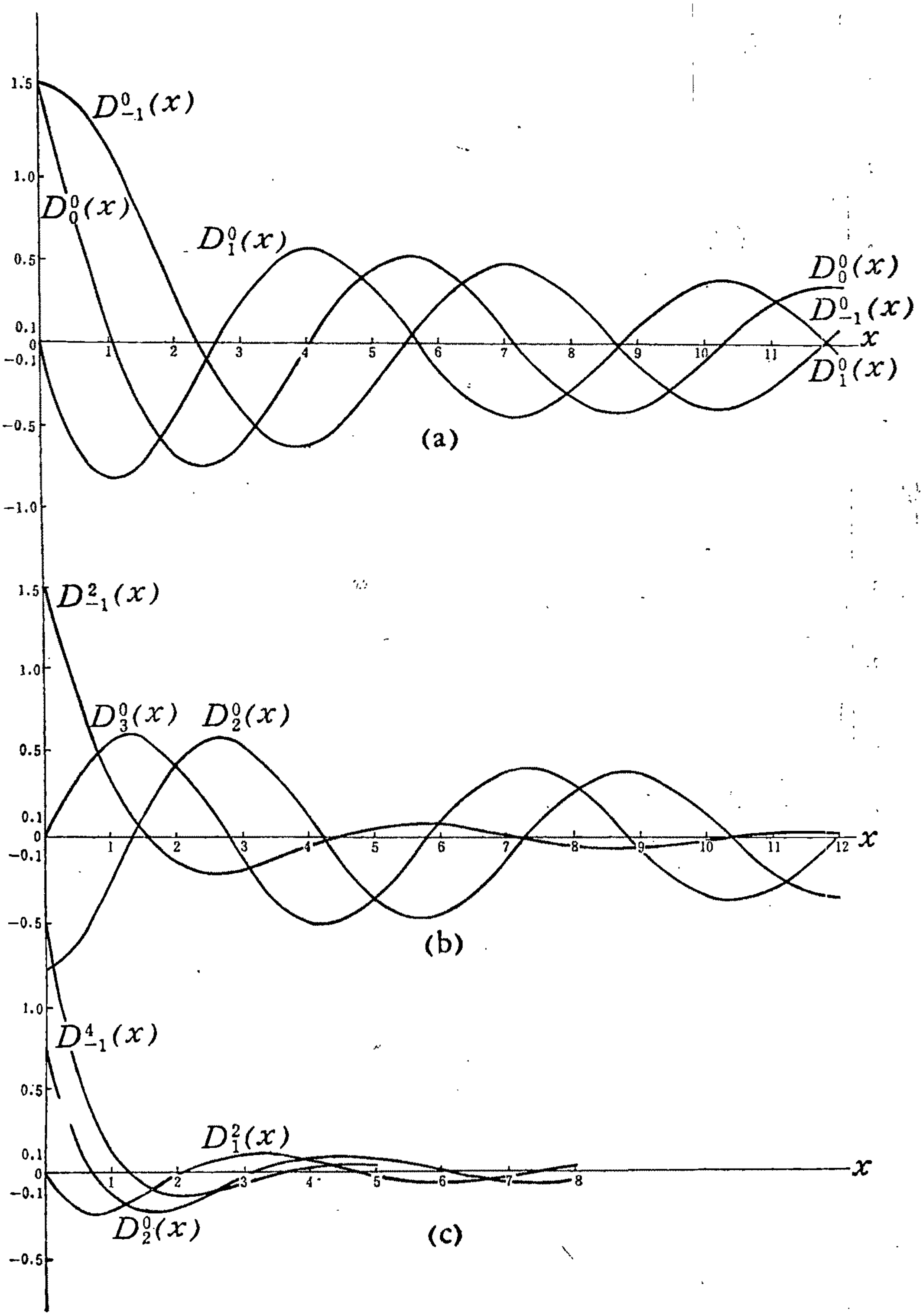

Fig. 2 Curves of *D*-Function

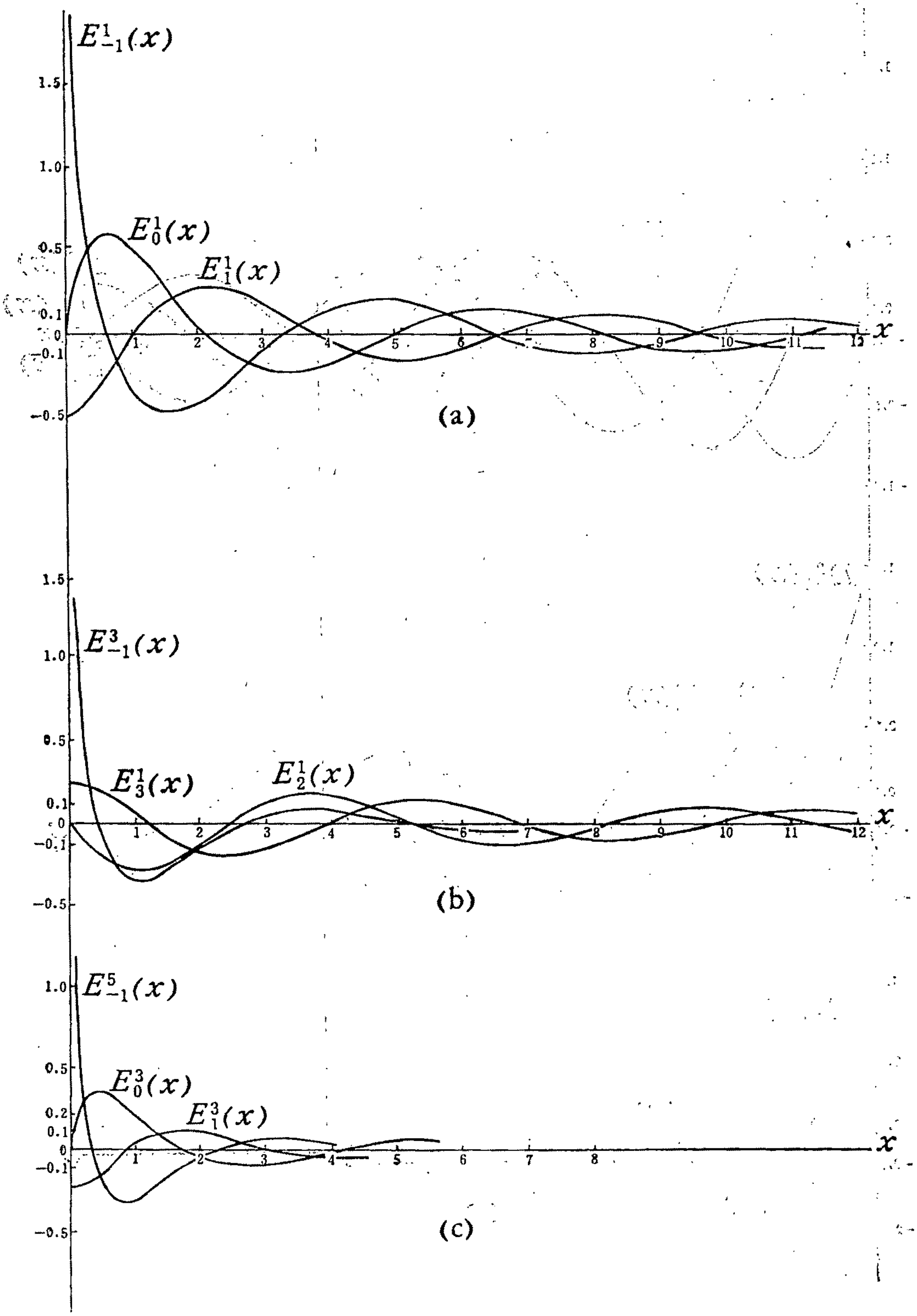

Fig. 3 Curves of E-Function

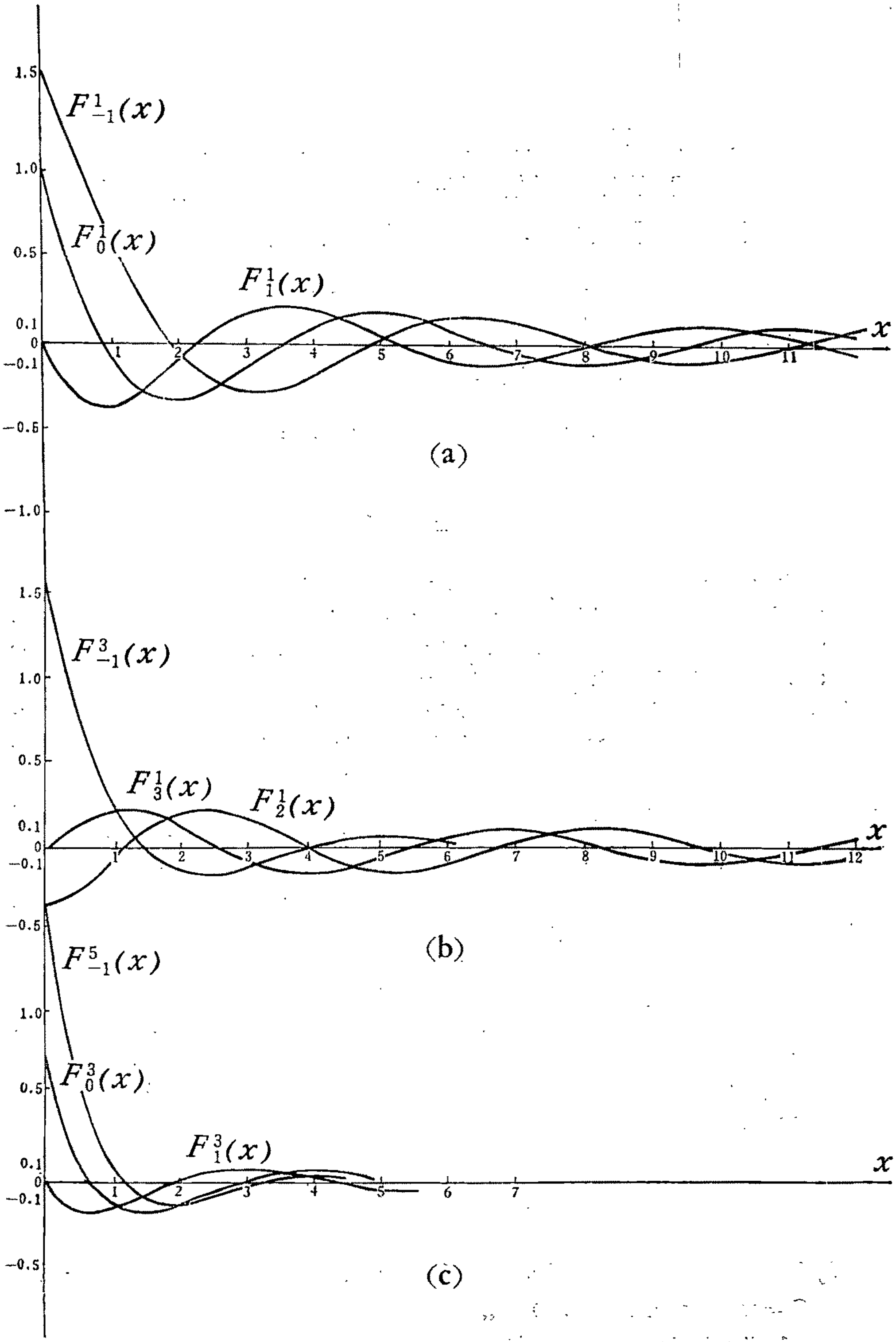

Fig. 4 Curves of *F*-Function

Annual of the CSNAME, Vol. 1, 1982

A STREAMLINE-ITERATION METHOD FOR CALCULATING TURBULENT FLOW AROUND THE STERN OF A BODY OF REVOLUTION AND ITS WAKE

ZHOU LIANDI (周连弟)
China Ship Scientific Research Center

SUMMARY

This paper presents a new numerical method for calculating viscous flow around the stern of a body of revolution and its wake using a two-equation (K-ε) model developed by Harlow and Nakayama[1] and modelled by Launder and Spalding[2]. The features of this method are: (1) The grid points calculated are taken on mean-flow streamlines and on radial straight lines, thus the convection terms of the governing equations for total pressure, turbulent kinetic energy and its dissipation rate can be written in the form of their variations along streamlines. For static pressure the radial pressure gradient equation is used. These equations are convenient for numerical calculations. The mean-flow streamlines, however, are not known beforehand and must be determined by an iterative scheme. (2) By means of a system of coordinate transformations, the calculating region is extended to infinity in both radial and axial direction. By doing so, the free-stream condition and the parabolic flow condition may be used at the outer and downstream boundary respectively. The flow in the boundary layer and the potential flow outside the boundary layer can be determined by an uniform equation system. (3) Assumptions for a thin boundary layer and partially parabolic flow etc. are exempted.

The velocity profiles, the variations of static pressure and turbulent properties calculated theoretically at some axial stations are compared with the experiments by Huang et al.[3], the agreements being satisfactory. For the wake, the accuracy of the present method is higher than that of Muraoka's method[4][5].

Nomenclature

C_1, C_2, C_D=constants of the (K-ε) turbulence model

C_p=pressure coefficient, $(p-p_\infty)/\frac{1}{2}\rho V_\infty^2$

f=distribution profile of K

g=distribution profile of l_m

K=turbulent kinetic energy

l=distance along spatial streamline

$\vec{l}^\circ$=unit vector in spatial streamline direction

l_m=mixing length

L=length of a body of revolution

m=meridional streamline, distance along meridional streamline

p=static pressure (time-averaged)

p_0=total pressure, $p+\frac{1}{2}\rho V^2$

p_∞=free-stream static pressure

q=arbitrary spatial curve, distance along an spatial curve

Q_0=mass rate of flow

r, θ, z=cylindrical polar coordinates

r_0=local radius of a body of revolution

$r_{\max}$=maximum radius of a body of revolution

R_n=Reynolds number

S=distance from the leading edge

u, v, w=axial, radial and circumferential velocity components in a cylindrical polar coordinate system (time-averaged)

V=velocity, $\sqrt{u^2+v^2+w^2}$

V_m=meridional velocity, $\sqrt{u^2+v^2}$

V_∞=free-stream velocity

z=axial coordinate

α=angle made by meridional streamlines with the z-axis

δ, δ_r=boundary layer thickness

ε=dissipation rate of turbulence energy

η, ξ=coordinate transformations of r, z

μ_e, μ_t, μ_{eff}, ν=coefficients of viscosity

ρ=density

$\sigma_{\mathrm{eff},K}$, $\sigma_{\mathrm{eff},\varepsilon}$=Prandtl/Schmidt number

τ=stress

φ=a general fluid variable

ω=relaxation factor used to modify the location of streamlines

I. Introduction

Theoretical predictions of flow field around ship stern and its wake are among the most important problems in naval hydrodynamics. In order to reduce cavitation erosion, vibration excitation and noise due to propeller-hull interaction and to prepare guidelines for afterbody design of ships, it is considered necessary to predict the flow around ship stern and its wake.

Many research workers are engaged in this work. Among the methods for calculating turbulence flow around ship stern, the numerical method adopting two-equation (K-ε) turbulence model and partially parabolic flow assumption is the most effective and popular one at present[4-8]. For example, two papers for calculating turbulent flow presented at the 13th Symposium of Naval Hydrodynamics both employed this method. As mentioned by Markatos and Wills[8], however, there is a serious drawback in the above method, namely, the necessity of prescribing the locations of the outer and downstream boundary and of determining boundary conditions at these boundaries by potential flow solution. As a result, additional calculations have to be carried out to evaluate these boundary conditions, and the accuracy of computed results also deteriorates. In this paper, the external flow field extended to infinity in both radial and axial directions is transformed into an internal flow field within a finite region by means of a system of coordinate transformations. By doing so, the free-stream condition and the parabolic flow condition may be used at the outer (infinity in radial direction) and the downstream boundary (infinity in axial direction), respectively; and the boundary layer flow and the potential flow outside the boundary layer can be determined by an uniform equation system, thus evading this drawback. Further steps will be taken to generalize this method to be applied to the case of ship stern.

Following the works of [9] [10], in this paper the streamline-iteration method, which has been widely employed for calculating internal flow field in turbine machine channels, is further generalized to the calculation of turbulent flow around the stren of a body of revolution and its wake using the popular two-equation (K-ε) turbulence model. A curvilinear non-orthogonal coordinate system is employed. One set of coordinate lines coincide with the mean-flow streamlines, the other set are composed of radial straight lines. So the convection terms of the governing equations for total pressure, turbulent kinetic energy and its dissipation rate in turbulent flow can be written in the form of their variations along streamlines. For static pressure the radial pressure gradient equation is used. These equations are convenient for numerical calculations. The mean-flow streamlines, however, are not known beforehand and must be determined by an iterative scheme. First, assume the initial locations of the streamlines and the initial distributions of the fluid variables along streamline, then solve the governing equations to evaluate the new distributions and the new locations of the streamlines. Repeat the calculation procedure until convergence is obtained. On solving differential equations, assumptions for a thin boundary layer and partially parabolic flow etc. are exempted.

Calculations have been carried out by using the present method for a body of revolution which is named Afterbody 1 by Huang et al.[3] The calculated results agree with Huang's experiment satisfactorily. For the wake, the accuracy of the computed results by using the present method is higher than that of Muraoka's[4][5].

II. Basic Equations

In calculating the three-dimensional incompressible turbulent flow by two-equation (K-ε)

turbulence model, the unknown variables are u, v, w; p and K, ε.

In a cylindrical polar coordinate system, the time-averaged velocity components and static pressure are governed by following equations:

Continuity equation:

$$\frac{\partial u}{\partial z}+\frac{1}{r}\frac{\partial}{\partial r}(rv)+\frac{1}{r}\frac{\partial w}{\partial \theta}=0 \qquad (1)$$

Axial momentum equation:

$$\frac{\partial}{\partial z}(uu)+\frac{1}{r}\frac{\partial}{\partial r}(ruv)+\frac{1}{r}\frac{\partial}{\partial \theta}(uw)$$

$$=-\frac{1}{\rho}\frac{\partial p}{\partial z}+\frac{1}{\rho}\left\{\underline{\frac{\partial}{\partial z}(\tau_{zz})}+\frac{1}{r}\left[\frac{\partial}{\partial r}(r\tau_{rz})+\frac{\partial}{\partial \theta}(\tau_{\theta z})\right]\right\}^{*} \qquad (2)$$

Radial momentum equation:

$$\frac{\partial}{\partial z}(vu)+\frac{1}{r}\frac{\partial}{\partial r}(rvv)+\frac{1}{r}\frac{\partial}{\partial \theta}(vw)-\frac{w^2}{r}$$

$$=-\frac{1}{\rho}\frac{\partial p}{\partial r}+\frac{1}{\rho}\left\{\underline{\frac{\partial}{\partial z}(\tau_{rz})}+\frac{1}{r}\left[\frac{\partial}{\partial r}(r\tau_{rr})+\frac{\partial}{\partial \theta}(\tau_{r\theta})\right]-\frac{\tau_{\theta\theta}}{r}\right\} \qquad (3)$$

Circumferential momentum equation:

$$\frac{\partial}{\partial z}(wu)+\frac{1}{r}\frac{\partial}{\partial r}(rwv)+\frac{1}{r}\frac{\partial}{\partial \theta}(ww)+\frac{vw}{r}$$

$$=-\frac{1}{\rho r}\frac{\partial p}{\partial \theta}+\frac{1}{\rho}\left\{\underline{\frac{\partial}{\partial z}(\tau_{\theta z})}+\frac{1}{r}\left[\frac{\partial}{\partial r}(r\tau_{r\theta})+\frac{\partial}{\partial \theta}(\tau_{\theta\theta})\right]+\frac{\tau_{r\theta}}{r}\right\} \qquad (4)$$

where ρ is the density; τ denotes the stress, which can be represented by the velocity gradient and the effective viscosity variated in the flow field. Its tensor form can be written as:

$$[\tau]=\mu_{\mathrm{eff}}(\nabla\vec{V}+\nabla\vec{V}^{T}) \qquad (5)$$

where

$$\nabla\vec{V}=\frac{\partial\vec{V}}{\partial r}\vec{e}_r+\frac{1}{r}\frac{\partial\vec{V}}{\partial\theta}\vec{e}_\theta+\frac{\partial\vec{V}}{\partial z}\vec{e}_z=\begin{pmatrix}\dfrac{\partial v}{\partial r} & \dfrac{\partial w}{\partial r} & \dfrac{\partial v}{\partial r}\\[2ex] \dfrac{1}{r}\dfrac{\partial v}{\partial\theta}-\dfrac{w}{r} & \dfrac{1}{r}\dfrac{\partial w}{\partial\theta}+\dfrac{v}{r} & \dfrac{1}{r}\dfrac{\partial u}{\partial\theta}\\[2ex] \dfrac{\partial v}{\partial z} & \dfrac{\partial w}{\partial z} & \dfrac{\partial u}{\partial z}\end{pmatrix} \qquad (6)$$

---

* In the formulas of this section, the underlined terms were neglected in the approximate assumption of the Spalding's partially parabolic flow[6].

The components of τ are

$$\left.\begin{aligned}
&\tau_{rr}=\mu_{\mathrm{eff}}\left(2\frac{\partial v}{\partial r}\right)\\
&\tau_{\theta\theta}=\mu_{\mathrm{eff}}\left[2\left(\frac{1}{r}\frac{\partial w}{\partial\theta}+\frac{v}{r}\right)\right]\\
&\tau_{zz}=\mu_{\mathrm{eff}}\left(2\frac{\partial u}{\partial \underline{z}}\right)\\
&\tau_{r\theta}=\tau_{\theta r}=\mu_{\mathrm{eff}}\left(\frac{\partial w}{\partial r}-\frac{w}{r}+\frac{1}{r}\frac{\partial v}{\partial\theta}\right)\\
&\tau_{z\theta}=\tau_{\theta z}=\mu_{\mathrm{eff}}\left(\frac{1}{r}\frac{\partial u}{\partial\theta}+\frac{\partial w}{\partial \underline{z}}\right)\\
&\tau_{zr}=\tau_{rz}=\mu_{\mathrm{eff}}\left(\frac{\partial u}{\partial r}+\frac{\partial v}{\partial \underline{z}}\right)
\end{aligned}\right\}\tag{7}$$

In expressions (5) and (7), μ_{eff} is the effective viscosity coefficient and defined by

$$\mu_{\mathrm{eff}}=\mu_l+\mu_t=\mu_l+C_L\rho\frac{K^2}{\varepsilon}\tag{8}$$

where μ_l and μ_t are the laminar and turbulent viscosity coefficient respectively.

The governing equations for turbulent kinetic energy K and its dissipation rate ε are

K-equation:

$$\begin{aligned}
&\frac{\partial}{\partial z}(uK)+\frac{1}{r}\frac{\partial}{\partial r}(rvK)+\frac{1}{r}\frac{\partial}{\partial\theta}(wK)\\
&=\frac{1}{\rho}\left\{\frac{1}{r}\frac{\partial}{\partial r}\left(r\frac{\mu_{\mathrm{eff}}}{\sigma_{\mathrm{eff},K}}\frac{\partial K}{\partial r}\right)+\frac{1}{r^2}\frac{\partial}{\partial\theta}\left(\frac{\mu_{\mathrm{eff}}}{\sigma_{\mathrm{eff},K}}\frac{\partial K}{\partial\theta}\right)\right.\\
&\left.\quad+\underline{\frac{\partial}{\partial z}\left(\frac{\mu_{\mathrm{eff}}}{\sigma_{\mathrm{eff},K}}\frac{\partial K}{\partial z}\right)}+GE-\rho\varepsilon\right\}
\end{aligned}\tag{9}$$

ε-equation:

$$\begin{aligned}
&\frac{\partial}{\partial z}(u\varepsilon)+\frac{1}{r}\frac{\partial}{\partial r}(rv\varepsilon)+\frac{1}{r}\frac{\partial}{\partial\theta}(w\varepsilon)\\
&=\frac{1}{\rho}\left\{\frac{1}{r}\frac{\partial}{\partial r}\left(r\frac{\mu_{\mathrm{eff}}}{\sigma_{\mathrm{eff},\varepsilon}}\frac{\partial\varepsilon}{\partial r}\right)+\frac{1}{r^2}\frac{\partial}{\partial\theta}\left(\frac{\mu_{\mathrm{eff}}}{\sigma_{\mathrm{eff},\varepsilon}}\frac{\partial\varepsilon}{\partial\theta}\right)\right.\\
&\left.\quad+\underline{\frac{\partial}{\partial z}\left(\frac{\mu_{\mathrm{eff}}}{\sigma_{\mathrm{eff},\varepsilon}}\frac{\partial\varepsilon}{\partial z}\right)}+C_1GE\frac{\varepsilon}{K}-C_2\rho\frac{\varepsilon^2}{K}\right\}
\end{aligned}\tag{10}$$

where

$$\begin{aligned}
GE=\mu_t&\left\{2\left[\left(\frac{\partial u}{\partial \underline{z}}\right)^2+\left(\frac{\partial v}{\partial r}\right)^2+\left(\frac{1}{r}\frac{\partial w}{\partial\theta}+\frac{v}{r}\right)^2\right]\right.\\
&\left.+\left(\frac{\partial w}{\partial r}-\frac{w}{r}+\frac{1}{r}\frac{\partial v}{\partial\theta}\right)^2+\left(\frac{\partial u}{\partial r}+\frac{\partial v}{\partial \underline{z}}\right)^2+\left(\frac{1}{r}\frac{\partial u}{\partial\theta}+\frac{\partial w}{\partial \underline{z}}\right)^2\right\}
\end{aligned}\tag{11}$$

In these equations, $\sigma_{\mathrm{eff},K}$ and $\sigma_{\mathrm{eff},\varepsilon}$ are Prandtl/Schmidt numbers; C_1, C_2, and C_D are proportionality constants. The values of C_1, C_2, C_D, $\sigma_{\mathrm{eff},K}$ and $\sigma_{\mathrm{eff},\varepsilon}$ are given in Table 1[6].

Table 1

C_1	C_2	C_D	$\sigma_{\mathrm{eff},K}$	$\sigma_{\mathrm{eff},\varepsilon}$
1.44	1.99	0.09	1	1.23

Equations (1) through (4), (9) and (10) may be used to obtain the six unknown variables u, v, w, p, K and ε, so they are closure. However, as these equations form a coupled system of non-linear equations, it is very difficult to solve them straightforwardly. Based upon the partially parabolic flow assumption, these equations were solved by using the marching integral technique in references [4~8]. This paper does not adopt the partially parabolic flow assumption and the streamline-iteration method is used to solve above equations. Owing to the fact that the grid points calculated are situated on the mean-flow streamlines, these equations can be rewritten in following simple froms:

Continuity equation: We employ its integral form

$$\iint_A \rho \vec{V} \cdot d\vec{A} = Q_0 = \text{const.} \tag{12}$$

where A is the area of any cross section in the channel; Q_0 is the mass rate of flow prescribed beforehand.

Energy equation: Substitute expression (7) and equation (1) into equations (2) through (4), then

$$u\frac{\partial u}{\partial z}+v\frac{\partial u}{\partial r}+\frac{w}{r}\frac{\partial u}{\partial \theta}=-\frac{1}{\rho}\frac{\partial p}{\partial z}+\frac{\mu_{\text{eff}}}{\rho}\left(\frac{\partial^2 u}{\partial z^2}+\frac{\partial^2 u}{\partial r^2}+\frac{1}{r}\frac{\partial u}{\partial r}+\frac{1}{r^2}\frac{\partial^2 u}{\partial \theta^2}\right)$$
$$+\frac{1}{\rho}\left(\frac{\partial \log \mu_{\text{eff}}}{\partial r}\tau_{zr}+\frac{1}{r}\frac{\partial \log \mu_{\text{eff}}}{\partial \theta}\tau_{z\theta}+\frac{\partial \log \mu_{\text{eff}}}{\partial z}\tau_{zz}\right) \tag{13}$$

$$u\frac{\partial v}{\partial z}+v\frac{\partial v}{\partial r}+\frac{w}{r}\frac{\partial v}{\partial \theta}-\frac{w^2}{r}=-\frac{1}{\rho}\frac{\partial p}{\partial r}+\frac{\mu_{\text{eff}}}{\rho}\left(\frac{\partial^2 v}{\partial z^2}+\frac{\partial^2 v}{\partial r^2}+\frac{1}{r}\frac{\partial v}{\partial r}\right.$$
$$\left.+\frac{1}{r^2}\frac{\partial^2 v}{\partial \theta^2}-\frac{v}{r^2}-\frac{2}{r^2}\frac{\partial w}{\partial \theta}\right)+\frac{1}{\rho}\left(\frac{\partial \log \mu_{\text{eff}}}{\partial r}\tau_{rr}+\frac{1}{r}\frac{\partial \log \mu_{\text{eff}}}{\partial \theta}\tau_{r\theta}+\frac{\partial \log \mu_{\text{eff}}}{\partial z}\tau_{rz}\right) \tag{14}$$

$$u\frac{\partial w}{\partial z}+v\frac{\partial w}{\partial r}+\frac{w}{r}\frac{\partial w}{\partial \theta}+\frac{vw}{r}=-\frac{1}{\rho r}\frac{\partial p}{\partial \theta}+\frac{\mu_{\text{eff}}}{\rho}\left(\frac{\partial^2 w}{\partial z^2}+\frac{\partial^2 w}{\partial r^2}+\frac{1}{r}\frac{\partial w}{\partial r}\right.$$
$$\left.+\frac{1}{r^2}\frac{\partial^2 w}{\partial \theta^2}+\frac{2}{r^2}\frac{\partial v}{\partial \theta}-\frac{w}{r^2}\right)+\frac{1}{\rho}\left(\frac{\partial \log \mu_{\text{eff}}}{\partial r}\tau_{\theta r}+\frac{1}{r}\frac{\partial \log \mu_{\text{eff}}}{\partial \theta}\tau_{\theta\theta}+\frac{\partial \log \mu_{\text{eff}}}{\partial z}\tau_{\theta z}\right) \tag{15}$$

Equations (13) through (15) can be grouped as:

$$(\vec{V}\cdot\nabla)\vec{V}=-\frac{1}{\rho}\nabla p+\frac{\mu_{\text{eff}}}{\rho}\nabla^2\vec{V}+\frac{1}{\rho}\nabla\log\mu_{\text{eff}}\cdot[\tau] \tag{16}$$

Substitute the formula of vector operation

$$(\vec{V}\cdot\nabla)\vec{V}=\nabla\left(\frac{V^2}{2}\right)-\vec{V}\times(\nabla\times\vec{V}) \tag{17}$$

into equation (16), then

$$\nabla\left(\frac{p}{\rho}+\frac{V^2}{2}\right)=\vec{V}\times(\nabla\times\vec{V})+\frac{1}{\rho}\left\{\mu_{\text{eff}}\nabla^2\vec{V}+\nabla\log\mu_{\text{eff}}\cdot[\tau]\right\} \tag{18}$$

Now if total pressure

$$p_0=p+\frac{\rho}{2}V^2 \tag{19}$$

is introduced and the following relations are utilized.

$$\vec{l^0} \cdot \nabla \left(\frac{p}{\rho} + \frac{V^2}{2} \right) = \vec{l^0} \cdot \nabla \left(\frac{p_0}{\rho} \right) = \frac{1}{\rho} \frac{dp_0}{dl} \bigg|_{\text{along streamline}}$$

$$\vec{l^0} \cdot \vec{V} \times (\nabla \times \vec{V}) = 0$$

where $\vec{l^0}$ is an unit vector in spatial flow direction, then following equation can be obtained from equation (18).

$$\frac{dp_0}{dl} \bigg|_{\text{along streamline}} = \vec{l^0} \cdot \left\{ \mu_{\text{eff}} \nabla^2 \vec{V} + \nabla \log \mu_{\text{eff}} \cdot [\tau] \right\} \tag{20}$$

Equation (20), which is called the energy equation of the incompressible turbulent flow, denotes the change of total pressure of turbulent flow along the streamline. When $\mu_{\text{eff}} = 0$ i.e. the fluid is inviscid, equation (20) becomes $\frac{dp_0}{dl} \Big|_{\text{along streamline}} = 0$. It means that total pressure remains constant along the streamline and becomes the well-known Bernoulli's equation for ideal fluid.

Pressure gradient equation: After shifting the terms, equation (16) can be rewritten as:

$$\nabla p = -\rho (\vec{V} \cdot \nabla) \vec{V} + \mu_{\text{eff}} \nabla^2 \vec{V} + \nabla \log \mu_{\text{eff}} \cdot [\tau] \tag{21}$$

Pressure gradients have to satisfy the above equation, which is called the pressure gradient equation. For any spatial curve q, equation (21) can be written in the form of direction derivative along curve q.

$$\frac{dp}{dq} = \vec{q^0} \cdot \left\{ -\rho (\vec{V} \cdot \nabla) \vec{V} + \mu_{\text{eff}} \nabla^2 \vec{V} + \nabla \log \mu_{\text{eff}} \cdot [\tau] \right\} \tag{22}$$

where $\vec{q^0}$ is an unit vector in the direction of curve q. Curve q can take three arbitrary linear independent directions. If we take the direction of the streamline to be one of the directions of curve q, then the energy equation (20) can be obtained from equation (22).

For equations (9) and (10), if we utilize equation (1) and following relation

$$\left(u \frac{\partial \varphi}{\partial z} + v \frac{\partial \varphi}{\partial r} + \frac{w}{r} \frac{\partial \varphi}{\partial \theta} \right) \bigg|_{\text{along streamline}} = V \frac{d\varphi}{dl} \bigg|_{\text{along streamline}} \tag{23}$$

then the left-hand side of equations (9) and (10) can also be rewritten as direction derivative along the streamline.

$$\begin{aligned} V \frac{dK}{dl} \bigg|_{\text{along streamline}} &= \frac{1}{\rho} \left\{ \frac{1}{r} \frac{\partial}{\partial r} \left(r \frac{\mu_{\text{eff}}}{\sigma_{\text{eff},K}} \frac{\partial K}{\partial r} \right) \right. \\ &\quad \left. + \frac{1}{r^2} \frac{\partial}{\partial \theta} \left(\frac{\mu_{\text{eff}}}{\sigma_{\text{eff},K}} \frac{\partial K}{\partial \theta} \right) + \frac{\partial}{\partial z} \left(\frac{\mu_{\text{eff}}}{\sigma_{\text{eff},K}} \frac{\partial K}{\partial z} \right) + GE - \rho \varepsilon \right\} \end{aligned} \tag{24}$$

$$\begin{aligned} V \frac{d\varepsilon}{dl} \bigg|_{\text{along streamline}} &= \frac{1}{\rho} \left\{ \frac{1}{r} \frac{\partial}{\partial r} \left(r \frac{\mu_{\text{eff}}}{\sigma_{\text{eff},\varepsilon}} \frac{\partial \varepsilon}{\partial r} \right) + \frac{1}{r^2} \frac{\partial}{\partial \theta} \left(\frac{\mu_{\text{eff}}}{\sigma_{\text{eff},\varepsilon}} \frac{\partial \varepsilon}{\partial \theta} \right) \right. \\ &\quad \left. + \frac{\partial}{\partial z} \left(\frac{\mu_{\text{eff}}}{\sigma_{\text{eff},\varepsilon}} \frac{\partial \varepsilon}{\partial z} \right) + C_1 GE \frac{\varepsilon}{K} - C_2 \rho \frac{\varepsilon^2}{K} \right\} \end{aligned} \tag{25}$$

For the turbulent flow around the stern of a body of revolution and its wake which is discussed in this paper, the flow is axisymmetric. Then, $w=0$, and partial derivatives of all flow variables with respect to θ must be equal to zero. The above basic equations can be further simplified and we can discuss the flow case only in a meridian plane. For the axisymmetric turbulent flow, the basic equations are

Continuity equation:

$$\int_{r_0(z)}^{r_1(z)} \rho \cdot 2\pi\, rudr = Q_0 = \text{const.} \tag{26}$$

where $r_0(z)$ and $r_1(z)$ are the locations of the lower and upper boundary of the channel in the meridian plane (z, r).

Energy equation: Since

$$V\frac{d\varphi}{dl}\bigg|_{\text{along streamline}} = V_m \frac{d\varphi}{dm}\bigg|_{\text{along streamline}} = u\frac{d\varphi}{dz}\bigg|_{\text{along streamline}} \tag{27}$$

where V_m is the meridian velocity, $\frac{d\varphi}{dm}\Big|_{\text{along streamline}}$ and $\frac{d\varphi}{dz}\Big|_{\text{along streamline}}$ denote the direction derivatives of φ with respect to the meridian streamline m and z along the spatial streamline respectively, the axisymmetric form of equation (20) can be written as:

$$\begin{aligned}\frac{dp_0}{dz}\bigg|_{\text{along streamline}} = \frac{1}{u}\bigg\{ \mu_{\text{eff}}\bigg[& u\left(\frac{\partial^2 u}{\partial z^2}+\frac{\partial^2 u}{\partial r^2}+\frac{1}{r}\frac{\partial u}{\partial r}\right)+v\bigg(\frac{\partial^2 v}{\partial z^2}+\frac{\partial^2 v}{\partial r^2} \\ & +\frac{1}{r}\frac{\partial v}{\partial r}-\frac{v}{r^2}\bigg)\bigg]+u\bigg[\frac{\partial \mu_{\text{eff}}}{\partial z}\left(2\frac{\partial u}{\partial z}\right)+\frac{\partial \mu_{\text{eff}}}{\partial r}\bigg(\frac{\partial u}{\partial r} \\ & +\frac{\partial v}{\partial z}\bigg)\bigg]+v\left[\frac{\partial \mu_{\text{eff}}}{\partial z}\left(\frac{\partial u}{\partial r}+\frac{\partial v}{\partial z}\right)+\frac{\partial \mu_{\text{eff}}}{\partial r}\left(2\frac{\partial v}{\partial r}\right)\right]\bigg\}\end{aligned} \tag{28}$$

Radial pressure gradient equation: For an axisymmetric flow, we may discuss the pressure gradient equation (22) only in the radial direction. Thus we have:

$$\begin{aligned}\frac{dp}{dr} = -\rho u\frac{dv}{dz}\bigg|_{\text{along streamline}} & +\mu_{\text{eff}}\left(\frac{\partial^2 v}{\partial z^2}+\frac{\partial^2 v}{\partial r^2}+\frac{1}{r}\frac{\partial v}{\partial r}-\frac{v}{r^2}\right) \\ +\frac{\partial \mu_{\text{eff}}}{\partial z}\left(\frac{\partial u}{\partial r}+\frac{\partial v}{\partial z}\right)+\frac{\partial \mu_{\text{eff}}}{\partial r}\left(2\frac{\partial v}{\partial r}\right) &\end{aligned} \tag{29}$$

K–equation:

$$\frac{dK}{dz}\bigg|_{\text{along streamline}} = \frac{1}{\rho u}\left[\frac{1}{r}\frac{\partial}{\partial r}\left(r\frac{\mu_{\text{eff}}}{\sigma_{\text{eff},K}}\frac{\partial K}{\partial r}\right)+\frac{\partial}{\partial z}\left(\frac{\mu_{\text{eff}}}{\sigma_{\text{eff},K}}\frac{\partial K}{\partial z}\right)+GE-\rho\varepsilon\right] \tag{30}$$

ε–equations:

$$\begin{aligned}\frac{d\varepsilon}{dz}\bigg|_{\text{along streamline}} = \frac{1}{\rho u}\bigg[& \frac{1}{r}\frac{\partial}{\partial r}\left(r\frac{\mu_{\text{eff}}}{\sigma_{\text{eff},\varepsilon}}\frac{\partial \varepsilon}{\partial r}\right) \\ & +\frac{\partial}{\partial z}\left(\frac{\mu_{\text{eff}}}{\sigma_{\text{eff},\varepsilon}}\frac{\partial \varepsilon}{\partial z}\right)+C_1 GE\frac{\varepsilon}{K}-C_2\rho\frac{\varepsilon^2}{K}\bigg]\end{aligned} \tag{31}$$

where

$$GE = \mu_t\left\{2\left[\left(\frac{v}{r}\right)^2+\left(\frac{\partial v}{\partial r}\right)^2+\left(\frac{\partial u}{\partial z}\right)^2\right]+\left(\frac{\partial u}{\partial r}+\frac{\partial v}{\partial z}\right)^2\right\} \tag{32}$$

For an axisymmetric turbulent flow, the unknown variables are u, v, p, K and ε. So equations (26), (28), (29), (30) and (31) are closure, and can be used to evaluate these unknown variables numerically.

III. Coordinate Transformations of the Flow Region and Calculations of the Derivatives of Fow Variables

The physical flow region of the turbulent flow around the stern of a body of revolution and its wake extends to infinity both in the radial and axial direction (see Fig. 1). It is impossible to perform finite difference calculation in this infinite region. In practical numerical calculations, it is a common practice to cut off the infinite region with finite boundaries (dotted lines in Fig. 1), resulting a region for performing numerical calculations. However, this practice arouses some difficulties: how to determine the locations and boundary conditions of the radial outer boundary and the axial downstream boundary rationally. Additional calculations have to be carried out to determine these boundary conditions (in References [4~8], the locations of the boundaries were prescribed empirically and the potential flow solutions were taken as the boundary conditions) and the accuracy of computed results also deteriorates[8]. In this paper, we adopt a technique which transforms the infinite flow region into a finite region with a set of coordinate transformations. As a result, the free-stream condition and the parabolic flow condition can be employed at the outer and downstream boundary respectively. Coordinate transformations are realized by using following expressions[10]

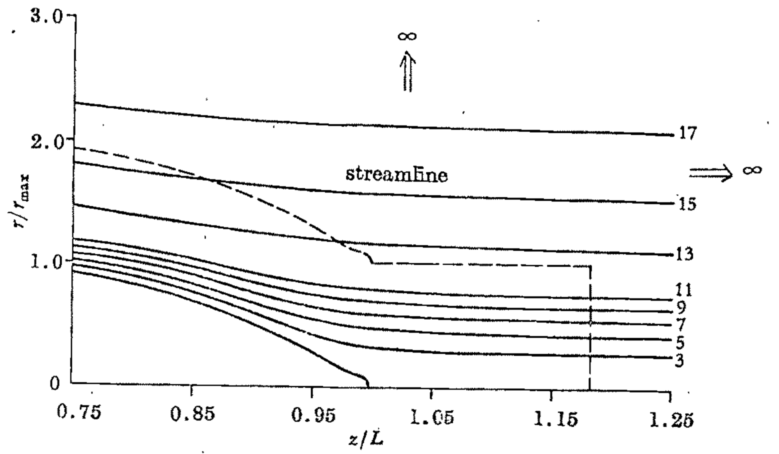

Fig. 1 Afterbody configuration and calculated streamlines for Afterbody 1

$$\left.\begin{aligned} \eta &= 1-e^{-\frac{r}{C_r}} \\ \xi &= \frac{2}{\pi}\,\mathrm{arc\,tg}\left(\frac{z}{C_z}\right) \end{aligned}\right\} \tag{33}$$

where C_r and C_z are radial and axial characteristic lengths. C_r is taken as the sum of the radius and the boundary layer thickness at the inlet station, and C_z is taken as the length of the stern. From expression (33), it is obvious that for $\eta=0$, 1, $r=0$, ∞ and for $\xi=0$, 0.5, 1, $z=0$, C_z, ∞. Thereby, equation (26) and (28) through (32) can be solved in the transformed flow region in the coordinate system (η, ξ), see Fig. 2. In this paper, the intersecting of the

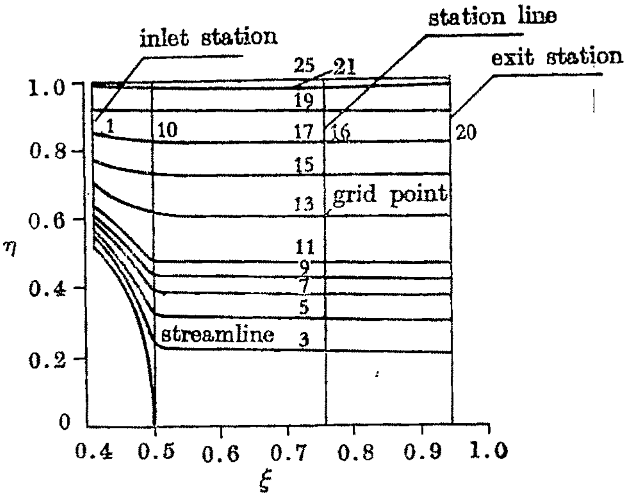

Fig. 2 Transformed flow region and calculated streamlines for Afterbody 1

straight-lines in η-direction (corresponding the radial straight-lines in physical meridian plane) and the transformed meridian streamlines are taken as the grid points. At these grid points, the partial derivatives of flow variables with respect to r and z and the direction derivatives appeared in equations (28) through (31) cannot be evaluated straightforwardly. Some operations must be made.

Let φ denote a certain flow variable. The first and second derivatives of φ with respect to ξ and η along the streamlines and the station-lines (straight-lines in η-direction), $\frac{d\varphi}{d\xi}$, $\frac{d^2\varphi}{d\xi^2}$, $\frac{d\varphi}{d\eta}$, $\frac{d^2\varphi}{d\eta^2}$, can be obtained by numerical differential method with the non-equidistant three point difference format[12]. Then, by the derivation rule for compound functions, the direction derivatives of φ can be obtained in the following form:

$$\left.\begin{aligned}
\left.\frac{d\varphi}{dr}\right|_{\text{along station-line}} &= \frac{d\varphi}{d\eta}\,\frac{(1-\eta)}{C_r} \\
\left.\frac{d^2\varphi}{dr^2}\right|_{\text{along station-line}} &= \frac{d^2\varphi}{d\eta^2}\left(\frac{1-\eta}{C_r}\right)^2 - \frac{d\varphi}{d\eta}\left(\frac{1-\eta}{C_r}\right)\cdot\frac{1}{C_r} \\
\left.\frac{d\varphi}{dz}\right|_{\text{along streamline}} &= \frac{d\varphi}{d\xi}\cdot\frac{2}{\pi}\,\frac{1}{C_z}\cos^2\left(\frac{\pi}{2}\xi\right) \\
\left.\frac{d^2\varphi}{dz^2}\right|_{\text{along streamline}} &= \left[\frac{2}{\pi}\,\frac{1}{C_z}\cos^2\left(\frac{\pi}{2}\xi\right)\right]^2\left[\frac{d^2\varphi}{d\xi^2} - \pi\frac{d\varphi}{d\xi}\operatorname{tg}\left(\frac{\pi}{2}\xi\right)\right]
\end{aligned}\right\} \tag{34}$$

In order to obtain the partial derivatives of flow variables with respect to r and z appeared in equations (28) through (31), the derivative properties and the meridian flow angle α in physical meridian plane must be utilized. From Fig. 3, it is easy to obtain:

$$\left.\begin{aligned}
\left.\frac{d\varphi}{dz}\right|_{\text{along streamline}} &= \frac{\partial\varphi}{\partial r}\operatorname{tg}\alpha + \frac{\partial\varphi}{\partial z} \\
\left.\frac{d\varphi}{dr}\right|_{\text{along station-line}} &= \frac{\partial\varphi}{\partial r}
\end{aligned}\right\} \tag{35}$$

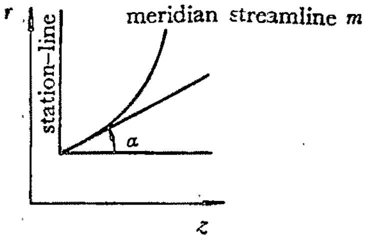

Fig. 3 Meridian flow angle

Thus, we have:

$$\left.\begin{aligned}\frac{\partial\varphi}{\partial r}&=\left.\frac{d\varphi}{dr}\right|_{\text{along station-line}}\\ \frac{\partial\varphi}{\partial z}&=\left.\frac{d\varphi}{dz}\right|_{\text{along streamline}}-\frac{\partial\varphi}{\partial r}\operatorname{tg}\alpha\end{aligned}\right\}\tag{36}$$

Perform the derivation operation once again on expression (35), we obtain:

$$\frac{\partial^2\varphi}{\partial r^2}=\left.\frac{d^2\varphi}{dr^2}\right|_{\text{along station-line}}\tag{37}$$

$$\frac{\partial^2\varphi}{\partial z^2}=\left.\frac{d^2\varphi}{dz^2}\right|_{\text{along streamline}}-\frac{\partial^2\varphi}{\partial r^2}\operatorname{tg}^2\alpha-2\frac{\partial^2\varphi}{\partial z\partial r}\operatorname{tg}\alpha-\frac{\partial\varphi}{\partial r}\left.\frac{d^2r}{dz^2}\right|_{\text{along streamline}}\tag{38}$$

On the right-hand side of expression (38), $\frac{\partial^2\varphi}{\partial z\partial r}$ and $\left.\frac{d^2r}{dz^2}\right|_{\text{along streamline}}$ are still unsolved. With the obtained $\frac{\partial\varphi}{\partial r}$ and $\frac{\partial^2\varphi}{\partial r^2}$, $\frac{\partial^2\varphi}{\partial z\partial r}$ can be derived from the following expression:

$$\frac{\partial^2\varphi}{\partial z\partial r}=\frac{\partial}{\partial z}\left(\frac{\partial\varphi}{\partial r}\right)=\left.\frac{d}{dz}\left(\frac{\partial\varphi}{\partial r}\right)\right|_{\text{along streamline}}-\frac{\partial^2\varphi}{\partial r^2}\operatorname{tg}\alpha\tag{39}$$

We can first obtain $\left.\frac{d}{d\xi}\left(\frac{\partial\varphi}{\partial r}\right)\right|_{\text{along streamline}}$ by numerical differentiation of $\frac{\partial\varphi}{\partial r}$, and then use the third equation of (34) to calculate $\left.\frac{d}{dz}\left(\frac{\partial\varphi}{\partial r}\right)\right|_{\text{along streamline}}$ appeared on the right-hand side of (39). $\left.\frac{d^2r}{dz^2}\right|_{\text{along streamline}}$ in (38) can be obtained by derivation of compound functions, employing the coordinates η, ξ of the grid points in the transformed meridian plane.

$$\begin{aligned}\left.\frac{d^2r}{dz^2}\right|_{\text{along streamline}}&=\left[\frac{2}{\pi}\frac{1}{C_z}\cos^2\left(\frac{\pi}{2}\xi\right)\right]^2\left\{\left[\frac{d^2\eta}{d\xi^2}\right.\right.\\&\left.\left.-\pi\frac{d\eta}{d\xi}\operatorname{tg}\left(\frac{\pi}{2}\xi\right)\right]\frac{C_r}{1-\eta}+\left(\frac{d\eta}{d\xi}\right)^2\left(\frac{C_r}{1-\eta}\right)^2\cdot\frac{1}{C_r}\right\}\end{aligned}\tag{40}$$

Thus, being given the coordinates η, ξ of the grid points and flow variable φ on these points, we may evaluate its direction derivatives and partial derivatives.

IV. Boundary Conditions

In order to solve the flow variables u, v, p, K and ε from equations (26) and (28) through

(31), it is necessary to determine the boundary conditions at each boundary of the flow region. They are defined as follows:

(1) Wall surface

$$u=v=K=\varepsilon=0$$

(2) Wake centreline

$$v=0,\ \frac{\partial u}{\partial r}=\frac{\partial v}{\partial r}=\frac{\partial K}{\partial r}=\frac{\partial \varepsilon}{\partial r}=\frac{\partial p}{\partial r}=0$$

(3) Outer boundary (infinity in the radial direction)

$$u=V_\infty,\ v=0,\ p=p_\infty,\ \frac{\partial K}{\partial r}=\frac{\partial \varepsilon}{\partial r}=0$$

where V_∞ and p_∞ are free-stream velocity and static pressure respectively.

(4) Inlet boundary

The inlet boundary may be located at about 75% of the length of a body of revolution, where thin boundary layer assumption is valid in general. Thus, the boundary layer thickness can be calculated either by the thin boundary layer theory or by Schlichting's formula for flat plate.

$$\delta=0.37S\left(\frac{V_\infty \cdot S}{v}\right)^{-1/5} \tag{41}$$

where ν is kinematic viscosity; S is the distance from the leading edge. The velocity components u and v are as follows:

$$\left.\begin{array}{l} u=\begin{cases} V_\infty\left[\dfrac{(r-r_0)}{\delta}\right]^{1/7}, & r-r_0\leqslant\delta \\ V_\infty & ;\ r-r_0>\delta \end{cases} \\ v \doteq 0 \end{array}\right\} \tag{42}$$

For static pressure p, either radial uniform distribution and $p=p_\infty$ or uniform distribution within and linear variation outside the boundary layer are assumed.

In order to predict turbulent properties in the flow region precisely, Muraoka improved the inlet conditions for K and ε[4][5]. For K, this paper adopts his proposal, i.e.

$$K=\begin{cases} f(r-r_0)\cdot V_\infty^2, & r-r_0\leqslant\delta \\ \doteq 0, & r-r_0>\delta \end{cases}$$

where $f(r-r_0)$ is determined from the experiment data of Klebanoff for flat plate (e.g. Rotta[12]).

For the mixing length l_m, we adopt the approximation proposed by Huang et al.[3]

$$l_m=l_{m0}\frac{\sqrt{(r_0+\delta)^2-r_0^2}}{3.33\,\delta} \tag{43}$$

where l_{m_0} is determined from the value of $g(r-r_0)$ which Bradshaw et al. have given for thin boundary layer[13].

$$l_{m_0}=\begin{cases} g(r-r_0), & r-r_0\leqslant1.2\delta \\ g(1.2\delta), & r-r_0>1.2\delta \end{cases}$$

The value of ε is determined from the mixing length as follows:

$$\varepsilon = \frac{C_D{}^{3/4} \cdot K^{3/2}}{l_m} \tag{44}$$

(5) Exit boundary (infinity in the axial direction)

The parabolic flow conditions are used, i.e.

$$\frac{\partial u}{\partial z} = \frac{\partial v}{\partial z} = \frac{\partial K}{\partial z} = \frac{\partial \varepsilon}{\partial z} = 0, \qquad \frac{\partial^2 u}{\partial z^2} = \frac{\partial^2 v}{\partial z^2} = \frac{\partial^2 K}{\partial z^2} = \frac{\partial^2 \varepsilon}{\partial z^2} = 0$$

V. Calculation Procedure

As mentioned above, the present calculation method has to adopt an iterative scheme. The sequence of calculation steps is as follows:

(1) Assumptions of the initial locations of the streamlines and of the initial distributions for u, K and ε

The calculation is performed in the transformed flow region which is in the ξ–η plane. Between interval [0,1] several straightlines in η–direction are taken as calculating station–lines. According to a prescribed distribution principle of the mass rate of flow along the station–line, the locations of streamlines at the inlet station can be determined from the known radial distribution of u at the same station by formula (26). Then, keeping the ratios of distances between streamlines at other stations to be the same as at the inlet station, the locations of corresponding streamlines at other stations can be assessed. Join the corresponding points for same streamlines at all stations with smooth curves, the initial calculating grid is formed by the intersecting points of station–lines and streamlines. For other stations, the initial radial distribution for u, K and ε on this grid are assumed to be the same as at the inlet station.

(2) Calculations of the meridian flow angle and of the distribution for v

According to its definition, the meridian flow angle α can be obtained by derivation of compound functions.

$$\operatorname{tg} \alpha = \left.\frac{dr}{dz}\right|_{\text{along streamline}} = \left.\frac{d\eta}{d\xi}\right|_{\text{along streamline}} \cdot \frac{2}{\pi} \frac{1}{C_z} \cos^2\left(\frac{\pi}{2}\xi\right) \cdot \frac{C_r}{1-\eta} \tag{45}$$

where $\left.\frac{d\eta}{d\xi}\right|_{\text{along streamline}}$ is calculated from the coordinates (ξ, η) of grid points by numerical differentiation method. Then, v can be obtained from

$$v = u \cdot \operatorname{tg} \alpha \tag{46}$$

(3) Calculations of new distributions for K, ε and μ_{eff}

For each streamline (except on the wall surface and the wake centreline), equations (30) and (31) can be solved simultaneously to obtain the new values of K and ε at the grid points on this streamline. Firstly, the terms appeared on the right–hand sides of equations (30) and (31) are calculated with the distributions for u, K and ε in previous iteration and the distribution for v in present iteration. Secondly, take the known values of K and ε at the inlet station as the initial values of the integral, and solve equations (30) and (31) by marching integration along this streamline from upstream to downstream. The above calculation procedure is repeated for all the streamlines in the flow field. For wall surface and wake centreline, K and ε can be obtained with conditions $K=\varepsilon=0$ and $\frac{\partial K}{\partial r}=\frac{\partial \varepsilon}{\partial r}=0$ respectively. Thus, new distributions for K and ε are obtained. New distribution for μ_{eff} is calculated from formula (8).

(4) Calculation of the distribution for static pressure p

Solve equation (29) for each station-line to obtain the distribution for p. On the right-hand side of this equation, the distribution for u should take the values of previous iteration and the distributions for v and μ_{eff} should take the calculated results at step (2) and (3) in present iteration. The right-hand side terms being known, equation (29) can solved by ordinary numerical integration. The interval of integration is from $\eta=1$ to the wall surface or to the wake centreline and the integral constant may take boundary condition $p=p_{\infty}$ at $\eta=1$ as its value.

(5) Calculation of the distribution for total pressure p_0

For each streamline (except on the wall surface and the wake centreline), the energy equation (28) can be solved in the same way as in step (4). Here, all the terms on the right-hand side of equation (28) are known, so p_0 can be evaluated by ordinary numerical integration. The integral constant may take the value of p_0 at the inlet station on the corresponding streamline, p_0 being calculated by expression (19) using the given radial distributions for u, v and p at the inlet station.

For wall surface, the wall surface condition $p_0=p$ (i.e. $u=v=0$) is used directly. For wake centreline, the axisymmetric condition $\frac{\partial u}{\partial r}=0$ is utilized to obtainthe value of u. Then p_0 can be calculated by expression (19) using the obtained u and p and the axisymmetric condition $v=0$.

(6) Calculation of the new distribution for u

p_0, p and $\mathrm{tg}\,\alpha$ being solved, V and u can be obtained as follows:

$$V=\sqrt{\frac{2(p_0-p)}{\rho}} \tag{47}$$

$$u=\frac{V}{\sqrt{1+tg^2\,\alpha}} \tag{48}$$

(7) Calculation of the new locations of the streamlines

From the obtained new distribution for u, the mass rates of flow at each station-line can be calculated by formula (26). According to the prescribed distribution principle of the mass rate of flow along the station-line, the new locations of the streamlines on station-line, η_{cal}, can be obtained by inverse interpolation of the mass rate of flow. With a relaxation factor ω which is less than 1.0, the assumed new locations of the streamlines, η_{new}, can be obtained as follows:

$$\eta_{\text{new}}=\eta_{\text{old}}+\omega(\eta_{\text{cal}}-\eta_{\text{old}})$$

Repeat steps (2) through (7) until the maximum deviation between the locations of the streamlines in two successive iteration calculations is within prescribed accuracy. Then, these distributions for u, v, p, K and ε and the locations of streamlines are the final results for the problem.

VI. Numerical Results

Numerical calculations are carried out for a body of revolution which is named Afterbody 1 by Huang et al.[3] The principal particulars of this body are given in Table 2 and the afterbody configuration is shown in Fig. 1. Numerical calculations are executed in the transformed flow region which is in the ξ–η plane.

Table 2

L(m)	$r_{\max}$(m)	R_n
3.066	0.1397	6.6×10^6

The calculating inlet and exit station are placed at $\xi=0.4131$ ($z/L=0.7553$) and $\xi=0.9425$ ($z/L=11$) respectively. The number of the station-lines is 20 along ξ-direction and the number of the streamlines is 25 along η-direction. Station-lines are spaced more closely near the stern and so are the streamlines near the wall surface and the outer boundary (at $\eta=1$), see Fig. 2. The calculated results are shown in Fig. 1, 2, and Fig. 4 to Fig. 6. The calculated mean-flow streamlines in the physical and the transformed flow region are shown in Fig. 1 and Fig. 2 respectively. From Fig. 1 it can be seen that in the region of $z/L<0.90$ the mean-flow streamlines are convex in shape and almost parallel to the surface of the body, and the boundary layer is thin. But in the region of the last 10% of the body length the mean-flow streamlines are concave in shape and divergent outwardly and the boundary layer becomes thick. This conclusion is consistent with that obtained by Huang et al.[3] and Patel et al.[14] from experiments.

Comparison of calculated and measured velocity components, u/V_∞ and $-v/V_\infty$ is shown in Fig. 4 and comparison of pressure coefficient C_p is shown in Fig. 5. It can be seen that the calculated results by the present method have the same high accuracy as Muraoka's numerical results[4][5], both being in fair agreement with experiment. The calculated axial velocity profile at $z/L=1.057$ by the present method is in better agreement with experiments than Muraoka's.

For turbulent properties, i.e. turbulent kinetic energy K and mixing length l_m, no comparison of calculated and measured results has been given in all the existent papers except Muraoka's[4][5]. Muraoka[4] improved the inlet conditions for K and ε and compared calculated and measured results for the first time. The agreement was satisfactory in general, but the accuracy of calculation became poor as z/L increased. In Fig. 6 of the present paper, calculated results by the present method are compared with measured turbulent properties by Huang et al.[3] The agreement between them is satisfactory and the accuracy of calculation at $z/L=1.057$

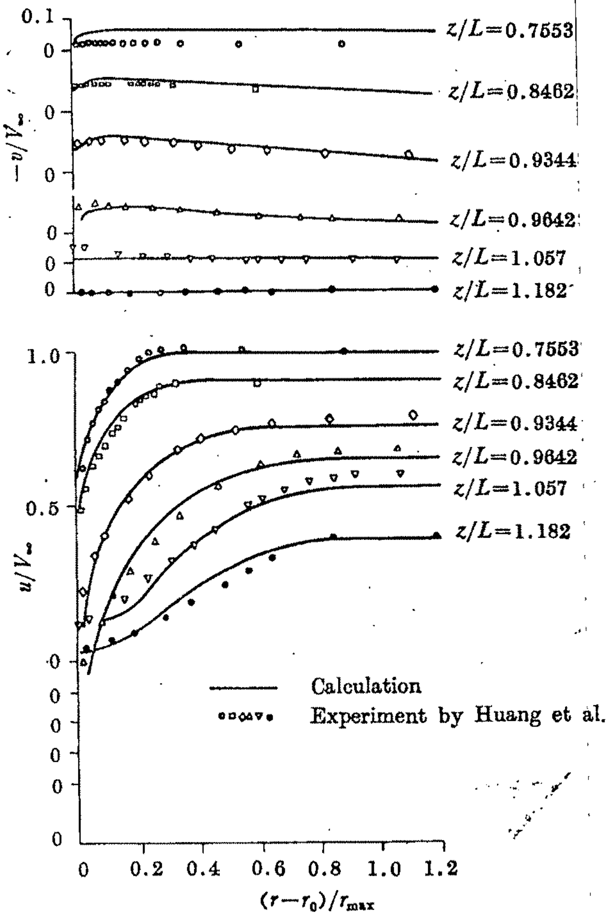

Fig. 4 Comparison of velocity components u/V_∞ and $-v/V_\infty$ for Afterbody 1

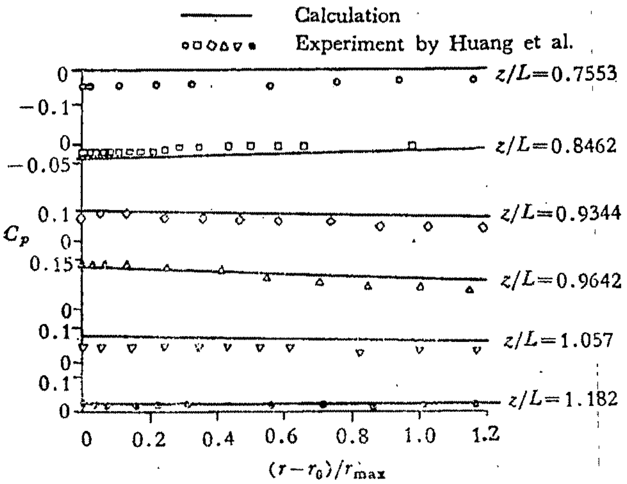

Fig. 5 Comparison of pressure variations in the flow around Afterbody 1

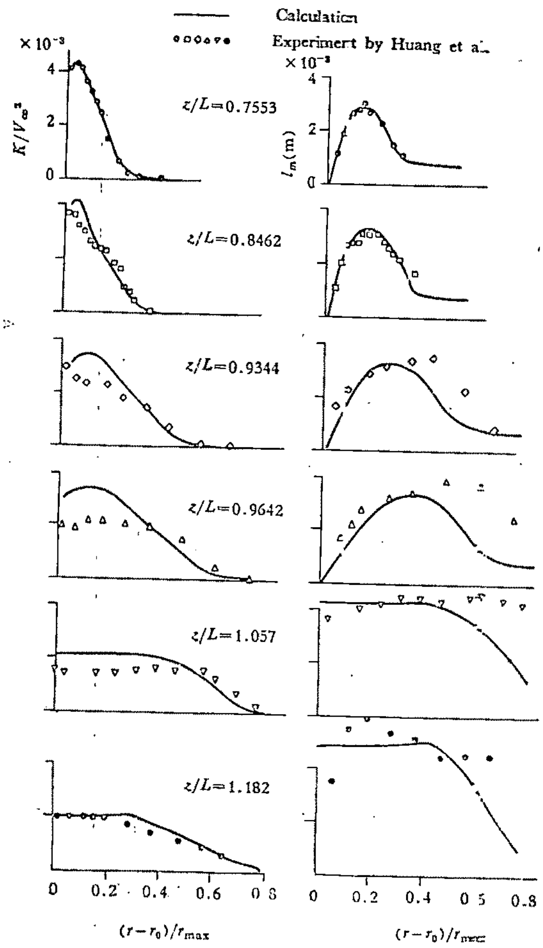

Fig. 6 Comparison of turbulent properties for Afterbody 1

is better than Muraoka's.

The calculating exit boundary in Muraoka's calculation was located at $z/L=1.182$[4][5]. As the accuracy of his calculation became poor, thereby no comparison of calculated and measured results at $z/L=1.182$ was given, though Huang et al. presented measured results at this station[3]. This paper presents comparisons of calculated and measured results for velocity components, static pressure coefficient and turbulent properties at $z/L=1.182$, the agreement being satisfactory.

VII. Concluding Remarks

From the calculated example in the previous section, it may be concluded that:

1. Based upon the two-equation (K-ε) turbulence model, the streamline-iteration method presented in this paper is effective for the theoretical prediction of the turbulent flow around the stern of a body of revolution and its wake on condition that no separation and recirculating flow are present. The agreement between measured and calculated results is encouraging.

2. The coordinate transformation given in this paper can transform the external flow problem which is extended to infinity both in the radial and axial direction into an internal flow problem in a finite region. Extending the calculating region to infinity in the radial direction, permits us to take the free-stream condition as the boundary condition at the outer boundary and the viscous flow in the boundary layer and the potential flow outside of that can be solved by an uniform equation system. The serious drawback in the existent differential method, namely the locations of the outer and downstream boundary were empirically prescribed and the potential flow solution was taken as the boundary conditions at these boundaries, can be evaded. By extending the calculating region to infinity in the axial direction, not only the parabolic flow condition can be taken as the boundary condition at the exit boundary, but also the accuracy of calculation in wake can be improved.

Works will be continued to extend the present streamline-iteration method to calculations of three-dimensional turbulent flow around ship stern and of the turbulent flow around the stern of a body of revolution and its wake with propeller in operation.

Acknowledgment

Before closing this paper, the author wishes to express his heartful thanks to Prof. Gu Maoxiang and Senior Engineer Liu Xin of CSSRC for their advices and encouragements. The author is grateful to Engineer Wang Xiliang of CSSRC and Lecturer Jiang Jinliang of Fudan University for their help during the preparation of this paper, and also to Engineer Wu Mingchuan of MARIC for revising the English manuscript.

References

[1] F. H. Harlow and P. I. Nakayama: *Transport of Turbulence Energy Decay Rate*, **Los Alamos Sci**, Lab. Univ. California, Rep. LA-3854, 1968.

[2] B. E. Launder and D. B. Spalding: Mathematical Models of Turbulence, Academic. Press, London and New York, 1972.

[3] T. T. Huang, N. Santelli and G. Belt: *Stern Boundary-Layer Flow of Axisymmetric Bodies*, **12th Symp. on Naval Hydrodynamic**, 1978.

[4] K. Muraoka: *Examination of a 2-Equation Model of Turbulence for Calculating the Viscous Flow around Ships*, **Jouranl of the Society of Naval Architects of Japan**, Vol. 147, 1980.

[5] K. Muraoka: *Calculation of Thick Boundary Layer and Wake of Ships by a Partially Parabolic Method*, **13th Symp. on Naval Hydrodynamics**, Tokyo, 1980.

[6] A. M. Abdelmeguid, N. C. G. Markatos, D. B. Spalding and K. Muraoka: *A Method of Predicting Three-Dimensional Turbulent Flow around Ships' Hulls*, **Int. Symp. on Ship Viscous Resistance**, Götebrog, 1978.

[7] K. Muraoke: *Calculation of Viscous Flow around Ship Stern*, **Transactions of the West-Japan Society of Naval Architects**, No. 58, 1978.

[8] N. C. Markatos and C. B. Wills: *Prediction of Viscous Flow around a Fully Submerged Appended Body*, **13th Symp. on Naval Hydrodynamics**, Tokyo, 1980.

[9] Jian Jinliang and Zhou Liandi: *Use Streamline-Iteration Metohd to Calculate Viscous Flow Problems Containing both Internal and External Flow Field,* **Rep. of CSSRC,** 1980.

[10] Yuan Jiale, Zhou Liandi and Jian Jinliang: *A Streamline-Interation for Calculating the Viscous Flow around a Axisymmetric Body,* **Rep. of CSSRC,** 1981.

[11] Jian Jinliang: *The Method of Streamline-Iteration for Computing the 2-Dimensional Viscous Flow,* **Shanghai Mechanics, Vol. 2,** No. 1, 1981.

[12] Von J. C. Rotta: Turbulence Stromungen, B. G. Teuber, 1972.

[13] P. Bradshaw, D. H. Ferris and N. P. Atwell: *Calculation of Boundary Layer Development Using the Turbulent Energy Equation,* **Journal of Fluid Mechanics,** No. 28, 1967.

[14] V. C. Patel, A. Nakayama and R. Damian: *Measurements in the Thick Axisymmetric Turbulent Boundary Layer near the Tail of a Body of Revolution,* **Journal of Fluid Mechanics,** Vol. 63, part **2, 1974.**

Annual of the CSNAME, Vol. 1, 1982

CALCULATION OF HYDRODYNAMIC COEFFICIENTS FOR BULBOUS SECTIONS AND TWIN-BODY SECTIONS USING THE MULTI-POLE EXPANSION METHOD

DAI YISHAN (戴遗山), JIANG XIAOXIONG (蒋小雄) AND MIN MAISONG (闵美松)
Harbin Shipbuilding Engineering Institute

SUMMARY

Multi-pole expansion method has been used successfully for 2-D hydrodynamic calculations of ordinary ship forms; but when used on bulbous sections, the error is too large. The authors analysed this situation and found that by suitably submerging the point source or doublet, this difficulty could be overcome. Expressions suitable for calculation of added mass and damping coefficient for different modes of oscillation of 2-D bulbous sections are given. Comparison of results so obtained with that obtained by the source-and-sink method indicates that the agreement is rather good for bulbous sections. The present method, however, obviates the problem of irregular frequencies usually encountered by the latter.

Taking the bulbous bow section of the S-175 container ship as an example, the paper analysed the influence of the submergence of point source or doublet on the calculated hydrodynamic coefficients. Finally the paper gives a method for calculating the hydrodynamic coefficients of twin-body sections in heave.

I. Introduction

The wide use of ship motion predictions in sea waves has long justified the use of strip method as an engineering tool. However, the multi-pole expansion method, though used most successfully on 2-D ordinary ship forms, failed to yield good results on bulbous sections. The errors were large enough to prompt the calculations employing the multi-pole expansion method to treat all bulbous sections as point sections with complete negligence of their hydrodynamic properties.

We analysed this situation and have traced this anamoly mainly to the rapid reduction of the waterline half-breadth y_w or the breadth-draft ratio. If the point source/doublet were still placed at the origin on the free surface, large numerical errors are bound to crop up, as the problem is ill-conditioned, using a combination of this point source/doublet together with a set of higher-order potentials to fit the boundary conditions at the waterline.

Ursell[3] and later Grim[4], Tasai[5] and Porter[6] introduced the multi-pole expansion method to the solution of 2-D ship motion problems by placing a point source/doublet at the origin. This is because the sections they treated belong either to semicircles, semi-ellipses or to Lewis ship forms of normal shape, where the waterline breadths are relatively large. The results of their calculations have been confirmed by experiments of Gerritsma[7], Vugts[8] and others. For the particular case of rather extreme bulbous sections, we have submerged the point source/doublet down along the x-axis a distance ξ, and found that the computed results improved conspicously, as easily identified by the improvement in agreement about check numbers.

Results of calculations using the present method have been compared with those using Maeda's (source-and-sink) method, both on Maeda's bulbous forms of $B/D=0.25$, 0.5[9]. The agreement is good. Investigations made on the optimum positions of submergence of point source/doublet were carried out on sections #0 (bulbous bow), #1 and #10 of container ship S-175. It was noted that generally the optimum position of submergence of the point source/doublet should be the draft of the maximum offset.

Finally, the paper deals with the calculation of hydrodynamic coefficients for 2-D twin-body sections in heaving motion.

II. Hydrodynamic Coefficients of Bulbous Sections

2.1. Expressions for hydrodynamic coefficients

The formulation and the solution of the potential problem for bulbous section can be derived in a similar way used for ordinary section[2]. As an example, the derivation of the hydrodynamical coefficients for 2-D section in heaving motion is given as follows.

The reference plane xoy is fixed in space with x-axis pointing down and y-axis lying in the equilibrium water surface pointing to right, $(\xi, 0)$ is the coordinates of the point source. C is the contour of the section when floating at its equilibrium position (Fig. 1 and 2).

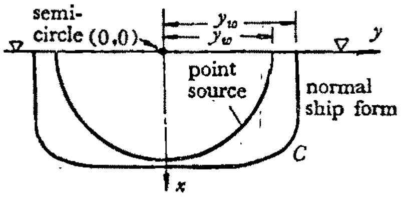

Fig. 1 Position of point source/doublet for normal ship section

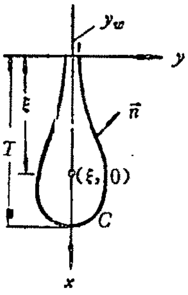

Fig. 2 Position of point source/doublet for bulbous section

Let the cylinder execute a small amplitude sinnusoidal heave oscillation of displacement $x=l_t \cos(\omega t+\varepsilon)$. The velocity potential external of contour C should satisfy Laplace equation $\nabla^2\phi=0$ and the following boundary conditions:

$$(C_1) \qquad k\phi+\frac{\partial\phi}{\partial x}=0 \qquad (x=0,\ |y|>y_w)$$

$$(D_1) \qquad \frac{\partial \phi}{\partial y} = 0, \qquad (y=0,\ x>T)$$

$$(E_1) \qquad \left.\frac{\partial \phi}{\partial n}\right|_C = U \left.\frac{\partial x}{\partial n}\right|_C, \text{ (wall condition on } C)$$

where $k=\omega^2/g$, $\vec{n}$ is the outward normal to C and $U=-l_s\omega\ \sin(\omega t+\varepsilon)$ is the velocity. In order to satisfy the radiation condition at infinity ($|y|=\infty$), a point source of suitable strength is placed at $x=\xi$, whose stream function is

$$\frac{gb}{\pi\omega} e^{k\xi} (\psi_c \cos \omega t + \psi_s \sin \omega t)$$

where b is the amplitude of radiated wave at infinity. The expressions of ψ_c and ψ_s in the first quadrant are as follows:

$$\psi_c = -\pi\, e^{-k(x+\xi)} \sin ky$$

$$\psi_s = \frac{1}{2} \operatorname{tg}^{-1} \frac{y}{x-\xi}\, \frac{1}{2} \operatorname{tg}^{-1} \frac{y}{x+\xi} + \pi e^{-k(x+\xi)} \cos ky$$
$$- \int_0^\infty e^{-kv}\, \frac{K \cos K(x+\xi) - k \sin K(x+\xi)}{k^2+K^2}\, dK$$

To seek the solution for the above boundary value problem, the region outside of contour C is mapped on $\zeta = re^{i\theta}$ plane as the region outside a semicircle of radius 1 by the following conformal transform:

$$z = \sum_n A_{2n-1} \zeta^{-(2n-1)}$$

In order to satisfy wall condition, take the higher-order stream functions

$$\psi_{2m} = -\frac{\sin 2m}{r^{2m}} + k \sum_n A_{2n-1} \frac{2n-1}{2(m+n)-1} \cdot \frac{\sin 2(m+n)-1}{r^{2(m+n)-1}} \qquad (m=1,2,3,\cdots)$$

A linear combination of ψ_c, ψ_s and ψ_{2m} is made as:

$$\psi = -\frac{gb}{\pi\omega} e^{k\xi} (\psi_c \cos \omega t + \psi_s \sin \omega t + \sum_m p_{2m} \psi_{2m} \cos \omega t + \sum_m q_{2m} \psi_{2m} \sin \omega t)$$

The coefficients p_{2m} and q_{2m} are determined by the following equations:

$$\sum_m p_{2m} f_{2m}(\theta) = \psi_{c0} + \psi_{c0} \Big|_{\theta=\pi/2} \cdot \sum_n A_{2n-1} \sin(2n-1)\,\theta / y_w$$

$$\sum_m q_{2m} f_{2m}(\theta) = \psi_{s0} + \psi_{s0} \Big|_{\theta=\pi/2} \cdot \sum_n A_{2n-1} \sin(2n-1)\,\theta / y_w$$

where

$$\psi_{c0} = \psi_c |_{r=1}, \qquad \psi_{s0} = \psi_s |_{r=1}$$

$$f_{2m}(\theta) = -\left[g_{2m}(\theta) + g_{2m}\left(\frac{\pi}{2}\right) \sum_n A_{2n-1} \sin(2n-1)\theta / y_w \right]$$

$$g_{2m}(\theta) = \psi_{2m} |_{r=1}$$

The wave amplitude ratio is given by

$$b/l_s = \frac{\pi k y_w}{\sqrt{A^2+B^2}} e^{-k\xi}$$

where

$$A=-\left[\psi_{c0}\big|_{\theta=\pi/2}+\sum_{m}p_{2m}g_{2m}\left(\frac{\pi}{2}\right)\right],\ B=-\left[\psi_{s0}\big|_{\theta=\pi/2}+\sum_{n}q_{2m}g_{2m}\left(\frac{\pi}{2}\right)\right]$$

Making use of energy relationship, the damping coefficient N_z may be obtained as:

$$N_z=\frac{\rho g^2}{\omega^3}\left(\frac{b}{l_z}\right)^2=\frac{\rho\pi^2\omega y_w^2}{A^2+B^2}e^{-2k\xi}$$

where ρ is the density of water.

Hydrodynamic force acting on the section is

$$P=-\int_{-\frac{\pi}{2}}^{\pi/2}\rho\frac{\partial\phi}{\partial t}\cdot\sum_{n}A_{2n-1}(2n-1)\cos(2n-1)\theta\,d\theta$$

where ϕ is the potential function. From the above equation, we can obtain the expression of added mass which is identical with that obtained for ordinary section[1].

$$M_z=2\rho y_w\cdot\frac{MB+NA}{A^2+B^2}$$

The following identity may be used as a check number to verity the correctness of calculation.

$$\frac{MA-NB}{y_w}e^{2k\xi}=\frac{\pi}{2}$$

The expression of hydrodynamic coefficients for 2-D section in swaying/rolling motion can be obtained similarily. The orientation of rolling angle θ is shown in Fig. 3.

2.2 Analysis of Results

(1) Calculations were conducted for two bulbous sections. The results (Fig. 4~14) are compared with that of Maeda's. For ease of comparison all coefficients have been converted to Maeda's non-dimensional form:

$$K_1=M_y/\tfrac{1}{2}\pi\rho D^2,\qquad K_2=M_x\tfrac{1}{2}\pi\rho D^2$$

$$K_3=I_\theta/\tfrac{1}{8}\pi\rho D^2$$

$$A_1=b/l_y,\qquad A_2=b/l_z$$

$$l_{ic}^*=l_{y\theta}/T,\qquad l_w^*=l_w/T$$

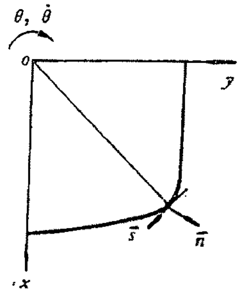

Fig. 3

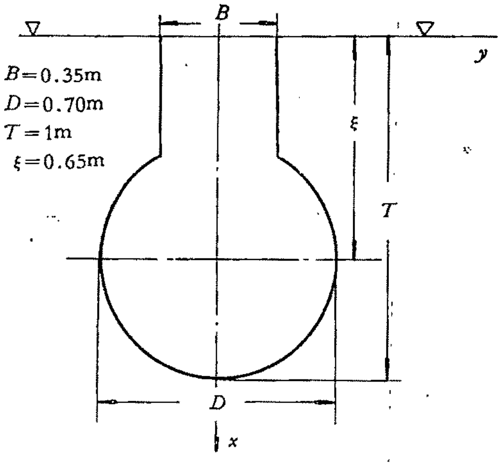

Fig. 4 Bulbous section

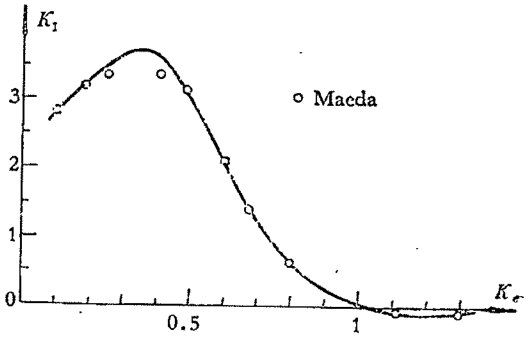

Fig. 5 Added mass coefficient for sway

It is seen that using the present multi-pole expansion method with a submerged point source/doublet, practically the same results could be obtained as with the source-and-sink method.

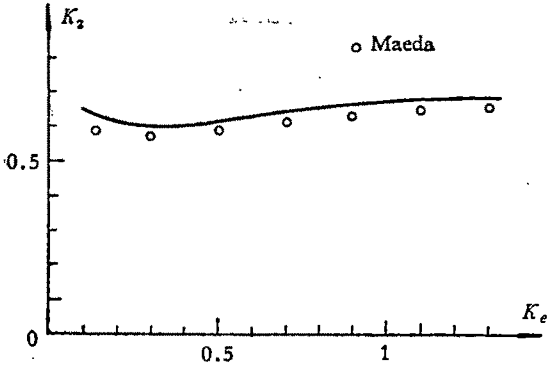

Fig. 6 Added mass coefficient for heave

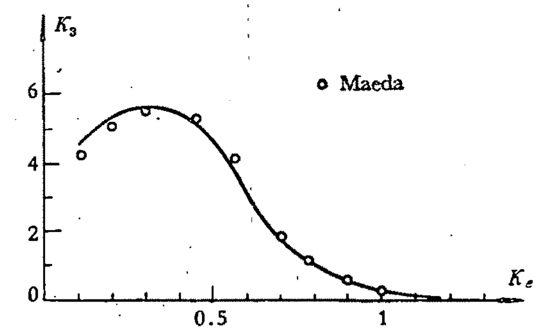

Fig. 7 Added moment of inertia coefficient for roll

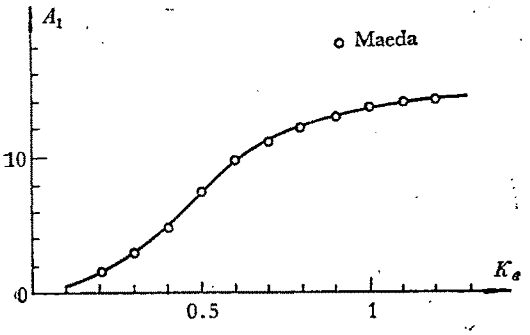

Fig. 8 Wave amplitude ratio for sway

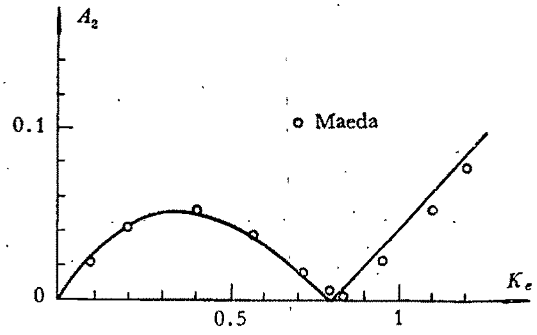

Fig. 9 Wave amplitude ratio for heave

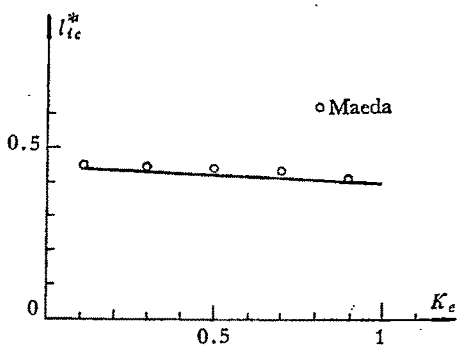

Fig. 10 Added moment of inertia lever arm for sway

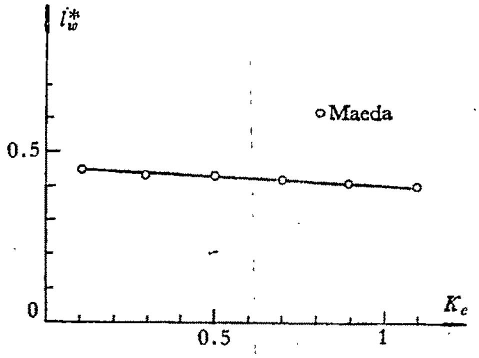

Fig. 11 Damping coefficient lever arm for sway

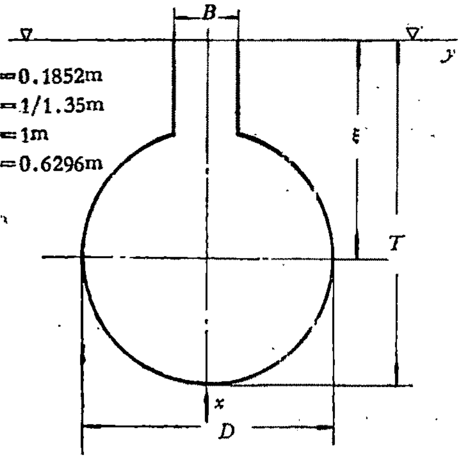

Fig. 12 Bulbous section $B/D=0.25$

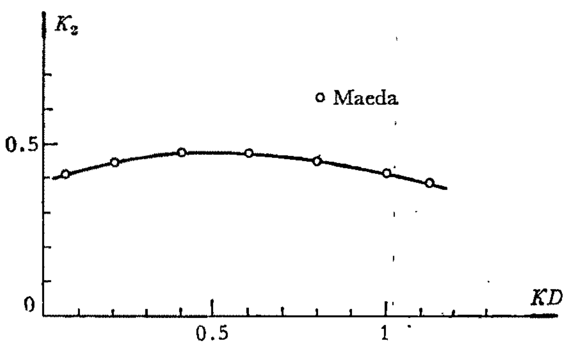

Fig. 13 Added mass coefficient for heave

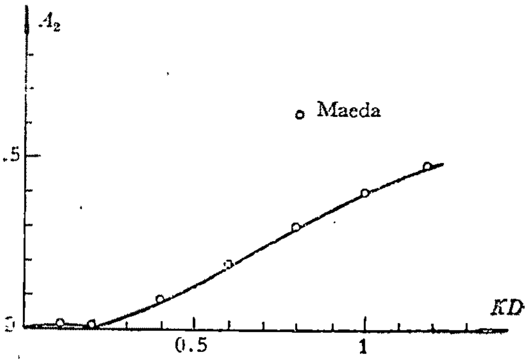

Fig. 14 Wave amplitude ratio for heave

(2) Investigations were made on Sections #0, #1, #10 of the S-175 container ship (Section #0 is the bulbous bow section), to compare the influence of submergence of the point source/doublet on hydrodynamic coefficients (Fig. 15~22).

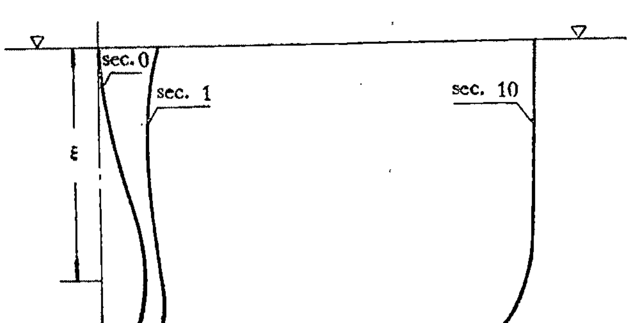

Fig. 15 Calculated sections for S-175

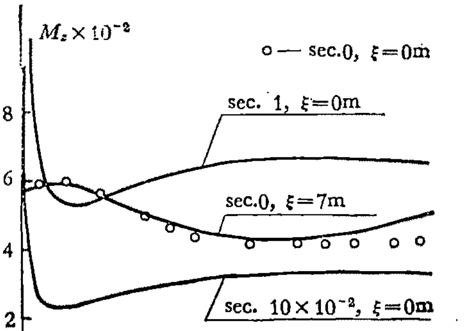

Fig. 16 Added mass for heave

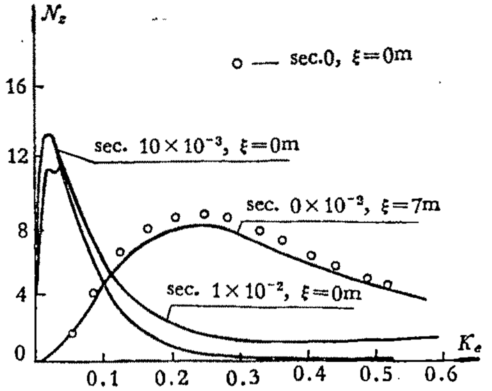

Fig. 17 Damping coefficient for heave

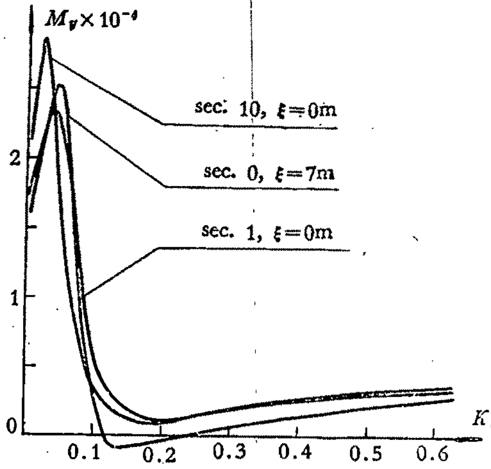

Fig. 18 Added mass for sway

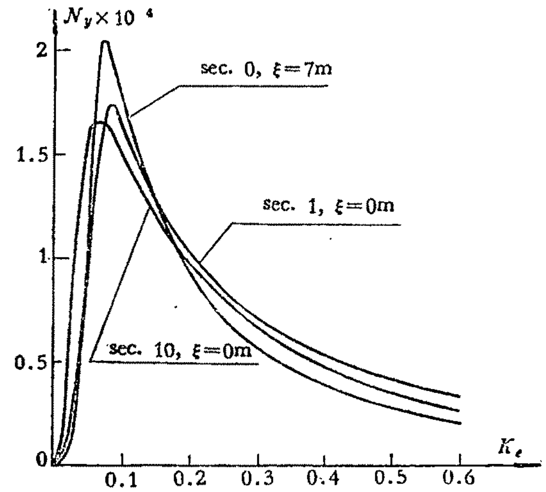

Fig. 19 Damping coefficient for sway

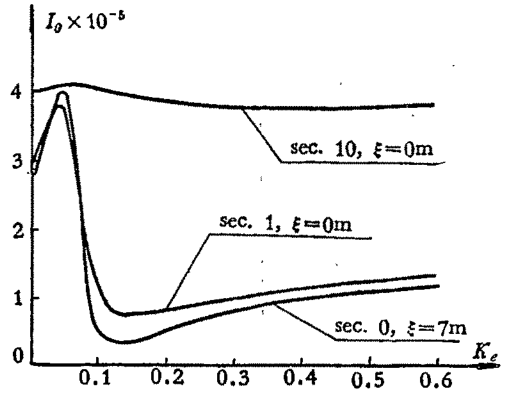

Fig. 20 Added moment of inertia for roll

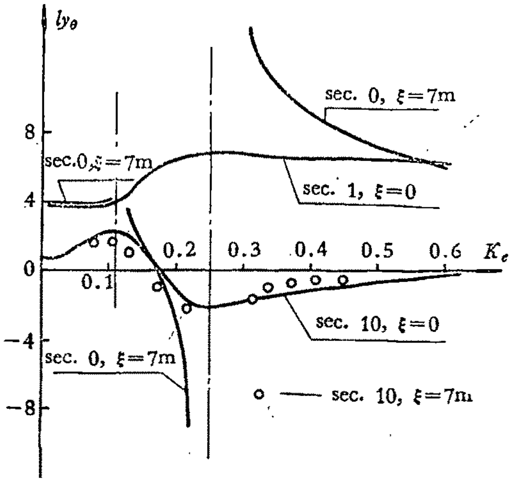

Fig. 21 Added moment of inertia lever arm for sway

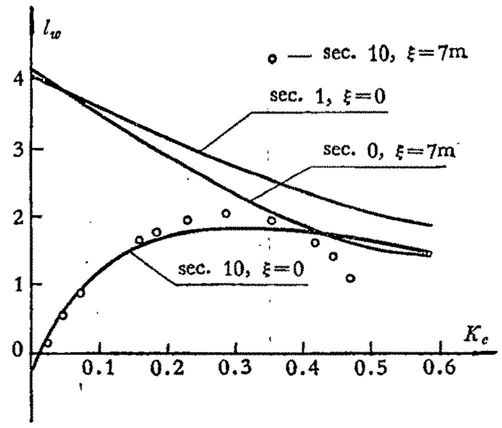

Fig. 22 Damping coefficient lever arm for sway

For heave, it is seen from Fig. 15 and 16 that there is no significant difference in hydrodynamic coefficients for the bulb section #0 between two cases of submergence $\xi=0$ and $\xi=7$m. However, the check numbers validate the results of the $\xi=7$m. case as the correct one. Even smaller differences were detected for the normal ship sections #1 and #10, but check numbers show that for these sections the $\xi=0$ case is the right one to choose. Physically this means that hydrodynamic forces induced by heaving motion act mainly on the bottom of the section, hence the relatively small error due to differences of submergence of point source, which mainly affect the close-fittedness of the boudary condition at the free surface.

For lateral motions (sway and roll), significant differences occur on hydrodynamic coefficients of Section #0 corresponding to different submergences of the doublet, $\xi=0$ and $\xi=7$m, as shown in the following table.

No.	K_e	$M_y \cdot 10^{-5}$ (kg·sec²/m)		$N_y \cdot 10^{-5}$ (kg·sec/m)		$I_\theta \cdot 10^{-6}$ (kg·sec²·m)	
		$\xi=0$	$\xi=7$	$\xi=0$	$\xi=7$	$\xi=0$	$\xi=7$
1	0.003	36.2	0.162	$0.354 \cdot 10^{-4}$	$0.2 \cdot 10^{-4}$	0.248	0.278
2	0.008	50.7	0.172	0.00113	0.00528	0.335	0.293
3	0.013	85.6	0.184	0.0115	0.00204	0.541	0.310
4	0.019	24.9	0.201	1.03	0.00632	1.46	0.334
5	0.027	−77.9	0.222	0.0636	0.0166	−0.417	0.362
6	0.035	−34.3	0.244	0.0244	0.04	−0.157	0.389
7	0.045	−20.4	0.252	0.016	0.0848	−0.0719	0.392
8	0.057	−13.6	0.218	0.0126	0.148	−0.0283	0.333
9	0.076	−8.53	0.102	0.0102	0.205	0.00805	0.0162
10	0.106	−5.08	0.00851	0.00847	0.174	0.0371	0.0443
11	0.142	−3.27	−0.01	0.00725	0.131	0.0570	0.0328
12	0.228	−1.51	−0.0033	0.00524	0.0796	0.0843	0.0617
13	0.334	−0.765	0.00895	0.00361	0.0497	0.101	0.0892
14	0.496	−0.345	0.0218	0.00222	0.0277	0.115	0.110
15	0.771	−0.124	0.0331	0.00126	0.0134	0.125	0.124

The check numbers show that the $\xi=7$m case is the right choice, and that the optimum position of the point doublet should approximately correspond to the draft of the maximum offset of the section. For normal ship sections #1 and #10, the differences between $\xi=0$ and $\xi=7$m are small. However, check numbers show that increasing the submergence tends to enlarge the error. This error is reflected more significantly in the values of sway to roll inertial lever arm $l_{y\theta}$ and the sway to roll damping lever arm l_ω (Fig. 21,22). Thus, it is important to use the correct submergence ξ for different types of ship sections in the case of lateral motions. Physically, this means that the near-surface offsets play an important role in determining the hydrodynamic coefficients.

III. Calculation of Twin-Body Motions in Heave

S. Wang and R. Wahab have applied multi-pole expansion method to the case of twin circular cylinders undergoing heave[10]. By applying method of conformal transformation, their method may be extended to the general case of twin-body sections of arbitrary shape.

3.1 Solution of Potential Flow

Consider two rigidly connected cylinders of arbitrary shape, having left-and-right symmetry and separated by a distance p (Fig. 23). Let the cylinders execute small-amplitude simple harmonic motions in the x direction and assuming the fluid to be inviscid and incompressible. 2-D potential flow theory may then be applied. Let the vertical displacement of the cylinders be $x=l\sin\omega t$ and velocity $U=l\omega\cos\omega t$, acceleration $-l\omega^2\sin\omega t$; $\phi(x,y,t)$ and $\psi(x,y,t)$ be velocity potential and stream functions of the fluid field respectively. They will have to satisfy Laplace equation in the external fluid field, the free surface condition at $x=0$ is

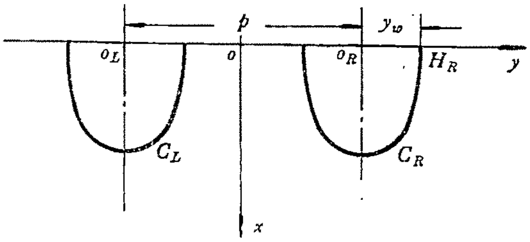

Fig. 23

$$\frac{\partial\phi}{\partial x}+k\phi=0\,,\quad \left(k=\frac{\omega^2}{g}\right)$$

and the boundary condition on the bodies is

$$\frac{\partial\phi}{\partial n}=U\frac{\partial x}{\partial n}$$

where $\vec{n}$ is the external normal (pointing into the fluid) of the section contours C_R and C_L. The corresponding stream function on the section contours should be

$$\psi=U_y+C(t) \tag{3-1-1}$$

where $C(t)$ is an arbitrary function of time t. Finally, ϕ and ψ must also satisfy the radiation conditions at $y=\pm\infty$ and the condition at the bottom $x=\infty$.

In the same way as the single body system is treated, we place at each center o_L and o_R, a point source and a doublet (axis horizontally). The source strengths are the same, while the strengths of the doublets differ only in sign for the two bodies. The corresponding stream function is

$$\begin{aligned}\psi^{(s)}(x,y,t)&=[p_c\psi_c^{(s)}(x,y)-p_s\psi_s^{(s)}(x,y)]\cos\omega t\\&\quad+[p_c\psi_s^{(s)}(x,y)+p_s\psi_c^{(s)}(x,y)]\sin\omega t \qquad (3\text{-}1\text{-}2)\\\psi^{(d)}(x,y,t)&=[q_c\psi_c^{(d)}(x,y)-q_s\psi_s^{(d)}(x,y)]\cos\omega t\\&\quad+[q_o\psi_s^{(d)}(x,y)+q_s\psi_c^{(d)}(x,y)]\sin\omega t\end{aligned}$$

where

$$\psi_c^{(s)}(x,y)=\pi e^{-kx}\left[\sin k\left(y-\frac{p}{2}\right)+\sin k\left(y+\frac{p}{2}\right)\right]$$

$$\psi_s^{(s)}(x,y)=\pi e^{-kx}\left[\operatorname{sgn}\left(y-\frac{p}{2}\right)\cos k\left(y-\frac{p}{2}\right)+\operatorname{sgn}\left(y+\frac{p}{2}\right)\cos k\left(y+\frac{p}{2}\right)\right]$$
$$-\int_0^\infty\left[\operatorname{sgn}\left(y-\frac{p}{2}\right)e^{-K|y-(p/2)|}+\operatorname{sgn}\left(y+\frac{p}{2}\right)\right.$$
$$\left.\times\ e^{-K|y+(p/2)|}\right]\frac{K\sin Kx+k\cos Kx}{k^2+K^2}dK$$

$$\psi_c^{(d)}(x,y)=-\pi e^{-kx}\left[\cos k\left(y-\frac{p}{2}\right)-\cos k\left(y+\frac{p}{2}\right)\right]$$

$$\psi_s^{(d)}(x,y)=\frac{x}{k\left[x^2+\left(y-\frac{p}{2}\right)^2\right]}-\frac{x}{k\left[x^2+\left(y+\frac{p}{2}\right)^2\right]}-\pi e^{-kx}$$
$$\times\left(\sin k\left|y-\frac{p}{2}\right|-\sin k\left|y+\frac{p}{2}\right|\right)$$
$$+\int_0^\infty dK\left(e^{-K|y-(p/2)|}-e^{-K|y+(p/2)|}\right)\frac{K\cos Kx-k\sin Kx}{k^2+K^2}$$

$$\operatorname{sgn}(z)=\begin{cases}-1, & z<0\\ 1, & z>0\end{cases}$$

Asymptotic expression for $\psi^{(s)}(x,y,t)+\psi^{(d)}(x,y,t)$ at infinity becomes

$$2\pi A\sin(\omega t-k|y|-x) \tag{3-1-3}$$

where

$$A=\sqrt{\left(p_c\cos\frac{kp}{2}+q_c\sin\frac{kp}{2}\right)^2+\left(p_s\cos\frac{kp}{2}+q_s\sin\frac{kp}{2}\right)^2}$$

$$\alpha=\operatorname{tg}^{-1}\frac{p_s\cos\frac{kp}{2}+q_s\sin\frac{kp}{2}}{p_c\cos\frac{kp}{2}+q_c\sin\frac{kp}{2}}$$

In order to obtain the actual stream function ψ, higher-order stream functions are superposed on $\psi^{(c)}$ and $\psi^{(d)}$. For this we apply conformal transform. Taking the right body as an example, shift the x-axis by $p/2$ to the right, and apply conformal transform to map half the plane $x>0$ external of C_R to the half plane $\xi>0$ external of a semicircle on ξ-η plane (Fig. 24).

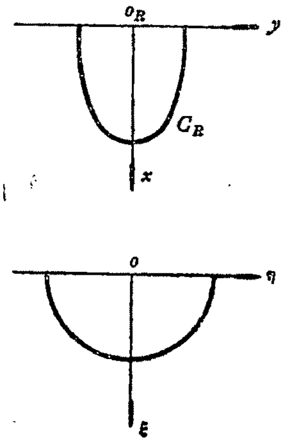

Fig. 24

Put $z=x+iy$, $\zeta=\xi+i\eta=re^{i\theta}$. The conformal transform is

$$z=C_{-1}\zeta+\frac{C_1}{\zeta}+\frac{C_3}{\zeta^3}+\frac{C_5}{\zeta^5}+\cdots-$$

In the single-body problem, the higher-order stream functions are

$$\left.\begin{aligned}\psi_{2m}^{(R)}&=-\frac{\sin 2m\theta}{r^{2m}}+k\sum_{0=u}^{\infty}C_{2n-1}\frac{2n-1}{2(m+n)-1}\cdot\frac{\sin[2(m+n)-1]\theta}{r^{2(m+n)-1}}\\ \psi_{2m+1}^{(R)}&=\frac{\cos(2m+1)\theta}{r^{2m+1}}-k\sum_{n=0}^{\infty}C_{2n-1}\frac{2n-1}{2(m+n)}\cdot\frac{\cos 2(m+n)\theta}{r^{2(m+n)}},\ (m=1,\ 2,\ 3\cdots)\end{aligned}\right\}\quad(3\text{-}1\text{-}4)$$

As before, the same symbols are used for stream functions in the x–y plane, denoted by $\psi_{2m}^{(R)}(x,y)$ and $\psi_{2m+1}^{(R)}(x,y)$. However, in the twin-body case, ψ_{2m} and ψ_{2m+1} are each composed of two components ,one corresponding to the right body and the other to the left body. The mapping planes of the conformal transform are different in each case. For distinction, we shall denote by $\omega=u+iv=\rho e^{i\varphi}$ the points mapped by the left body. Changing the variables (r,θ) of (3–1–4) into $(\rho,\ \varphi)$, and we obtain the higher-order stream functions $\psi_{2m}^{(L)}$ and $\psi_{2m+1}^{(L)}$ for the left body. As the right and left body have the same shape, the coefficients of conformal transform C_{2n-1} remains unchanged. Thus

$$\left.\begin{aligned}\psi_{2m}^{(L)}&=\frac{\sin 2m\varphi}{\rho^{2m}}+k\sum_{n=0}^{\infty}C_{2n-1}\frac{2n-1}{2(m+n)-1}\cdot\frac{\sin[2(m+n)-1]\varphi}{\rho^{2(m+n)-1}}\\ \psi_{2m+1}^{(L)}&=\frac{\cos(2m+1)\varphi}{\rho^{2m+1}}-k\sum_{n=0}^{\infty}C_{2n-1}\frac{2n-1}{2(m+n)}\cdot\frac{\cos 2(m+n)\varphi}{\rho^{2(m+n)}}\end{aligned}\right\}\quad(3\text{-}1\text{-}4)'$$

Combine (3–1–2), (3–1–4) and (3–1–4)′ into a linear set, the total stream function is

$$\begin{aligned}\psi(x,y,t)=\Big\{&p_c\psi_c{}^{(s)}(x,y)-p_s\psi_s{}^{(s)}(x,y)+q_c\psi_c{}^{(d)}(x,y)-q_s\psi_s{}^{(d)}(x,y)\\&+\sum_{m=2}^{\infty}p_m\Big[\psi_m{}^{(R)}+(-1)^m\psi_m{}^{(L)}\Big\}\cos\omega t+\Big\{p_c\psi_s{}^{(s)}(x,y)+p_s\psi_c{}^{(s)}(x,y)\\&+q_c\psi_s{}^{(d)}(x,y)+q_s\psi_c{}^{(d)}(x,y)+\sum_{m=2}^{\infty}q_m\Big[\psi_m{}^{(R)}+(-1)^m\psi_m{}^{(L)}\Big]\Big\}\sin\omega t\end{aligned}\quad(3\text{-}1\text{-}5)$$

and the corresponding velocity potential is

$$\begin{aligned}\phi(x,y,t)=\Big\{&p_c\phi_c{}^{(s)}(x,y)-p_s\phi_s{}^{(s)}(x,y)+q_c\phi_c{}^{(d)}(x,y)-q_s\phi_s{}^{(d)}(x,y)\\&+\sum_{m=2}^{\infty}p_m\Big[\phi_m{}^{(R)}+(-1)^m\phi_m{}^{(L)}\Big]\Big\}\cos\omega t+\Big\{p_c\phi_s{}^{(s)}(x,y)+p_s\phi_c{}^{(s)}(x,y)\\&+q_c\phi_s{}^{(d)}(x,y)+q_s\phi_c{}^{(d)}(x,y)+\sum_{m=2}^{\infty}q_m\Big[\phi_m{}^{(R)}+(-1)^m\phi_m{}^{(L)}\Big]\Big\}\sin\omega t\end{aligned}\quad(3\text{-}1\text{-}6)$$

where

$$\phi_c{}^{(s)}(x,y)=\pi e^{-kx}\Big[\cos k\Big(y-\frac{p}{2}\Big)+\cos k\Big(y+\frac{p}{2}\Big)\Big]$$

$$\phi_s{}^{(s)}(x,y)=\pi e^{-kx}\Big(\sin k\Big|y-\frac{p}{2}\Big|+\sin k\Big|y+\frac{p}{2}\Big|\Big)-\int_0^{\infty}(e^{-k|y-(p/2)|}+e^{-k|y+(p/2)|})\frac{K\cos Kx-k\sin Kx}{k^2+K^2}dK$$

$$\phi_c{}^{(d)}(x,y)=-\pi e^{-kx}\Big[\sin k\Big(y-\frac{p}{2}\Big)-\sin k\Big(y+\frac{p}{2}\Big)\Big]$$

$$\phi_s{}^{(d)}(x, y) = \frac{y-\frac{p}{2}}{k\left[x^2+\left(y-\frac{p}{2}\right)^2\right]} - \frac{y+\frac{p}{2}}{k\left[x^2+\left(y+\frac{p}{2}\right)^2\right]} + \pi e^{-kx}$$

$$\times\left[\operatorname{sgn}\left(y-\frac{p}{2}\right)\cos k\left(y-\frac{p}{2}\right) - \operatorname{sgn}\left(y+\frac{p}{2}\right)\cos k\left(y+\frac{p}{2}\right)\right]$$

$$-\int_0^\infty\left[\operatorname{sgn}\left(y-\frac{p}{2}\right)e^{-K|y-(p/2)|} - \operatorname{sgn}\left(y+\frac{p}{2}\right)e^{-K|y+(p/2)|}\right]$$

$$\times\frac{K\sin Kx+k\cos Kx}{k^2+K^2}dK$$

$$\phi_{2m}^{(R)} = \frac{\cos 2m\,\theta}{r^{2m}} - k\sum_{n=0}^{\infty}C_{2n-1}\frac{2n-1}{2(m+n)-1}\cdot\frac{\cos[2(m+n)-1]\theta}{r^{2(m+n)-1}}$$

$$\phi_{2m+1}^{(R)} = \frac{\sin(2m+1)\theta}{r^{2m+1}} - k\sum_{n=0}^{\infty}C_{2n-1}\frac{2n-1}{2(m+n)}\cdot\frac{\sin 2(m+n)\theta}{r^{2(m+n)}}$$

$$\phi_{2m}^{(L)} = \frac{\cos 2m\,\varphi}{\rho^{2m}} - k\sum_{n=0}^{\infty}C_{2n-1}\frac{2n-1}{2(m+n)-1}\cdot\frac{\cos[2(m+n)-1]\varphi}{\rho^{2(m+n)-1}}$$

$$\phi_{2m+1}^{(m)} = \frac{\sin(2m+1)\varphi}{\rho^{2m+1}} - k\sum_{n=0}^{\infty}C_{2n-1}\frac{2n-1}{2(m+n)}\cdot\frac{\sin 2(m+n)\varphi}{\rho^{2(m+n)}}, \quad (m=1,\ 2,\ 3\cdots)$$

The stream function given in (3–1–5) satisfies Laplace equation ,free surface condition, radiation condition at $y=\pm\infty$, and the bottom condition at $x=\infty$. So, it remains for us to apply the boundary condition (3–1–1) to determine the coefficients p_c, p_s, q_c, q_s, p_m and q_m $(m=2,3,4\ldots)$. Note from the antisymmetrical property of stream function (3–1–5), it is only necessary to seek a solution satisfying Eq. (3–1–1) on the wall of the right body C_R, viz:

$$\psi(x, y, t) = l\,\omega y\cos\omega t + C(t), \qquad (x, y)\in C_R \tag{3-1-7}$$

The above condition, of course, applies for point $H_R\left(0,\frac{p}{2}+y_w\right)$; i. e.

$$\psi\left(0,\frac{p}{2}+y_w, t\right) = l\,\omega\left(\frac{p}{2}+y_w\right)\cos\omega t + C(t) \tag{3-1-8}$$

Subtracting (3–1–8) from (3–1–7) to eliminate $C(k)$, we have:

$$\psi(x, y, t) - \psi\left(0,\frac{p}{2}+y_w, t\right) = l\,\omega\left[y-\left(\frac{p}{2}+y_w\right)\right]\cos\omega$$

Whence, we obtain the following two equations:

$$\frac{1}{l\omega}\left\{p_c\left[\psi_c{}^{(s)}(x, y) - \psi_c{}^{(s)}\left(0,\frac{p}{2}+y_w\right)\right] - p_s\left[\psi_s{}^{(s)}(x,y) - \psi_s{}^{(s)}\left(0,\frac{p}{2}+y_w\right)\right]\right.$$

$$\left.+\,q_c\left[\psi_c{}^{(d)}(x,y) - \psi_c{}^{(d)}\left(0,\frac{p}{2}+y_w\right)\right] - q_s\left[\psi_s{}^{(d)}(x, y) - \psi_s{}^{(d)}\left(0,\frac{p}{2}+y_w\right)\right]\right\}$$

$$+\frac{1}{l\omega}\sum_{m=2}^{\infty}p_m\left\{\left[\psi_m{}^{(R)}(x,y) - \psi_m{}^{(R)}\left(0,\frac{p}{2}+y_w\right)\right]\right.$$

$$\left.+(-1)^m\left[\psi_m{}^{(L)}(x, y) - \psi_m{}^{(L)}\left(0,\frac{p}{2}+y_w\right)\right]\right\} = \left[y-\left(\frac{p}{2}+y_w\right)\right] \tag{3-1-9}$$

$$\frac{1}{l\,\omega}\Big\{p_c\Big[\psi_s^{(s)}(x,y)-\psi_s^{(s)}\Big(0,\frac{p}{2}+y_w\Big)\Big]+p_s\Big[\psi_c^{(s)}(x,y)-\psi_c^{(s)}\Big(0,\frac{p}{2}+y_w\Big)\Big]$$
$$+q_c\Big[\psi_s^{(d)}(x,y)-\psi_s^{(d)}\Big(0,\frac{p}{2}+y_w\Big)\Big]+q_s\Big[\psi_c^{(d)}(x,y)-\psi_c^{(d)}\Big(0,\frac{p}{2}+y_w\Big)\Big]\Big\}$$
$$+\frac{1}{l\,\omega}\sum_{m=2}^{\infty}q_m\Big\{\Big[\psi_m^{(R)}(x,y)-\psi_m^{(R)}\Big(0,\frac{p}{2}+y_w\Big)\Big]$$
$$+(-1)^m\Big[\psi_m^{(L)}(x,y)-\psi_m^{(L)}\Big(0,\frac{p}{2}+y_w\Big)\Big]\Big\}=0 \qquad (3\text{-}1\text{-}10)$$

Write the above two equations to form a set of algebraic equations and applying the method of least squares, we obtain the following coefficients:

$$a_0^{(c)}=p_c/l\,\omega,\quad a_0^{(s)}=p_s/l\,\omega,\quad a_1^{(c)}=q_c/l\,\omega,\quad a_1^{(s)}=q_s/l\,\omega$$
$$a_m^{(c)}=p_m/l\,\omega,\quad a_m^{(s)}=q_m/l\,\omega,\quad (m=2,\ 3,\ \cdots)$$

From our experience gained in past calculations, the number of control points on C_R needs about twice the number used in the source-and-sink method.

3.2 Damping coefficient and added mass

The vertical hydrodynamic force on the twin-body is

$$F=-2\rho\int_{C_R}\frac{\partial\phi}{\partial\epsilon}\,dy\overset{\triangle}{=}-l\,\omega(n_0\cos\omega t-m_0\sin\omega t)$$

Write

$$\left.\begin{aligned}\bar{n}_0&=\int_{C_R}dy\Big\{a_0^{(c)}\phi_s^{(s)}+a_0^{(s)}\phi_c^{(s)}+a_1^{(c)}\phi_s^{(d)}+a_1^{(s)}\phi_c^{(d)}\\&\quad+\sum_{m=2}^{\infty}q_m[\phi_m^{(R)}+(-1)^m\phi_m^{(L)}]\Big\}\\ \bar{m}_0&=\int_{C_R}dy\Big\{a_0^{(c)}\phi_c^{(s)}-a_0^{(s)}\phi_s^{(s)}+a_1^{(c)}\phi_c^{(d)}-a_1^{(s)}\phi_s^{(d)}\\&\quad+\sum_{m=2}^{\infty}p_m[\phi_m^{(R)}+(-1)^m\phi_m^{(L)}]\Big\}\end{aligned}\right\} \qquad (3\text{-}2\text{-}1)$$

then

$$n_0=2\rho\omega\,\bar{n}_0,\qquad m_0=2\rho\omega\,\bar{m}_0$$

Let N and M be the damping coefficient and added mass respectively, then

$$F=-M\ddot{U}-N\dot{U}$$

or

$$-n_0\cos\omega t+m_0\sin\omega t=M\,\omega\sin\omega t-N\cos\omega t$$

and $$M=m_0/\omega,\ N=n_0$$

Thus the expressions for damping coefficient and added mass are

$$M=2\rho\bar{m}_0,\qquad N=2\rho\bar{n}_0\,\omega \qquad (3\text{-}2\text{-}2)$$

where $\bar{m}_0$ and $\bar{n}_0$ are given by (3-2-1).

We may still approach the damping problem by the wave energy relationship as before. In fact, the wave amplitude at infinity is from (3-1-3)

$$b=2\,\pi\omega\,A/g$$

and the wave amplitude ratio is

$$\frac{b}{l} = 2\pi k \cdot \frac{A}{l\,\omega} = 2\pi\, k \sqrt{\left(a_0{}^{(c)}\cos\frac{kp}{2} + a_1{}^{(c)}\sin\frac{kp}{2}\right)^2 + \left(a_0{}^{(s)}\cos\frac{kp}{2}\, a_1{}^{(s)}\sin\frac{kp}{2}\right)^2}$$

whence, the damping coefficient expressed in terms of wave amplitude ratio is

$$N = \frac{\rho g^2}{\omega^3}\left(\frac{b}{l}\right)^2$$

Comparing this with (3-2-2), we have:

$$\omega \cdot 2\rho\, \bar{n}_0 = \frac{\rho g^2}{\omega^3} \cdot 4\pi^2 k^2 (A_0^2 + B_0^2) \tag{3-2-3}$$

where

$$A_0 = a_0{}^{(c)} \cos\frac{kp}{2} + a_1{}^{(c)} \sin\frac{kp}{2}$$

$$B_0 = a_0{}^{(s)} \cos\frac{kp}{2} + a_1{}^{(s)} \sin\frac{kp}{2}$$

Then, from (3-2-3), we obtain a check relationship:

$$\frac{\bar{n}_0}{A_0^2 B_0^2} = 2\pi^2$$

which may be used to check the accuracy of the calculation.

IV. Conclusions

The present work extended the application of multi-pole expansion method to all modes of motion of bulbous sections including rather extreme shapes; it also gives a method for calculating hydrodynamic coefficients of heaving motion of a twin-body section of arbitrary demi-hull shape. A similar method dealing with hydrodynamic coefficients of lateral motions of such bodies (completely submerged bodies excluded) looks also prospective.

The main conclusions reached by submerging the point source/doublet in calculating the single body shapes are as follows:

1. By properly submerging the point source/doublet, the multi-pole expansion method may be used to calculate hydrodynamic coefficients of bulbous sections of extremely small y_w with the same degree of accuracy as that of the source-and-sink method, but without the difficulty of irregular frequencies met by the latter.

2. The submergence ξ is very sensitive for lateral motion calculations of such sections. Negligence of attending to this detail will lead to totally unrealistic results. This is a point of importance in applying it to SWATH ships or semisubmerged platforms. The submergence ξ is not a controlling factor for heaving motions of single-body bulbous shapes.

3. For bulbous sections, the value of submergence ξ should generally correspond to the draft of the maximum offset of the section.

4. **For normal ship sections where the maximum offset of the section is located at the equilibrium waterline, the submergence ξ should be zero, which confirms the ordinary strip method.**

References

[1] Y. S. Dai, M. X. Gu and T. S. Wang: *Method for Calculating Seakeeping Motions of Ships——Longitudinal Motions in Head Waves*, Publication of Harbin Shipbuilding Engineering Institute, January 1977.

[2] Y. S. Dai, M. X. Gu and T. S. Wang: *Method for Calculating Seakeeping Motion of Ships——Five Degrees of Freedom*, Publication of Harbin Shipbuilding Engineering Insitute, January 1978.

[3] F. Ursell: *On the Heaving Motion of a Circular Cylinder on the Surface of a Fluid*, **Quarterly Journal of MAM**, Vol. 2, 1949.

[4] O. Grim: *Rechnung der Durch Schwingungen Eines Schiffskörpers Erzeugten Hydrodynamischen Kräfte*, J. S. T. G. 47, 1953.

[5] F. Tasai: *On the Damping Force and Added Mass of Ships Heaving and Pitching*, **Report of RIAM**, Kyushu University, Japan, 1960.

[6] Wm. R. Porter: *Pressure Distributions, Added Mass, and Damping Coefficient for Cylinders Oscillating in a Free Surface*, University of California, Institute of Engineering Research, Report 82–16, Berkeley, California, 1960.

[7] J. Gerritsma: *Distribution of Damping and Added Mass Along the Length of a Ship Model*, **ISP**, Vol. 10, No. 103, March 1963.

[8] Vugts: *The Hydrodynamic Coefficients for Swaying, Heaving and Rolling Cylinders in a Free Surface*, Technische Hochschule Delft, Report No. 194, 1968.

[9] H. Maeda: *Hydrodynamical Forces on a Cross-section of a Stationary Structure*, **Proc. of the International Symp. on the Dynamics of Marine Vehicles and Structure in Wave**, April 1974.

[10] S. Wang and R. Wahab: *Heaving Oscillations of Twin Cylinders in a Free Surface*, **Journal of Ship Research**, Vol. 15, No. 1, pp. 33–48, March 1971.

Annual of the CSNAME, Vol. 1, 1982

APPROXIMATE METHOD FOR CALCULATION OF HYDRODYNAMIC DERIVATIVES OF AN INTERSECTING TAIL FIN ON A BODY OF REVOLUTION

ZHANG ZHONGLAI (张中骙)

China Ship Scientific Research Center

SUMMARY

This paper, using Jones' low aspect ratio wing theory[2], presents simplified expressions for hydrodynamic derivatives of tail fin including the body-fin interaction. With these expressions, calculations are performed for some contours of a submerged body and compared with existing test data[6][7][8]. The computational results, in general, give good agreement with test data.

I. Introduction

One of the important problems in ship maneuvering is to determine the hydrodynamic force and moment acting on a ship. According to the slender characteristics of ship, corresponding hydrodynamic theory has been established for many years. However, there has been significant discrepancy between results of slender body theory and experiment. The reason seems to be due to negligence of ship wake in the theory. And a variety of semi-empirical formulae have been used for engineering applications.

The hydrodynamic force and moment of a slender body of revolution with a tail fin may be considered as consisting of two parts: the one caused by the body of revolution and other caused by the fin. While we deal with the hydrodynamics of the fin, the interaction between the hull and fin must be considered. For a body of revolution with afterbody cross-section gradually contracted to zero, Karman's formula which can be used to evaluate the actual load acting on the afterbody is applied to the calculation of the viscous force. In this approach, the influences of ship wake which develope rapidly behind the maximum cross-section may be estimated. Hence we may calculate the hydrodynamic force acting on the body of revolution by superposing the viscous force to inertial force. We may yet use the method in Ref. [1] to calculate the inertial force. This method may be deemed accurate enough for engineering purposes[6]. However, concerning the force acting on the fin under the influence of the hull, as the fin lie partly, or completely in the hull's wake, the problem becomes more difficult. An appropriate calculating method has yet to be sought. In this article, having made a closer investigation into the features of the tail fin and their near field flow, we suggest an approximate calculating method for the hydrodynamic derivatives of a slender body of revolution with an intersecting plate tail fin.

General speaking, we may take the intersecting plate fin as a combination of two low aspect wings and it is possible to use the two-dimensional strip approach. Thus, the treatment of interference between the body and fin can be simplied. In this paper, a method of calculation for the derivatives of intersecting plate fin including body-fin interaction has been suggested. It was done according to following steps: first, body-fin interaction is considered but without the body's wake; second, only the interaction of the body wake on the fin, not vice versa, is considered. We shall treat the body-fin interaction as the interaction of the added masses between the body and the fin. For a fin of simple form, there exist analytic functions for calculating the sectional added mass of the tail fin. In the case of slender body of revolution at zero angle of attack, the velocity profile near the tail fin can also be found either experimentally or by calculation. This velocity profile will be applied for the calculation of hydrodynamic forces acting on the fin. Based on Jone's low aspect ratio wing theory, all the aforesaid situations have been considered, and a computational method for its hydrodynamic derivatives has been developed, simplifications are made based on practical conditions, and integral expressions for the case of an intersecting plate tail fin are developed.

By the method suggested here, calculations were performed for some contours of a submerged body for which have been existing experimental data. The calculations agree well, in general, with test results.

Nomenclature

$oxyz$=Moving coordinate system, taking origin "0" at the centre of gravity

L=Length of body of revolution

L_t=Longitudinal coordinate at stern of a body of revolution

S=Maximum cross-section of the body

D=Maximum diameter of the body

∇=Volume of the body of revolution

ρ=Density of fluid

V_∞=Velocity at the origin of the coordinate system

α=Angle of attack

$\bar{v}$=Non-dimensional average velocity along the span

$\bar{q}$=Spanwise averaged non-dimensional squared velocity term

u=Local velocity in boundary layer, $\left(\bar{u}=\frac{u}{V_\infty}\right)$

L_{fH}=Longitudinal coordinate of the foremost leading edge of fin

L_{ft}=Longitudinal coordinate of trailing edge of fin

b_t=Semi-span of the trailing edge of fin, viz. distance from tip of tailing edge to x-axis

r_t=Radius of the body of revolution at trailing edge of fin

ω=Rotatory angular velocity of body of revolution about z-axis, $\left(\Omega=\frac{\nabla^{1/3}\omega}{V_\infty}\right)$

b=Local semi-span of "delta wing", viz. distance from outer edge of fin to x-axis

Y=Lift force

M=Pitching moment

C_y^α=First-order derivative of lift coefficient with respect to $\alpha=\left(\frac{Y}{\frac{1}{2}\rho V_\infty \nabla^{2/3}}\right)'_\alpha$

m^α=First-order derivative of pitching moment coefficient with respect to $\alpha=\left(\frac{M}{\frac{1}{2}\rho V^2_\infty \nabla}\right)'_\alpha$

C_y^Ω=First-order derivative of lift coefficient with respect to $\Omega=\left(\frac{Y}{\frac{1}{2}\rho V_\infty \nabla^{2/3}}\right)'_\Omega$

m^Ω=First-order derivative of pitching moment coefficient with respect to $\alpha=\left(\frac{M}{\frac{1}{2}\rho V^2_\infty \nabla}\right)'_\Omega$

$\triangle$=Relative error $=\left|\frac{\text{computed value–experimental value}}{\text{experimental value}}\right|$

II. Calculation of Hydrodynamic Derivatives of Tail Fin

Jones' low aspect ratio wing theory is appropriate for wings with aspect ratios less than 1.5, with sweep-back leading edges (either straight or curvilinear), and with straight trailing edges perpendicular to the free stream. For such wings, Jones' mathematical expression is rather straightforward. Referring to our coordinate system, the lift force acting on a spanwise slice can be expressed as:

$$dY=-\pi\rho V_\infty^2 x d(b^2) \tag{1}$$

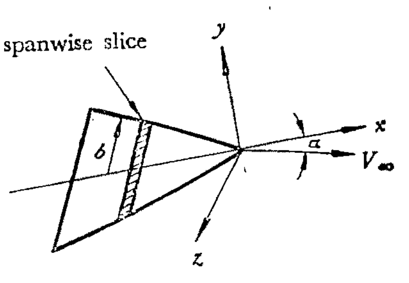

Fig. 1 Scheme of low aspect ratio "delta" wing

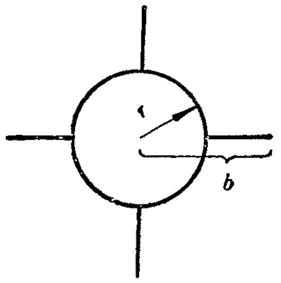

Fig. 2 Section of intersecting fin

For low aspect ratio wings measured data show that pressure distribution along the spanwise slice approaches a maximum value at the tip and the load distribution may be regarded as uniform along the span approximately. Hence, the load per unit span is constant, and we have:

$$\frac{d}{dz}\,(dY) = -\pi\rho\, V_\infty^2 \alpha\, \frac{1}{2b}\, d(b^2) \tag{2}$$

The sectional added mass λ_{22}[3] of a cross-section of the intersecting fin in y-direction is

$$\lambda_{22} = \pi\rho\,\left[r^2 + \left(\frac{b^2-r^2}{b} \right)^2 \right] \tag{3}$$

where the first term on the right-hand side is the added mass of cylinder, and the second term is the added mass of the fin including hull–fin interactions. In this respect, $\frac{b^2-r^2}{b}$ may be regarded as an equivalent local semi-span of a "delta" wing with the implication that interactions between the hull and the intersecting fin are thus considered.

Reynolds number with characteristic length L is, in general, about 1.7×10^7 for the model and it will be still greater for the full scale body. At such Reynolds numbers, the wake at the stern corresponds to turbulent boundary layeres, for which the velocity profile is relatively even in contour. For the model illustrated in this paper, the velocity at a position 5 mm away from the hull surface is of the order of 50% of V_∞. By attributing the effect of viscosity to only a reduction of free-stream velocity, the low aspect ratio wing theory stated above may be equally applied inside the wake region by taking into account the actual local velocity and angle of attack. Substituting the local angle of attack and the corresponding semi-span into (2), we have:

$$d^2Y = -\pi\rho\, u^2\, \frac{1}{2(b-r)}\, d\left(\frac{b^2-r^2}{b} \right)^2 \cdot \left(\alpha - \frac{V_\infty \Omega}{\nabla^{1/3}} \cdot \frac{x}{u} \right) dz \tag{4}$$

Or integrating along the z-axis and x-axis, thus

$$\begin{aligned} Y = & -\pi\rho V_\infty^2 \alpha \int_{L_{fl}}^{L_{fH}} \frac{d\left[\left(\frac{b^2-r^2}{b} \right)^2 \right]}{dx} dx \int_r^b \frac{\bar{u}^2(\alpha,\ \Omega,\ x,\ z)}{b-r} dz \\ & + \frac{\pi\rho V_\infty^2 \Omega}{\nabla^{1/3}} \int_{L_{fl}}^{L_{fH}} x\, \frac{d\left[\left(\frac{b^2-r^2}{b} \right)^2 \right]}{dx} dx \int_r^b \frac{\bar{u}(\alpha,\ \Omega,\ x,\ z)}{b-r} dz \\ = & -\pi\rho\, V_\infty^2\, \alpha \int_{L_{fl}}^{L_{fH}} \bar{q}\,(\alpha,\ \Omega,\ x) \frac{d\left[\left(\frac{b^2-r^2}{b} \right)^2 \right]}{dx} dx \\ & + \frac{\pi\rho V_\infty^2 \Omega}{\nabla^{1/3}} \int_{L_{fl}}^{L_{fH}} \bar{v}(\alpha,\ \Omega,\ x)\, x\, \frac{d\left[\left(\frac{b^2-r^2}{b} \right)^2 \right]}{dx} dx \end{aligned} \tag{5}$$

Similarly, we have pitching moment as follows:

$$M = -\pi\rho\, V_\infty^2\, \alpha \int_{L_{fl}}^{L_{fH}} \bar{q}(\alpha,\ \Omega,\ x)\, x\, \frac{d\left[\left(\frac{b^2-r^2}{b} \right)^2 \right]}{dx} dx$$

$$+\frac{\pi\rho V_\infty^2\Omega}{\nabla^{1/3}}\int_{L_{fl}}^{L_{fH}}\bar{v}\,(\alpha,\ \Omega,\ x)\,x^2\frac{d\left[\left(\frac{b^2-r^2}{b}\right)^2\right]}{dx}dx \tag{6}$$

where

$$\bar{q}\,(\alpha,\ \Omega,\ x)=\frac{1}{b-r}\int_r^b\bar{u}^2\,(\alpha,\ \Omega,\ x,\ z)\,dz \tag{7}$$

$$\bar{v}\,(\alpha,\ \Omega,\ x)=\frac{1}{b-r}\int_r^b\bar{u}\,(\alpha,\ \Omega,\ x,\ z)\,dz \tag{8}$$

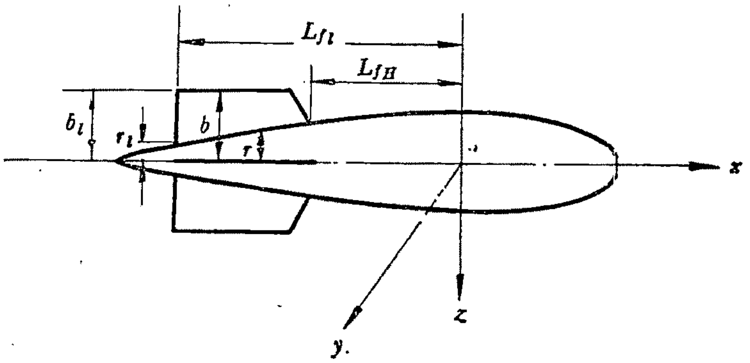

Fig. 3 Scheme of intersecting tail fin with body of revolution taking the origin "0" at the centre of gravity

For reasons to be discussed in the following section, $\bar{q}$, $\bar{v}$ may be regarded as constants independent of α and Ω and calculated from the velocity profile at the stern of body. Thus they can be moved out of the integral sign. Changing equations (5) and (6) into non-dimensional forms, integrating by parts and then differentiating with respect to α and Ω respectively. We obtain:

$$\left.\begin{aligned}
C_y^{\alpha}&=\frac{2\pi\bar{q}}{\nabla^{2/3}}\left(\frac{b_l^2-r_l^2}{b_l}\right)^2\\
m^{\alpha}&=\frac{2\pi\bar{q}}{\nabla}\left[L_{fl}\left(\frac{b_l^2-r_l^2}{b_l}\right)^2+\int_{L_{fl}}^{L_{fH}}\left(\frac{b^2-r^2}{b}\right)^2dx\right]\\
C_y^{\Omega}&=-\frac{2\pi\bar{v}}{\nabla}\left[L_{fl}\left(\frac{b_l^2-r_l^2}{b_l}\right)^2+\int_{L_{fl}}^{L_{fH}}\left(\frac{b^2-r^2}{b}\right)^2dx\right]\\
m^{\Omega}&=-\frac{2\pi\bar{v}}{\nabla^{4/3}}\left[L_{fl}^2\left(\frac{b_l^2-r_l^2}{b_l}\right)^2+2\int_{L_{fl}}^{L_{fH}}x\left(\frac{b^2-r^2}{b}\right)^2dx\right]
\end{aligned}\right\} \tag{9}$$

where

$$\bar{q}=\frac{1}{b_l-r_l}\int_0^{b_l-r_l}\bar{u}^2\,(0,\ 0,\ L_l,\ z)\,dz \tag{10}$$

$$\bar{v}=\frac{1}{b_l-r_l}\int_0^{b_l-r_l}\bar{u}\,(0,\ 0,\ L_l,\ z)\,dz \tag{11}$$

If the chord of fin is small in comparison with L_{fl}, the integrals in equations (9) may be ignored and following simplified forms are obtained.

$$\left.\begin{aligned}
C_y{}^{\alpha} &= \frac{2\pi\bar{q}}{\nabla^{2/3}}\left(\frac{b_l^2-r_l^2}{b_l}\right)^2 \\
m^{\alpha} &= \frac{2\pi\bar{q}}{\nabla}\left[\ L_{fl}\left(\frac{b_l^2-r_l^2}{b_l}\right)^2\ \right] \\
C_y{}^{\Omega} &= -\frac{2\pi\bar{v}}{\nabla}\left[\ L_{fl}\left(\frac{b_l^2-r_l^2}{b_l}\right)^2\ \right] \\
m^{\Omega} &= -\frac{2\pi\bar{v}}{\nabla^{4/3}}\left[\ L_{fl}^2\left(\frac{b_l^2-r_l^2}{b_l}\right)^2\ \right]
\end{aligned}\right\} \qquad (12)$$

The physical meaning of equations (12) is that a concentrated load acts at the trailing edge.

We shall stress again on the point that the present approach of calculating fin hydrodynamic derivatives is based on Jones' low aspect ratio theory, and equations (9) and (12) apply only to fins of low aspect ratio.

III. Calculation of $\bar{q}$ and $\bar{v}$

Although boundary layer theory has been much developed, the state-of-art with regard to 3-D bodies is such that the theory can apply only to slender bodies of revolution with zero angle of attack for which the velocity distribution within boundary layer may be calculated. Knowledge about three-dimension boundary layers is still quite insufficient. However, since the actual motion of a slender body generally involves certain angle of attack, or a rotary motion, or both, so the boundary layer is three-dimensional. Under such conditions, it is obviously impossible to calculate integration for equations (7), (8). In addition, the tail fin may partly protrude from the wake of the hull. If the fin protrudes from the boundary layer, then the potential flow outside of the boundary layer must be also solved, strictly speaking, to integrate the expressions (7) and (8). This would further complicate the integration of (7) and (8).

Fortunately, the problem discussed in this paper is rather specific, namely we are interested only in cases for which the fin is near the stern of the hull and, its extreme span generally does not extend beyond the maximum diameter, hence it has little area exposed to the potential flow. Further, by definition, the derivatives calculated are for small perturbation in the vicinity of $\alpha=\Omega=0$. Hence it is reasonable to assume:

(1) If the fin is partly exposed to the potential flow, the velocity at the interface of the potential flow and viscous flow is assumed to apply to all flow in the potential flow region along steamlines normal to the local normal of the body of revolution.

(2) $\bar{u}$ may be substituted by its value at zero angle of attack and rotatory angular velocity.

(3) the velocity distribution at the fin is the same as velocity distribution at the tail of the body without the existence of the fin.

With above assumptions, $\bar{u}$ is independent of α and Ω, and both $\bar{q}$ and $\bar{v}$ are constant. If the velocity distribution in the boundary layer at the tail of the hull is known, then $\bar{q}$ and $\bar{v}$ may be found by equations (10) and (11).

For practical calculations it is inconvenient to calculate the velocity distributions by cumbersome numerical methods. In Ref. [4], regression analysis from test data of 64 models of body of revolution are given, and empirical formulae connecting velocity distributions and geometric parameters of the body are presented. Using these, it is relatively easy to calculate $\bar{q}$ and $\bar{v}$ by means of a pocket calculator.

IV. Comparison between Computed Results and Test Data

The derivatives listed in this section were obtained from the tests made in the wind-tunnel and rotating arm facility in CSSRC. In Table 1 with the exception of model (5) for which the definition of non-dimensional quantities is in accord with the present paper, the remaining data are referred to characteristic areas, characteristic volume SL, and non-dimensional angular velocity $\frac{L\omega}{V_\infty}$.

(1) Comparision of static derivatives for body of revolution with fin

Table 1 presents static derivatives of some bodies of revolution with fin. The test data of model 1-4 and 6 are taken from Ref. [6], and model 5 from Ref. [8]. For all these models, the fin is made of thin plates. The derivatives of body of revolution were computed by the method in Ref. [5]. It is seen that the computed results agree reasonably well with test data. For models 1 and 2 both the theoretical and simplified methods give the same order of magnitude in relative errors. For model 3 and 4, however, as $b_l \Big/ \frac{D}{2}$ is greater than 1.0, the length of the fin chord seems to be too great to neglect the effect of load distribution in the chordwise direction; and the deviations corresponding to the simplified expressions seem to indicate this. Nevertheless, cases of $b_l \Big/ \frac{D}{2} > 1$ are probably few in practice. The theoretical results for model 5 are appropriate, but the Δ value by simplified formulae is too great, the cause may be traced to the fact that in this case the length of the chord is nearly equal to L_{fl}.

(2) Rotary derivatives of tail fin

The rotary derivatives of the tail fins are presented in Table 2. Test data are taken from Ref. [7]. We can see from table 2 that the theoretical Δ's values are rather greater than the simplified ones, and that calculations by simplified methods actually agree better with experiment.

Table 1. Static derivatives of body–fin combination

Model No	$b_l\Big/\frac{D}{2}$	C_y^{α}			m^{α}					Form of fin
		Tested	Theor.	Δ	Tested	Theor.	Δ (Theor.)	Simpl.	Δ (Simpl.)	
1	0.89	1.37	1.41	3%	0.89	0.87	3%	0.84	6%	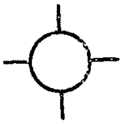
2	1.1	2.15	2	7%	0.55	0.58	5%	0.52	5%	
3	1.28	2.75	2.76	0%	0.21	0.21	0%	0.11	48%	
4	1.47	3.76	3.63	3%	-0.28	-0.19	32%	-0.38	36%	
5	1	1.63	1.43	12%	-0.76	-0.89	17%	-1.27	67%	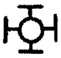
6		0.71	0.74	3%	1.13	1.15	2%			Hull alone for model 1-4

Note: Model 6 represents hull data alone for model 1-4.

Table 2. Rotary derivatives of fin

Model No	$b_l\Big/\frac{D}{2}$	C_y^{Ω}					m^{Ω}					Form of fin
		Tested	Theor.	Δ	Simpl.	Δ (Simpl.)	Tested	Theor.	Δ (Theor.)	Simpl.	Δ (Simpl.)	
7	0.87	0.5	0.45	10%	0.49	2%	-0.25	-0.22	12%	-0.26	4%	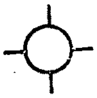
8	1.07	1	0.76	24%	0.83	17%	-0.48	-0.36	25%	-0.44	8%	
9	1.27	1.36	1.14	16%	1.28	6%	-0.7	-0.53	24%	-0.67	4%	
10	1.47	1.98	1.56	21%	1.8	9%	-0.93	-0.21	24%	-0.94	1%	

V. Concluding Remarks

In this paper, clear physical ideas are given in the method of calculation. Results as computed seem to yield reasonable agreement with test data.

The method examined here is analytical though simple. It may be conveniently employed to analyse the effect of geometric parameters on stability derivatives. The aid of a pocket calculator only is necessary as compared to the more tedious methods of numerical calculation, especially in preliminary design stage.

The deficiency of the present method is that it is limited to rather simple and specific fin features, since it is difficult to present analytical expressions for the added mass of complex fin systems.

Acknowledgments

The author is grateful to research engineers Messrs Shen Hongcui and Li Tiansen who performed a great number of tests; and to senior engineer Mr. Wan Tingdeng for his guidance and for his initiating this investigation.

References

[1] Wan Tingdeng: *Computational Method of Added Mass*, 65-10 Report of CSSRC, 1965.
[2] A. Robinson and J. A. Laurnann: Wing Theory, Cambridge at the University Press, 1956.
[3] J. N. Newman: Marine Hydrodynamics, MIT Press, Cambridge and London, 1977.
[4] Shen Hongcui and Xu Hongsheng: *Regression Analysis of a Five-variate Orthogonal Series of Body of Revolution*, unpublished.
[5] Zhang Zhonglai: *Two-dimensional Strip Theory Approach Applied to Hydrodynamic Computation of Slender Bodies of Revolution*, unpublished.
[6] Li Tiansen and Shen Junhao: *Static Derivative Series Tests of on a Body of Revolution*, unpublished.
[7] Li Tiansen and Qian Zaidi: *Orthogonal Designs for Rotary Derivative Series Tests of a Body of Revolution*, unpublished.
[8] Zhang Zhonglai: *Wind-tunnel Tests for Underwater Sonar Sheath with It's Tow Cable*, Report of CSSRC, 1981.

Annual of the CSNAME, Vol. 1, 1982

AN EXACT SOLUTION FOR AXISYMMETRICALLY LOADED THICK ANNULAR PLATES

SUN QUANXIN (孙全新) AND LUO ZUDAO (罗祖道)

Shanghai Jiao Tong University

SUMMARY

In the present paper, an exact solution for axisymmetric bending of a thick annular plate is obtained directly from three dimensional theory of elasticity. It is for the plate of which one boundary is fixed rigidly and the other free. As reference [9], the solution is expressed in the form of the sum of two infinite series such that all the prescribed boundary conditions are satisfied exactly. For illustration, numerical examples of the plate under uniform load and part-uniform load are computed and the results are compared with those of Panc's component theory. It is noted that for the case studied, Panc theory as well as other prevailing theories of thick plates yields considerably different stress behaviors from the present exact solution. This fact seems worthy to draw the attention of the designers.

I. Introduction

Since the plates are frequently used in ship and many other engineering structures as the main components, the bending theory of elastic plates is therefore deemed to be of great practical importance. Although the plate problems in nature are indeed within the scope of three-dimensional theory of elasticity, the classical plate theory has simplified them through Kirchhoff assumptions to rather simple two-dimensional problems. It is understood that the theory will give good approximation in most of the plate problems as long as the thickness of the plate relative to any linear dimension in its plane remains much smaller than unity. Nevertheless, it becomes inadequate and loses its accuracy with the increasing thickness. In some cases, the classical theory may even lead to serious errors while applying to thicker plates. Owing to the fact that the sandwich plates and thick plates have been found wide applications in modern engineering structures, the investigations on exploring a new and further refined theory for thick plates have been the interest of many researchers and scientists for more than thirty years.

In the middle 40's, Reissner[1] and Henky[2] developed independently the thick plate theories by making some corrections and improvements on the classical theory, such as taking into account for the effects of transverse shear strains (γ_{xz} and γ_{yz}) and normal stress (σ_z) in the direction normal to the plate plane. Their new theories are then capable to satisfy all three natural boundary conditions as suggested earlier by Poisson, hence Kirchhoff's approximate boundary treatment becomes unnecessary. Further researches along this line have been done successively by Kromm[3], Власов[4] and Panc[5] during the later years. In short, these refined theories are on the basis of classical plate theory. In early 60's, by using the method of asymptotic analysis, Friedrichs[6] studied the boundary layer effect of the plate based on three-dimensional theory of elasticity. In addition, Donnell[7] and Lee[8] also proposed another theory for calculating thick rectangular plates. Generally speaking, the prevailing theories of thick plates may satisfy exactly the boundary conditions on both upper and lower surfaces of the plate; however, the conditions around the lateral surfaces could only be satisfied in average or in the manner of St.Venant's statical equivalence, i.e. the stress or displacement boundary conditions are prescribed instead by their average effects of the whole thickness by performing the integration along it. As the results, these theories would inevitably cause some errors in various degrees, especially for the plate with rigidly fixed boundary.

In this paper, a thick annular plate of which one boundary is fixed rigidly while the other free of surface traction, and under the axisymmetric load is investigated. An analytical solution is obtained by solving directly the three dimensional problem of theory of elasticity. The same method as in reference [9] is employed, so the stress and displacement fields are expressed in terms of the sum of two infinite series–Fourier series and Fourier–Bessel series, such that all the prescribed boundary conditions are completely satisfied. In order to fulfil the upper and lower surface conditions of the plate, we decompose the problem into two parts, i.e. symmetric and anti-symmetric parts with respect to the middle plane ($z=o$) of the plate. They are solved separately and then superimposed together so as to yield the exact solution of the given problem. For illustration, several examples of the plate under uniform load and part-uniform load are computed numerically. And the results are used to compare with those from Panc's component theory. Appreciable discrepancies have been found between them. This fact seems to deserve some attention.

II. Theoretical Analysis

As shown in Fig. 1, let a,b and $2h$ represent respectively the outer, inner radius and the thickness of an annular plate. Assume there is no shear load exerting the upper and lower surfaces, and the axisymmetrical normal load on these surfaces are expressed as $p(r)$ and $q(r)$

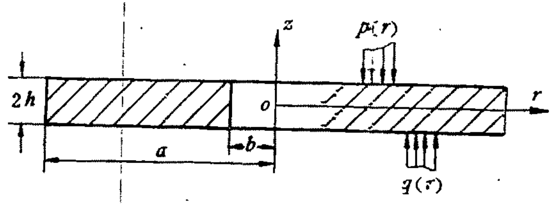

Fig. 1

respectively. Polar cylindrical coordinates system $or\theta z$ is chosen with its origin o coinciding with the center of the annular plate. Due to axisymmetry, the radial and axial displacement components will be in the forms:

$$u=u(r,\ z),\qquad w=w(r,\ z) \tag{1}$$

According to Filon's analysis of axisymmetry three-dimensional problems of elasticity[10], the partial differentiations of the displacements, $\left(\frac{\partial u}{\partial z}\right)$ and $\left(\frac{\partial w}{\partial r}\right)$ have to satisfy the following type of partial differential equation:

$$(\vartheta^2+D^2)^2F(r,\ z)=0 \tag{2}$$

where, differential operator $\vartheta^2(\quad)=\frac{\partial}{\partial r}\left[\frac{1}{r}\ \frac{\partial}{\partial r}r(\quad)\right]$, $D^2(\quad)=\frac{\partial^2}{\partial z^2}(\quad)$. It is easy to show that the solution of equation (2) may be expressed as:

$$F(r,\ z)=\left\{\begin{matrix}\text{ch}\,\alpha_m^* z\\ z\,\text{sh}\,\alpha_m^* z\end{matrix}\right\}\left\{\begin{matrix}J_1(\alpha_m^* r)\\ N_1(\alpha_m^* r)\end{matrix}\right\}+\cos k_n^* z\left\{\begin{matrix}I_1(k_n^* r)\\ K_1(k_n^* r)\\ rI_0(k_n^* r)\\ rK_0(k_n^* r)\end{matrix}\right\},\quad (m,\ n=1,\ 2,\ \cdots) \tag{3}$$

$$F(r,\ z)=\left\{\begin{matrix}\text{sh}\,\alpha_m^* z\\ z\,\text{ch}\,\alpha_m^* z\end{matrix}\right\}\left\{\begin{matrix}J_1(\alpha_m^* r)\\ N_1(\alpha_m^* r)\end{matrix}\right\}+\sin k_n^* z\left\{\begin{matrix}I_1(k_n^* r)\\ K_1(k_n^* r)\\ rI_0(k_n^* r)\\ rK_0(k_n^* r)\end{matrix}\right\},\quad (m,\ n=1,\ 2,\ \cdots) \tag{3'}$$

where $J_k(x)$, $N_k(x)$ are Ist, 2nd kind of Bessel Functions of kth order respectively; $I_k(x)$, $K_k(x)$ are Ist, 2nd kind of modified Bessel Functions of kth order respectively; and α_m^*, k_n^* are arbitrary constants.

By integrating equation (3), it is not difficult to obtain the general expressions of axisymmetric displacements which satisfy the Navier's equations of equilibrium in terms of the sum of the two infinite series.

Assume the plate is rigidly fixed on the outer boundary and free on the inner boundary, and introduce dimensionless variables and parameters

$$\rho=r/a,\ \zeta=z/a,\ \beta=b/a,\ \gamma=h/a,\ \alpha_m=\alpha_m^* a,\ k_n=k_n^* a \tag{4}$$

then, the boundary conditions can be written as:

$$\rho=\beta:\qquad \tau_{rz}=0 \tag{5a}$$

$$\sigma_r=0 \tag{5b}$$

$$\rho=1:\qquad u=0 \tag{6a}$$

$$w=0 \tag{6b}$$

In general case of loads $p(\rho)\neq q(\rho)$, we may separate the loads into two parts, i.e. symmetric and antisymmetric loads. Then the solution that satisfies boundary load conditions on both the upper and lower surfaces can readily be obtained by principle of superposition. The symmetric part of load will be

$$p_1(\rho)\equiv\tfrac{1}{2}[p(\rho)+q(\rho)]$$

and the boundary conditions can be written as:

$$\zeta=\pm\gamma:\qquad \sigma_z(\rho)=P_1(\rho),\qquad \tau_{rz}(\rho)=0 \tag{7}$$

so that the relevant displacements have the properties of even and odd functions:

$$u(\rho,\ -\zeta)=u(\rho,\ \zeta),\qquad w(\rho,\ -\zeta)=-w(\rho,\ \zeta) \tag{8}$$

As far as the antisymmetry part, the corresponding relationships are

$$P_2(\rho)\equiv\tfrac{1}{2}[p(\rho)-q(\rho)]$$

$$\zeta=\pm\gamma:\quad \sigma_z(\rho)=\pm P_2(\rho),\quad \tau_{rz}(\rho)=0 \tag{9}$$

$$u(\rho,\ -\zeta)=-u(\rho,\ \zeta),\quad w(\rho,\ -\zeta)=w(\rho,\ \zeta) \tag{10}$$

Let us now consider the symmetric problem first. The displacements u and w in this case are chosen to conform to equation (8) as:

$$\frac{u}{a}=u_0\,\rho+\frac{u_1}{\rho}+\sum_m\frac{A_m}{\alpha_m}\left[\zeta\ \mathrm{sh}\ \alpha_m\zeta+\left(B_m-\frac{1}{\alpha_m}\right)\mathrm{ch}\ \alpha_m\zeta\right]\Phi_1\ (\alpha_m\rho)$$
$$-\sum_n\frac{\cos k_n\zeta}{k_n}[D_nI_1(k_n\,\rho)+E_nK_1(k_n\,\rho)+F_n\,\rho\,I_0\ (k_n\,\rho)+G_n\,\rho\ K_0(k_n\,\rho)] \tag{11a}$$

$$\frac{w}{a}=w_1\zeta-\sum_m\frac{A_m}{\alpha_m}\left[\zeta\ \mathrm{ch}\ \alpha_m\zeta+\frac{\alpha_mB_m-4(1-\nu)}{\alpha_m}\mathrm{sh}\ \alpha_m\zeta\right]\Phi_0\ (\alpha_m\,\rho)+\sum_n\frac{\sin k_n\zeta}{k_n}\Big\{\ D_nI_0(k_n\,\rho)$$
$$-E_nK_0(k_n\,\rho)+F_n\left[\ \rho\,I_1(k_n\ \rho)+\frac{4(1-\nu)}{k_n}\ I_0\ (k_n\,\rho)\right]+G_n\left[\rho K_1(k_n\rho)+\frac{4(1-\nu)}{k_n}K_0(k_n\ \rho)\ \right]\Big\} \tag{11b}$$

then, the stress components will be

$$\frac{\sigma_r}{2G}=\frac{u_0}{1-2\nu}-\frac{u_1}{\rho^2}+\frac{w_1}{1-2\nu}+\sum_m\frac{A_m}{\alpha_m}\Big\{[\alpha_m\zeta\ \mathrm{sh}\ \alpha_m\zeta+(\alpha_mB_m-1+2\nu)\,\mathrm{ch}\ \alpha_m\zeta]\Phi_0\ (\alpha_m\,\rho)$$
$$-\frac{1}{\rho}\left[\zeta\ \mathrm{sh}\ \alpha_m\zeta+\left(B_m-\frac{1}{\alpha_m}\right)\mathrm{ch}\ \alpha_m\zeta\right]\Phi_1\ (\alpha_m\rho)\Big\}-\sum_n\frac{\cos k_n\zeta}{k_n}\Big\{\ D_n\Big[I_0\ (k_n\,\rho)\ k_n$$
$$-\frac{1}{\rho}I_1\ (k_n)\Big]-E_n\left[K_0\,(k_n\,\rho)\ k_n+\frac{1}{\rho}K_1\ (k_n\,\rho)\right]+F_n\ [(1-2\nu)I_0(k_n\,\rho)+k_n\,\rho\,I_1(k_n\,\rho)]$$
$$+G_n[(1-2\nu)K_0(k_n\,\rho)-k_n\,\rho\,K_1(k_n\ \rho)]\ \Big\} \tag{12a}$$

$$\frac{\sigma_z}{2G}=[2\nu\ u_0+(1-2\nu)\,w_1]/(1-2\nu)-\sum_m\frac{A_m}{\alpha_m}[\alpha_m\zeta\,\mathrm{sh}\,\alpha_m\zeta+(\alpha_mB_m-3+2\nu)\,\mathrm{ch}\,\alpha_m\zeta]\Phi_0(\alpha_m\rho)$$
$$+\sum_n\frac{\cos k_n\zeta}{k_n}\ \{D_nk_nI_0(k_n\,\rho)-E_nk_nK_0(k_n\,\rho)-F_n[\rho\ k_nI_1(k_n\,\rho)+2(2-\nu)I_0(k_n\,\rho)]$$
$$+G_n\ [-\rho\ k_nK_1(k_n\,\rho)+2(2-\nu)K_0(k_n\,\rho)]\} \tag{12b}$$

$$\frac{\sigma_\theta}{2G}=u_0\left(1-\frac{1}{\rho^2}\right)+\frac{\nu}{1-2\nu}\ (2u_0+w_1)+\sum_m\frac{A_m}{\alpha_m}\Big\{2\nu\ \mathrm{ch}\ \alpha_m\,\zeta\Phi_0(\alpha_m\rho)+\Big[\zeta\ \mathrm{sh}\ \alpha_m\zeta$$
$$+\left(\ B_m-\frac{1}{\alpha_m}\right)\mathrm{ch}\ \alpha_m\zeta\Big]\Phi_1\ (\alpha_m\rho)/\rho\Big\}-\sum_n\frac{\cos k_n\zeta}{k_n}[D_nI_1(k_n\,\rho)/\rho+E_nK_1(k_n\,\rho)/\rho$$
$$+F_n\ (1-2\nu)I_0\ (k_n\,\rho)+G_n(1-2\nu)K_o(k_n\,\rho)] \tag{12c}$$

$$\frac{\tau_{rz}}{2G}=\sum_m\ A_m\ \left\{\zeta\ \mathrm{ch}\ \alpha_m\zeta+\left[B_m-\frac{2(1-\nu)}{\alpha_m}\right]\mathrm{sh}\ \alpha_m\zeta\right\}\Phi_1\ (\alpha_m\rho)+\sum_n\sin k_n\,\zeta\Big\{D_n\,I_1\ (k_n\,\rho)$$

$$+E_n K_1(k_n\rho)+F_n\Big[\rho I_0\ (k_n\rho)\ +\frac{2(1-\nu)}{k_n}I_1\ (k_n\rho)\Big]+G_n\Big[\ \rho K_0\ (k_n\rho)$$

$$-\frac{2(1-\nu)}{k_n}\ K_1\ (k_n\rho)\ \Big]\Big\} \tag{12d}$$

where $\Phi_k(x)\equiv J_k(x)+C_mN_k(x)$, $(k=1,\ 2)$ (13)

and A_m, B_m, ……F_n, G_n are undetermined constants.

In order to satisfy the boundary conditions $\tau_{rz}(\rho,\pm\gamma)=0$, we choose:

$$B_m = \frac{1}{\alpha_m}\Big[2\ (1-\nu)\ -\frac{\alpha_m\gamma\ \mathrm{ch}\ \alpha_m\gamma}{\mathrm{sh}\ \alpha_m\gamma}\Big] \tag{14}$$

$$\sin k_n\gamma = 0 \quad \text{or} \quad k_n = \frac{n\pi}{\gamma},\ (n=1,\ 2,\ \cdots) \tag{15}$$

Besides, from the boundary condition (6a), we have:

$$u_0+u_1=0 \tag{16a}$$

$$J_1(\alpha_m)+C_mN_1(\alpha_m)=0 \tag{16b}$$

$$D_nI_0(k_n)+E_nK_1(k_n)+F_nI_0(k_n)+G_nK_0(k_n)=0 \tag{16c}$$

and from the boundary condition (5a), yield

$$J_1(\alpha_m\beta)+C_mN_1(\alpha_m\beta)=0 \tag{17a}$$

$$D_n I_1(k_n\beta)+E_n K_1(k_n\beta)+F_n\Big[\beta I_0\ (k_n\beta)\ +\frac{2(1-\nu)}{k_n}I_1\ (k_n\beta)\Big]$$

$$+G_n\Big[\beta K_0\ (k_n\beta)-\frac{2(1-\nu)}{k_n}K_0\ (k_n\beta)\Big]=0 \tag{17b}$$

From equation (16b):

$$C_m=-J_1(\alpha_m)/N_1(\alpha_m) \tag{18}$$

Substituting the expression into equation (17a), we find that the constants α_m are the eigenroots of the transcendental equation:

$$J_1(x)N_1(\beta x)-J_1(\beta x)N_1(x)=0 \tag{19}$$

By equation (16c) and (17b), F_n and G_n can be expressed as linear functions of D_n and E_n, i.e.

$$F_n=L_n^{(1)}D_n+L_n^{(2)}E_n,\qquad G_n=L_n^{(3)}D_n+L_n^{(4)}E_n \tag{20}$$

where $$L_n^{(1)}\equiv-\Big\{I_1\ (k_n)\Big[\beta K_0(k_n\beta)\ -\frac{2(1-\nu)}{k_n}K_1\ (k_n\beta)\Big]-K_0(k_n\beta)I_1(k_n\beta)\Big\}\Big/\Delta_n \tag{21a}$$

$$L_n^{(2)}\equiv-\Big\{I_0\ (k_n)\Big[\beta K_0\ (k_n\beta)-\frac{2(1-\nu)}{k_n}K_1\ (k_n\beta)\Big]-K_0(k_n\beta)\ K_1(k_n\beta)\Big\}\Big/\Delta_n \tag{21b}$$

$$L_n^{(3)}\equiv-\Big\{I_0(k_n)I_1\ (k_n\beta)-I_1\ (k_n)\Big[\beta I_0\ (k_n\beta)+\frac{2(1-\nu)}{k_n}I_1\ (k_n\beta)\Big]\Big\}\Big/\Delta_n \tag{21c}$$

$$L_n^{(4)}\equiv-\Big\{I_0\ (k_n)\ K_1\ (k_n\beta)-K_1(k_n)\Big[\beta I_0\ (k_n\beta)\ +\frac{2(1-\nu)}{k_n}I_1\ (k_n\beta)\Big]\Big\}\Big/\Delta_n \tag{21d}$$

$$\Delta_n\equiv I_0\ (k_n)\Big[\beta\ I_0\ (k_n\beta)-\frac{2(1-\nu)}{k_n}K_1\ (k_n\beta)\Big]-K_0\ (k_n)\Big[\beta I_0\ (k_n\beta)$$

$$+\frac{2(1-\nu)}{k_n}I_1\ (k_n\beta)\ \Big] \tag{22}$$

Moreover, from the boundary condition (6b), yield

$$w_1 \zeta - \sum_{m=1}^{\infty} \frac{A_m}{\alpha_m}\left\{ \zeta \operatorname{ch} \alpha_m \zeta + \left[B_m - \frac{4(1-\nu)}{\alpha_m} \right] \operatorname{sh} \alpha_m \zeta \right\} \Phi_0\,(\alpha_m)$$

$$= \sum_{n=1}^{\infty} [H_n^{(1)} D_n + H_n^{(2)} E_n] \sin k_n \zeta \tag{23}$$

where $H_n^{(1)} \equiv \left\{ I_0\,(k_n) + L_n^{(1)}\left[I_1\,(k_n) + \frac{4(1-\nu)}{k_n} I_0\,(k_n) \right] + L_n^{(3)}\left[-K_1\,(k_n) + \frac{4(1-\nu)}{k_n} K_0\,(k_n) \right] \right\} \Big/ k_n$

$$H_n^{(2)} \equiv \left\{ -K_0\,(k_n) + L_n^{(2)}\left[I_1\,(k_n) + \frac{4(1-\nu)}{k_n} I_0\,(k_n) \right] + L_n^{(4)}\left[-K_0\,(k_n) + \frac{4(1-\nu)}{k_n} K_0\,(k_n) \right] \right\} \Big/ k_n$$

The left-hand side of equation (23) may be expanded into Fourier sine series in the interval $[-\gamma, \gamma]$, since it is the odd function of ζ. Then, comparing the coefficients of the like terms on both sides of the equation, we have:

$$\frac{-2(-1)^n}{k_n} w_1 + \sum_{m=1}^{\infty} \frac{2(-1)^n \Phi_0(\alpha_m) k_n}{\gamma\,(\alpha_m^2 + k_n^2)\,\alpha_m}\left[\gamma \operatorname{ch} \alpha_m \gamma - \frac{2\alpha_n}{\alpha_m^2 + k_n^2} \operatorname{sh} \alpha_m \gamma + \frac{\alpha_m B_m - 4(1-\nu)}{\alpha_m} \operatorname{sh} \alpha_m \gamma \right]$$

$$\times A_m + H_n^{(1)} D_n + H_n^{(2)} E_n = 0, \qquad (n = 1,\ 2,\ \cdots) \tag{24}$$

From the boundary (5b), we obtain:

$$\left(\frac{1}{1-2\nu} + \frac{1}{\beta^2} \right) u_0 + \frac{\nu}{1-2\nu} w_1 + \sum_{m=1}^{\infty} A_m \left[\zeta \operatorname{sh} \alpha_m \zeta + \left(B_m - \frac{1-2\nu}{\alpha_m} \right) \operatorname{ch} \alpha_m \zeta \right] \Phi_0\,(\alpha_m \beta)$$

$$= \sum_{n=1}^{\infty} [H_n^{(3)} D_n + H_n^{(4)} E_n] \cos k_n \zeta \tag{25}$$

where $H_n^{(3)} \equiv \left\{ k_n I_0\,(k_n \beta) - \frac{1}{\beta} I_1(k_n \beta) + L_n^{(1)}\,[(1-2\nu) I_0(k_n \beta) + \beta\, k_n I_1\,(k_n \beta)] + L_n^{(3)}[(1-2\nu) K_0(k_n \beta) - \beta\, k_n K_1\,(k_n \beta)] \right\} \Big/ k_n$

$$H_n^{(4)} \equiv \left\{ -k_n I_0(k_n \beta) - \frac{1}{\beta} K_1(k_n \beta) + L_n^{(2)}[(1-2\nu) I_0(k_n \beta) + \beta\, k_n I_1\,(k_n \beta)] + L_n^{(4)}[(1-2\nu) K_0(k_n \beta) - \beta\, k_n K_1\,(k_n \beta)] \right\} \Big/ k_n$$

Similarly, expanding the left-hand side of equation (25) into Fourier cosine series in the interval $[-\gamma, \gamma]$ and comparing the coefficients, we have:

$$2\left(\frac{1}{1-2\nu} + \frac{1}{\beta^2} \right) u_0 + \frac{2\nu}{1-2\nu} w_1 + \sum_{m=1}^{\infty} \frac{\Phi_0(\alpha_m \beta)}{\alpha_m}\,[\gamma \operatorname{ch} \alpha_m \gamma + (B_m - 2 + \nu) \operatorname{sh} \alpha_m \gamma]\, A_m = 0 \tag{26}$$

$$-\sum_{m=1}^{\infty}\frac{2(-1)^n\Phi_0(\alpha_m\beta)}{\gamma\,(\alpha_m^2+k_n^2)}\left[\alpha_m\gamma\ \mathrm{ch}\ \alpha_m\gamma-\frac{\alpha_m^2-k_n^2}{\alpha_m^2+k_n^2}\mathrm{sh}\ \alpha_m\gamma+(\alpha_m B_m-1+2\nu)\,\mathrm{sh}\ \alpha_m\gamma\right]A_m$$
$$+H_n^{(3)}D_n+H_n^{(4)}E_n=0,\qquad (n=1,\ 2,\ \cdots)\tag{27}$$

Finally, based on the loading condition $P_1\ (\rho)$ on $\zeta=\pm\gamma$, we obtain from equation (7) and (12b):

$$\varphi_1\ (\rho)\ =\ \sum_{m=1}^{\infty}\frac{A_m}{\alpha_m}[\alpha_m\gamma\ \mathrm{sh}\ \alpha_m\gamma+(\alpha_m B_m-3+2\nu)\ \mathrm{ch}\ \alpha_m\gamma]\,\Phi_0\,(\alpha_m\rho)\tag{28}$$

Here, we let

$$\varphi_1\ (\rho)\equiv\frac{2\nu u_0+(1-2\nu)w_1}{1-2\nu}+\sum_{n=1}^{\infty}\frac{(-1)^n}{k_n}\{D_n\,[k_n I_0\ (k_n\rho)+L_n^{(1)}P_n+L_n^{(3)}Q_n]$$
$$+E_n\,[-k_n K_0\ (k_n\rho)+L_n^{(2)}P_n+L_n^{(4)}Q_n]\}+P_1\ (\rho)/2G\tag{29}$$

where $P_n\equiv k_n\,\rho\,I_1(k_n\rho)+2(2-\nu)I_0(k_n\rho)$, $\quad Q_n\equiv-k_n\,\rho\,K_1(k_n\rho)+2(2-\nu)K_0(k_n\rho)$

Utilizing the property that $\{1,\Phi_0\,(\alpha_1\ \rho),\ \cdots,\ \Phi_0\,(\alpha_m\rho),\ \cdots\}$ forms a completely orthogonal function system in the interval $[\beta,1]$, we may thus expand $\varphi_1(\rho)$ into Fourier-Bessel series of zeroth order

$$\varphi_1\ (\rho)=\beta_0+\sum_{m=1}^{\infty}\beta_m\,\Phi_0\ (\alpha_m\rho)\tag{30}$$

in which

$$\beta_0\ \equiv\ \frac{2}{1-\beta^2}\int_\beta^1\varphi_1\ (\rho)\ \rho\ d\ \rho=\frac{2}{1-\beta^2}\left\{\frac{\int_\beta^1 P_1(\rho)\rho\ d\rho}{2G}+\frac{1-\beta^2}{2(1-2\nu)}\,[2\nu\ u_0+(1-\nu)\ w_1]\right.$$
$$\left.+\ \sum_{n=1}^{\infty}\,[H_n^{(5)}D_n+H_n^{(6)}E_n]\right\}$$

$$\beta_m\ \equiv\ \frac{1}{\varDelta_m}\int_\beta^1\varphi_1(\rho)\ \Phi_0\ (\alpha_m\rho)\rho\ d\ \rho=\frac{1}{\varDelta_m}\left\{\frac{\int_\beta^1 P_1(\rho)\rho\ \Phi_0(\alpha_m\rho)d\rho}{2G}+\sum_{n=1}^{\infty}\,[T_{n1}^{(m)}\ D_n\right.$$
$$\left.+T_{n2}^{(m)}\ E_n]\ \right\}$$

the normalization factor $\varDelta_m\equiv\frac{1}{2}[\Phi_0^2(\alpha_m)-\beta^2\,\Phi_0^2(\alpha_m\,\beta)]$[11]

$$H_n^{(5)}\equiv\frac{(-1)^n}{k_n}\{[k_n+2(2-\nu)L_n^{(1)}]h_n^{(1)}+L_n^{(1)}h_n^{(2)}+L_n^{(3)}[2(2-\nu)h_n^{(3)}-L_n^{(4)}]\}$$

$$H_n^{(6)}\equiv\frac{(-1)^n}{k_n}\{[-k_n+2(2-\nu)L_n^{(4)}]h_n^{(3)}-L_n^{(4)}h_n^{(4)}+L_n^{(2)}[2(2-\nu)h_n^{(1)}+h_n^{(2)}]\}$$

$$h_n^{(1)}\equiv[I_1(k_n)-\beta\,I_1(k_n\,\beta)]/k_n,\qquad h_n^{(2)}\equiv I_0(k_n)-\beta^2\,I_0(k_n\,\beta)-2h_n^{(1)}$$
$$h_n^{(3)}\equiv-[K_1(k_n)-\beta\,K_1(k_n\,\beta)]/k_n,\qquad h_n^{(4)}\equiv-K_0(k_n)+\beta^2K_0(k_n\,\beta)-2h_n^{(3)}$$

$$T_{n1}^{(m)}\ \equiv\frac{(-1)^n}{k_n}\left\{\ t_{n1}^{(m)}\ \left[k_n+2\ (2-\nu)\ \ L_n^{(1)}\right]+2\ (2-\nu)\,t_{n2}^{(m)}L_n^{(3)}+k_n t_{n3}^{(m)}\,L_n^{(1)}\right.$$
$$\left.-k_n t_{n4}^{(m)}\ L_n^{(3)}\right\}$$

$$T_{n2}^{(m)} \equiv \frac{(-1)^n}{k_n} \{ t_{n2}^{(m)} [-k_n + 2(2-\nu) L_n^{(4)}] + 2(2-\nu)\, t_{n1}^{(m)} L_n^{(2)} + k_n\, t_{n3}^{(m)} L_n^{(2)} - k_n\, t_{n4}^{(m)} L_n^{(4)} \}$$

$$t_{n1}^{(m)} \equiv \frac{k_n}{\alpha_m^2 + k_n^2} [I_1(k_n) \Phi_0(\alpha_m) - \beta\, I_1(k_n \beta) \Phi_0(\alpha_m \beta)]$$

$$t_{n2}^{(m)} \equiv \frac{k_n}{\alpha_m^2 + k_n^2} [K_1(k_n) \Phi_0(\alpha_m) - \beta\, K_1(k_n \beta) \Phi_0(\alpha_m \beta)]$$

$$t_{n3}^{(m)} \equiv \frac{k_n}{\alpha_m^2 + k_n^2} [I_0(k_n) \Phi_0(\alpha_m) - \beta^2 I_0(k_n \beta) \Phi_0(\alpha_m \beta) - 2 t_{n1}^{(m)}]$$

$$t_{n4}^{(m)} \equiv \frac{k_n}{\alpha_m^2 + k_n^2} [K_0(k_n) \Phi_0(\alpha_m) - \beta^2 K_0(k_n \beta) \Phi_0(\alpha_m \beta) - 2\, t_{n2}^{(m)}]$$

Substituting equation (30) into equation (28) and then comparing the coefficients of the like terms on both sides of this equation, we get:

$$\frac{1-\beta^2}{2(1-2\nu)} [2\nu\, u_0 + (1-\nu)\, w_1] + \sum_{n=1}^{\infty} [H_n^{(5)} D_n + H_n^{(6)} E_n] = -\frac{1}{2G} \int_\beta^1 P_1(\rho) \rho\, d\rho \tag{31}$$

$$- \Delta_m \left[\gamma \operatorname{sh} \alpha_m \gamma + \left(B_m - \frac{3-2\nu}{\alpha_m} \right) \operatorname{ch} \alpha_m \gamma \right] A_m + \sum_{n=1}^{\infty} [T_{n1}^{(m)} D_n + T_{n2}^{(m)} E_n],$$

$$= -\frac{1}{2G} \int_\beta^1 P_1(\rho)\, \Phi_0(\alpha_m \rho) \rho\, d\rho, \qquad (m=1, 2, \cdots) \tag{32}$$

Now, all the boundary conditions of the problem have been completely satisfied. Furthermore, the undetermined coefficients can be solved from the system of simultaneous linear algebraic equations as formulation in equation (16a), (24), (26), (27), (31) and (32). The solution of the problem thus obtained may approach to exact as more terms m and n are taken in both series.

As for the plate under the antisymmetric loading, we take

$$\frac{u}{a} = \sum_m \frac{A_m}{\alpha_m} \left[\zeta \operatorname{ch} \alpha_m \zeta + \left(B_m - \frac{1}{\alpha_m} \right) \operatorname{sh} \alpha_m \zeta \right] \Phi_1(\alpha_m \rho) + \sum_n \frac{\sin k_n \zeta}{k_n} [D_n I_1(k_n \rho)$$
$$+ E_n K_1(k_n \rho) + F_n \rho\, I_0(k_n \rho) + G_n \rho K_0(k_n \rho)] \tag{33a}$$

$$\frac{w}{a} = w_0 - \sum_m \frac{A_m}{\alpha_m} \left\{ \zeta \operatorname{sh} \alpha_m \zeta + \left[B_m - \frac{4(1-\nu)}{\alpha_m} \right] \operatorname{ch} \alpha_m \zeta \right\} \Phi_0(\alpha_m \rho) + \sum_n \frac{\cos k_n \zeta}{k_n} \Big\{ D_n I_0(k_n \rho)$$
$$- E_n K_0(k_n \rho) + F_n \left[\rho\, I_1(k_n \rho) + \frac{4(1-\nu)}{k_n} I_0(k_n \rho) \right]$$
$$+ G_n \left[- \rho\, K_1(k_n \rho) + \frac{4(1-\nu)}{k_n} K_0(k_n \rho) \right] \Big\} \tag{33b}$$

from which stress components are derived as:

$$\frac{\sigma_r}{2G} = \sum_m \frac{A_m}{\alpha_m} \Big\{ [\alpha_m \zeta \operatorname{ch} \alpha_m \zeta - (\alpha_m B_m - 1 + 2\nu) \operatorname{sh} \alpha_m \zeta]\, \Phi_0(\alpha_m \rho)$$
$$- \left[\zeta \operatorname{ch} \alpha_m \zeta + \left(B_m - \frac{1}{\alpha_m} \right) \operatorname{sh} \alpha_m \zeta \right] \Phi_1(\alpha_m \rho)/\rho \Big\}$$
$$+ \sum_n \frac{\sin k_n \zeta}{k_n} \Big\{ D_n \left[I_0(k_n \rho)\, k_n - \frac{1}{\rho} I_1(k_n \rho) \right]$$

$$- E_n \left[K_0 (k_n \rho)\, k_n+\frac{1}{\rho}K_1 (k_n \rho)\right]+F_n[(1-2\nu)I_0(k_n \rho)+\rho\, k_n\, I_1(k_n \rho)]$$

$$+G_n[(1-2\nu)K_0(k_n \rho)-\rho\, k_n\, K_1 (k_n \rho)]\Big\} \tag{34a}$$

$$\frac{\sigma_z}{2G}=-\sum_m \frac{A_m}{\alpha_m}[\alpha_m \zeta \operatorname{ch} \alpha_m \zeta+(\alpha_m B_m-3+2\nu)\operatorname{sh} \alpha_m \zeta]\Phi_0(\alpha_m \rho)$$

$$-\sum_n \frac{\sin k_n \zeta}{k_n}\{D_n k_n I_0(k_n \rho)-E_n k_n K_0(k_n \rho)+F_n[\rho\, k_n\, I_1(k_n \rho)$$

$$+2(2-\nu)I_0(k_n \rho)]+G_n[-\rho\, k_n K_1(k_n \rho)+2(2-\nu)K_0(k_n \rho)]\} \tag{34b}$$

$$\frac{\sigma_\theta}{2G}=\sum_m \frac{A_m}{\alpha_m}\Big\{2\nu \operatorname{sh} \alpha_m \zeta\, \Phi_0 (\alpha_m \rho) +\Big[\zeta \operatorname{ch} \alpha_m \zeta+ \Big(B_m - \frac{1}{\alpha_m}\Big)\operatorname{sh} \alpha_m \zeta\Big]\Phi_1 (\alpha_m \rho)/\rho\Big\}$$

$$+\sum_n \frac{\sin k_n \zeta}{k_n}[D_n I_1(k_n \rho)/\rho+E_n\, K_1(k_n \rho)/\rho+F_n(1-2\nu)I_0 (k_n \rho)$$

$$+G_n(1-2\nu)K_0(k_n \rho)] \tag{34c}$$

$$\frac{\tau_{rz}}{2G}=\sum_m A_m \Big\{\zeta \operatorname{sh} \alpha_m \zeta +\Big[B_m - \frac{2(1-\nu)}{\alpha_m}\Big]\operatorname{ch} \alpha_m \zeta\Big\}\Phi_1 (\alpha_m \rho)$$

$$+\sum_n \cos k_n \zeta \Big\{D_n\, I_1(k_n \rho)+E_n\, K_1(k_n \rho)+F_n \Big[\rho\, I_0(k_n \rho)$$

$$+\frac{2(1-\nu)}{k_n} I_1 (k_h \rho)\Big]+G_n\Big[\rho\, K_0 (k_n \rho)- \frac{2(1-\nu)}{k_n}K_1(k_n \rho) \Big]\Big\} \tag{34d}$$

Like the previous, to satisfy boundary conditions here we choose:

$$B_m = \frac{1}{\alpha_m}\left[2 (1-\nu)- \frac{\alpha_m \gamma \operatorname{sh} \alpha_m \gamma}{\operatorname{ch} \alpha_m \gamma}\right] \tag{35}$$

$$\cos k_n \gamma=0 \quad \text{or} \quad k_n=\frac{2n-1}{2\gamma}\pi, \qquad (n=1,\ 2,\ \cdots) \tag{36}$$

From the boundary conditions $u(1,\ \zeta)=0$ and $\tau_{rz} (\beta,\ \zeta)=0$, we again obtain equation (16b)~(22).

The boundary condition $w(1,\ \zeta)=0$ yields

$$-w_0+ \sum_{m=1}^{\infty} \frac{A_m}{\alpha_m}\Big\{\zeta \operatorname{sh} \alpha_m \zeta+ \Big[B_m - \frac{4(1-\nu)}{\alpha_m}\Big]\operatorname{ch} \alpha_m \zeta\Big\} \Phi_0 (\alpha_m)$$

$$= \sum_{n=1}^{\infty} [H_n^{(1)}D_n+H_n^{(2)}E_n]\cos k_n \zeta \tag{37}$$

here, $H_n^{(1)}$ and $H_n^{(2)}$ are expressed in equation (23). Similarly, using the orthogonal property of Fourier series, we get from equation (37):

$$\frac{-2(-1)^n}{\gamma k_n}+ \sum_{m=1}^{\infty} \frac{2(-1)^n k_n\Phi_0(\alpha_m)}{\gamma (\alpha_m^2+k_n^2)\, \alpha_m}\left[\gamma \operatorname{sh} \alpha_m \gamma-\frac{2\alpha_m \operatorname{ch} \alpha_m \gamma}{\alpha_m^2+k_n^2} + \frac{\alpha_m B_m-4(1-\nu)}{\alpha_m}\operatorname{ch} \alpha_m \gamma\right]$$

$$\times A_m+H_n^{(1)} D_n+H_n^{(2)} E_n=0, \qquad (n=1,\ 2,\ \cdots) \tag{38}$$

Furthermore, from the boundary condition $\sigma_r(\beta,\ \zeta)=0$, we obtain:

$$-\sum_{m=1}^{\infty}\frac{2(-1)^n\Phi_0(\alpha_m\beta)}{\gamma\,(\alpha_m^2+k_n^2)}\left[\alpha_m\gamma\,\mathrm{sh}\,\alpha_m\gamma-\frac{\alpha_m^2-k_n^2}{\alpha_m^2+k_n^2}\mathrm{ch}\,\alpha_m\gamma+(\alpha_m B_m-1+2\nu)\,\mathrm{ch}\,\alpha_m\gamma\right]A_m$$

$$+H_n^{(3)}D_n+H_n^{(4)}E_n=0,\qquad (n=1,\ 2,\ \cdots)\tag{39}$$

where $H_n^{(3)}$ and $H_n^{(4)}$ are the same with those in equation (25).

Finally, in order to satisfy the boundary condition of the upper and lower surfaces of the plate, i.e. $\sigma_z(\rho,\pm\gamma)=\pm P_2(\rho)$, we must have:

$$\sum_{m=1}^{\infty}[H_n^{(5)}D_n+H_n^{(6)}E_n]=-\frac{1}{2G}\int_{\beta}^{1}P_2(\rho)\,\rho\,d\rho\tag{40}$$

$$-\triangle_m\left[\gamma\,\mathrm{ch}\,\alpha_m\gamma+\left(B_m-\frac{3-2\nu}{\alpha_m}\right)\mathrm{sh}\,\alpha_m\gamma\right]A_n+\sum_{n=1}^{\infty}[T_{n1}^{(m)}D_n+T_{n2}^{(m)}E_n]$$

$$=-\frac{1}{2G}\int_{\beta}^{1}P_2(\rho)\Phi_0(\alpha_m\rho)\rho\,d\rho\qquad (m=1,\ 2,\ \cdots)\tag{41}$$

where $H_n^{(5)}$, $H_n^{(6)}$, $\triangle_m$, $T_{n1}^{(m)}$ and $T_{n2}^{(m)}$ are the same with those in equation (31) and (32).

If we let a represent the inner radius of the plate and b the outer radius, the above analysis may be used to solve the problems with the inner boundary rigidly fixed and the outer boundary free, i.e. for the case of $\beta=b/a>1$.

III. Numerical Computation

In order to compare with previous approximate theories of thick plates, some practical problems are considered here as illustration. Assume a thick annular plate is loaded on its upper surface with uniform pressure σ_0 or uniform pressure with the part-annular area as shown in Fig. 2, and is free of traction on the lower surface, i.e. $q(r)=0$. For numerical computation, we take

$$\beta=b/a=0.25,\qquad \gamma=h/a=0.18\qquad \sigma_0/2G=10^{-5}$$

and Poisson ratio $\nu=0.3$. In addition, the width of the loading zone is assumed to be $\frac{1}{5}$ of the whole plate, under the total load $(1-\beta^2)\pi\sigma_0/2G$ acting between the interval $\rho_1\leqslant\rho\leqslant\rho_2$, i.e. $\rho_2-\rho_1=\frac{1}{5}(1-\beta)=0.15$. The cases of $\rho_1=0.25$, 0.40, 0.55, 0.70 and 0.85 are computed as well as the case of uniformly distributed pressure over the whole plate. All the computations are carried out on the computer machine DJS-6. The first n eigenroots of the transcendental equation (19) are computed, then the simultaneous linear algebraic equations are solved for their undetermined coefficients. In the process of computation it has been noted that 1 st, 2nd kind of modified Bessel Functions increase or decrease monotonically in the exponential manner so that very large numerical differences between the elements in the coefficient matrix of the algebraic equations would appear. Some measures to eliminate such phenomenon must be taken before attempting to solve the algebraic equations so as to improve the accuracy of the solu-

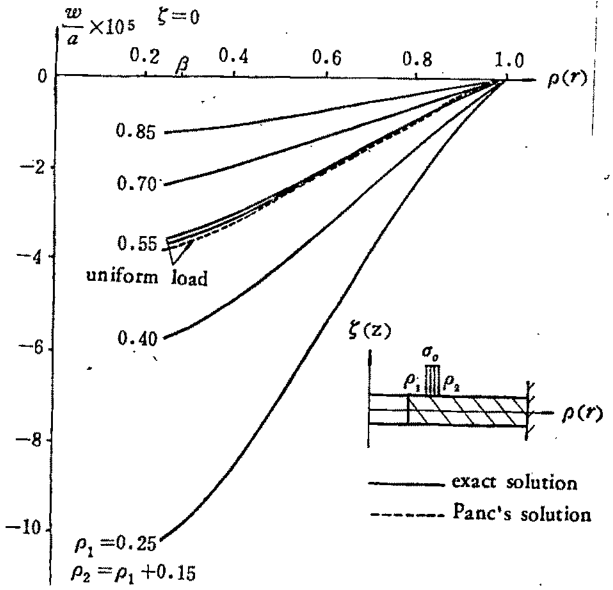
w/a ×10⁵
ζ=0
0.2
β
0.4
0.6
0.8
1.0
ρ(r)
0
−2
−4
−6
−8
−10
0.85
0.70
0.55
uniform load
0.40
ρ₁=0.25
ρ₂=ρ₁+0.15
ζ(z)
σ₀
ρ₁
ρ₂
ρ(r)
exact solution
Panc's solution

Fig. 2

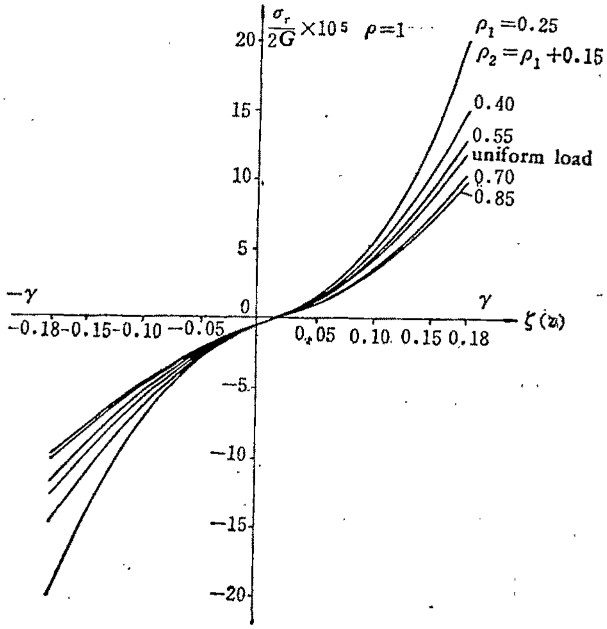
σᵣ/2G ×10⁵
ρ=1
ρ₁=0.25
ρ₂=ρ₁+0.15
0.40
0.55
uniform load
0.70
0.85
20
15
10
5
0
−5
−10
−15
−20
−γ
γ
−0.18
−0.15
−0.10
−0.05
0.05
0.10
0.15
0.18
ζ(z)

Fig. 3

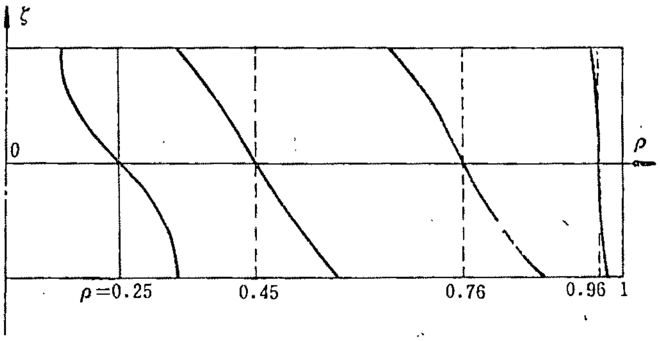

Fig. 4

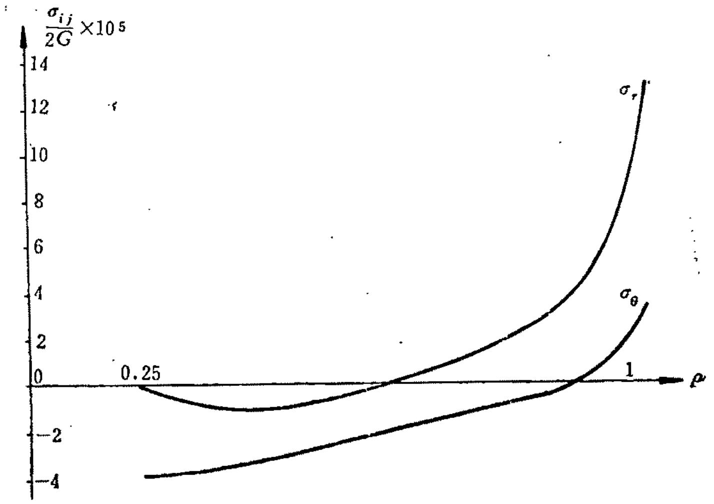

Fig. 5

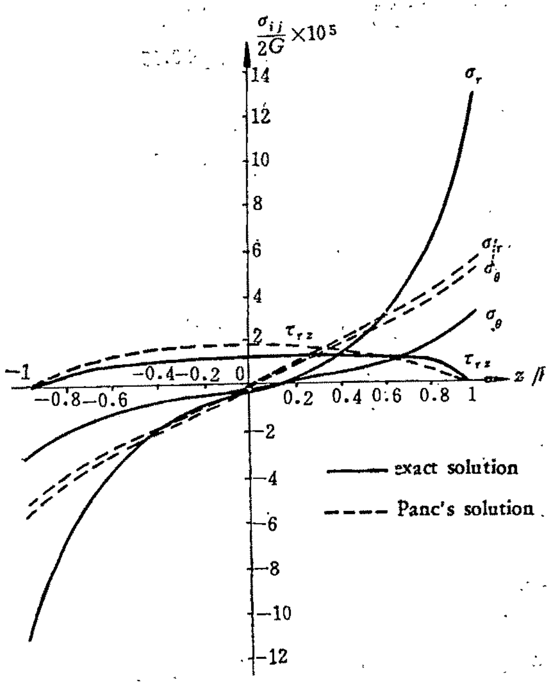

Fig. 6

tions. It is also found that Fourier series expansion converge much faster to the required functions than Bessel series expansion, and so by taking $m \geqslant 80$, $n \geqslant 9$, we have already acquired steady and accurate results. For more details in computation and the related computing program, the reader may refer to Reference [12].

Finally, all the results are plotted in curves as shown in Fig. 2~Fig. 6 respectively. Fig. 2 shows the transverse deformation w of the middle plane versus dimensionless radius ρ under the different cases of loading. The results from Panc's theory are also drawn for comparison. In Fig. 3, the radial stress σ_r along the thickness of plate at the rigidly fixed boundary is plotted, Fig. 4 gives the curves of the radial displacements at various sections versus the dimensionless thickness of the plate, and Fig. 5 indicates σ_r and σ_θ vs. ρ curves on $\zeta=\gamma$. From both figures, it may be seen that the normal stress σ_r of the upper surface changes its sign from positive to negative as the radius ρ approaches to the value of its hole radius.

IV. Discussion

1. As shown in Fig. 2, the computed deflection of the middle surface in the example of uniform load is in fairly good agreement with that of Panc's approximate solution except in the neighborhood of fixed boundary. It should be pointed out that in the exact solution, the slopes of normal displacements at fixed boundary are

$$\left[\frac{\partial w}{\partial r}\right]_{\substack{r=a \\ z=\pm h}}=0$$

and

$$\left[\frac{\partial w}{\partial r}\right]_{\substack{r=a \\ z=0}}\neq 0$$

It is because the transverse shearing stress are, in fact, equal to zero on $z=\pm h$, and on $z=0$, however, it is non-zero. Nevertheless, the deflection itself in general reflects the global effect, and as the consequence, Panc's solution still has a sufficient accuracy.

2. There exist appreciable discrepancies which reflect mainly the local effects, between the present computation results and those of Panc's as shown in Fig. 6. This largely due to the erroneous conventional description of the rigidly fixed boundary conditions by the classical plate theory as well as all the prevailing theories of thick plates. In these theories, both the deflection w and its slope on the middle surface ($z=0$) are taken to be zero as for the fixed-edge boundary conditions. It is apparent that the latter condition contradicts with the consideration of transverse shear strain, which is not equal to zero at $z=0$. This fact seems worthy to draw the attention of the designers.

References

[1] E. Reissner: *The Effect of Transverse Shear Deformation on the Bending of Elastic Plates,* **J. Appl. Mech.** Vol. 12, A-68, 1945.

[2] H. Henky: *Über die Berücksichtigung der Schubverzerrungen in ebenen Platten,* **Ing.-Arch.** Vol. 16, 27, 1947.

[3] A. Kromm: *Über die Randguerkräfte bei gestutzten Platten,* **ZAMM**, 35, 231, 1955.

[4] Б. Ф. Власов: Об Уравнениях Теории Изгиба Пластинок, *Известия*. Стн. АН. СССР № 12, 1957.

[5] V. Panc: Theory of Elastic Plates, Noordhoff International Publishing, Leyden, The Netherlands, 1975.

[6] K. O. Friedrichs and R. F. Dressler: *A Boundary-Layer Theory for Elastic Plates,* **Comm. Pure Appl. Math.** Vol. 14, 1, 1961.

[7] L. H. Donnell: *A Theory for thick Plates,* **Proc. 2nd U. S. National Congress of Appl. Mech.** 369, 1955.

[8] C. W. Lee: *Three Dimensional Solution for Simply Supported Thick rectangular Plates,* **Nucl. Eng. and Design.** Vol. 6, 155, 1967.

[9] Luo Zudao: *On Axisymmetric Deformation of a Finite Hollow Cylinder,* **Acta Mechanica Sinica**, The Chinese Soc. of Theo. and Appl. Mech, Vol. 3, 219, 1979.

[10] L. N. G. Filon: *On the Elastic Equilibrium of Circular Cylinders under Certain Practical Systems of Load,* Phil. Trans. Roy. Soc. London, Ser. A, Vol. 198, 147, 1902.

[11] Raja Sundara, K. T. Iyengar and C. V. Yogananda: *The End Problem of Hollow Cylinders,* **J. Appl. Mech.** Vol. 33, 685, 1966.

[12] Sun Quanxin: *An Exact Solution of Thick Annular Plates,* Graduate Student Thesis, Shanghai Jiao Tong University, 1980.

Annual of the CSNAME, Vol. 1, 1982

STRENGTH IN OPENING WITH VARIOUS REINFORCEMENTS IN SPHERICAL AND CYLINDRICAL STRUCTURES

XU BINGHAN* (徐秉汉) AND PEI JUNHOU (裴俊厚)

China Ship Scientific Research Center

SUMMARY

For solving the problems encountered in ocean engineering, underwater structures and high pressure vessels, several simplified formulas are presented in this paper for the estimation of the strength of circular opening with various reinforcements to cylindrical and spherical shells. Meanwhile, several charts are also introduced for designers to determine the maximum stress on structures in the case of

1. Opening with coaming reinforcement in cylindrical shell
2. Opening with coaming reinforcement and strengthened plate in cylindrical shell
3. Opening with coaming reinforcement in spherical shell
4. Opening with coaming reinforcement and strengthened plate in spherical shell

From the above charts the maximum stress can be determined by designers easily and economically comparing with the numerical solution on a large capacity computer. Comparing this solution with experiment and finite element method it has been found that the simplified method presented in this paper gives the solution with sufficient accuracy.

I. The Basic Method

In ocean engineering, underwater structures, high pressure vessels and deep ocean vehicles, problems of strength in circular opening on spherical and cylindrical shells must be encountered. In order to reduce high stress around the opening strengthening must be taken in the form of coaming reinforcement or strengthened plate. The stress analysis of these shells is very important. Although many investigations on this problem have been made, the results are still difficult to use by designers, because it is too complex to calculate a long series, coefficients of each term of which is also represented by a series of cylindrical functions. Of course, the finite element method is effective to resolve this problem, but the use of a large capacity computer is quite costly, while a great number of shell elements must be taken in order to obtain the precise solution. A simplified and reliable method is always expected by designers. For this purpose, in this paper, some simplifications were made to the stress function and displacement around opening based on the phenomena observed in actual tests. The shallow shell theory and the polar coordinates (ρ, θ) are adopted. The zero of the coordinates is taken at the center of the circular opening. The following are the main simplifications:

---

* The author was invited to deliver a lecture at the University of Trondheim Norway in June 1980. Part of the lecture are from this paper.

1. From the analysis of the experimental data it has been found that the normal displacement function W around the circular reinforcement mainly depend on the (ρ) direction, as its variation at the (θ) direction is much smaller than the former. So the normal displacement function (W) can be considered as the function of (ρ^{-2}), while the stress on median plane is calculated.

2. On analyzing the experimental data it has also been found that the stress on the median plane around the reinforced opening can be expressed as the polynomial of the function of angle (θ), but the terms with (0), (2θ) are dominant, and the terms with (4θ), (6θ) can be neglected, so that only terms with (0) and (2θ) have to be considered in the calculation of the stress function.

In resolving the shallow shell equations, the variational principle for shells and the Myskhelishvili method in elastic plane theory were adopted. Thus the formulas for estimation of the strength of circular opening on cylindrical shells with coaming reinforcement or with both the coaming reinforcement and the strengthened plate have obtained in paper [1], [2], and for spherical shells in paper [3], [4].

II. The Simplified Formula for Estimation of the Maximum Stress around the Opening

It is verified that the maximum stress around the opening with coaming reinforcement on a cylindrical shell occurred on the intersections of the edge of the opening and the generatrix passing through the center of the opening in the circumference direction $(\theta=0°)$. This maximum stress is usually taken as the basis of the strength design. Here this stress is represented by the following formulas and design charts. The stress distributions on the median plane are also presented in the appendix of this paper.

Take the symbol C_s as the stress concentration factor, thus

$$C_s=\frac{\text{maximum stress}}{\text{nominal shell stress}} \tag{1}$$

1. Opening on cylindrical shell with coaming reinforcement (Fig. 1)

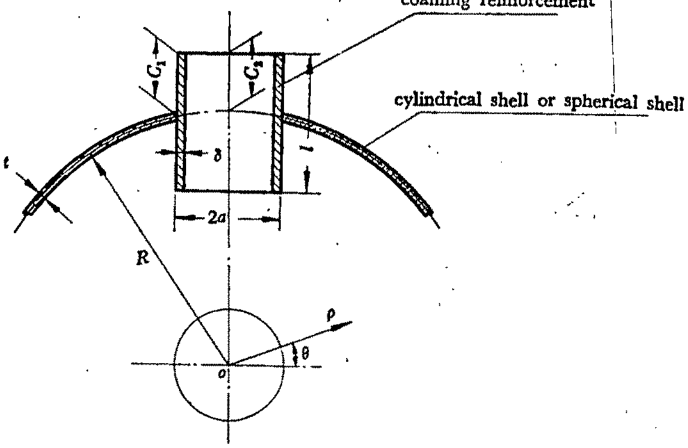

Fig. 1

The stress concentration factor C_s can be easily calculated by the following simple formula:

$$\left.\begin{aligned}
C_s &= 1.5+K_1+K_2+0.5W_0 \\
K_1 &= \frac{\left(-1.5+\frac{t}{\delta}\frac{a}{R}-W_0\right)\frac{F}{at}}{1+(1+\nu)\frac{F}{at}} \\
K_2 &= \frac{1+\nu\frac{F}{at}+1.5\left[1+(1+\nu)\frac{F}{at}\right]W_0}{1+(3+\nu)\frac{F}{at}} \\
W_0 &= \frac{\left(\frac{a}{R}\right)^3\frac{R}{t}}{\frac{\frac{20}{3}-4\nu}{3(1-\nu^2)}\frac{t}{R}\frac{R}{a}+\frac{16}{3}\frac{\sqrt[4]{3(1-\nu^2)}}{1-\nu^2}\frac{F}{at}\frac{\delta}{t}\frac{1}{\zeta}+\frac{3}{4}\left(\frac{a}{R}\right)^3\frac{R}{t}}
\end{aligned}\right\} \quad (2)$$

where

a=radius of the circular opening on cylindrical shell
R=radius of cylindrical shell
t=thickness of cylindrical shell
δ=thickness of coaming reinforcement
ν=Poisson's ratio
F=effective area of coaming reinforcement $=\zeta\delta\sqrt{a\delta}$, ζ can be found directly from Fig. 2.

The parameters used in the Fig. 2 are as follows:

$$\xi=\frac{1.285\,l}{\sqrt{a\delta}}, \qquad \eta=\frac{0.6425(C_1+C_2)}{\sqrt{a\delta}}$$

l, C_1, C_2 are the dimension of coaming reinforcement (Fig. 1). Using the new parameter

$\frac{a}{R}\sqrt[4]{\frac{R}{t}}\zeta$ further simplification to formula (2) can be made. Therefore we obtain:

$$\left.\begin{aligned}
C_s &= 1.5+K_1+K_2+0.5W_0 \\
K_1 &= \frac{\left[-1.5+0.1\left(\frac{F}{at}\right)^{-2/3}\left(\frac{a}{R}\sqrt[4]{\frac{R}{t}\zeta}\right)^{2/3}-W_0\right]\frac{F}{at}}{1+(1+\nu)\ \frac{F}{at}} \\
K_2 &= \frac{1+\nu\frac{F}{at}+1.5\left[1+(1+\nu)\ \frac{F}{at}\right]W_0}{1+(3+\nu)\ \frac{F}{at}} \\
W_0 &= \frac{1}{\frac{\frac{0.4}{3}-0.08\nu}{6(1-\nu^2)}\left(\frac{a}{R}\sqrt[4]{\frac{R}{t}\zeta}\right)^{-4}+3.44\frac{\sqrt[4]{3(1-\nu^2)}}{1-\nu^2}\left(\frac{F}{at}\right)^{5/3}\left(\frac{a}{R}\sqrt[4]{\frac{R}{t}\zeta}\right)^{-8/3}+\frac{3}{4}}
\end{aligned}\right\} \quad (3)$$

Based upon formula (3) design chart for C_s can be established in Fig. 3. By means of chart (3) the value C_s can be easily determined by two parameters $\frac{F}{at}$, $\frac{a}{R}\sqrt[4]{\frac{R}{t}}\zeta$.

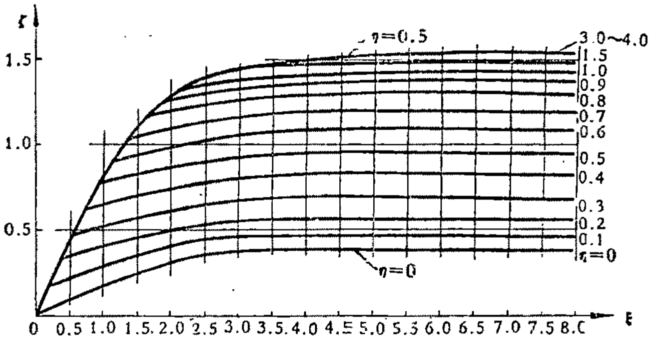

Fig. 3

2. Opening on cylindrical shell with both coaming reinforcement and strengthened plate (Fig. 4)

Take the symbol $\bar{C}_s$ as the stress concentration factor in above case and it can be calculated by the following formula:

$$\bar{C}_s = \frac{C_s}{\gamma} \quad (4)$$

where

C_s=stress concentration factor for opening with coaming reinforcement only and determined by Fig. 3

γ=coefficient affected by the strengthened plate.

The coefficient γ is calulated by following formula:

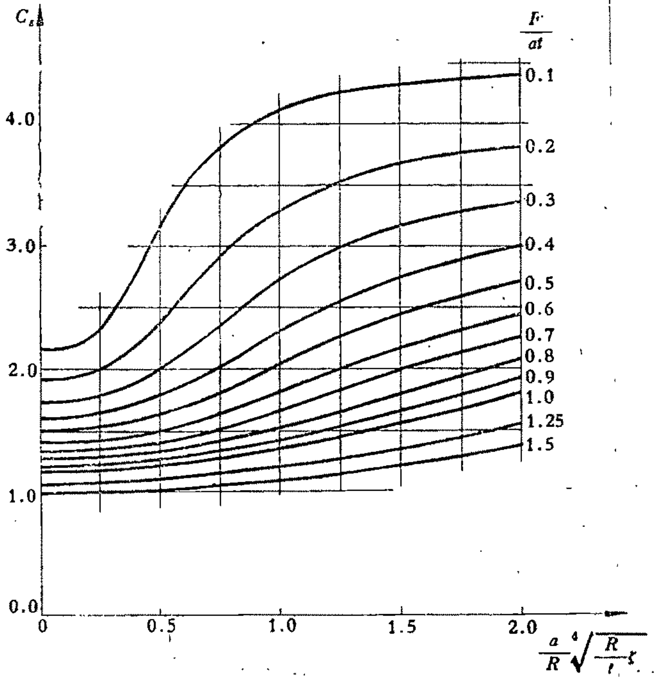

Fig. 3

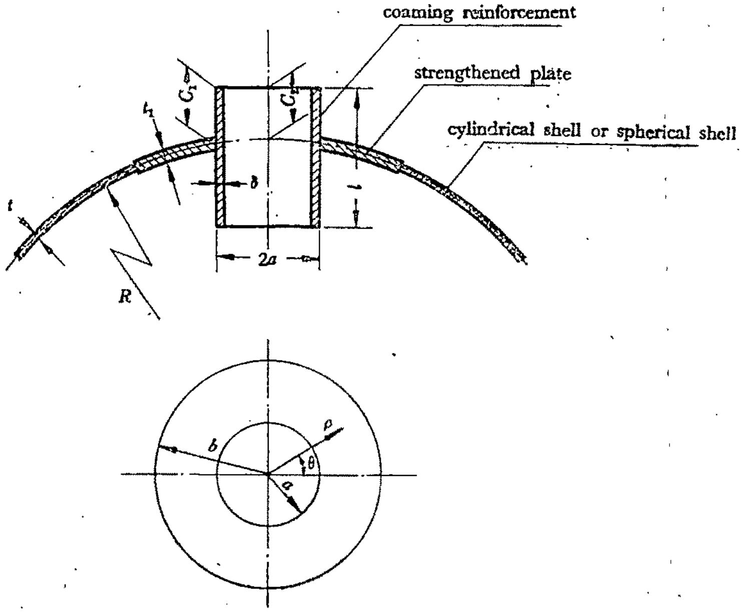

Fig. 4

$$\gamma = 1 + \alpha\left(\frac{t_1}{t} - 1\right) \tag{5}$$

where t_1 = thickness of the strengthened plate

α can be found directly from Fig. 5 employing the parameter $\frac{a}{R}$, $m=\frac{b}{a}$. b is the width of the strengthened plate.

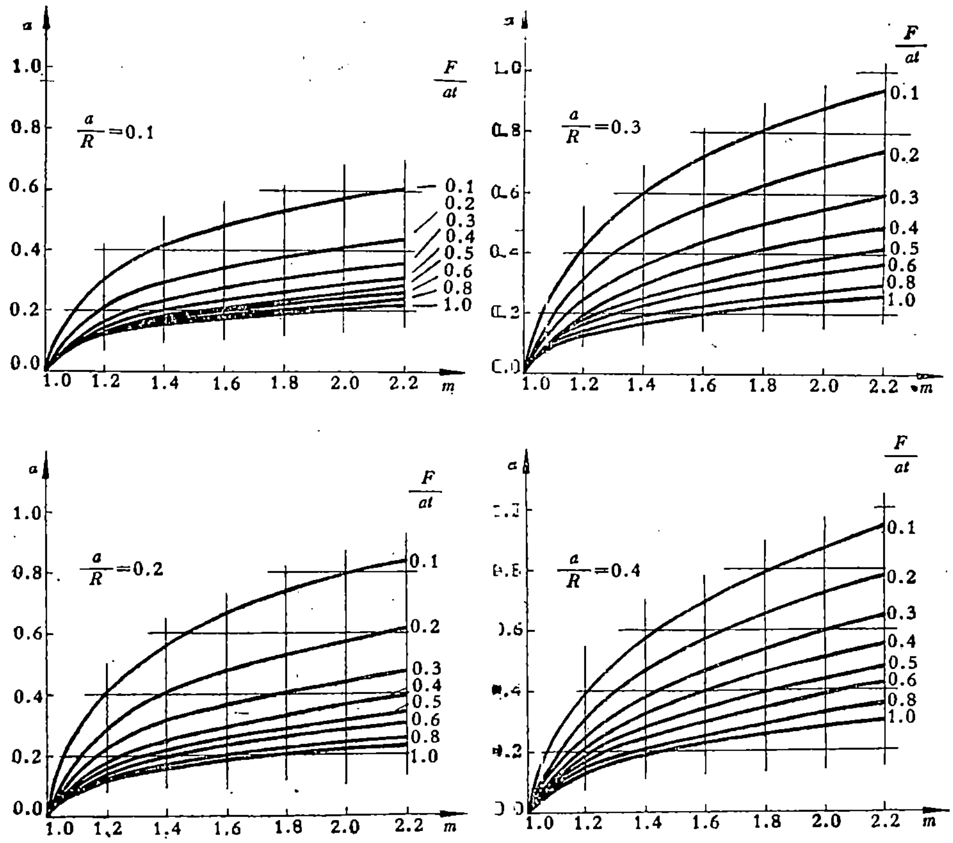

Fig. 5

3. Opening on spherical shell with coaming reinforcement (Fig. 1)

As in the case of cylindrical shell, the value of C_s can also be obtained as follows:

$$C_s=2-\frac{2\,\frac{F}{at}\left[1+W_0-0.1\left(\frac{F}{at}\right)^{-2/3}\left(\frac{a}{R}\sqrt[4]{\frac{R}{t}}\,\zeta\right)^{2/3}\right]}{1+(1+\nu)\frac{F}{at}}+2W_0$$

$$W_0=\frac{1-\dfrac{2\,\frac{F}{at}\left[1-0.1\left(\frac{F}{at}\right)^{-2/3}\left(\frac{a}{R}\sqrt[4]{\frac{R}{t}}\,\zeta\right)^{2/3}\right]}{1+(1+\nu)\frac{F}{at}}}{\dfrac{\frac{0.4}{3}-0.08\nu}{12(1-\nu^2)}\left(\frac{a}{R}\sqrt[4]{\frac{R}{t}}\,\zeta\right)^{-4}+1+\dfrac{2\,\frac{F}{at}}{1+(1+\nu)\frac{F}{at}}+1.72\dfrac{\sqrt[4]{3(1-\nu^2)}}{1-\nu^2}\left(\frac{F}{at}\right)^{5/3}\left(\frac{a}{R}\sqrt[4]{\frac{R}{t}}\,\zeta\right)^{-8/3}} \qquad (5)$$

Based upon formula (6) the design chart for C_s can be established as in Fig. 6. It is very convenient to determine the value of C_s by Fig. 6 using two parameters $\frac{F}{at}$, $\frac{a}{R}\sqrt[4]{\frac{R}{t}}\zeta$.

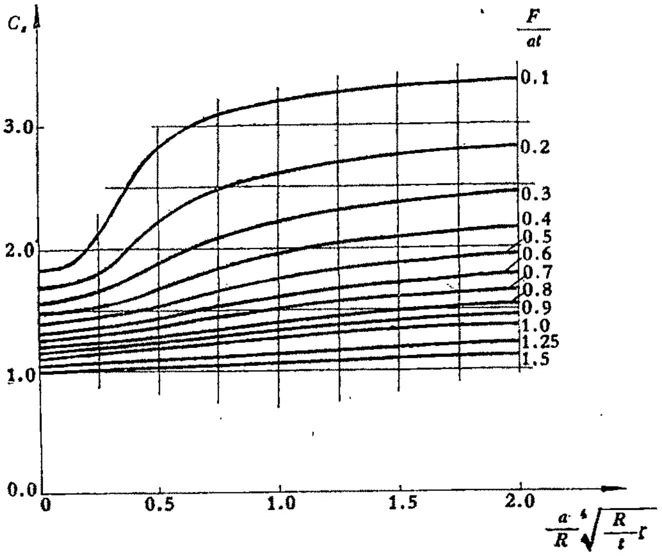

Fig. 6

It is supplemented here that for opening on spherical shell with reinforcement, we can also make the solution directly from the shallow shell equations using Tomson's function. The value of C_s was obtained by author[4] in such a way and expressed as follows:

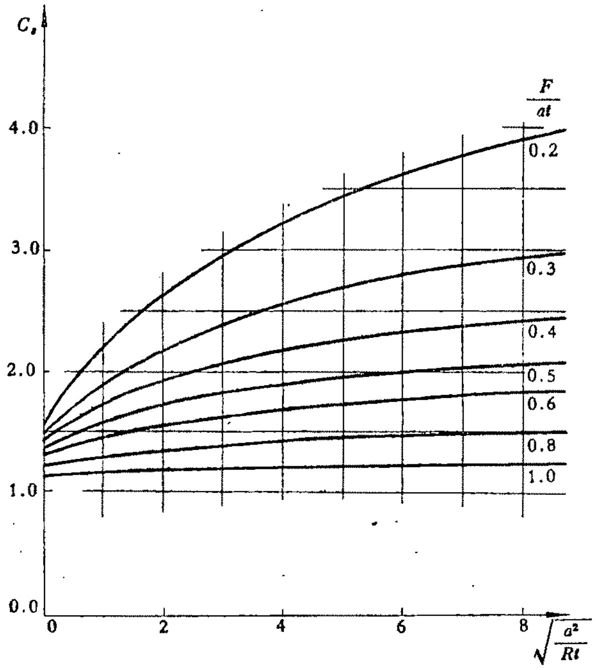

Fig. 7

$$C_s = 1+\left(1-0.7\frac{F'}{at}\right)\frac{\alpha_1+\alpha_2}{(\alpha_1+1.3\alpha_2)\frac{F'}{at}+\alpha_2} \tag{7}$$

where

$$\alpha_1=1.82\sqrt{\frac{a^2}{Rt}}+\left(\frac{t}{\delta}\right)^{2.5}\sqrt{\frac{a}{R}}\left(0.252+0.90\sqrt{\frac{a^2}{Rt}}\right)$$

$$\alpha_2=1.55+0.55\sqrt{\frac{Rt}{a^2}}+\left(\frac{t}{\delta}\right)^{2.5}\sqrt{\frac{a}{R}}\left(0.354+0.2\sqrt{\frac{Rt}{a^2}}\right)$$

$$F'=F+\delta t \tag{8}$$

After futher simplification, the design chart for C_s value can be presented as in Fig. 7[5]. This is also very convenient for use.

4. Opening on spherical shell with both coaming reinforcement and strengthened plate (Fig. 4)

Take the symbol $\bar{C}_s$ as the stress concentration factor in above case, and it can be calculated as follows:

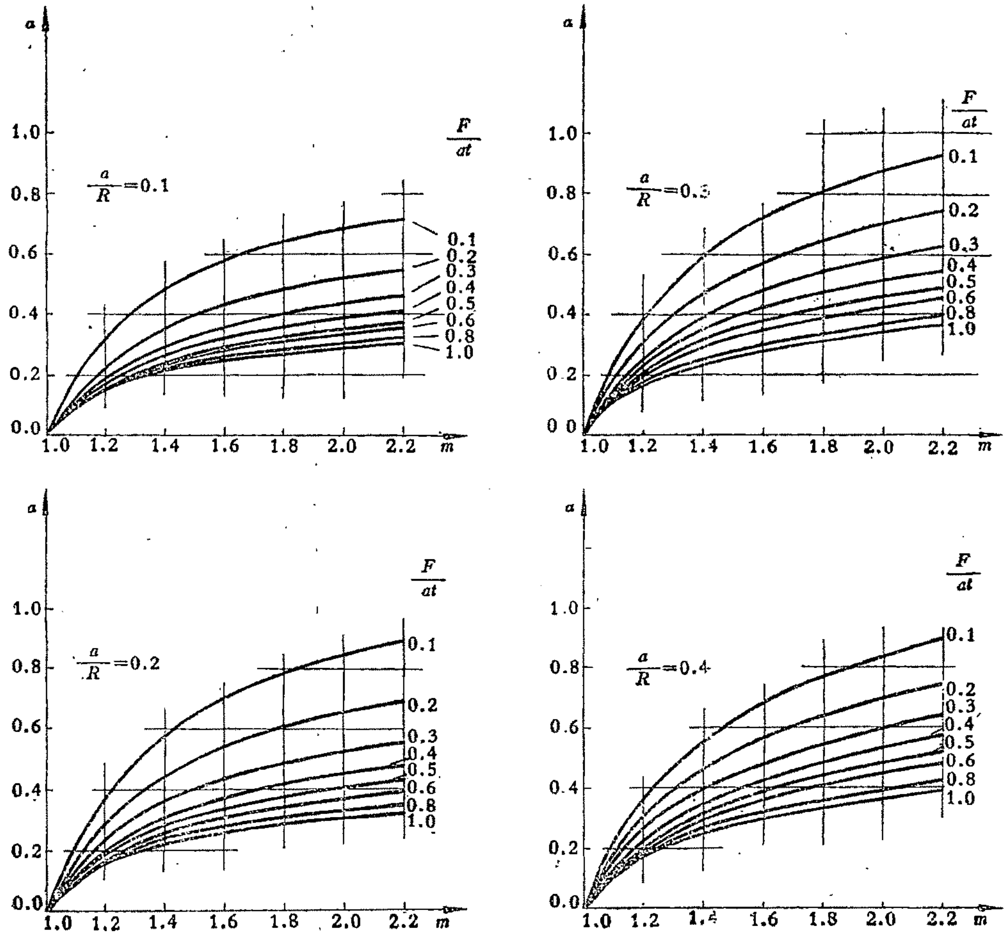

Fig. 8

$$\bar{C}_s = \frac{C_s}{\gamma} \tag{9}$$

where

C_s=stress concentration factor for spherical shell with coaming reinforcement only and determined by Fig. 6

γ=coefficient affected by the strengthened plate and calculated by formula (10)

$$\gamma=1+\alpha\left(\frac{t_1}{t}-1\right) \tag{10}$$

α can be found directly from the Fig. 8, using the parameters $\frac{a}{R}$, $m=\frac{b}{a}$.

III. Some Discussions

Comparison of value C_s, $\bar{C}_s$ obtained by the method in this paper with the experimental results from CSSRC are presented as follows:

1. In Table 1 we tabulate the values of C_s obtained by theoretical prediction and from experimental results for various parameters of $\frac{a}{R}$, $\frac{F}{at}$, $\frac{R}{t}$ and ζ.

Table 1

$\frac{R}{t}$	ζ	$\frac{a}{R}$	$\frac{a}{R}\sqrt[4]{\frac{R}{t}}\zeta$	$\frac{F}{at}$	C_s theoretical	C_s experimental
100	1.55	0.1	0.353	0.2	2.10	2.10
				0.4	1.67	1.67
				0.8		
		0.2	0.706	0.2	2.80	2.08
				0.4	1.95	1.98
				0.8	1.39	1.36
		0.3	1.058	0.2	3.33	3.35
				0.4	2.35	2.30
				0.8	1.55	1.50
		0.4	1.411	0.2	3.63	3.70
				0.4	2.68	2.56
				0.8	1.75	1.70
		0.5	1.764	0.2	3.78	3.85
				0.4	2.88	2.70
				0.8	1.95	1.80
50	1.55	0.1	0.297	0.2		
				0.4		
				0.8		
		0.2	0.593	0.2		
				0.4		
				0.8		
		0.3	0.890	0.2	3 14	3.11
				0.4	2.18	2.04
				0.8	1.45	1.40
		0.4	1.187	0.2	3.48	3.48
				0.4	2.50	2.36
				0.8	1.64	1.60
		0.5	1.484	0.2	3.68	3.70
				0 4	2.74	2.60
				0.8	1.80	1.70
100	0.388	0.4	0.998	0.2	3.28(3.8*)	3.26
	1.09	0.3	0.969	0.433	2.20	2.10
	1.44	0.3	1.039	1.039	1.90	1.80

* C_s value by finite element method, using 381 elements with 816 nodal points[6].

2. In Table 2 $\bar{C}_s$ values are tabulated for cylindrical shell from theoretical prediction and from experimental results.

Table 2

$\frac{R}{t}$	$\frac{a}{R}$	$\frac{F}{at}$	$\frac{t_1}{t}$	m	$\bar{C}_s$ theoretical	$\bar{C}_s$ experimental
112.5	0.3	0.266	2.0	1.965	1.87	1.8
112.5	0.3	0.266	2.0	1.519	2.05	2.0
112.5	0.3	0.266	2.0	1.222	2.30	2.1

3. In Table 3 the C_s values are tabulated for spherical shell from theoretical prediction and from experimental results.

Table 3

$\frac{R}{t}$	ζ	$\frac{a}{R}$	$\frac{a}{R}\sqrt[4]{\frac{R}{t}}\zeta$	$\frac{F}{at}$	I	II	III
40	1.55	0.27	0.76	0.583	1.55	1.46	1.37

Note: I=C_s value obtained by Fig. 6

II=C_s value obtained by Fig. 7, but in the case $\frac{F'}{at}=0.685$

III=C_s value obtained by strain gage measurement near the welded joint of the coaming reinforcement and shell

4. In Table 4 the $\bar{C}_s$ values are tabulated for spherical shell from our theoretical predication and finite element method.

Table 4

$\frac{R}{t}$	$\frac{a}{R}$	$\frac{F}{at}$	$\frac{t_1}{t}$	m	I	II
333	0.052	0.202	1.33	1.45	1.65	1.82
714	0.082	0.44	1.71	1.46	1.36	1.399

Note: I=$\bar{C}_s$ value from our theoretical calculation

II=$\bar{C}_s$ value from finite element method

From Table 1, 2, 3, 4 it has been verified that the results obtained by the simplified method in this paper have a sufficient accuracy comparing with the experimental results. It must be pointed out here that all formulas which are used to calculate the strength around opening on spherical and cylindrical shells with various reinforcements come from an unified theory, so they can be transfered from one case to another. The C_s value for spherical and cylindrical shell can be obtained from $\bar{C}_s$ value for each shell. The C_s, $\bar{C}_s$ value for the plate can be directly transfered from C_s, $\bar{C}_s$ value for the shell[1-4].

IV Conclusion

Comparing the results from this paper with the results from a series of model experiments and full scale measurements it has been found that the simplified formulas and design charts for estimation of the strength in opening on spherical and cylindrical shell with various reinforcements are reliable and accurate. They are convenient in use to calculate the stress concentration $\left(\frac{a}{R} < 0.5\right)$ on underwater marine structures, deep ocean vehicles, high pressure vessels, etc.

References

[1] 徐秉汉、朱邦俊、洪海宝：用围壁加强的圆柱壳开孔的应力计算方法，中国造船，63，1978.

[2] 裴俊厚：有加强圆形切口壳体的应力分析，中国船舶科学研究中心研究报告，1979.

[3] 裴俊厚：围壁或围壁、环板组合加强的球壳开孔的应力分析，中国船舶科学研究中心研究报告，1980.

[4] 徐秉汉：球面结构开孔加强后的强度计算，中国船舶科学研究中心研究报告，1976.

[5] 朱根兴：球面隔壁开孔用围壁加强后的强度计算的简化，中国船舶科学研究中心研究报告，1980.

[6] 朱邦俊、郭庆恒等：用有限元混合法解壳体开孔，中国船舶科学研究中心研究报告，1980.

Appendix

Formulas for Stress Distribution Factor

Based upon the simplifications adopted in this paper the stress function Φ can be determined by the solution of the shallow shell equations. The unknown coefficient in stress function Φ and normal displacement function W may be obtained by the boundary conditions and the variational principle. Then the stress distribution on a median plane can be determined by the stress function Φ. Take the symbol $C_{s\theta}$ as the stress distribution factor in the circumference direction.

$$C_{s\theta} = \frac{\text{Stress on Median Plane}}{\text{Nominal shell stress}} \tag{1}$$

The stress distribution factor $C_{s\theta}$'s for four cases 1, 2, 3, 4 are presented as follows:

1. Opening on cylindrical shell with coaming reinforcement

$$C_{s\theta} = -A\beta^{-2} + 2B + (2C + 6D\,\beta^{-4})\cos 2\theta + [(1 - \ln\beta) - \tfrac{1}{2}\cos 2\theta]W_0\,\beta^{-2} \qquad (2)$$

where $\beta = \frac{\rho}{a}$

$$\left.\begin{aligned}
A &= \frac{\left[3(1-\nu)-4\frac{t}{\delta}\frac{a}{R}+4W_0\right]\frac{F}{at}-3}{4\left[1+(1+\nu)\frac{F}{at}\right]}\\
B &= \frac{3}{8}, \qquad C=\frac{1}{8}\\
D &= \frac{1-(1-\nu)\frac{F}{at}+2\left[1+(1+\nu)\frac{F}{at}\right]W_0}{8\left[1+(3+\nu)\frac{F}{at}\right]}\\
E &= -\frac{\left[1+(1+\nu)\frac{F}{at}\right](1+W_0)}{4\left[1+(3+\nu)\frac{F}{at}\right]}\\
W_0 &= \frac{\left(\frac{a}{R}\right)^3\frac{R}{t}}{\frac{\frac{20}{3}-4\nu}{3(1-\nu^2)}\frac{t}{R}\frac{R}{a}+\frac{16\sqrt[4]{3(1-\nu^2)}}{3}\frac{F}{1-\nu^2}\frac{\delta}{at}\frac{1}{t}\frac{1}{\zeta}+\frac{3}{4}\left(\frac{a}{R}\right)^3\frac{R}{t}}
\end{aligned}\right\} \quad (3)$$

2. Opening on cylindrical shell with both coaming reinforcement and strengthened plate

Take the symbol $\bar{C}_{s\theta}$ as the stress distribution factor in the circumference direction on strengthened plate and $C_{s\theta}$ on shell as:

$$\left.\begin{aligned}
\bar{C}_{s\theta} &= \frac{t}{t_1}\Big[-A_1\beta^{-2}+2B_1+(2D_1+12E_1\beta^2+6F_1\beta^{-4})\cos 2\theta+(1-\ln\beta\\
&\quad -\tfrac{1}{2}\cos 2\theta)\frac{t_1}{t}W_0\beta^{-2}\Big]\\
C_{s\theta} &= -A_2\beta^{-2}+2B_2+(2D_2+6F_2\beta^{-4})\cos 2\theta+(1-\ln\beta-\tfrac{1}{2}\cos 2\theta)W_0\beta^{-2}
\end{aligned}\right\} \quad (4)$$

where A_1, B_1, D_1, E_1, F_1, A_2, B_2, D_2, F_2, W_0 are determined by the following equations:

$$\left.\begin{aligned}
&A_1+2B_1=N_a'\\
&\frac{A_1}{m^2}+2B_1+\frac{t_1}{t}m^{-2}\ln m\,W_0=N_b'\\
&-2D_1-6F_1-4G_1-\tfrac{1}{2}\frac{t_1}{t}W_0=N_{a_1}'\\
&2D_1+6E_1-6F_1-2G_1+\frac{t_1}{t}W_0=N_1'\\
&-2D_1-\frac{6}{m^4}F_1-\frac{4}{m^2}G_1+\frac{1}{2}\frac{t_1}{t}m^{-2}(1-4\ln m)W_0=N_{b_1}'\\
&2D_1+6m^2E_1-\frac{6}{m^4}F_1-\frac{2}{m^2}G_1+\frac{t_1}{t}m^{-2}(1-\ln m)W_0=N_2'\\
&\frac{A_2}{m^2}+2B_2+m^{-2}\ln m W_0=N_b'\\
&B_2=\frac{3}{8}
\end{aligned}\right\}$$

$$\left.\begin{aligned}
&D_2=\frac{1}{8}\\
&-2D_2-\frac{6}{m^4}F_2-\frac{4}{m^2}G_2+\frac{1}{2}\,m^{-2}(1-4\ln m)\,W_0=N_b'\\
&2D_2-\frac{6}{m^4}F_2-\frac{2}{m^2}G_2+m^{-2}(1-\ln m)W_0=N_2'\\
&-(1+\nu)\,A_1+2(1-\nu)\,B_1+\frac{t_1}{t}\,W_0=\frac{t_1}{t}\frac{N_a'}{\frac{F}{at}}+\frac{t_1}{t}\frac{a}{R}\frac{t}{\delta}\\
&N_1'=2N_{a_1}'\\
&2(1+\nu)\,D_1+12E_1+6(1+\nu)\,F_1+4\nu\,G_1-\frac{t_1}{2t}\,(1+\nu)\,W_0=\frac{t_1}{t}\frac{N_{a_1}'}{\frac{F}{at}}\\
&\frac{1+\nu}{m^2}\,A_1-2(1-\nu)\,B_1=\frac{t_1}{t}\left[\frac{1+\nu}{m^2}\,A_2-2(1-\nu)\,B_2\right]\\
&(1+\nu)\,D_1+2\nu\,m^2\,E_1-\frac{1+\nu}{m^4}F_1-\frac{2}{m^2}G_1=\frac{t_1}{t}\left[(1+\nu)\,D_2-\frac{1+\nu}{m^4}F_2-\frac{2}{m^2}G_2\right]\\
&(1+\nu)\,D_1+(3+\nu)\,m^2\,E_1+\frac{1+\nu}{m^4}F_1-\frac{1-\nu}{m^2}G_1=\frac{t_1}{t}\Big[(1+\nu)\,D_2+\frac{1+\nu}{m^4}F_2\\
&\quad-\frac{1-\nu}{m^2}G_2\Big]\\
&4\ln m\,B_1+4\ln m\,D_1+6(m^2-1)\,E_1+\frac{3}{4}\,\frac{t_1}{t}\,(1-m^{-2})\,W_0\\
&\quad+\frac{3}{4}\left[m^{-2}-\left(\frac{2R}{a}\right)^{-2}\right]W_0+\frac{1}{6\,(1-\nu^2)}\left(\frac{40}{3}-8\nu-\frac{64}{3}\,m^{-6}\right)\left(\frac{t_1}{t}\right)^3\cdot\frac{R^2t^2}{a^4}W_0\\
&\quad+\frac{32}{9\,(1-\nu^2)}\frac{R^2t^2}{a^4}m^{-6}W_0-(1+2\ln m)+\frac{16\sqrt[4]{3\,(1-\nu^2)}}{3\quad 1-\nu^2}\frac{R^2\delta^{5/2}}{a^{7/2}\,t}\,W_0=0
\end{aligned}\right\}\quad(5)$$

3. Opening on spherical shell with coaming reinforcement

$$C_{s\theta}=1+\left[1-\frac{2\,\frac{F}{at}\left(1+W_0-\frac{a}{R}\frac{t}{\delta}\right)}{1+(1+\nu)\frac{F}{at}}\right]\beta^{-2}+2W_0\,\beta^{-2}(\,1-\ln\beta)\qquad(6)$$

where

$$W_0=\frac{\left[1-\frac{2\,\frac{F}{at}\left(1-\frac{a}{R}\frac{t}{\delta}\right)}{1+(1+\nu)\frac{F}{at}}\right]\left(\frac{a}{R}\right)^3\frac{R}{t}}{\frac{\frac{40}{3}-8\nu}{12\,(1-\nu^2)}\,\frac{R}{a}\,\frac{t}{R}+\left[1+\frac{2\,\frac{F}{at}}{1+(1+\nu)\,\frac{F}{at}}\right]\left(\frac{a}{R}\right)^3\frac{R}{t}-\frac{8}{3}\,\frac{\sqrt[4]{3\,(1-\nu^2)}}{1-\nu^2}\,\frac{1}{\zeta}\,\frac{F}{at}\,\frac{\delta}{t}}$$

4. Opening on spherical shell with both coaming reinforcement and strengthened plate

$$\left.\begin{aligned}
\bar{C}_{s\theta} &= \frac{2t}{t_1}\left[\frac{m^2\left(N_b' - \frac{t_1}{t}\frac{1}{m^2}W_0\ln m\right) - N_a'}{m^2-1} - \frac{m^2\left(N_a' - N_b' - \frac{t_1}{t}\frac{1}{m^2}W_0\ln m\right)\beta^{-2}}{m^2-1}\right. \\
&\qquad \left. + W_0\frac{t_1}{t}\beta^{-2}(1-\ln\beta)\right] \\
C_{s\theta} &= 1 - 2m^2\left(N_b' - \frac{1}{2} - \frac{1}{m^2}W_0\ln m\right)\beta^{-2} + 2W_0\beta^{-2}(1-\ln\beta)
\end{aligned}\right\} \quad (7)$$

where N_a', N_b', W_0 are determined by the following equations:

$$\left.\begin{aligned}
&\left[1 + \frac{m^2+1+\nu(m^2-1)}{m^2-1}\frac{t}{t_1}\frac{F}{at}\right]N_a' - \frac{2m^2}{m^2-1}\frac{t}{t_1}\frac{F}{at}N_b' \\
&\qquad - \left(1 - \frac{2\ln m}{m^2-1}\right)\frac{F}{at}W_0 + \frac{F}{at}\frac{a}{R}\frac{t}{\delta} = 0 \\
&\frac{2}{m^2-1}N_a' - \frac{(1+\nu) + m^2(1-\nu) + (m^2-1)(1-\nu)\frac{t_1}{t}}{m^2-1}N_b' + \frac{2W_0\ln m}{m^2-1}\frac{t_1}{t} = -\frac{t_1}{t} \\
&\left(2 - \frac{4\ln m}{m^2-1}\right)N_a' + \frac{4m^2\ln m}{m^2-1}N_b' + \left\{\left[\frac{\frac{40}{3} - 8\nu}{12(1-\nu^2)}\left(\frac{t_1}{t}\right)^3 + \frac{16}{9}\frac{1-\left(\frac{t_1}{t}\right)^3}{1-\nu^2}m^{-6}\right]\right. \\
&\qquad \times\left(\frac{R}{a}\right)^4\left(\frac{t}{R}\right)^2 + \frac{t_1}{t}(1-m^{-2}) + m^{-2}\frac{4(\ln m)^2}{m^2-1}\frac{t_1}{t} + \frac{8}{3}\frac{\sqrt[4]{3(1-\nu^2)}}{1-\nu^2} \\
&\qquad \left.\times\frac{1}{\zeta}\left(\frac{R}{a}\right)^3\frac{F}{at}\frac{\delta}{t}\frac{t}{R}\right\}W_0 = 1 + 2\ln m
\end{aligned}\right\} \quad (8)$$

Annual of the CSNAME, Vol. 1, 1982

SUPERELEMENT METHOD OF MODAL SYNTHESIS AND ITS APPLICATION TO DYNAMIC CALCULATION OF SHIP STRUCTURE

YUN WEIJUN (恽伟君), DUAN GENBAO (段根宝) AND HU ZHONGGEN (胡仲根)

Shanghai Ship & Shipping Research Institute

SUMMARY

A novel dynamic substructure method — superelement method of model synthesis — is developed on the basis of dynamic transformation and superelement modal analysis. Not like ordinary modal synthesis method, the present superelement method has its apparent merits in that it uses only the coordinate of superelement (i.e. substructure) interface nodes as the generalized degree of freedom, so that the dynamic stiffness matrix of direct stiffness assembling system can be applied and the dimension of eigenvalue problem will not depend on the number of modes of the bound substructures involved in synthesizing procedure. This superelement method has been applied by the authors to accurately predict the principal normal mode characteristics of an ideal model of a 5,000 ton large hatch barge of 1224 deg of freedom. The calculated numerical values are compared with test results obtained through system (mode) identification by hammer testing and measuring in-plane vibration by Molré method and the agreement has been found to be reasonably satisfactory.

I. Introduction

In recent years, with the application of the Method of Modal Synthesis of component parts in shipbuilding industry[1][2], the structure of a ship has been permitted to be calculated by being subdivided into several component parts, such as superstructure, mast, stern post, hull girders, and etc., thus allowing the dynamic response characteristics of the overall hull structure be obtained by modal synthesis[3][4]. This does not solve only the problem of limited capacity of computers and thus makes it possible for most enterprises that have only medium or small size computers to undertake calculations for large complex structures, but also facilitates the analysis of the relative importance of each component part in the overall vibration of the structure more directly through the description of its dynamic characteristics by the principal normal modes of component parts[5]. This is also a necessary step for the analysis of structural failure.

Superelement method, or substructure method, has two different categories when applied to dynamic analysis. One is based mainly on modal synthesis which predicts the dynamic characteristics of a superelement by partial modes (component modes). The other regards an overall system as composed of degrees of freedom of masters and slaves, with the master degree of freedom being defined as those which contributes mainly to the analysis of dynamic characteristics, slave degree of freedom being defined as these which contributes minorly to the dynamic characteristics, and makes use of certain static and dynamic relationships to eliminate the slave degree of freedom from the system so as to yield condensed motion equations. This latter category is represented by the static transformation method of Guyan[6] and Irons[7] and the dynamic transformation method of Kuhar[8].

Although static transformation method is now in wide use, but due to its neglect of the inertial forces of the slaves (i.e. the reduced degree of freedom), it is only applicable to the calculation of engineering problems of lower order frequency, and its error from actual frequency values will increase with the increasing of the order of frequency being calculated. Especially, when the moderate frequency structural problem is being considered, its error will significantly exceed that permitted for engineering calculations.

Kuhar et al. made some improvements to this method and developed dynamic transformation on its basis in 1974. But Kuhar's dynamic transformation only approximately includes dynamic effect because it uses as dynamic modification a known value $\bar{\omega}_j$ which is only approximate to system frequency ω_j. Besides, in solving large complex structure problem in small capacity computers, Kuhar's method has inherent limitations to the storage of both masters and slaves in computer due to the fact that it is unavoidable to solve the normal mode problem of the system comprising of slave degrees of freedom even if large amount of slaves can be eliminated. While storage of information in computers is a problem, what is the sense of talking about computation.

This present paper integrately combines Kuhar's dynamic transformation with modal synthesis of bound substructure and derives the superelement method of model synthesis. This method first subdivides the overall ship hull structure into several superelements, the dynamic characteristics of each bound substructure (i.e. at fixed interface bounderies of superelement) of which are calculated separately; and then perform dynamic transformation for each superelement by the method of order-reduction which will eliminate all the mode coordinates, so that the dynamic characteristics of the superelement can be condensed to node coordinates of interfacing points. This does not resolve only the problem of computer storage limitation, but also overcomes the demerits of the modal synthesis method that node coordinates must be transformed to mode coordinates which being assembled and therefore it is very difficult to incorporate FEM technique.

Ship's structure is a very complex system. It is extremely difficult to make accurate theoretical predictions for its dynamic characteristic, even if for its stern segment only. Applying this present method, we have developed in this paper a general program for dynamic response calculation of large complex structure to be performed in small computers, thus providing means for vibration analysis of stern post and superstructure. Good agreement has been found between theoretical predictions and test results of both modal identification by hammer testing and measuring in-plane vibration by Moiré method.

II. Static and Dynamic Transformation

1. Guyan's static transformation

As early as in 1965, Guyan proposed an order-reduction technique for structural dynamic analysis, the principle of which is depicted as follows.

Assuming the kinetic and potential energy of a structure are

$$T=\tfrac{1}{2}\delta^T M\dot{\delta} \qquad (1)$$

$$U=\tfrac{1}{2}\delta^T K\delta \qquad (2)$$

Let

$$\delta=\begin{Bmatrix}\delta_m\\ \delta_s\end{Bmatrix} \qquad (3)$$

where δ_m = generalized displacement corresponding to master degrees of freedom

δ_s = generalized displacement corresponding to slave degrees of freedom

The expansions of equation (1) for masters and slaves respectively are

$$U=\tfrac{1}{2}\delta_m^T K_{mm}\delta_m+\delta_m^T K_{ms}\delta_s+\tfrac{1}{2}\delta_s^T K_{ss}\delta_s \qquad (4)$$

According to extreme value conditions of potential energy for slave degrees of freedom

$$\frac{\partial U}{\partial \delta_s}=0 \qquad (5)$$

$$K_{sm}\delta_m+K_{ss}\delta_s=0 \qquad (6)$$

Thus we obtain:

$$\delta_s=-K_{ss}^{-1}K_{sm}\delta_m \qquad (7)$$

$$\delta=\begin{Bmatrix}\delta_m\\ \delta_s\end{Bmatrix}=\left[\frac{I}{-[K_{ss}]^{-1}[K_{sm}]}\right]\delta_m=E\,\delta_m \qquad (8)$$

$$E=\left[\frac{I}{-[K_{ss}]^{-1}[K_{sm}]}\right] \qquad (9)$$

Therefore:

$$K_0=E^TKE=K_{mm}-K_{ms}K_{ss}^{-1}K_{sm} \qquad (10)$$

The same applies for

$$M_0=E^TME=M_{mm}-M_{ss}K_{ss}^{-1}K_{sm}-K_{ms}K_{ss}^{-1}M_{sm}+K_{ms}K_{ss}^{-1}M_{ss}K_{ss}^{-1}K_{sm} \qquad (11)$$

As a result, we have the condensed free vibration equation:

$$K_0\overline{\delta}_m=\omega^2M_0\overline{\delta}_m \qquad (12)$$

and the free vibration equation before being condensed:

$$\begin{bmatrix}K_{mm} & K_{ms}\\ K_{sm} & K_{ss}\end{bmatrix}\begin{Bmatrix}\overline{\delta}_m\\ \overline{\delta}_s\end{Bmatrix}=\omega^2\begin{bmatrix}M_{mm} & M_{ms}\\ M_{sm} & M_{ss}\end{bmatrix}\begin{Bmatrix}\overline{\delta}_m\\ \overline{\delta}_s\end{Bmatrix} \qquad (13)$$

The second line of the above is

$$K_{sm}\overline{\delta}_m+K_{ss}\overline{\delta}_s=\omega^2(M_{sm}\overline{\delta}_m+M_{ss}\overline{\delta}_s) \qquad (14)$$

The comparison of equation (14) with equation (6) reveals that Guyan's method lose inertia effect of slaves. For high frequency problem where the slaves of high order mode have sig ficant inertial forces, this neglect of inertial effect of slave degrees of freedom will make calculated frequency much larger than its actual value.

2. Kuhar's dynamic transformation[8]

In equation (13), corresponding to the *j*th eigenvalue ω_j and eigenvector $\delta_j=\{\delta_m/\delta_s\}_j$, the second line of which is written as:

$$(K_{ss}-\omega_j^2 M_{ss})\bar{\delta}_s^j=-(K_{sm}-\omega_j^2 M_{sm})\bar{\delta}_m^j \tag{15}$$

then
$$\bar{\delta}_s^j=-(K_{ss}-\omega_j^2 M_{ss})^{-1}(K_{sm}-\omega_j^2 M_{sm})\bar{\delta}_m^j \tag{16}$$

As shown in equations (15) and (16), $\omega_j^2 M_{ss}$ and $\omega_j^2 M_{sm}$ are the dynamic effect corresponding to the respective frequency. In applying Kuhar's method in specific calculation, ω_j is unknown, and therefore a known value $\bar{\omega}_j$ which is approximated to ω_j is substituted. Consequently, equation (16) is simplified as:

$$\bar{\delta}_s = R\bar{\delta}_m \tag{17}$$

$$R=-(K_{ss}-\bar{\omega}_j^2 M_{ss})^{-1}(K_{sm}-\bar{\omega}_j^2 M_{sm}) \tag{18}$$

Substitute equation (18) into the free vibration equation, we have:

$$[K^*(\bar{\omega}_j)-\omega^2 M^*(\bar{\omega}_j)]\bar{\delta}_m=0 \tag{19}$$

$$\bar{\delta} = \begin{bmatrix} I \\ \hline R \end{bmatrix}\bar{\delta}_m=H\bar{\delta}_m \tag{20}$$

$$M^*=H^T MH \tag{21}$$

$$K^*=H^T KH \tag{22}$$

Substitute $\bar{\omega}_{j_1}$, which is obtained from equation (19), for $\bar{\omega}_j$ in equation (17), and solve equation (19) again, we obtain the approximate $\tilde{\omega}_j$ for equation (13). By solving equation (20), we have the complete solution of the modes of an overall system.

III. Superelement Method of Modal Synthesis

The above discussed dynamic transformation method still has the following two drawbacks, although it eliminated errors inherent in static condensation method which completely neglects the dynamic effect of slaves.

Firstly, Kuhar's dynamic transformation method makes dynamic modification on the assumption that $\bar{\omega}_j$ is close to the eigenvalue ω_j of a certain order of the system. This means that, even after first iteration, the solution is still an approximated condensation unless $\bar{\omega}_{j_1}$ value used for the second iteration is very close to $\bar{\omega}_j$. But it is very difficult to choose $\bar{\omega}_j$ which is very close to ω_j.

Secondly, if for a large structure, the number of slaves is taken to be very large, it will be difficult for small capacity computer to store $[K_{ss}]$ and $[M_{ss}]$. It will be shown later in this paper that the result of Kuhar's dynamic transformation will be a condensed non-linear eigen equation. In order to automatically search for the potential root of this non-linear eigen equation, one must first of all obtain the normal mode of bound substructure represented by slaves. It is, therefore, impractical to excessively increase the condensation ratio so as to directly solve the condensed eigen equations, while at the same time to avoide analysing the dynamic characteristics of the bound system[9].

The superelement method of modal synthesis presented in this paper may effectively overcome the above mentioned drawbacks. The principle of this method is explained as follows.

Firstly we can subdivide a large complex structural system into several superelements (substructures) according to the capacity of the specific computer, then assume m master coordinates for the interface boundaries of each superelement and s slave coordinates for the internal part of each superelement. When the overall structural system vibrates with frequency, each superelement can be regarded as being subjected to the counterforce excitation from interface boundaries, i.e.

$$f=\bar{f}e^{i\omega t} \tag{23}$$

At that time, the superelement is subjected to forced vibration, the variation of displacement being equal to that of interfacing force, i.e.

$$\delta=\bar{\delta}e^{i\omega t}=\left\{\frac{\bar{\delta}_m}{\bar{\delta}_s}\right\}e^{i\omega t} \tag{24}$$

Therefore the motion equation of the superelement can be expressed as:

$$\begin{bmatrix} K_{mm} & K_{ms} \\ K_{sm} & K_{ss} \end{bmatrix}\cdot\begin{Bmatrix}\bar{\delta}_m \\ \bar{\delta}_s\end{Bmatrix}-\omega^2\begin{bmatrix} M_{mm} & M_{ms} \\ M_{sm} & M_{ss}\end{bmatrix}\begin{Bmatrix}\bar{\delta}_m \\ \bar{\delta}_s\end{Bmatrix}=\begin{Bmatrix}\bar{f} \\ 0\end{Bmatrix} \tag{25}$$

From the second line of the above equation, we obtain:

$$\bar{\delta}_s=-(K_{ss}-\omega^2M_{ss})^{-1}(K_{sm}-\omega^2M_{sm})\bar{\delta}_m=R\bar{\delta}_m \tag{26}$$

$$R=-(K_{ss}-\omega^2M_{ss})^{-1}(K_{sm}-\omega^2 M_{sm}) \tag{27}$$

The overall displacement of the superelement is expressed as:

$$\bar{\delta}=\begin{Bmatrix}\bar{\delta}_m \\ \bar{\delta}_s\end{Bmatrix}=\begin{Bmatrix} I \\ R\end{Bmatrix}\cdot\bar{\delta}_m=H\bar{\delta}_m \tag{28}$$

Substitute equation (28) into equation (25) and left multiply it by H^T, we have:

$$(H^TKH)\bar{\delta}_m-\omega^2(H^TMH)\bar{\delta}_m=H^T\bar{f} \tag{29}$$

$$K^*\bar{\delta}_m-\omega^2M^*\bar{\delta}_m=\bar{F} \tag{30}$$

where $\quad K^*=H^TKH \qquad M^*=H^TMH \qquad \bar{F}=H^T\bar{f}$ (31)

There we can introduce the normal mode of the fixed interface boundaries of the superelement which is determined by the following eigen solution:

$$(K_{ss}-\omega^2M_{ss})\phi=0 \tag{32}$$

Solve this eigen equation and perform normal orthogonality for the modes of all orders considered, i.e.

$$\phi^TM_{ss}\phi=\phi[I]; \qquad \phi^T K_{ss}\phi\begin{bmatrix}\ddots & & \\ & \Omega_i^2 & \\ & & \ddots\end{bmatrix} \quad i=1,\ 2,\ \cdots s \tag{33}$$

substitute equation (33) into equation (27), then

$$R=-K_{ss}^{-1}(I+\Gamma)(K_{sm}-\omega^2M_{sm}) \tag{34}$$

Let

$$[\Lambda]=\begin{bmatrix}\ddots & & \\ & \dfrac{\omega^2}{\Omega_i^2-\omega^2} & \\ & & \ddots\end{bmatrix} \tag{35}$$

then

$$[\Gamma]=(\phi^T)^{-1}\Lambda\,\phi^{-1} \tag{36}$$

To solve equation (33), one must first solve for the condensed stiffness matrix K^* and condensed mass Matrix M^*.

$$M^*=M_{mm}+M_{ms}R+R^TM_{sm}+R^TM_{ss}R=M_m+\mathrm{I}-\mathrm{II}+\mathrm{III} \tag{37}$$

$$\mathrm{I}=M_{ms}R=-M_{ms}K_{ss}^{-1}K_{sm}-M_{ms}\phi\Lambda\Omega^{-2}\phi^TK_{sm}+M_{ms}\phi\Lambda\phi^TM_{sm} \tag{38}$$

$$\mathrm{II}=R^TM_{sm}=-K_{ms}K_{ss}^{-1}M_{sm}-K_{sm}\phi\Omega^{-2}\Lambda\phi^TM_{sm}+M_{ms}\phi\Lambda\phi^TM_{sm} \tag{39}$$

$$\begin{aligned}\mathrm{III}=R^TM_{ss}R=&K_{ms}K_{ss}^{-1}M_{ss}K_{ss}^{-1}K_{sm}+K_{ms}\phi\Omega^{-2}\Lambda\Omega^{-2}\phi^TK_{sm}-M_{ms}\phi\Lambda\Omega^{-2}\phi^TK_{sm}\\&+K_{ms}\phi\Omega^{-2}\Lambda\Omega^{-2}\phi^TK_{sm}+K_{ms}\phi\Omega^{-2}\Lambda\Lambda\Omega^{-2}\phi^TK_{sm}-M_{ms}\phi\Lambda\Lambda\Omega^{-2}\phi^TK_{sm}\\&-K_{ms}\phi\Omega^{-2}\Lambda\phi^TM_{sm}-K_{ms}\phi\Omega^{-2}\Lambda\Lambda\phi^TM_{sm}+M_{ms}\phi\Lambda\Lambda\phi^TM_{sm}\end{aligned} \tag{40}$$

Let

$$A=M_{ms}\phi-K_{ms}\phi\Omega^{-2} \tag{41}$$

$$\Omega^{-2}=\begin{bmatrix}\ddots&&\\&\Omega_i^{-2}&\\&&\ddots\end{bmatrix} \tag{42}$$

then

$$M^*=M_0+2A\Lambda A^T+A\Lambda\Lambda A^T \tag{43}$$

where $M_0=M_{mm}-M_{ms}K_{ss}^{-1}K_{sm}-K_{ms}K_{ss}^{-1}M_{sm}+K_{ms}K_{ss}^{-1}M_{ss}K_{ss}^{-1}K_{sm}$

The subsequent result is identical to that given by static condensation.

Following the same computational procedure, we can obtain the condensed stiffness matrix.

$$\begin{aligned}K^*&=K_{mm}+K_{ms}R+R^TK_{sm}+R^TK_{ss}R\\&=K_{mm}-K_{ms}K_{ss}^{-1}K_{sm}+A\Lambda\Omega^2\Lambda A^T\\&=K_0+A\Lambda\Omega^2\Lambda A^T\end{aligned} \tag{44}$$

Substitute equations (43), (44) into equation (30), we have:

$$(K_0-\omega^2M_0-\omega^2A\Lambda A^T)\overline{\delta}_m=\overline{F} \tag{45}$$

This result is identical to the conclusions given by the reciprocal theorem applied in Reference[10].

The above expression can be rewritten as:

$$(K_0-\omega^2M(\omega))\overline{\delta}_m=\overline{F} \tag{46}$$

$$M^*(\omega)=M_0-A\Lambda A^T \tag{47}$$

Equation (46) can also be expressed as:

$$D^*(\omega)\overline{\delta}_m=\overline{F} \tag{48}$$

The difference between equation (45) and the statically condensed (static condensation) motion equation lies in the fact that this present equation includes a dynamic modification term $A\Lambda A^T$, and that the derivation is completely based on accurate dynamic condensation. Now let us identify

$$A=M_{ms}\phi-K_{ms}\phi\Omega^{-2} \tag{49a}$$

It can further be rewritten as:

$$A=M_{ms}\phi-\phi_0^TM_{ss}\phi \tag{49b}$$

Where ϕ_0 is the bound mode and it satisfies $\phi_0^T=K_{ms}K_{ss}^{-1}$. The physical meaning of ϕ_0 is: it represents the static mode of the internal degree of freedom when the boundary degree of freedom δ_m of the superstructure is given a unit displacement $[I]_{m\times m}$ in succession.

Equation (49b) describes the dynamic coupling of dynamic mode ϕ with static mode ϕ_0. The presence of A is not only due to the inertial coupling M_{sm} of the internal coordinate of component parts with the interface coordinates, but also to the fact that these two kinds of mode shape do not have orthogonality about the mass matrix of the superelement. From the equations of virtual work, we can however judge that the above two kinds of mode shape of the superelement do have orthogonality about the stiffness matrix of the superelement.

Summing up, the following important conclusion can be made: Because of the dynamic coupling of bound modes with the normal modes of the fixed interface boundaries, the resonant vibration of bound mode shape of the superelement is sure to cause the vibration of normal mode shape, or vice versa. The demerits of the method of Guyan and Irons are just the neglect of this important fact.

It should also be emphasized that: It is not necessary to solve for all the ϕ values in equation (49b) since the really significant mode shapes which influence frequency ω in engineering frequency spectrum are those lower order normal modes of the fixed interface boundaries. Therefore, the normal mode can be truncated according to frequency criteria, that performs modal synthesis with $\phi=[\phi]_{s\times q}$, $(q\ll s)$. As a result, the dimension of A matrix will not be large (will be reduced) i.e. $m\times q$, thus greatly simplifies calculation.

The motion of the over all system is therefore expressed as:

$$M^* = \sum_{j=1}^{N} \left(M_0^{(j)}+2A^{(j)}\Lambda^{(j)}A^{(j)^T}+A^{(j)}\Lambda^{(j)}A^{(j)^T}\right) \tag{50}$$

$$K^* = \sum_{j=1}^{N} \left(K_0^{(j)}+A^{(j)}\Lambda^{(j)}\Omega^{(j)^{-2}}\Lambda^{(j)}A^{(j)^T}\right) \tag{51}$$

The final solution will be

$$D^*(\omega)\delta_m^*=0 \tag{52}$$

where δ_m^* is the condensed displacement column matrix after the interfacing of the superelement.

By solving this non-linear eigen equation, one obtains the eigen value and δ_m^* for the overall system, and subsequently solves the modes of the system from equations (26) and (28).

IV. Calculation of Non-Linear Eigenvalue

Sturm sequence bisection method has normally been applied for identifying eigen roots of linear eigen equations.

Assuming
$$P_n(\omega)=\det(K-\omega^2 M)=\det D(\omega) \tag{53}$$
choose ω_i, then $D(\omega_i)$ can be decomposed to the following:

$$D(\bar{\omega}_i)=L\Delta L^T \tag{54}$$

where Δ is a diagonal matrix. The number of negative elements in the diagonal term is just the number of eigen roots below $\bar{\omega}_i$. Then choose $\bar{\omega}_{i+1}$, gradually decrease the interval between $\bar{\omega}_i$ and $\bar{\omega}_{i+1}$ until an accurate root is isolated. This method is to be applied to obtain the eigen values ω_i (i=1, 2,..., $s+m$) for all orders.

However, the eigen equation of (52) represents a non-linear eigen value problem, thereof $M^*(\omega)$ is frequency-dependent. Judging from appearance, $D^*(\omega)$ involves only m order eigenvalue. But as dynamic stiffness matrix varies with the variation of ω, it actually involves $m+s$ order eigen value, which corresponds to the natural frequency of the $m+s$ order system. But if compared with the sign variation of $m+s$ in the standard polynomial $D(\omega)$, it will have $m+2s$ variations of signs[2]. The sign variation of the eigen function of this equation will exceed s, and corresponding with s singularities in the fixed interfacing points of each superelement, there are also s natural frequencies of the superelement. Therefor, the number of non-linear eigen value accord with this characteristics[11] is

$$J(\bar{\omega}_i)=J_\Delta+J_0(\bar{\omega}_i) \qquad (55)$$

where $J(\bar{\omega}_i)$ represents the number of roots below $\bar{\omega}_i$ in the eigen equation (52), J_Δ represents the number of principal diagonal negative elements of Δ below $\bar{\omega}_i$, $J_0(\bar{\omega}_i)$ represents the number of frequency of bound substructure below $\bar{\omega}_i$.

In order to illustrate the procedure of solving the non-linear eigen value and its subsequent results, we performed calculations for a two-story space frame as an example. The two-story space frame, constructed of beams and rods of same length (30 cm) and diameter (8 mm), has altogether 144 deg of freedom. (A) is a substructure with bound boundaries and (B) is a free suspended substructure with 6 deg of freedom of rigid body, each having 48 and 72 internal degrees of freedom respectively and 24 interface degrees of freedom.

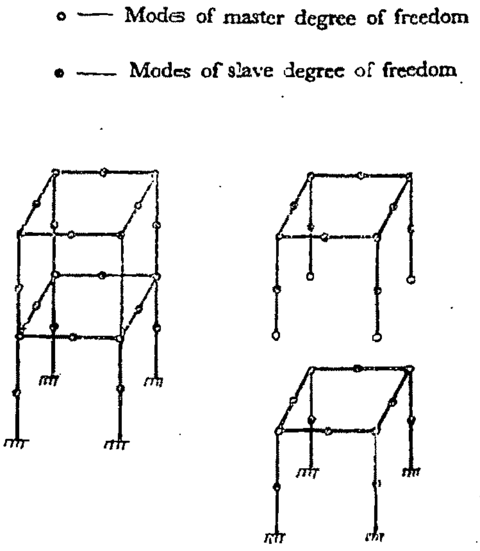
○ —— Modes of master degree of freedom
● —— Modes of slave degree of freedom

Fig. 1 Two-story space frame structure

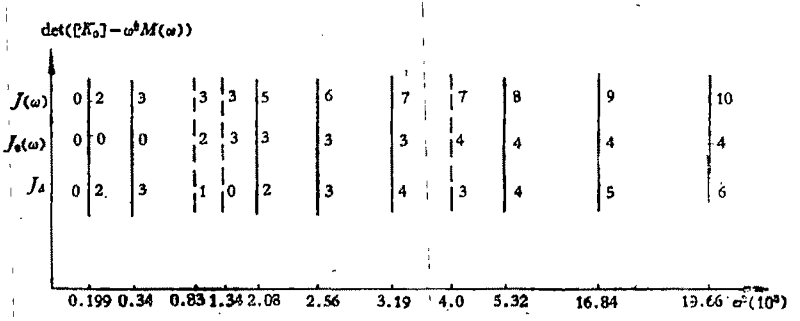

Fig. 2 Root value calculation for the eigen values of the two-story space frame by bisection method

Substituting the frequency of different orders of the two-story space frame as isolated by the above method in the equation (52), and solving the eigen equation under linear system conditions, one can obtain the dynamic characteristics of the original system.

V. Calculation of an Ideal Model of 5,000 Ton Large Hatch Barge and Its Comparison of Results with Tests

Applying the computational method presented in this paper we have developed a computer program which has been validated through two mechanic models, one being a two-story space frame and the other being a composite structure of plates and beams. Shown below are the calculated results.

(1) Two story space frame[12]

Order	1	2	3	4	5
superelement A	412.88744	412.88744	412.88744	412.88744	412.88744
superelement B	45.82465	45.82465	58.69319	100.51329	193.61316
Order	**6**	**7**	**8**	**9**	**10**
superelement A	412.88744	412.88744	412.88744	412.88744	412.88744
superelement B	231.03007	231.46107	250.09256	250.09256	316.37808

Order	1	2*	3	4	5*
Guyan	24.63947	24.63947	32.14948	90.107	90.107
present method ($\hat{\phi}_{SA}$ SA=0 $\hat{\phi}_{LB}$ SB=5)	22.47087	22.47087	29.35103	72.640	72.640
present method ($\hat{\phi}_{SA}$ SA=0 $\hat{\phi}_{SA}$ SB=10)	22.45656	22.45656	29.33556	72.26364	72.26364
accurate solution	22.45621	22.45621	29.33452	72.26317	72.26317
experimental results	22.6	22.6	29.6	73.3	73.3

(continued)

Order	6	7	8	9	10
Guyan	136.54929	178.97057	229.178	397.65341	484.70672
present method ($\hat{\phi}_{SA}$ SA=0 $\hat{\phi}_{SB}$ SB=5)	80.574	89.891	116.083	206.543	223.1523
present method ($\hat{\phi}_{SA}$ SA=0 $\hat{\phi}_{SB}$ SB=10)	80.11065	89.67124	115.69367	185.65567	197.59492
accurate solution	80.09116	89.64251	115.64644	185.52913	197.46086
experimental results	81.6	90.8	118	184.5	195.8

*: indicates the frequency of superimposed degenerate mode.

$\hat{\phi}$: represents the collections of modes after truncation.

The vibration modes of the two story space frame are depicted as:

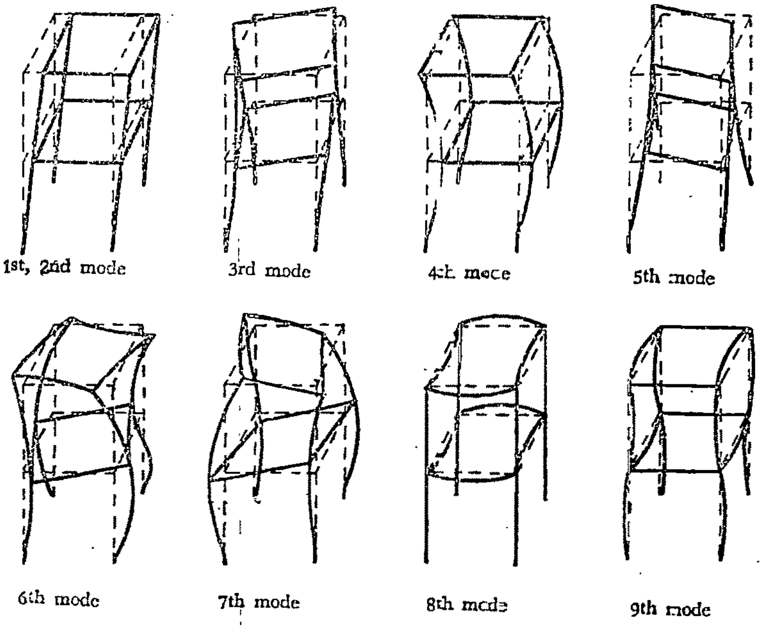
1st, 2nd mode
3rd mode
4th mode
5th mode
6th mode
7th mode
8th mode
9th mode

Fig. 3 Vibration modes of the two story space frame

(2) Composite structure of plates and beam[15]

Order	1	2	3	4	5
complete solution	223.1493	519.7105	924.8099	954.308008	988.6857
present method	223.9837	520.3037	925.6342	955.7481	991.8631

(continued)

Order	6	7	8	9	10
complete solution	1310.2348	1350.9039	1577.2970	1733.6862	2009.6806
present method	1318.2031	1361.6031	1590.1436	1757.7875	2031.1035

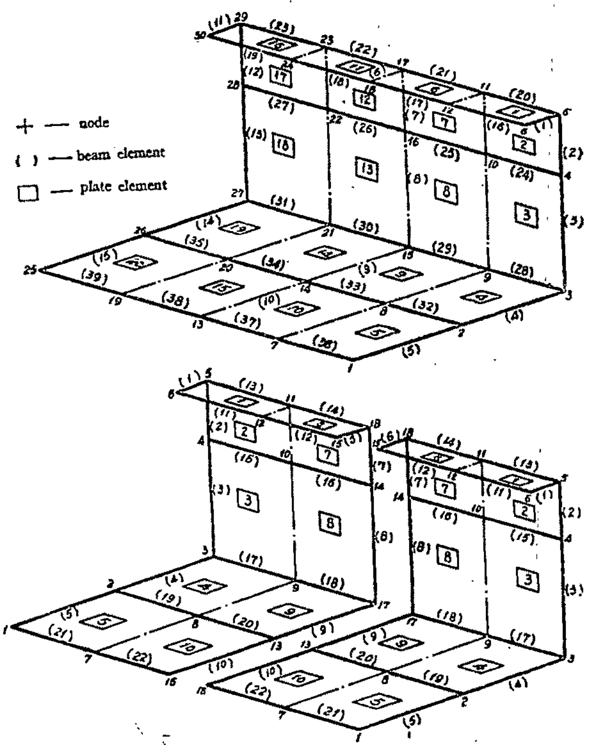

Fig. 4 Geometry of the composite structure of plates and beams

After being validated by the above mentioned two mechanic models, the program was applied for the calculation of a 5,000 ton large hatch barge. Only one–fourth of the model was calculated because the model is symmetrical. The dynamic characteristics of the entire ship can be calculated by further subdividing the one–fourth part into 4 superelements I, II, III, IV, as shown in Fig. 6, each comprising of the hold segments of composite structure of plates and beams.

We performed calculations for two models. One is constructed of transparent plexiglass sheets of 4–mm thickness and its E=27,000 kg/cm^2 (Model I). The other is constructed of opal plexiglass sheets of 3 mm thickness and its E=28,000 kg/cm^2 (Model II). In order to verify the correctness of calculation, the two models were tested separately, with Model I subjected to mode identification by hammer testing and Model II measured in–plane vibration by Moiré method. Results of calculation:

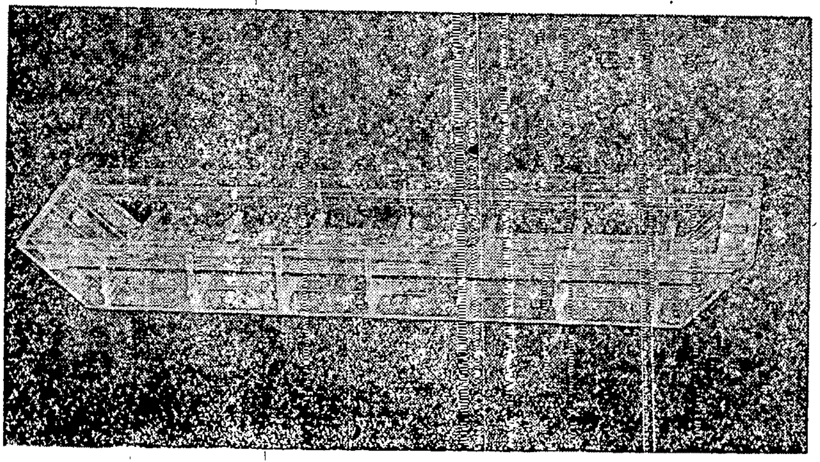

Fig. 5 The ideal model of a 5,000 ton large hatch barge

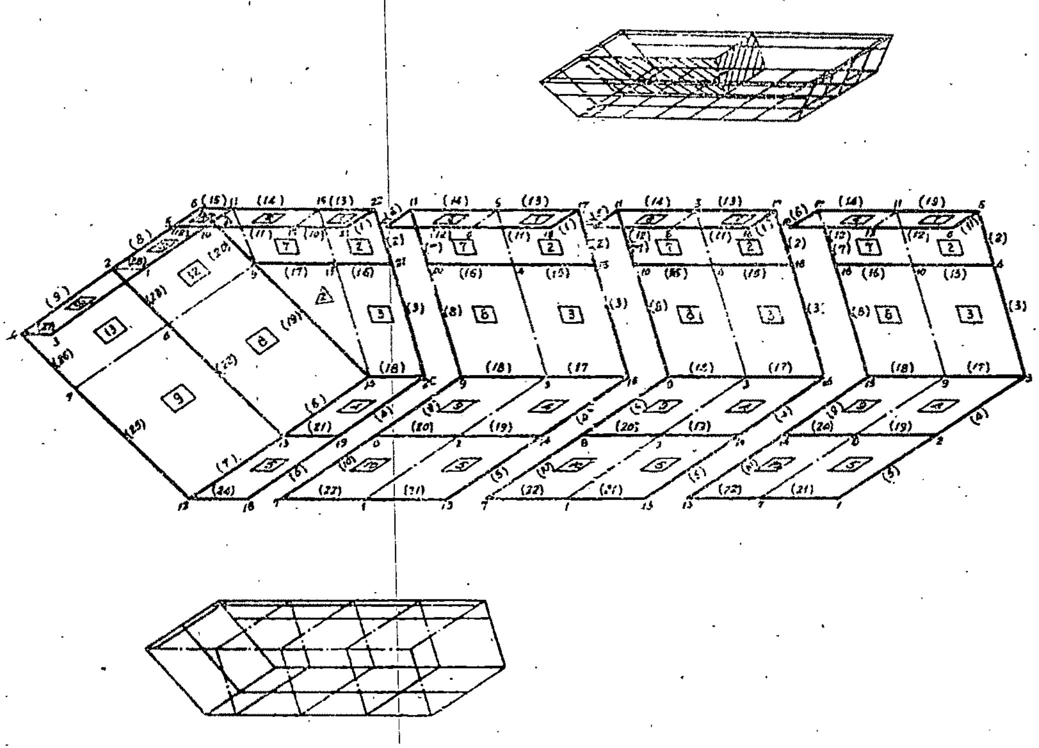

Fig. 6 The calculation of the mechanic model of a 5,000 ton large hatch barge by the superelement method of modal synthesis

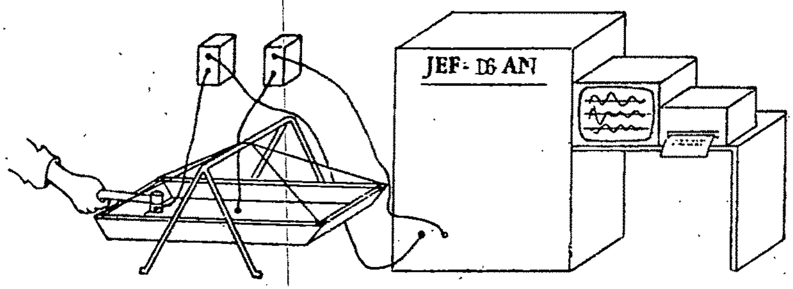

Fig. 7 Diagram showing the modal identification testing and real-time data processing

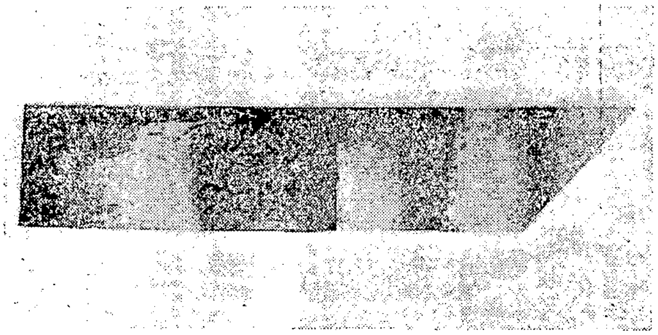

Fig. 8 Stripe of measuring in-plane by Moiré method

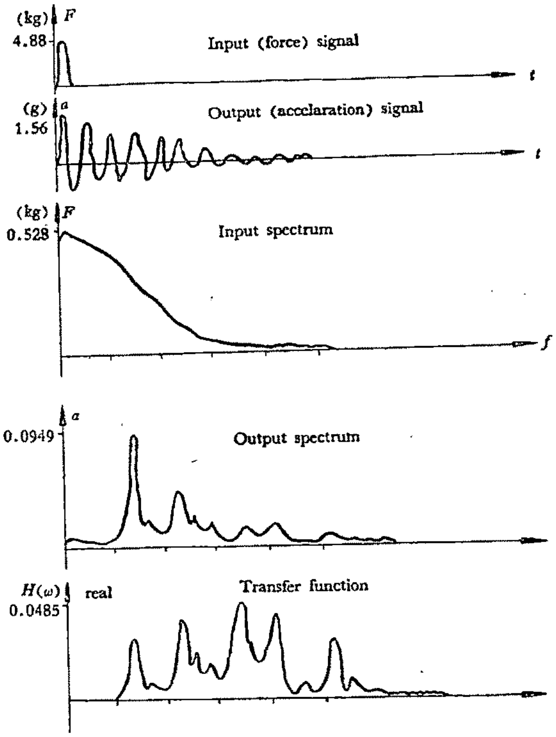

Fig. 9 Data analysis for mode identification testing

The calculated numerical values obtained by applying this method are compared as follows with test results given by mode identification testing and Moiré method.

Model I

Order	1	2	3	4	5
Present method	193.0132	234.0613	319.0114	396.7834	407.7456
Mode identification test result	192.2	235.7	326	390.2	401.9

(continued)

Order	6	7	8	9
Present method	454.6117	519.5733	580.5334	658.3548
Mode identification test result	448.5	512.6	576.6	634

Model II

Order	1	2	3	4.
Present method	140.6531	201.3481	291.3019	369.4312
Molré test result	138	/	/	352

Note: Measuring in-plane vibration by Moiré method were not carried out for high orders due to the limitations of testing apparatus.

VI. Conclusions

From the calculated numerical values of a two-story space frame which has already had accurate theoretical solutions and test results, and that of a 5,000 ton large hatch barge, some conclusions can be drawn as follows:

1. The present method can yield higher calculating accuracy than the static condensation method and dynamic condensation method respectively proposed by Guyan and Irons and Kuhar.

2. As compared with the ordinary modal synthesis method which uses the degree of freedom of part mode as the generalized coordinate, the present method is more convenient to incorporate FEM technique and is applicable to the development of general programs.

3. The present method is most conveniently applicable to the calculation of systems having identical superelements. By interfacing the calculated results of one of the several parallel superelements, the complete solution is obtained through only one computation. Thus the time involved in the computation is greatly reduced. Therefore it is also preferable to employ this method in large capacity computers.

4. The present method is more applicable to calculations involving large amount of computational work than FEM technique for complete solution, thus allowing the calculation of the coupled vibrations of large complex structures (such as stern post hold segment) with ship's hull, and of superstructure with ship's hull, be performed in small capacity computers.

5. The calculated results of the modes of the 5,000 ton large hatch barge model provide necessary basis for the further study vibrations of coupled fluid-structural system.

The results with regard to the plexiglass model in accordance with measuring in-plane vibration by Moiré method has been given by Mr. Mei Jiafon from Laser's Division of the

Marine Engineering Department of the Shanghai Ship & Shipping Research Institute. Mode identification test has been cooperated separately by the Calculation Department of China Ship Scientific Research Center and the Electrical Testing Department of Xing Xing Machinery workes.

Acknowledgments

We have also got many informative helps in writing this paper from Mr. Zhang Xiao-yong, the Directer of the Ship Structural Department Shanghai Ship & Shipping Research Institute, and Wang Wenliang, the Lecturer of Mathematic series of Fu Dan University. We are glad to take the opportunity to express our hearty thanks for their great assistances.

References

[1] Koji Kagawa: *A study on higher mode vibration of ships,* **Journal of the Society of Naval Architects of Japan,** Vol. 143, 1978.

[2] W. S. Vorus and R. E. Sandstrom: *An extension of component mode synthesis and its application to ship vibrations,* **Proceeding of Euromech Colloquium,** 122, Sept. 1979.

[3] 王文亮、杜作润、陈康元：模态综合技术短评和一种新的改进，航空学报， No. 3, 1979.

[4] 邹经湘、安为民：模态综合法中的几个问题，"振动理论和实验"学术交流会，西安交通大学， Dec. 1978.

[5] 恽伟君、颜新扬、高志龙：船舶耦合振动部件模态综合法，中国造船， No. 2, 1981.

[6] R. J. Guyan: *Reduction of stiffness and mass matrices,* **AIAA,** Vol. 3, No. 2, p. 380, Feb. 1965.

[7] B. M. Irons: *Structural eigenvalue problem: elimination of unwanted variables,* **AIAA,** Vol.3, pp. 961–962, 1966.

[8] E. J. Kubar and C. V. Stable: *Dynamic transformation method for modal synthesis,* **AIAA,** Vol. 12, No. 5, pp. 672–678, May 1974.

[9] 胡仲根、恽伟君、段根宝：动态子结构法中的非线性特征值计算，上海船舶运输科学研究所报告，1980.

[10] Leung Yeetak: *An accurate method of dynamic substructuring with simplified computation,* **Numerical Methods in Engineering,** Vol. 14, No. 8, 1979.

[11] W. H. Wittrick and F. W. Williams: *A general algorithm for computing natural frequencies,* **Q. J. Mech. APPL. Math.** 24, pp. 263–284.

[12] 川井忠彦：マトリッワス法振動わよひ応答，コンピエータによる构造工学讲座，I—4—B，日本钢构造协会，1970.

[13] 段根宝、胡仲根、恽伟君：板梁组合结构船舶立体舱段动态计算，上海船舶运输科学研究所报告，1980.

Annual of the CSNAME, Vol. 1, 1982

SFFJ METHOD AND APPLICATION IN OPTIMUM DESIGN OF STRUCTURES

CUI CHENGXIAN (崔承宪)

Wuhan Ship Design and Research Institute

SUMMARY

A method of structure optimum design is given in this paer. It is more suitable for engineering practice than other direct search methods.

The optimum design of structure is often reduced to a problem of non-linear program by constraint. The mathematic model shown as follows:

$$\min f(x) \qquad X \in R^n$$

Subject to

$$h_i(x) = 0, \qquad i = 1, \cdots p$$

$$g_j(x) = 0, \qquad j = 1, \cdots q$$

Where $x = (x_1, x_2, \cdots, x_n)^T$

n = the number of variable quantities.

Firstly, it is necessary to construct a constrained specific function $T(x)$ which is gained by weighting the computing result with FEM or other methods.

In order to reduce the times of reanalysis, two following techniques are used:

(1) Pattern move;

(2) Variable classification.

The times of reanalysis is about to 3n by using these two above so as enough to meet the needs of engineering.

The advantages of this method can be summarized as follows:

(1) There is only one search process which is simple and convenient;

(2) Not necessary to be afraid of convergent problem;

(3) The accuracy is dependable. It is important for improving the accuracy to make use of the weighting coefficients (u, v, ··· etc.) correctly.

Compare with other methods, two examples given in this paper are proved to be satisfactory.

Introduction

With wide application of the electronic computers, the optimization method has been developed rapidly in recent twenty years. Some good methods have appeared at home and abroad, for example, simplex method, complex method, Powell method, SUMT and direct search method. But they can't be suitable well for the optimization of marine complex structure, because of two following reasons:

(1) The optimum design of structure is often reduced to solve a non–linear programing problem by constraints, and it is necessary to find out the direction of minimum objective function and to check the constrained conditions at the same time in every step of search, but they are restrained each other, so that the convergent speed is very slow.

(2) The constrained conditions can't be expressed as obvious formulae.

Therefore, this paper may give a method which can solve these two difficult problems, and it is named for SFFJ method. This method is more suitable for marine engineering practice than other search method.

I. General Concept

1.1. Mathematical model

The mathematical model for a non–linear programing problem with constrained formulae is

$$\min f(x) \qquad X\in R^n \tag{1-1}$$

Subject to

$$\left.\begin{aligned} &h_i(x)=0 \qquad i=1,\cdots,p \\ &g_j(x)\geqslant 0 \qquad j=1,\cdots,q \end{aligned}\right\} \tag{1-2}$$

where $x=(x_1,x_2,\cdots,x_n)^T$

n=the number of variable quantity

Weight function is only considered for the objective function $f(x)$, and the constrained conditions (formula 1–2) contain the conditions of normal stress, shearing stress, deformation etc., in the problem of structural optimization.

1.2. Constraint specific function

Constraint specific function is

$$T(x)=\left\{\sum_{i=1}^{m} u_i\,(\sigma^i_{\max}-\sigma_g)^2+\sum_{i=1}^{m} v_i\,(\tau^i_{\max}-\tau_g)+\sum_{i=1}^{m} w_i\,(f^i_{\max}-f_g)^2\right\}^{\frac{1}{2}} \tag{1-3}$$

where $\sigma^i_{\max}$, $\tau^i_{\max}$, $f^i_{\max}$=the maximum value of normal stress, shearing stress, deformation computed by FEM or other methods

σ_g=material allowable normal stress

τ_g=material allowable shearing stress

f_g=allowable deformation of structure

i=a structural member number

m=the number of the structural member quantity

u_i, v_i, w_i=weighting coefficient

When $\begin{cases}\sigma^i_{\max}\leqslant\sigma_g\\ \tau^i_{\max}\leqslant\tau_g\\ f^i_{\max}\leqslant f_g\end{cases}$ then $\begin{cases}u_i=0\\ v_i=0\\ w_i=0\end{cases}$ else $\begin{cases}u_i=1\\ v_i=1\\ w_i=1\end{cases}$

In order to improve the accuracy of result, these weighting coefficients may also employ experiment coefficient array.

1.3. The relationship between the objective function and the variables

Generally, for the structural problem $f(x)$ only contains weight function. If variable x_i

increases a Δx_i, but other variables are not changed, then

$$\Delta f(x)=\gamma\times\Delta x_i\times l_i=\Delta f(x_i) \tag{1-4}$$

where

$\Delta f(x)$=variation of the whole structural weight

Δx_i=variation of ith variable

l_i=size coefficient, it is gained in the optimization of arrangement

γ=material specific gravity

II. Basic Principle

2.1. Basic principle

In this method, the search starts from $x0$ which is a space point chosen from the unfeasible region and moves forward till appoach to the constrained surface according to following steps. At the same time, $T(x)$ is reduced from $T(x0)\neq 0$ to $T(x)=0$, then the optimum point x^* is obtained.

(1) Exploratory move

A variation of objective function $\Delta f(x)$ may be expressed by every variable independently. Taking same $\Delta f(x)$ and comparing the value of $\Delta T(x)$ for all variables, the variable which has maximum value of ΔT can be chosen, then this variable can be taken as the fastest search direction. That is to say, this method actually is a method of comparing weight to every variable.

(2) Pattern accelerative move

Obviously, the times of reanalysis in the last step is too long, therefore, it is necessary to find out the second fast direction while finding out the fastest direction, and don't repeat at once after the end of the first step, and continue to move a same quantity as last step. If the fastest $\Delta T(x_i)$ of this time is greater than the last second $\Delta T(x^c)$, then it is yet the fastest direction of next time, so continue to move on the fastest direction. This procedure is named as pattern accelerative move. It is very important to reduce the times of reanalysis.

(3) Variable classification

The action of every variable can be seen through from the first analysis to structure object, and the variable classification is carried out according to the grade of these actions.

The search principle of two variables is shown in Fig. 2-1.

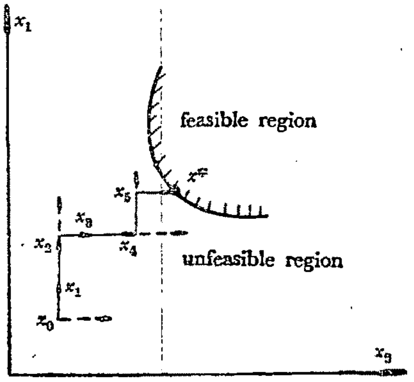

Fig. 2-1

"Exploratory move" and "pattern accelerative move" in this paper are actually not the same with that in pattern accelerative search method shown in literatures.

2.2. Simple procedure

(1) Constructing constrained specific function $T(x)$

It is necessary to choose an analysis program that is able to analyse for structural objects with FEM or other methods. Therefore, $T(x)$ is obtained through weighting the computing result, which only contains normal stress, shearing stress and deformation in this paper.

(2) Computing step length matrix

At first, it is not difficult for a shipbuilding engineer to choose a beginning point $x0$ in unfeasible region and give a variation of weight (f). For example, a step is chosen as 5 kg. If ith variable means a cross-section area, matrix α can be obtained after computing every variable.

(3) Exploratory move

Exploratory move started from beginning point $x0$, and set

$$x^i = x0 + \alpha\, e^{(i)}, \quad 1 \leqslant i \leqslant n$$

where $e^{(i)}$ = a unit matrix of expressing direction, for example $i=2$

$$e^{(2)} = \begin{pmatrix} 0 & & & & 0 \\ & 1 & & & \\ & & 0 & & \\ & & & 0 & \\ 0 & & & & \ddots \end{pmatrix}$$

thus, n space points are formed.

Compare $\Delta T(x^i)$ for n space points, express x^i which has max $[T(x0) - T(x^i)]$ as x^l, and express x^i which has max $[T(x0) - T(x^i)]$ $(i \neq l)$ as x^c. That is, $e^{(l)}$ = the fastest direction, $e^{(c)}$ = the second fast direction.

(4) Pattern accelerative move

In Kth step, $x^l_{K1} \Leftarrow x^l_K + \alpha_k e^{(l)}$, if $T(x^l_K) - T(x^l_{K1}) > T(x^i_K) - T(x^c_K)$, then $e^{(l)}$ is still the fastest direction, otherwise, repeat 3rd step after $x^0_{K+1} \Leftarrow x_{K1}$, thus, that is the end for one cycle.

III. Computed Example

3.1 Example 1

It is a optimum design of the bottom framing of a planing boat. The model is shown in Fig. 3-1.

The given conditions:

$q=2.57$ kg/cm²,	uniform pressure load
$t=0.6$ cm,	bottom plat thickness
$\sigma_s=4500$ kg/cm²,	material yield point
$\sigma_g=0.8\sigma_s=3600$ kg/cm²,	material allowable normal stress
$\tau_g=0.57\sigma_s=2600$ kg/cm²,	material allowable shearing stress

The boundary conditions are shown in Fig. 3-1. In order to understand whole search procedure, the results in middle procedure are shown in Table 3-1.

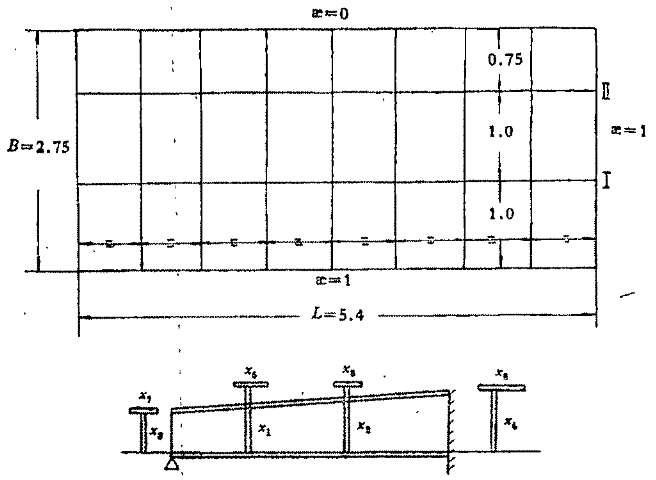

Fig. 3-1

Table 3-1

x_1	x_2	x_3	x_4	x_5	x_6	x_7	x_8	f(kg)	$T(x)$
	20	20	30	3.0	3.0	2.5	2.5		
		21.87						273.2	9.712
		22.80						279.37	9.041
		23.74						285.61	8.518
		24.67						291.95	8.146
			31.70					303.78	7.200
			32.55					309.83	6.914
		26.66						324.31	6.072
			34.01					335.24	5.430
			34.74					340.80	5.22
		28.37						354.11	4.61
			37.258					386.06	3.39
			37.734					390.91	3.23
				4.175				395.86	2.92
			38.158					406.81	2.6
			38.715					415.33	2.36
			39.206					419.64	2.26
						3.085		424.03	2.105
			40.079					431.76	1.89
			40.899					439.12	1.74
						3.616		443.11	1.6
			41.652					449.94	1.43

(continued)

x_1	x_2	x_3	x_4	x_5	x_6	x_7	x_8	f(kg)	T(x)
				5.05				453.62	1.29
				5.488				455.47	1.24
				5.925				457.31	1.20
		32.358						468.31	1.05
							2.925	471.51	0.917
							3.138	473.11	0.854
							3.531	474.7	0.815
						3.988		477.51	0.742
							3.705	480.16	0.645
							3.882	481.49	0.625
								⋮	⋮
						4.574		490.92	0.369
						4.783		492.48	0.337
							4.741	493.91	0.292
20	20	32.358	41.652	5.925	3.0	4.783	4.741	493.91	$0.292 < \varepsilon = 0.3$

The state of deformation and stress for optimum result is shown in Fig. 3-2 and Fig. 3-

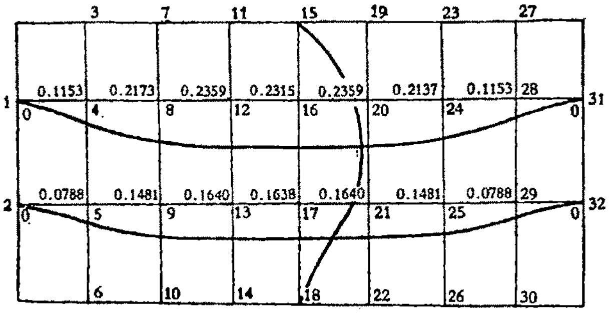

Fig. 3-2 Deformation

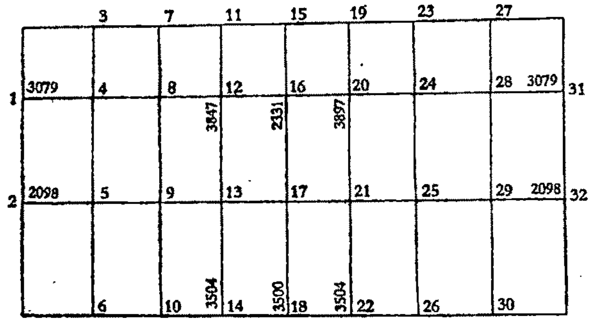

Fig. 3-3 Normal stress

The result in Table 3-2 is obtained by taking $x_4 \sim x_8$ as constants, so two following conclusions may be able to get.

(1) Increasing weight on the short direction beam is more advantageous than on the long direction beam, it agrees with traditional conclusions.

(2) The difference of weight optimum will be caused due to the difference of the size of short direction beam, but the difference is not very great.

Table 3-2

	x_1	x_2	x_3	x_4	x_5	x_6	x_7	x_8	weight (kg)
n=6	20	20	30.81	50.17	8	8	5	5	534.37
n=7	20	20	30.57	44.32	8	8	5	5	535.5

3.2 Example 2

In order to research the suitability of this method for non-linear programing problem with constrained formulae, another example may be given, it is the hatchcover problem, which is well-known in the general literature.

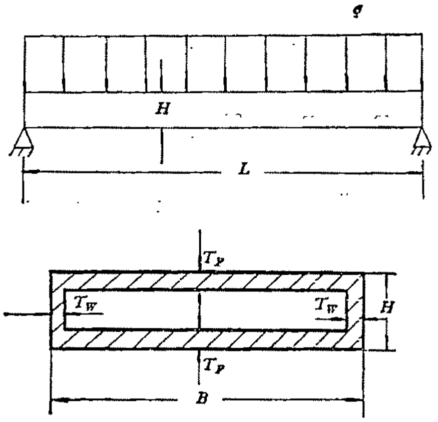

Fig. 3-2 Simply supported box-section beam

The given conditions:

$L=600$ cm,	length of beam
$B=60$ cm,.	width of beam
$E=700$ N/mm,	material modulus of elasticity
$q=0.1$ kg/cm^2,	uniform pressure

Taking the following parameters as variables x_1, x_2 and x_3:

T_P=top plat thickness

H=height of beam

T_W=side plat thickness

and the area of cross-section as objective function:

$$A=2HT_W+2BT_F \tag{3-1}$$

$$\min A(T_F,\ H,\ T_W)$$

Subject to constrained conditions:

(1) $T_F>0,\ H>0,\ T_W>0$

(2) $\tau\leqslant\tau_g$ Maximum shearing stress is equal or less than its allowable value

(3) $\sigma\leqslant\sigma_g$ Bending stress is equal or less than its allowable value

(4) $\sigma\leqslant\sigma_K$ Bending stress is equal or less than critical yield stress

(5) Maximum value of deformation $\leqslant L/400$, where $\tau_g=45$ N/mm^2, $\sigma_g=70$ N/mm^2

Put above into non-dimensional quantities as formula (3.2).

$$T_F=\frac{x_1}{100},\ H=x_2,\ T_W=\frac{x_3}{100}$$

$$\left.\begin{aligned}\sigma&=\frac{M}{BT_FH}\\ \tau&=\frac{Q}{2HT_W}\\ \sigma_K&=\frac{\pi^2 E}{3(1-\nu)}\left(\frac{T_F}{B}\right)^2\\ \frac{\delta}{L}&=\frac{5}{384}\cdot\frac{qL^3}{EI}\end{aligned}\right\} \tag{3-2}$$

In above formulae, $M=27000$ kg-cm, $Q=6$ kg/cm, $\gamma=0.3$ (Poisson's ratio).

Put above in non-dimensional quantities as following forms:

$$g_1(x)=1.2x_1+\frac{x_2x_3}{50} \tag{3-3}$$

$$\left.\begin{aligned}g_2(x)&=\frac{x_1}{100} & g_6(x)&=\frac{7x_1x_2}{4500}-1\\ g_3(x)&=x_2 & g_7(x)&=\frac{7x_1^3x_2}{45000000}-1\\ g_4(x)&=\frac{x_3}{100} & g_8(x)&=1-\frac{32000}{x_1x_2^2}\\ g_5(x)&=\frac{x_2x_3}{200}-1 & &\end{aligned}\right\} \tag{3-4}$$

The formula (3-3) is objective function, but the formula (3-4) is constrained condition. The optimum result is shown in Table 3-3 comparing with the result of other methods. The search process is also shown in Fig. 3-5 comparing with the result of other methods.

Table 3-3

method	SUMT	SUMT	SUMT	SDD	SDD	SFFJ$_I$	SFFJ$_{II}$	SFFJ$_{III}$
x_1^0			70	70	55	40	50	30
x_2^0			30	30	22	15	15	10
x_3^0						(50)	(50)	(50)
T_F^*	0.6362	0.626	0.6331	0.63699	0.6078	0.6148	0.6366	0.5976
H^*	26	26	25.32	24.8784	28.6207	28	24.94	30.8538
A	102.3476	101.42	101.30	101.31	101.56	101.78	101.34	102.56

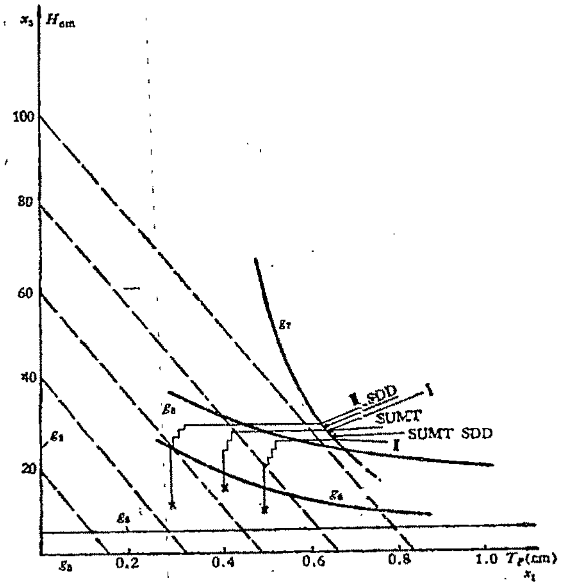

Fig. 3-5 Diagrammatic sketch in search process

IV. Discussion and Result Analysis

The principle of the method is shown in Fig. 4-1.

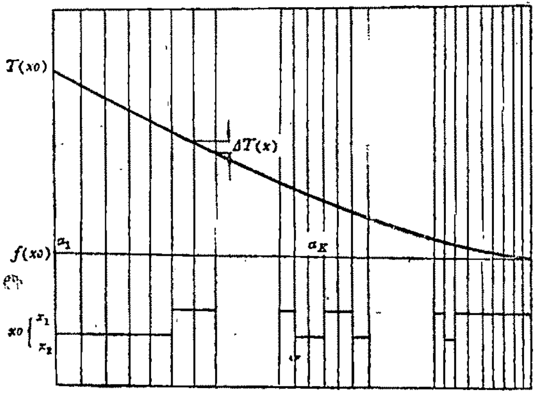

Fig. 4-1 Principle sketch

It is not difficult to understand it, if variation of weight is small, the optimum result can be obtained at Kth cycle, then

$$f(x^*)=K\bullet\Delta f(x)$$

$$T(x)=K\bullet\Delta T(x)$$

$$K=\frac{f(x^*)}{\Delta f(x)}=\frac{T(x)}{\Delta T(x)}$$

$$f(x^*)=\frac{T(x)}{\Delta T(x)}\bullet\Delta f(x)$$

Replace $f(x)$ with $f(x_i)$ (on the basis of formula 1–4), then

$$f(x^*)=\frac{T(x)}{\Delta T(x_i)}\bullet\Delta f(x_i)$$

Because $T(x0)$, $f(x_i)$=constant, and so the objective of search is to find maximum value of $T(x_i)$ for all variables in every step.

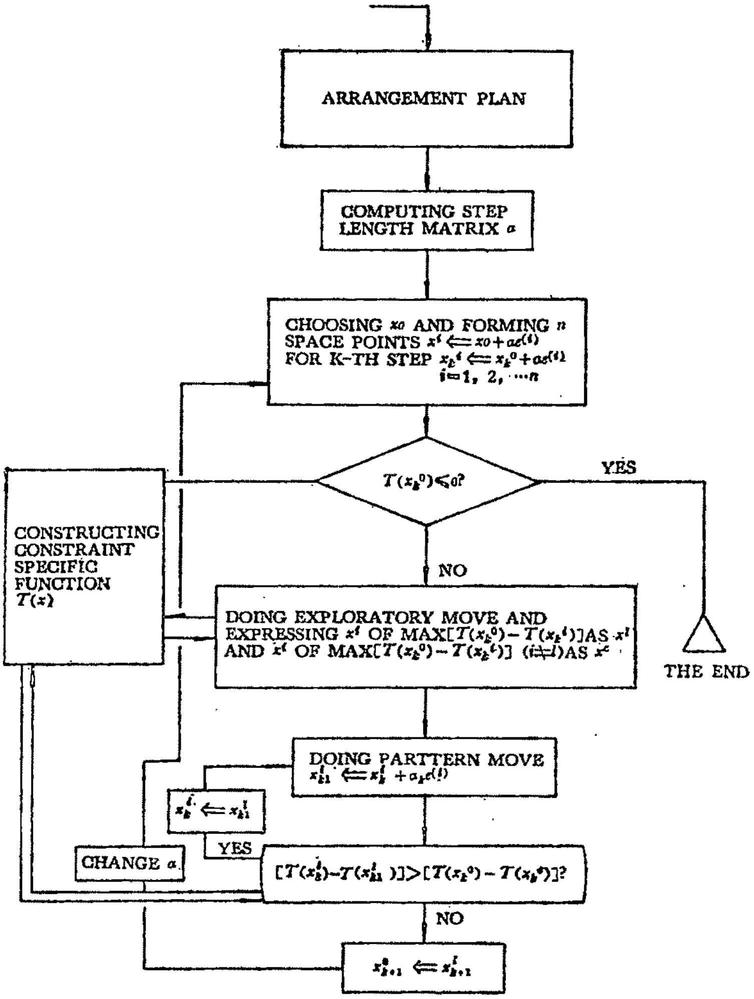
ARRANGEMENT PLAN
COMPUTING STEP LENGTH MATRIX a
CHOOSING x_0 AND FORMING n SPACE POINTS $x^i \Leftarrow x_0+ae^{(i)}$ FOR K-TH STEP $x_k^i \Leftarrow x_k^0+ae^{(i)}$ $i=1, 2, \cdots n$
$T(x_k^0)\leqslant 0?$
YES
THE END
NO
CONSTRUCTING CONSTRAINT SPECIFIC FUNCTION $T(x)$
DOING EXPLORATORY MOVE AND EXPRESSING x^i OF MAX$[T(x_k^0)-T(x_k^i)]$AS x^l AND x^i OF MAX$[T(x_k^0)-T(x_k^i)]$ $(i\neq l)$AS x^c
DOING PARTTERN MOVE $x_{k1}^l \Leftarrow x_k^l+a_k e^{(l)}$
$x_k^l \Leftarrow x_{k1}^l$
YES
CHANGE a
$[T(x_k^l)-T(x_{k1}^l)]>[T(x_k^0)-T(x_k^c)]?$
NO
$x_{k+1}^0 \Leftarrow x_{k+1}^l$

Fig. 4–2 Flow chart of calculating program

The effect beyond imagination is gained for optimization of marine structure with this method, the cause is may be to exist a inner law in marine structure object, besides the advantage of this method itself.

The result comparing with simplex method is shown in the following Table (4–1).

Table 4–1

method	the number of variables	times of reanalysis	convergent time (minute)
simplex method	8	400	150～120
SFFJ method	8	70	25～30

The flow chart of calculating program is shown in Fig. 4–2.

Conclusion

1. There is only one search process in this method, so it is simple and convenient, a good effect has been gained for the optimization of marine structure.

2. It is unnecessary to be afraid of its convergent problem. For the times of reanalysis and the convergent speed a greater progress has been made than other direct search methods.

3. The accuracy is dependable, it is important to use weighting coefficient correctly for improving the accuracy.

4. This method is not only suitable for the optimum design of marine structure but also for the design in checking the effect and the analysing the failture of structures, thus a good method is provided for the marine engineering design system.

Acknowledgement

I am heartily very much obliged to famous mechanics specialist in China, Prof. Qian Lingxi, who has given some useful guides and suggestions in my work.

References

[1] 李炳威：结构的优化设计.

[2] 中国科学院计算所三室规划组：最优化设计方法.

[3] 胡毓达等：SDD法的两个应用及计算机程序.

[4] 上海交通大学数学组：船舶最优设计的数学方法.

[5] 船体构造の最适设计，船の科学，I，1979.

[6] 华东水利学院：弹性力学问题的有限元法.

[7] K. P. Beier, H. Nowacki, C. Schubert and A. Weichbrodt: *A General Purpose Software System for Optimization in Ship Design, Computer Application in the Automation of Shipyard Operation and Ship Design*, II, North-Holland Publishing Company, 1976.

[8] R. H. Gallangher and O. C. Zienkiewicz: *Optimum Structural Design Theory and Applications*, Johns. Wiley and Sons. Ltd.

Annual of the CSNAME, Vol. 1, 1982

EXPERIENCE OF ADOPTING CIRCULAR-ARC-PROFILE REDUCTION GEAR ONBOARD SHIP AND IT'S RELATED PROBLEMS

HUA JIASHOU (花家寿)

Shanghai Jiao Tong University

SUMMARY

Experience onboard ship is presented in this paper to show that the advantages of circular-arc-profile gear for onland use can also be brought into full play in marine application if the design parameters of the gear are properly chosen and appropriate manufacturing and fitting accuracies are ensured. Some related problems such as sensitivity to the deviation of center distance and lubricating conditions are discussed in detail with comparisons with conventional involute gear. Theoretical analysis and experiment have all indicated that circular-arc-profile gear has much higher contacting strength, and hence larger load-carrying capability than involute gear, and that the problem of sensitivity to the deviation of center distance is solvable for marine use. Therefore, the present doubt about circular-arc-profile gear as regards its marine application is considered to be unnecessary and its future wide-spread use is expected to be promising.

I. Introduction

It is well known that the rotational speed of medium-speed marine diesel engine is relatively high (over 400 rpm) and usually does not match the design speed of propeller. This requires reduction gears to be used to reduce main engine speed to the speed desirable for the optimal operation of propeller, so as to ensure high propulsive efficiency and fuel oil economy, thus making reduction gear one of the key equipments for marine power plant. The installation of reduction gear can not only make one engine drive one propeller through one shaft, but combine several engines to drive one propeller through one shaft, or drive auxiliary machineries through shafts coming out of gear box. In so doing, the power range applicable can thus be greatly increased.

At present, nearly all ships built both at home and abroad have chosen involute gears a main transmission gear for marine medium-speed diesel engines. In the case where engine power is very large, carburized hardened and ground involute gears are generally used. Bu for the manufacturing of this kind of involute gears, it is necessary to have gear grinding (gear shaving) machines of high manufacturing accuracy and its machining must be carried out in constant temperature environment. These stringent requirements result in high production cost, and thus limiting its wide application to ships.

It has, however, been proved by large amount of experimental results and actual industrial applications since 1955 that circular-arc-profile reduction gear has high load-carrying capability and that it does not require high-precision machine for its manufacturing. Since then, circular-arc-profile gear has won widespread application to various power units in industry, transportation, agriculture, etc.

In the year of 1971, we installed an experimental circular-arc-profile gear in a 2400 hp passenger-cargo ship for one of the two identical main engines (each delivering 1200 hp) for the first time, with the other one engine still applying conventional involute gear. This circular-arc-profile gear has successfully operated onboard the ship for six continuous years over 30,000 hours, and is still on service normally. In the past, those involved in shipbuilding and shipping at home and abroad had little interest in the application of circular-arc-profile gear to marine transmission in believing that circular-arc-profile gear is sensitive to the deviation of center distance, which is easily affected by hull deformation, and there is likely possibility of the gear getting into trouble. Once any failure of reduction gear occurs, ships propulsive power will be totally lost and serious accidents may occur in some certain conditions such as steaming in ports or in rapid current, since reduction gear is a key equipment for ships power plant, and hence, its reliability is of utmost importance. Our successful long-term experiment of circular-arc-profile gear onboard the ship has not only cleared away the unnecessary doubts about this kind of reduction gear, but also increased confidence in its application to marine main transmission. The tests results have also shown that the thickness of oil film on circular-arc-profile gear teeth is much larger than on involute gears. This phenomenon helps to improve the vibration characteristics of shafting system and increase gear's transmission efficiency. The comparisons with the involute gear, which is installed for the other main engine in the same ship, at the same working and loading conditions, indicate that circular-arc-profile gear has much higher "Hertz" strength than involute gear. From this we can see that circular-arc-profile gear's advantages, when applied in land use, also exist in marine application. This foresees competitiveness of circular-arc-profile gear and its future application is surely to be expected for ships of larger power in the near future.

II. Experiment Onboard Ship

Two main engines are installed on the passenger-cargo ship for the testing of the circular-arc-profile gear, one being coupled to a circular-arc-profile gear (box) and the other to an involute gear (box). Transmission for both gear boxes is of vertical type with common axis. Main particulars of these two gear boxes are listed in Table 1.

Table 1 Main parameters of gearbox

Item	notation	units	circular-arc-profile gear		involute gear	
			I	II	I	II
Power	N	hp	1200	1200	1200	1200
Speed	n	rpm	520/364	364/262	520/364	364/262
Center distance	A	mm	650		650	
Number of teeth	Z		105/150	90/125	105/150	90/125
Normal Module	Mn	mm	5	6	5	6
Helix angle	β	°	11°14′18″	8°6′40″	11°14′18″	7°6′40″
Gear ratio	i		1.428	1.389	1.428	1.389
Pitch diameter	d	mm	535.294/764.701	544.186/755.814	535.294/764.701	544.186/755.814
Face width	B	mm	250	325	250	325
Pitch circle circumferential velocity	V	m/s	14.57	10.37	14.57	10.37
loading factor	K	kg/cm²	7.84	8.44	7.84	8.44
Bending stress	σ	kg/cm²	1800/1540	1800/1500	1800/1640	1800/1500
Thickness of oil film	h_0	μ	7.4	11.7		

Both gears are made of the same material (40 Cr) by forging, their blanks having been undergone temper treatment with a resultant hardness of between HB260～280. The profiles were hobbed in Type 16M (Czechoslovak) hobbing machine. The accuracy of its transmission chain and static geometry had been adjusted within permissible limits before hobbing operation started. The machining accuracy for both circular-arc-profile gear and involute gear is all of "AA" (Chinese standard). The hobbing accuracy and accuracy of teeth surface undulation were kept within permissible allowances. But teeth surface smoothness was not quite good, the value of the surface roughness was less than 5 microns.

The gear and shaft were shrink fitted. The maximum shrink δ_T is $0.8\sim0.1\%\ D_0$ (without key) or $0.5\%\ D_0$ (with key). Here D_0 is the diameter of the journal. The gear was then put into turbine oil with a flash point$\leqslant$215°C for heating. The resultant temperature rise is $\Delta t=$

$\frac{\delta_T+\delta_0}{\alpha \cdot D_0}$, where δ is the initial backlash which generally equals to 0.15mm; α is the linear expansion coefficient of metal, for 40 Cr, $\alpha=11.7\times 10^{-6}$. Oil temperature $t°C=t_0$ (room temperature)$+\Delta t$. From this, the heating temperature for fitting procedure was calculated to be $150°C<t°C<190°C$. This temperature would not have much effect on the additional stress on teeth roots.

In the case of circular-arc-profile gear fitting, the deviation of center distance was chosen to be less than or equal to 0.1mm, the deviation of shafting (shaft) parallelism and inclination less than or equal to 0.035mm, and the flank backlash less than 0.41mm.

More than 30,000 hour's continuous operation of this gear onboard ship shows that circular-arc-profile gear has the same temperature rise and noise level as the involute gear, with the oil temperature being within 50°C and the overall noise level (including the contribution of the noise of the main engines and the generator) dB (A) being 107 dB. The frequency analysis of the overall noise level reveals that the noise level for both reduction gears is below 85 dB. The noise level of these two gearboxes as measured by the "Denmark BK" instrument is shown in Table 2.

During the testing operation, pitting began to occur on involute gear teeth after the gear had operated $N=6\times 10^5$ times. And then pitting began to disappear gradually when $N=10^7$. Apparent deep pitting appeared on teeth surface when $N>10^{10}$ (Here N is of gear's rotation times expressed as $N=60\ nT$, where n is the rotational speed of gear in rpm, T is time of operation in hours). But on the circular-arc-profile teeth no apparent pitting ever occurred during the whole testing operation.

Shaft torsional vibration data measured by "Geiger" show that the shaft connected with the involute gear box experienced resonant torsional vibration in the speed range of 280~340 rpm. This resonant vibration was then avoided from the normal speed range by the use of a elastic coupling of dual stiffness. But for the shaft connected to the circular-arc-profile gear box, which was of the same machining and fitting accuracy and operated in the same shafting and working conditions, no resonant torsional vibration was experienced until $N=10^7$. We have also incorporated coupling of dual stiffness in the shafting system for this kind of reduction gear, but it is so used only for noise reduction.

This long-term testing has convinced us that reliable ship can as well be realized, provided the design parameters of the gear have been properly chosen and due consideration has been given to its accuracy of machining and fitting. According to theoretical calculations and test verification, the sensitivity of circular-arc-profile gear to the deviation of center distance is solvable. Analysis of the test results has also indicated that oil film existing on circular-arc-profile gear teeth surface is much thicker than on involute gear teeth. This is beneficial to the increasing of gear's load-carrying capability.

Table 2 Transmission noise level (dB) of circular-arc-profile gear (designated as "C") and involute gear (designated as "In")

Freguency (hz) / Main engine speed (rpm)	position of measur-ment	31.5		63		125		250		500		1000		2000		4000		8000		A		Lin		Components of the main noise: calculated frequency of mating (hz)		measured frequency (hz)		noise levle (dB)	
		C	In	C	In	C	In	C	In	C	In	C	In	C	In	C	In	C	In	C	In	C	In	C	In	C	In	C	In
260	I	102	95	101	98	102	97.5	103	100	101	99	99	95	88	90	84	86	84	77	103	99.5	109	107	454.65 272.7	454.65 272.7	500 250	500 250	102 103	100 100
	II	101	102	100	98	101	96	102	98	101	100	97	95	84	89	81	85	72	75	102	100	110	108						
	III	106	109	101	102	101	96	100	99	102	99.5	97	95	84	89	80	86	71	76	102	100	110	112						
320	I	100	96	102	94	99.5	98	101	101	100	102	96	97	84	90	82	87	71	78	101	100	108	108	559.65 335.7	559.65 335.7	500~ 1000 250~500	500~ 1000 250~500	102 103	100 100
	II	101	102	98	100	99	97	99.5	98	103	100	96	96	84	92	80	88	72	77	102	101	108	110						
	III	106	109	101	102	97	96	100	99	102	104	97	95	84	92	81	88	71	80	102	102	110	103						
360	I	101	100	102	101	100	100	101	100	104	102	99.5	95	87	96	84	95	74	74	104	102	110	108	630 378	630 378	500~ 1000 250~500	500~ 1000 250~500	102 103	100 100
	II	100	102	98	101	98	98	89	97	103	102	99	97	86	86	85	83	74	72	102	102	109	109						
	III	105	108	102	104	99	97	99	99	104	101	101	96	86	85	83	82	74	72	105	102	110	112						
400~420	I	100	100	101	102	102	102	103	103	104	103	102	93	88	89	85	87	80	81	107	94	110	110	735 441	735 441	~1000 ~500	~1000 ~500	104	96
	II	101	100	100	98	99	99	101	98	105	103	104	96	89	91	88	91	86	85	107	104	110	109						
	III	105	108	103	104	98	97	99	90	103	91	102	92	88	88	86	86	80	71	104	103	110	102						

Note: Positions of measurement as disignated "I" (gear input) "II" (gear box body) and "III" (gear output) are all 0.5 m apart from the gear box.

III. Related Problems with the Application of Circular-Arc-Profile Gear Onboard Ship

1. Sensitivity to deviation of center distance

For the widespeed application of circular-arc-profile gear onboard ships, it is necessary first of all to know well about the effect the deviation of center distance may have on the load-carrying capability of the gear.

Theoretically, a circular-arc-profile gear is a point meshing system of higher pair without constraints. That is why this kind of meshing system was formerly believed by M. L. Novikov[1] and P. B. Федякин[2] to be not sensitive to manufacturing deviation and deflection of transmission elements, nor to the deviation of center distance. But later experiments performed by И. Н. Гришель[3] did demonstrate that this meshing system was rather sensitive to the above mentioned deviation and deflections. Our testing has proved that, for circular-arc-profile gear with a module of 3∼5mm, its load-carrying capability amounts to the maximum if a negative deviation of center distance, i.e. increased by 0.15∼0.1mm, is applied. In this circumstance, its fatigue failure resisting ability is 3.2 times larger than involute gear of the same size, and its bending strength is also higher. However, if positive or negative deviation applied is larger than 0.3mm, the load-carrying capability will be greatly reduced or even reduced to a value unallowable.

Another important problem which has been affecting marine use of circular-arc-profile gear is the deviation of center distance due to the fact that gear box is installed between main engine and propeller shaft and that ship hull deformation will surely have effect on the normal operation of reduction gear.

Theoretically, gear teeth contact with each other by meshing points, but actually they mate through an arc along teeth faces when the gear rotates under load. Therefore its load-carrying capability depends to a large extent upon the length and position of the contacting arc along the height of the tooth, which in turn has much to do with the deviation of center distance. When the deviation of center distance increases toward positive, the position of contacting arc moves up towards the top of the concave (Fig. 1a), the nominal pressure angle decreases and consequently the load-carrying capability of the gear decreases. If in this time the deviation of center distance decreases towards negative, the position of contacting arc moves down to the root of the concave (Fig. 1b), the nominal pressure angle increases and consequently the load-carrying capability of the gear increases, thus making it beneficial for the gear to run properly, however, if positive or negative deviation is excessive, it will cause both concave and convex of the teeth to approach their contacting limit and bring about early pitting and wearing. To sum up, the load-carrying capability of circular-arc-profile gear is sensitive to deviation of center distance, a problem deserving serious consideration. As we stated earlier in this paper, however, this problem is not unsolvable when it comes for marine application. In our application onboard the passenger-cargo ship, we incorporated the following measures, which have been proved to be feasible and effective by practice.

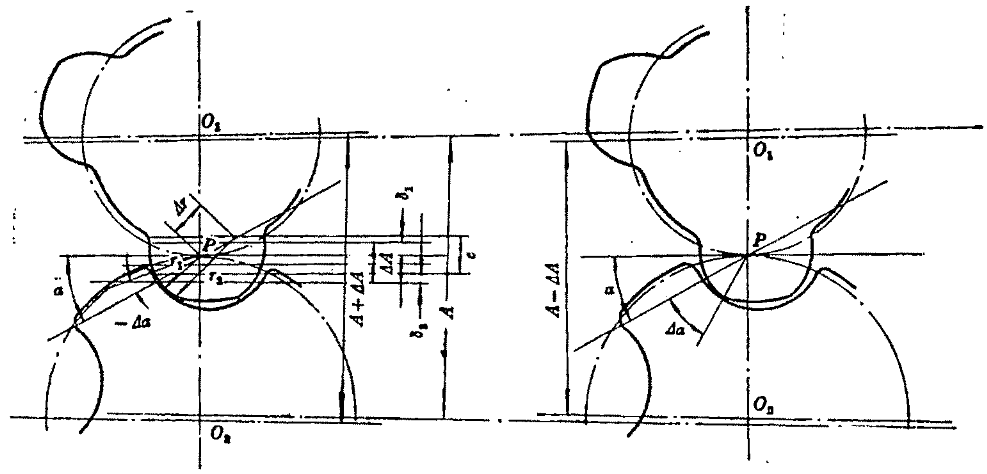

Fig. 1

(1) The use of gearbox of larger rigidity so as to minimize or to actively avoid the effect of hull deformation on teeth meshing.

(2) Strict control of the unparallelism and unverticality of the centerlines of shaft holes in gear box, and uniform distribution of contacting area along the whole axial length of teeth The actual deviation of unparallelism and unverticality of the center line of our test gear was maintained within the limit of 0.01 mm and 0.035 mm respectively.

(3) Adjustment of the deviation of center distance by fitting bearing linings so as to ensure proper position of the contacting arc of the meshing teeth. The deviation of center distance is largely affected by the deviation of fitting, and that of cutting depth δ_1 mm and δ_2 mm, which is in itself unavoidable because the nominal pitch line for hobbing can never exactly coincide with the technological hobbing pitch line. The actual normal pressure angle α as shown in Fig. 1 is expressed as:

$$\sin\alpha=\frac{e-(A-\delta_1-\delta_2)}{\Delta r}=\frac{e}{\Delta r}+\frac{\delta_1+\delta_2-\Delta A}{\Delta A}$$

The normal pressure angle for a single tooth profile α_K (Fig. 1) is written as:

$$\sin\alpha_K=\frac{e}{\Delta r}$$

so that

$$\sin\alpha-\sin\alpha_K=\frac{\delta_1+\delta_2-\Delta A}{\Delta r} \qquad (1)$$

where ΔA=deviation of center distance

$\Delta r=r_2-r_1$, r_2 and r_1 are radii of tooth profile for concave and convex respectively.

e=distance between the tooth profile center for cutter and the nominal pitch line

According to Eq. (1), it is evident that radial position of the contacting arc on circular-arc-profile gear teeth is the result of the combined effect of the deviation of center distance and cutting depth δ_1 and δ_2. For a given cutting depth deviation, appropriate α value can be obtained through the adjustment of the deviation of center distance by fitting bearing lining in the gear box so that proper position of contacting arc on gear teeth can be ensured. From this, we may say that the problem of sensitivity to the deviation of center distance can properly solved for marine use.

(4) Application of negative deviation of center distance. In our test gear onboard the ship, the actual center distance for the primary reduction is 649.94 mm, and 649.90 mm for the secondary reduction, while its normal center distance is 650 mm, thus resulting in a negative deviation of 0.06 mm for the first stage and 0.01 mm for the second. As ΔA is negative in this case, from Eq. (1) we obtain:

$$\alpha > \alpha_K$$

The length of the contacting arc along the height of the teeth will increase when α becomes larger. That means an increase in the meshing area between teeth and consequently an increase of the contacting strength of gear teeth. From the comparison of test results shown in Fig. 2, we see that the pitting area rate for circular-arc-profile gear is much smaller than that for involute gear of the same size.

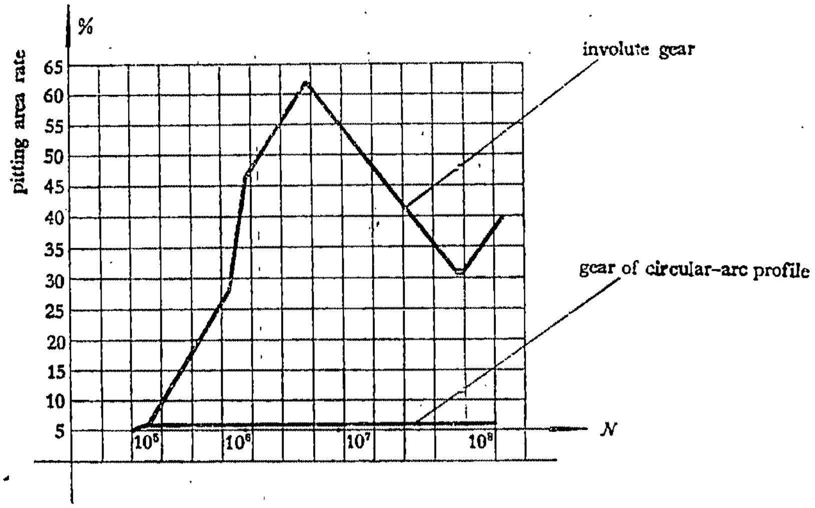

Fig. 2

Further more, let us consider the bending stress according to the following relationship as proposed by P. B. Федякин[4]:

$$\sigma = \frac{P_N H_c}{B S_0^2/6} \tag{2}$$

where P_N=normal force acting on teeth, which is expressed as the following for pinion:

$$P_N = \frac{P}{\cos\alpha_K}\sqrt{1+\frac{\cos^2\alpha_K}{\mathrm{ctg}^2\beta}}$$

H_0=distance between the point, where normal force is acted upon, and the weakest section

B=width of teeth face

S_0=thickness of the tooth in the weakest section

Judging from Eq. (2), we know that if negative deviation of center distance is applied, the value of H_0 can be made to decrease so as to minimize the value of tooth root bending stress, and consequently to increase its bending strength.

Besides, surface stress existing around the circular-arc-profile gear tooth root was also measured for the speed range of 200~260 rpm dynamically by miniature strain gauges manner. Typical results measured for a pinion tooth root are shown in Fig. 3.

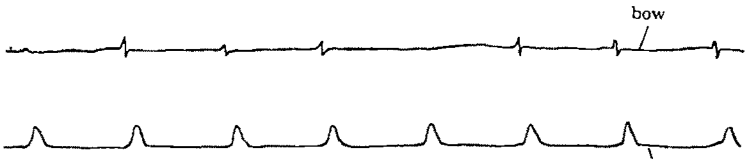

a. n_1=200~220rpm, N=104hp

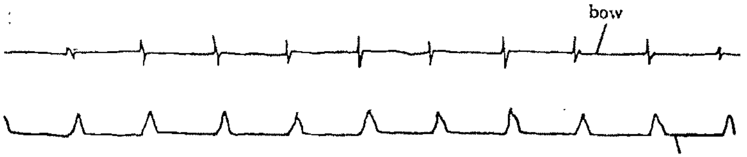

b. n_1=240~260rpm, N=174hp

Fig. 3

2. Lubricating conditions

Gear teeth operational life, their load-carrying capability, frictional property and rate of wear are all very closely related to gear lubricating conditions, which mainly depend upon the thickness of oil film existing between intermeshing teeth surfaces. Gear teeth parameter has great effects on the forming of such oil films. The pressure distribution and elastic deformation of an oil film existing between contacting teeth surfaces, which are oil lubricated but nevertheless are heavily loaded, are very like that existing between unlubricated metal-to-metal contacting surfaces, as pointed out by Hertez. In elastic-hydrodynamic contacts, the elastic deformation is large as compared to the thickness of oil film, which remains almost constant within the whole Hertez contacting zone excluding exits. The minimum film thickness h_0 for cylindrical contacts can be calculated by the following classical formula developed by Dowson[5] et al (1970).

$$h_0 = 2.65\frac{\alpha^{0.54}(\eta_0\mu)^{0.7}R^{0.43}}{W^{0.13}E^{0.03}} \qquad (3)$$

where α=pressure viscosity exponent

η_0=absolute viscosity at ambient temperature and pressure

E=equivalent Young's modulus, expressed as:

$$\frac{1}{E}=\frac{1}{2}\left[\frac{1-\nu_1^2}{E_1}+\frac{1-\nu_2^2}{E_2}\right]$$

In this equation,

ν=Poisson's ratio, E_1 and E_2 are modulus of elasticity of surfaces 1 and 2 respectively

W=normal load of unit tooth width

μ=relative rolling velocity$=\frac{V_{K_1}+V_{K_2}}{2}$

For involute gear, we have $\mu=V=\frac{\pi d_1 n_1}{60}$ from the equation proposed by A. Gu[7], where V is the pitch line peripheral velocity; while for circular-arc-profile gear, we have $\mu=V\cdot\text{ctg}\beta=\frac{\pi d_1 n_1}{60}\,\text{ctg}\,\beta$ from [8] if the unidentified relative rotation between teeth surface is neglected.

R=relative radius of curvature; for involute helical gear, we obtain from the generally used Eq. (1) for machine parts design the following expression:

$$R=\frac{A\cdot i\cdot\sin\alpha_n}{(i+1)^2\cos^2\beta}$$

where A is center distance, α_n is normal pressure angle and in general cases $\alpha_n=20°$.

For circular-arc-profile gear, we obtain the following expression from [4]:

$$R=R_1\frac{(1+\text{ctg}^2\beta)\,\text{ocs}\,\alpha}{\left[1-\left(\frac{1}{i}\right)^2\right]l+\left[1+\left(\frac{1}{i}\right)\right]\sin\alpha}\times\sqrt{1+\frac{\cos^2\beta}{\text{ctg}^2\beta}}$$

where R_1 is pinion pitch diameter and is expressed as $R_1=\frac{A}{1+i}$, α is the pressure angle and was chosen to be $\alpha=30°$ for the testing, l is relative displacement and is expressed as $l=\frac{0.873\,L}{R_1}$ (here L=working arc of the standard rack). In general, the values of $\left[1-\left(\frac{1}{i}\right)^2\right]l$ and $\sqrt{1+\frac{\cos^2\beta}{\text{ctg}^2\beta}}$ are very small and may be neglected. This being the case, the relative radius of curvature of circular-arc-profile gear can be written as:

$$R=\frac{A\cdot i}{(1+i)^2\sin^2\beta\,\text{tg}\,\alpha}$$

Substitute this into Eq. (3) and make rearrangements, we obtain the minimum oil film thickness for involute gear:

$$h_0=2.65\,\frac{\alpha^{0.54}\,\eta_0^{0.7}\left(\frac{\pi d_1 n_1}{60}\right)^{0.7}\left[\frac{A_t\sin\alpha_n}{(1+i)^2\cos^2\beta}\right]^{0.43}}{W^{0.13}\,E^{0.03}} \tag{4}$$

and also that for circular-arc-profile gear:

$$h_0'=2.65\,\frac{\alpha^{0.54}\cdot\eta_0^{0.7}\left(\frac{\pi d_1 n_1}{60}\text{ctg}\beta\right)^{0.7}\left[\frac{A_i}{(1+i)^2\sin\beta\,\text{tg}\,\alpha}\right]^{0.43}}{W^{0.13}\,E^{0.03}} \tag{5}$$

From (4) and (5) we have:

$$\frac{h_0'}{h_0}=(\mathrm{ctg}\,\beta)^{1.13}\left(\frac{\mathrm{ctg}\,\beta}{\sin\alpha_n\,\mathrm{tg}\alpha}\right)^{0.43}$$

Substitute $\alpha_n=20°$, $\alpha=30°$ into the above, it is then rewritten as:

$$\frac{h_0'}{h_0}=2.08(\mathrm{ctg}\,\beta)^{1.56} \qquad (6)$$

From Eq. (6) we can see that, for both circular-arc-profile gear and involute gear of the same size and at the same working conditions, the minimum oil film thickness ratio h_0'/h_0 tends to increase or decrease depending on the helical angle β. The $h_0'/h_0\sim\beta$ curve drawn according to Eq. (6) is shown in Fig. 4. The minimum oil film thickness for circular-arc-profile gear h_0' is 10 times larger than that for involute gear when $\beta=10°\sim14°$, and 3.6 times larger when $\beta\leqslant30°$. This obviously shows that the lubricating conditions of gear tooth profile are much better for circular-arc-profile gear than for involute gear. During the period of full-scale testing we regularly cleaned the lubricating oil magnetic filters once a month, and found that the magnetic filter of circular-arc-profile gear caught far less iron chips than of involute gear. This shows that circular-arc-profile gear has a better wear resisting property than involute gear.

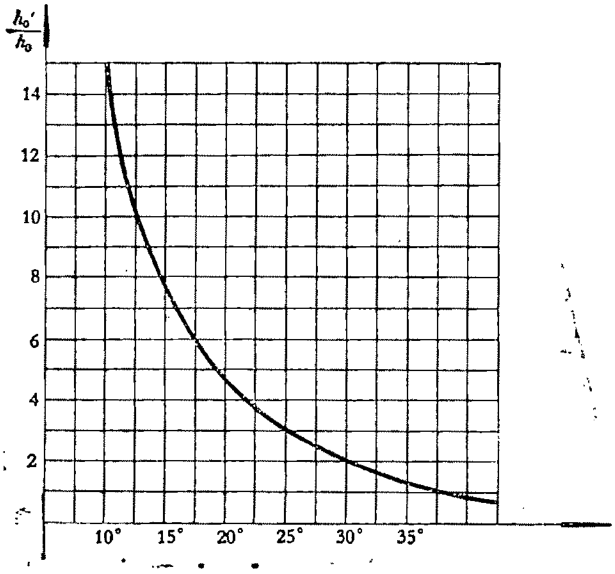

Fig. 4

On the same ship with the same main engine and shafting, and under the same working conditions as the circular-arc-profile gear, involute gear shaft experienced resonant torsional vibration and serious impact occurred to the gear in the speed range of 280~340 rpm. To cope with this torsional vibration problem, the original coupling was replaced by one of dual stiffness. The primary stiffness effects when the main engine operates at low speeds. It restricts the 6th order critical rotational speed to less than 250 rpm. The secondary stiffness raises the two nodes 3rd order critical rotational speed to the service speed range of the main engine or above. As a result, the resonant torsional vibration was kept away from the operating speed range.

But under the same shafting and working conditions, there appeared no single node 3rd order harmonic resonance for circular-arc-profile gear shaft in the speed range of 200∼400 rpm. The whole speed range was dominated by two nodes 6th order resonance. Although there appeared 12th and 18th order high-frequency pulse waves, i.e. three nodes resonance, in the speed range of 190∼280 rpm, additional stress was found to be very little. At the speed of 190 rpm, the obtained maximum additional stress generated by the 6th order excitation moment is only $\tau_{\max}=104.5$ kg/cm^2, much smaller than the permissible value (605.6 kg/cm^2) specified by the Rules for the Classification and Construction of Steel Ships for Changjiang River Operation.

Our experiment has indicated that, other conditions being the same, to replace involute gear with circular-arc-profile gear alone will result in obvious improvements to shafting vibration. The reason for this improvement still needs to be further investigated in order to understand its nature. According to our preliminary analysis, this might have some bearing to the oil film thickness. The thicker oil film that exists between circular-arc-profile gear teeth surfaces may possibly change the stiffness and damping of the whole meshing system. We may say with some certainty that the advantages of circular-arc-profile gear can be expected to be brought into full play for marine application so long as its profile is proper and the lubricating oil is appropriately chosen.

IV. Conclusions

1. Experience onboard ship has convinced us that circular-arc-profile gear is highly applicable to marine use and that its advantages for onland use can as well be brought into full play so long as its design parameters are properly chosen and appropriate manufacturing and fitting accuracies are ensured.

2. The problem of sensitivity of circular-arc-profile gear to the deviation of center distance is solvable through centain measures when it is for marine use. It is recommended here to apply negative deviation of center distance in order to increase contacting strength and bending strength.

3. Theoretical analysis has indicated a thicker oil film for circular-arc-profile gear teeth meshing than for involute gear. This thicker oil film is very beneficial to the increasing of gear's load-carrying capability, the decreasing of teeth wearing and scoring, and hence the increase of transmission efficiency. Particularly, the damping effect in vibration of shaft will be much better than that of involute gearing. These improvements are all important problems for marine main transmission gear worthwhile.

References

[1] M. L. Novikov: U. S. S. R. Patent, 1956.

[2] Р. В. Федякин и В. А. Чесноков: Вестник Машиностроения, № 4, № 5, 1959.

[3] И. Н. Гришель: Вестник Машиностроения, № 5, 1959.

[4] Р. В. Федякин: *Раочёт*, Конструирование и Исследование Передач, Том. 1, 1958.

[5] D. Dowson and G. R. Higginson: **Elasto-Hydrodynamic Lubrication, 1977.**

[6] A. Gu: *Elasto-hydrodynamic Lubrication of Involute Gears*, **The mechanisms conference and international symposium on gearing and transmissions,** Vol. 1, 1972.

[7] *Раочёт*, Конструирование и Исследование Передач, Том. 3, 1958.

[8] 许镇宇等：机械零件，机械工业出版社，1965.

Annual of the CSNAME, Vol. 1, 1982

DETERMINATION OF THE MAXIMUM HEAT FLUX OF EVAPORATING TUBES IN MARINE BOILERS AND THE FILM COEFFICIENT OF HEAT TRANSFER AT THE INNER SURFACE OF THE TUBE

GONG SANSHENG (龚三省)

College of Naval Engineering

SUMMARY

To calculate the maximum heat flux of evaporating tube in boiler is the first step in the determination of the wall temperature of the tube. There are two components of heat flow: radiant and convective. In this paper the methods to calculate these components will be introduced. On the other hand, in order to choose the material of evaporating tube, the coefficient of heat convection from inner wall of tube to the boiling water, α_2 must also be known. About 30 years ago, as the coefficient of heat convection of non-boiling water in tube was chosen, so that the value of α_2 was only about 5000 to 6000 kcal/m^2 hr ℃. It is wrong for steam evaporating tube especially for high heat marine boilers. According to the results of many experiments, we found exact value of α_2' of boiling water about 20 times more than the value of α_2 of non-boiling water. Therefore, in this paper the experimental formula to calculate α_2 for exactly determining the wall temperature of steam evaporating tube in boiler will be also introduced.

The heat transfer rate (heat flux) of each row of tubes of convective evaporating tube bank of boiler is different. Being in the highest temperature region of gas, the first row of tubes absorbs much more convective heat than the other rows, and therefore maximum heat flux is found at the first row of tubes nearest to the furnace. It is more important that the first row also absorbs radiant heat from the flame in the furnace.

Let us take a look at a row of tubes. Because the temperature field in the furnace and the gas flow at inlet of the tube bank are both non-uniform, the heat absorbed by each tube is different. For example, with the oil-burning boilers fired at both ends, tubes at the central position absorb more heat than the other tubes of the same row, but with boilers fired at one end, the tubes near to the rear wall of the furnace absorb more heat. So far as a single tube is concerned, the maximum heat flux is at the front side of the tube directly facing the furnace, because of the flame radiation in the furnace. And the back side can not get any radiant heat at all. With regard to the rate of convection heat transfer, the maximum value is at the point facing the gas flow, as the gas velocities around the tube are not the same.

With the intensification of heat release in the furnace (volumetric heat release rate of furnace for non-supercharged furnace q_T is increased from 1×10^6 to 6×10^6 kcal/m^2 hr), the local heat flux $q_{\text{лоб}}$ of the first row of tubes nearest to the furnace has been raised from $(0.3\sim0.5)\times10^6$ kcal/m^{2}hr to 1×10^6 kcal/m^{2}hr.

With respect to the selection of tube materials, in order to determine the outside tube wall temperature, it is used to fix the temperature rise of the boiling water film and the metal tube wall at $(50\sim100)$ °C, or fix the convection heat transfer coefficient of boiling water film of evaporating tube α_2 at $5{,}000\sim6{,}000$ kcal/m^{2}hr °C. Obviously these values are not suitable for the present marine boilers with high heat flux. For example, if we take $\alpha_2=5{,}000$ kcal/m^{2}hr °C with $q_{\text{лоб}}$ equal to 1×10^6 kcal/m^{2}hr, the temperature rise of boiling water film only will reach 200°C. Certainly, this is unreasonable. If the tube material is selected according to the above mentioned values in the calculation of the temperature rise of the boiling water film and the tube wall, it is doubtless that we shall unnecessarily waste the tube material. The reason why we used to fix α_2 at this value was the heat flux of the old boilers is low. In the process of heat transfer, the film coefficient α_1 of the gas is no more than 50 kcal/m^{2}hr °C in old boilers, which is two orders of magnitude lower as compared with the film coefficient of boiling water α_2, so there will be almost no influence on the over-all heat transfer coefficient K, if film coefficient of non-boiling hot water is used directly as α_2.

With the advent of nuclear power plant, investigations in heat transfer of the steam generator in the secondary circuit show that the film coefficient of high pressure water of the primary circuit on the heating side and lower pressure boiling water on the other side are naerly the same. It is therefore necessary to make further study in the film coefficient of boiling water. Investigations revealed that the film coefficient α_2 of boiling water is proportional to the heat flux q to the 0.7 power in case of nucleate boiling, and its numerical value is much larger than the film coefficient of hot water, because motion of steam bubbles in the boundary layer is extremely helpful to improve the rate of heat transfer. Unfortunately, some of the scientific design organizations still use the old calculation method at the present time. This paper is written to introduce a calculation method of maximum heat flux $q_{\text{лоб}}$ and film coefficient α_2 of boiling water in order to obtain proper tube wall temperature of the evaporating tube bank. Example of comparison of the new calculation method with original method is given at the end of the paper.

I. Calculation of the Maximum Local Heat Flux $q_{\text{лоб}}$ of the Evaporating Tube Bank Adjacent to the Furnace

The maximum local heat flux of the first row of evaporating tube bank nearest to the furnace consists of two parts:

$$q_{\text{лоб}}=q^{\text{л}}_{\text{лоб}}+q^{\text{к}}_{\text{лоб}} \qquad (\text{kcal/m}^2\,\text{hr}) \qquad (1)$$

where $q^{\text{л}}_{\text{лоб}}$, $q^{\text{к}}_{\text{лоб}}$ = the maximum local radiant and convection heat flux of the first row of convective evaporating tube bank nearest to the furnace and directly facing it.

1. Calculation method of maximum radiant heat flux $q^{\text{л}}_{\text{лоб}}$

Method of calculation of $q^{\text{л}}_{\text{лоб}}$ has been presented in Reference [1], with the use of the following equation:

$$q^{\text{л}}_{\text{лоб}}=2.5\,\frac{Q^{\text{л}}_{1}}{n_1\pi\,dl}=2.5\,\frac{Q^{\text{л}}_{\text{к}}\varphi_1}{n_1\pi\,dl} \qquad (\text{kcal/m}^2\text{hr}) \qquad (2)$$

where $Q^{\text{л}}_{\text{к}}$ =the radiant heat absorbed by the convective evaporating tube bank adjacent to the furnace

$$Q^{\text{л}}_{\text{к}}=Q_{\text{л}}\cdot\frac{H^{\text{л}}_{\text{к}}}{H_{\text{л}}} \qquad (\text{kcal/hr}) \qquad (3)$$

here $Q_{\text{л}}$ =the radiant heat absorbed by the furnace, kcal/hr

$H^{\text{л}}_{\text{к}}$ =the radiant heat absorbing surface (RHAS) of convective evaporating tube bank adjacent to the furnace, m²

$H_{\text{л}}$ =the total RHAS of furnace, m²

$Q^{\text{л}}_{1}$ =the radiant heat absorbed by the first row of convective tube bank adjacent to the furnace, kcal/hr

φ_1=the radiant angle coefficient of the first row of convective tube bank adjacent to the furnace, i.e.

$$\varphi_1=\left[1-\sqrt{1-\left(\frac{d}{s_1}\right)^2}+\frac{d}{s_1}\operatorname{arctg}\sqrt{\left(\frac{s_1}{d}\right)^2-1}\right]$$

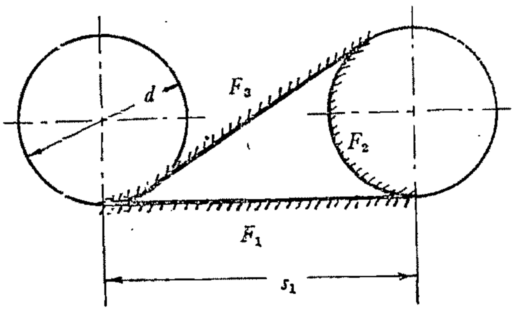

$\varphi_1=(F_1+F_2-F_3)/F_1$

Fig. 1 Sketch to show the method of determination of the angle coefficient of first row

See Fig. 1,

n_1=the number of tubes of the first row

d=the outside diameter of tube, m

s_1=the longitudinal tube pitch of the first row, m

l=the length of tube, m

Obviously, it can be easily seen from equation (2), that this calculation method is, at first, to have the radiant heat absorption of the first row of the tube bank uniformly distributed to the tube circumference. And then, use a constant 2.5 to modify the difference between the average radiant heat flux around the tube circumference and the maximum local heat flux. This modification is not rational, for the coefficient of modification should not be constant, it should be a function of the longitudinal pitch to diameter ratio s_1/d of the first row of tubes.

The calculation method in Reference [2] is more rational, which has considered the unequal heat absorbed by each tube in the first row due to non-uniform temperature field in the furnace. It uses a corrective coefficient ψ, and $\psi=1.3$. The equation used for calculation is

$$q_{лоб}^{л} = \varphi \frac{Q_{к}^{л}\varphi_1}{\pi_1 \pi dl}\psi \qquad (\mathrm{kcal/m^2hr}) \tag{4}$$

Comparing equation (4) with equation (2), it is not difficult to see that φ in equation (4) actually replaces the constant 2.5 in equation (2). This corrective coefficient φ is called coefficient of unequal radiant heat around the tube circumference, and is shown in Fig. 2 as $\varphi=f(s_1/d)$. No calculation formula of φ is given in Reference [2].

The equation given in Reference [3] is

$$q_{лоб}^{л} = \psi k_{тр}^{л}\frac{Q_{к}^{л}\varphi_1}{n_1 \pi dl} \qquad (\mathrm{kcal/m^2hr}) \tag{5}$$

Here, $k_{тр}^{л}$ is the coefficient of unequal radiant heat around tube circumference, which is taken as constant 1.8, and is related with s_1/d and s_2/d. Obviously, there is a mistake here. The radiant heat flux of the first row of tube bank has nothing to do with s_1/d. $k_{тр}^{л}=1.8$ actually means $\psi k_{тр}^{л}=(1.3)1.8\approx 2.5$. It is suggested that $q_{лоб}^{л}$ should be calculated from the following equation:

$$q_{лоб}^{л} = \frac{Q_{к}^{л}}{(n_1-1)s_1 l}\psi \tag{6}$$

here $(n_1-1)s_1 l$=RHAS of the tube bank adjacent to the furnace

The radiant heat flux on this RHAS actually represents the maximum local radiant heat flux of this tube row facing the furnace. It is not necessary to convert the total radiant heat $Q_{к}^{л}$ absorbed by the tube bank to the radiant heat $Q_1^{л}=Q_{к}^{л}\varphi_1$ absorbed by the first row, and then to distribute it to total circumference uniformly and finally to revise it with a coefficient [such as 2.5 in equation (2) and $k_{тр}^{л}$ in equation (5)].

Comparing equation (6) with equation (4), the following equation can be easily obtained

$$\frac{\varphi\varphi_1}{n_1\pi dl} = \frac{1}{(n_1-1)s_1 l}$$

or

$$\varphi = \frac{n_1 \pi d}{(n_1-1)s_1\varphi_1} \approx \frac{\pi}{\frac{s_1}{d} - \sqrt{\left(\frac{s_1}{d}\right)^2 - 1} + \mathrm{arctg}\sqrt{\left(\frac{s_1}{d}\right)^2 - 1}} \tag{7}$$

From Fig. 2, we can see that the curve $\varphi=f(s_1/d)$ is constructed according to equation (7), although it is said in Reference [2] that this curve was made according to Ramthin's graphical method. In equation (7), we use the approximation $n_1 \approx n_1-1$.

We can get the following equation, if we compare equation (6) with equation (5).

$$\psi k_{\text{тр}}^{\text{л}} \frac{\varphi_1}{n_1 \pi dl} = \frac{1}{(n_1-1)s_1 l}\psi$$

i.e.

$$k_{\text{тр}}^{\text{л}} = \frac{n_1 \pi d}{\varphi_1 (n_1-1) s_1}$$

$$\approx \frac{\pi}{\frac{s_1}{d}\sqrt{\left(\frac{s_1}{d}\right)^2-1}+\operatorname{arctg}\sqrt{\left(\frac{s_1}{d}\right)^2-1}} \qquad (8)$$

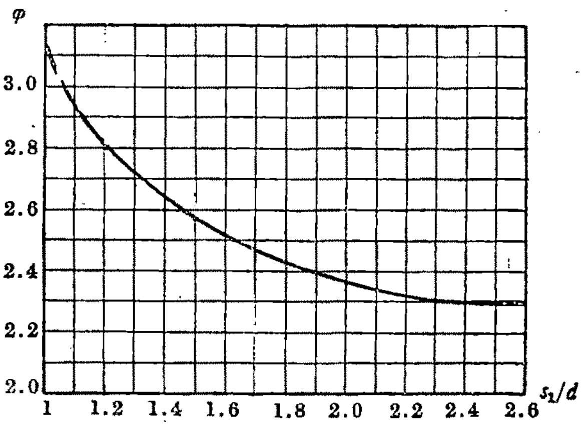

Fig. 2 Corrective coefficient for difference between the maximum and average radiant heat flux

It seems that in equation (7) φ is the same as $k_{\text{тр}}^{\text{л}}$ in equation (5). In that case, $k_{\text{тр}}^{\text{л}}$ should not be a constant but a function of (s_1/d). Also $k_{\text{тр}}^{\text{л}}=1.8$ is not suitable, because when $\varphi=1.8$, $s_1/d \gg 2.6$, which is far from the common value of s_1/d used in marine boilers.

Comparing equation (6) with equation (2), if we think that the heat non-uniformity of every tube in the tube rows is not considered in equation (2), We get the following equation:

$$\frac{2.5\varphi_1}{n_1 \pi dl} = \frac{1}{(n-1)s_1 l} \qquad (9)$$

If the heat non-uniformity of every tube in tube rows is considered, we can get:

$$\frac{2.5\varphi_1}{n_1 \pi dl} = \frac{\psi}{(n_1-1)s_1} \qquad (10)$$

By further conversion, we get:

$$2.5 \approx \frac{\pi}{\frac{s_1}{d}\sqrt{\left(\frac{s_1}{d}\right)^2-1}+\operatorname{arctg}\sqrt{\left(\frac{s_1}{d}\right)^2-1}} \qquad (9')$$

or

$$2.5 \approx \frac{\psi\pi}{\frac{s_1}{d}\sqrt{\left(\frac{s_1}{d}\right)^2-1}+\operatorname{arctg}\sqrt{\left(\frac{s_1}{d}\right)^2-1}} \qquad (10')$$

Evidently, the influence of s_1/d has not been considered by constant 2.5 in Reference [1]. In fact, only with a certain fixed value of s_1/d (such as $s_1/d=1.61$), can we obtain 2.5 from equation (9'). With regard to equation (10'), which is equivalent to taking $\psi k_{\text{тр}}^{\text{л}}=2.5$ in equation (5), it is unreasonable to take $k_{\text{тр}}^{\text{л}}=\varphi=1.8$, such as recommended in Reference [3].

From the above analysis, it is not difficult to get the following conclusions:

(1) The calculation method of $q^{\text{л}}_{\text{лоб}}$ in Reference [1] has not considered the radiant heat absorption non-uniformity of every tube in the first row and the influence of s_1/d to φ.

(2) The calculation method in Reference [2] is in accordance with the actual fact. But in Reference [2], was not given verification of the source of φ-equation which is only given through graphical solution to get the curve $\varphi=f(s_1/d)$.

(3) Equation (5) recommended by Reference [3] is basically a reproduction of equation in Reference [1]. It seems to have modified the heat non-uniformity of every tube in first row by giving $\psi k^{\text{л}}_{\text{тр}}=2.5$ but this does not represent the actual practice of marine boilers.

(4) Equation (6) presented in this paper is much clearer in physical concept, for the point on the first row tube directly facing the furnace is lying on the RHAS of the tube bank. It is in agreement with Reference [2], and is easier for calculation. It is not necessary to convert $Q^{\text{л}}_{\text{к}}$ to heat absorbed by the $Q^{\text{л}}_1=Q^{\text{л}}_{\text{к}}\varphi_1$, and then to distribute it uniformly around the circumference to get $\overline{q}^{\text{л}}_{1\text{ср}}=\dfrac{Q^{\text{к}}_{\text{л}}\varphi_1}{\pi n_1 dl}$, and finally to revise it with a coefficient φ.

2. Calculation of maximum convection heat flux $q^{\text{к}}_{\text{лоб}}$

In Reference [1] is given as:

$$q^{\text{к}}_{\text{лоб}}=\frac{Q_{1\text{к}}}{H_1}\xi_{\text{л}} \tag{11}$$

where $Q_{1\text{к}}$=the convection heat absorbed by first tube row, kcal/hr.

The method of calculation of $Q_{1\text{к}}$ is to use the common method of distribution of convection heat in water circulation calculation. With the use of $(\theta-t_{\text{н}})\sim H$ curve, and by graphical method we can obtain:

$$Q_{1\text{к}}=Q_{1\text{к}}\cdot\frac{\theta'-\theta''_1}{\theta'-\theta''_x} \tag{12}$$

where $Q_{1\text{к}}$=the convection heat absorbed by the tube bank adjacent to the furnace, kcal/h

θ', θ''_x, θ''_1=the gas temperature at inlet and outlet of the tube bank and at the back side of the first row, °C. The former two is known from thermal calculation of furnace and tube bank. The later is known by using the $(\theta-t_{\text{н}})\sim H$ curve

H_1=the overall heating surface of the first tube row, i.e. $=\pi n_1 dl$, m^2,

$\xi_{\text{л}}$ =coefficient used to modify for the non-uniformity in convection heat around the circumference. For staggered tube banks, according to Reference [1],

$$\xi_{\text{л}}=3.15Re_{\text{ст}}^{-0.09}\left(1-\frac{d}{s_1}\right)^{0.52} \qquad (1\ )$$

and for in-line arranged tube bank,

$$\xi_x = 5Re_{\text{ст}}^{-0.04}\left(1 - \frac{d}{s_1}\right)^{0.52} \tag{14}$$

$Re_{\text{ст}}$=the Reynolds number of gas flow, Use kinematic viscosity $v_{\text{ст}}$ at the tube wall temperature $t_{\text{ст}}$ in $Re_{\text{ст}} = \frac{wd}{v_{\text{ст}}}$

In Reference [2],

$$q^{\text{к}}_{\text{лоб}} = \frac{Q_{1\text{к}}}{H_1} k_\alpha \cdot \psi \tag{15}$$

where k_α=corrective coefficient of convection heat transfer for non-uniformity around the tube circumference, according to Reference [2], by using Fig. 3, it is known that k_α varies from 1.2 to 1.6 depending upon Reynolds number Re, of gas flow.

ψ=corrective coefficient for non-uniformity in distribution of gas flow, which leads to difference between maximum and average values of film coefficients of different tubes in the first row. Take ψ=1.3.

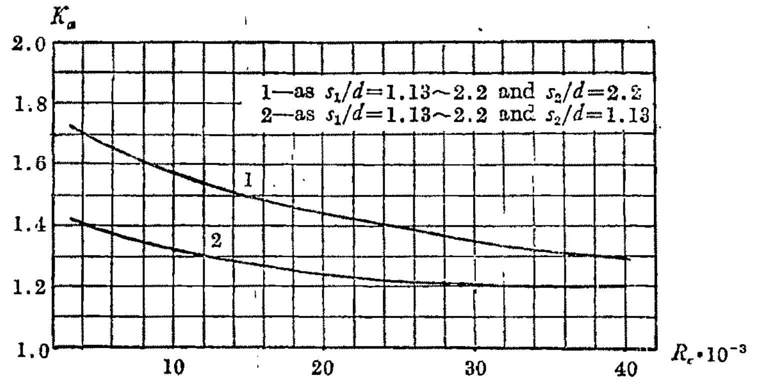

Fig. 3 Corrective coefficient for difference between the maximum and average convection heat flux

In Reference [3],

$$q^{\text{к}}_{\text{лоб}} = \psi \alpha^{\text{к}}_{\text{лоб}} (\theta' - t_{\text{ст}}) \tag{16}$$

where $\alpha^{\text{к}}_{\text{лоб}}$=the local film coefficient at the point around the tube circumference facing directly the furnace $\alpha^{\text{к}}_{\text{лоб}} = \alpha_K \cdot k_\alpha$

Here k_α is related with Re. when $Re \leqslant 1 \times 10^4$, $k_\alpha = 1.6$; and when $Re = 8.5 \cdot 10^4, k_\alpha = 1.23$. The influence of tube row numbers should be considered when α_K is calculated, that is $\alpha_K = \alpha_{\text{H}} \cdot C_{z=1}$. $C_{z=1}$ is the modification coefficient for α_K in case of number of rows $Z=1$, $R_{z=1}=0.65$. α_K is calculated for temperature $\theta' = \theta''_{\text{т}}$, i.e. the temperature of gas leaving the furnace. $t_{\text{ст}}$ is the local tube wall temperature, °C.

From an analysis of the above calculating method, we know:

(1) The method in Reference [1] still does not give any consideration to the non-uniformity in convection heat caused by the non-uniform distribution of gas flow in the tube row. The

calculation method implies that the film coefficient of the first row and the average film coefficient $\bar{\alpha}_K$ of the tube bank are the same. That means the unmodified α_K of the first row is a little lower than the avergae value $\bar{\alpha}_K$.

(2) The calculation method in Reference [2] does not include the specific method of calculating Q_{1K}. If the convective heat absorption Q_{1K} of the first row is correct, this method is somewhat in accordance with the actual condition.

(3) The calculation method in Reference [3] is correct in physical concept. However, in calculation, the tube wall temperature t_{CT}' is an unknown value, which should be obtained by cut and try method. Choose a certain value at first and then verify it later. And, the method correctly consider the influence of number of tube rows.

In this paper, author would like to give a new method of calculation of $q^{\text{к}}_{\text{лоб}}$:

(1) At first, determine the average convection heat flux $q^{\text{cp}}_{1\text{к}}$ of first tube row by using graphical method of solution

With the use of equation of convection heat transfer of evaporating heat surface and the heat balance equation of gas flow, the following equation is obtained.

$$\lg\frac{\theta'-t_H}{\theta''-t_H}=aH_x \tag{17}$$

$$a=\frac{k}{2.3\Sigma VCB_\eta}\qquad (1/\text{m}^2)$$

where, k=the overall heat transfer coefficient of the bank nearest the furnace, kcal/m²hr°C

ΣVC=the specific heat of gas produced by unit weight of fuel, kcal/°C kg

B=oil consumption rate, kg/hr

η=effective coefficient of heat transfer

t_H=saturated temperature at boiler working pressure,°C

H_x=evaporating heat surface, m²

Equation (17) gives a straight line relationship by plotting in semi-log coordinates. The boundary condition is $H_x=0$, $\theta'=\theta''_T=\theta''$. θ''_T is the temperature of gas leaving the furnace i.e. it is also the temperature of gas at inlet of first tube row. When $H_x=H_I$, $\theta''=\theta''_I$. H_I is the heating surface of tube bank adjacent to the furnace. θ''_I is the gas temperature at outlet of the tube bank adjacent to the furnace.

Fig. 4 shows how to draw this straight line. Let ordinate be $(\theta''-t_H)$ with log scale and abscissa be H_x with common scale. Mark point A on the ordinate for (θ''_T-t_H) and point B on the abscissa for H_I. Draw a vertical line through point B, mark point C for (θ''_I-t_H) on this vertical line. Join A and C with a straight line. θ''_T, θ''_I and H_I are known by the results of thermal calculation of boiler. And then, obtain point D for $H_I=\eta_I\pi dl$, m², on the abscissa. Draw a vertical line through D, which intersects the straight line A,C at E. The ordinate of point E is (θ''_I-t_H). Therefore the outgoing gas temperature θ''_I of first row can

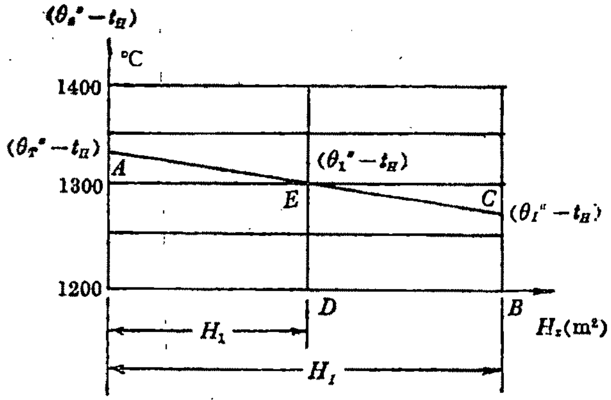

Fig. 4 Semi-log plot of $(t''-t_B)\sim H_\lambda$ curve

be obtained and the convection heat absorption of first tube row can be calculated by following equation:

$$Q_{1K}=Q_{1K}\frac{\theta_T''-\theta_1''}{\theta_T''-\theta_I''}\qquad \text{(kcal/hr)} \tag{18}$$

The convection heat absorbed by tube bank adjacent to the furnace Q_{1K} is a known value from the result of thermal calculation of boiler.

Thus, the average heat flux of the first row can be calculated with the following equation:

$$q_{1K}^{\mathrm{cp}}=\frac{Q_{1K}}{H_1}\qquad \text{(kcal/m}^2\text{hr)} \tag{19}$$

(2) Make all kinds of relevant modifications

Modify for the non-uniformity of heat transfer of each tube in the first row, use coefficient $\psi=1.3$.

Modify for the unequal heat distribution at tube circumference, usually take $k_\alpha=1.6$ approximately. Because high heat flux marine boiler has a relative high exhaust gas temperature leaving the furnace, therefore although the incoming gas velocity to the tube bank is high, but *Re* number is low ($\sim$10,000).

Modify for the influence of number of tube rows. Obviously, it is not agreement with fact to take the overall heat transfer coefficient k of the tube bank as a constant in the above mentioned graphical method of solution. If we want to modify for this influence, the following should be considered:

(i) If the number of tube rows $Z\geqslant 10$, use $C_{z=}=0.65$.

(ii) If $Z=(2\sim3)$, use $C_z=\dfrac{0.65}{C_{z=(2\sim3)}}$.

This is because the influence of number of tube rows has been considered when Q_{1K} was calculated. For the modification of the first row (namely $Z=1$), we should first eliminate the modification of the rows number $Z=(2\sim3)$, then modify the influence caused by $Z=1$.

One point should be pointed out: The calculation method used here (actually in thermal calculation of boiler), to calculate film coefficient α_K is for the average gas temperature $\theta_{\text{ср}} = \frac{1}{2}(\theta_{\text{т}}'' + \theta_{\text{т}}')$). Normally, calculation temperature should be $\theta_{\text{т}}''$ as shown in Reference [3]. Common marine boilers often use large-sized tubes for the tube bank adjacent to the furnace with a row number $Z=(2\sim3)$, so it would not cause much error if we take $\bar{\alpha}_K$ at $\theta_{\text{ср}}$ to replace α_K at $\theta_{\text{т}}''$.

Therefore, we can get the following equation for calculation:

$$q_{\text{зоб}}^{\text{к}} = \psi k_\alpha C_z q_{1\text{к}}^{\text{ср}} \qquad (\text{kcal/m}^2\text{hr}) \qquad (20)$$

Taking a certain marine boiler for example, the total modification should be (according to the above calculation)

$$\psi \cdot k_\alpha \cdot C_z = 1.3 \times 1.6 \times \frac{0.65}{0.85} = 1.59$$

The original thermal calculation for this boiler uses the method of Reference [1] with $\xi_{\text{л}} = 0.745$, which clearly has a too big error.

Finally, calculate the maximum heat flux $q_{\text{зоб}}$ of the first row tube directly facing the furnace according to equation (1).

II. Calculation of Film Coefficient α_2 of the Boiling Water at Inner Wall of the Tube

In the 50's of this century, some the Russians' boiler handbooks or references gave $\alpha_2 = 5000\sim6000$ kcal/m²hr C. In Reference [3], the following equation was given

$$\alpha_2 = C q^{0.7} \qquad (21)$$

C=coefficient related with working pressure of boiler, see Fig. 5.

The calculation equation of α_2 for stainless steel tube is also given in Reference [4], as

$$\alpha_2 = 3(P^{0.14} + 1.82 \cdot 10^{-4} P^2) q^{0.7} \qquad (\text{kcal/m}^2\text{hr°C}) \qquad (22)$$

where P=boiler working pressure

For common steel tube, the oxide film of the inner wall surface must be considered, use following equation to calculate.

$$\alpha_2' = \frac{1}{\frac{0.4}{\alpha_2} + 0.5 \cdot 10^{-4}} \qquad (\text{kcal/m}^2\text{hr°C}) \qquad (23)$$

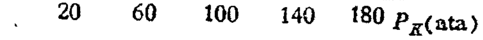

Fig. 5 C in the formula of calculation of the film coefficient α_2 of boiling water in stainless steel tube

Use equation (22) to calculate α_2 in the denominator of above equation.

The calculation formula of α_2 introduced in Reference [5] shows:

$$\alpha_2 = 1.95(P)^{0.24}(q)^{0.72} \qquad (\text{watt/m}^2\text{°K}) \qquad (24)$$

In the above equation, the unit of pressure P is bar, and the unit of q is watt/m². If we convert the pressure to kg/cm² and the heat flux to kcal/m²hr, this equation can be rewrite as follows:

$$\alpha_2 = 1.37(P)^{0.24}(q)^{0.72} \qquad (\text{kcal/m}^2\text{hr°C}) \qquad (24')$$

If we take $q_{\text{лоб}} = 1\times10^6$ kcal/m²hr for example, we can use equation (21), (22) and (24′) to obtain $\alpha_2 \approx 10^5$ kcal/m²hr°C. It is twenty times bigger than $\alpha_2 = 5000 \sim 6000$ kcal/m²hr°C used in the past. So the rise of temperature of the boiling water film is no more than 10°C. If the heat resistance of oxide film of the inner wall surface is considered, film coefficient will be $\alpha_2 \approx 1.8\times10^4$ kcal/m²hr°C when carbon steel tube is selected for use.

The temperature rise of both the boiling water film and oxide film in inner wall is no more than 55°C. The temperature rise is 150°C lower than using $\alpha_2 = 5000 \sim 6000$ kcal/m²hr°C. This is extremely important to the saving of evaporating tube materials.

Appendix

Example of calculation of the maximum heat flux of first tube row of generating tube bank.

1. Calculation of $q^{\text{л}}_{\text{лоб}}$

Tube outside diameter $d_{\text{Н}} = 38$ mm;

Longitudinal tube pitch $s = 61.3$ mm;

Tube pitch diameter ratio $s/d = 1.613$;

The angle coefficient of the first row $\varphi_1 = 0.79$ (the original stress calculation of this boiler uses 0.77, which is incorrect); The total radiant heat absorbed by RHAS in the furnace

$$Q_{\text{л}} = 10.58\times10^6 \qquad (\text{kcal/hr})$$

The total RHAS of furnace $H_{\text{л}} = 18.9$ (m²);

The RHAS of convective tube bank $H^{\text{л}}_{\text{к}} = 9.68$ m²;

The radiant heat absorbed by the convective tube bank

$$Q^{\text{л}}_{\text{к}} = Q_{\text{л}} \cdot \frac{H^{\text{л}}_{\text{к}}}{H_{\text{л}}} = 10.58\times10^6 \frac{9.68}{18.9} = 5.42\times10^3 \qquad (\text{kcal/hr})$$

(in the original stress calculation it is 4.76×10^6 kcal/hr taken from the result of water circulating calculation, the actual value should be 5.43×10^6 kcal/hr).

The radiant heat absorbed by the first row tube

$$Q^{\text{л}}_{1\text{к}} = Q^{\text{л}}_{\text{к}} \cdot \varphi_1 = 5.42\times10^6\times0.79 = 4.28\times10^6 \qquad (\text{kcal/hr})$$

The convective heating surface of the first row tube

$$H_1 = n_1 \pi d_{\text{Н}} l = 39\times\pi\times38\times10^{-3}\times4.1 = 19.1 \qquad (\text{m}^2)$$

The average radiant heat flux around the tube circumference of the first row $q^{\text{ср}}_{1\text{л}} = \dfrac{Q^{\text{л}}_{1\text{к}}}{H_1}$ $= \dfrac{4.28\times10^6}{19.1} = 0.224\times10^6$ kcal/m²hr (There is an error in the original stress calculation $q^{\text{ср}}_{1\text{л}} = 0.2185\times10^6$ kcal/m²hr).

The maximum radiant heat flux on the front point of first row tube directly facing the furnace

$$q_{\text{лоб}}=\psi\varphi q_1^{\text{л}}=1.3\times2.5\times0.224\times10^6=0.73\times10^6\qquad(\text{kcal/m}^2\text{hr})$$

The above calculation is made basically according to the method of Reference [2].

We can use the easier method of calculation proposed in this paper.

$$q_{\text{лоб}}=\psi\cdot\frac{Q_{\text{л}}}{H_{\text{л}}}=1.3\times\frac{10.58\times10^6}{18.9}=0.73\times10^6\qquad(\text{kcal/m}^2\text{hr})$$

The results are the same.

2. Calculation of $q^{\text{к}}_{\text{лоб}}$

The convection heat absorbed by tube bank adjacent to the furnace $Q_1^{\text{к}}=2.61\times10^6$ kcal/h (according to the calculation of water circulation);

The total effective convection heating surface of tube bank $H_{\text{I}}=32.6$ m² (namely $H_{\text{I}}=H_1+H_2=16.5+16.1$ m²);

The gas temperature at outlet from the furnace $\theta_{\text{т}}''=1610$°C;

The saturated temperature of water at boiling working pressure is $t_{\text{H}}=280$°C;

The gas temperature of outlet from the tube bank $\theta_I''=1551$°C;

Using the graphical method of solution introduced in this paper, the gas temperature at outlet from the first row is $\theta_I''=1300+280=1580$°C;

The heat contained in gas under temperature θ_I'' is

$$I_I''=\frac{8200-7908}{1550-1500}\times80+7908=8375\qquad(\text{kcal/kg})$$

The convection heat absorbed by the first row is

$Q_{\text{I}}^{\text{к}}=B\eta(I_{\text{т}}''-I_1'')=7600\times0.987(8550-8375)=1.320\times10^6$ (kcal/hr) (same with the original calculation).

The average heat flux of the first row is

$$q_{1\text{к}}^{\text{cp}}=\frac{1.32\times10^6}{16.5}=0.08\times10^6\qquad(\text{kcal/m}^2\text{hr})$$

The velocity of gas flow in the tube bank by furnace

$$w=\frac{BV_{\text{г}}(273+\theta_{\text{OP}})}{3200f_I\cdot273}=\frac{7600\times13.85(272+1595)}{3600\times3.14\times273}=63.8\quad(\text{m/sec})$$

The Reynolds number of gas flow

$$Re=\frac{wd}{\nu}=\frac{63.8\times38\times10^{-3}}{323\times10^{-6}}=7530$$

Modify for the convection heat transfer coefficient non-uniformity around the tube circumference $k_\alpha=1.6$;

When the tube row number Z is equal to 2, the corrective coefficient $C_{Z=2}=0.85$;

The maximum convection heat flux at the point of the tube of first row directly facing the furnace

$$q^{\text{н}}_{\text{лоб}} = q^{\text{ср}}_{1\text{н}} \cdot \psi \cdot k_{\alpha} \cdot \frac{C_{Z=1}}{C_{Z=3}} = 0.08\times 10^{6}\times 1.3\times 1.6\times \frac{0.65}{0.85}=0.127\times 10^{6} \quad (\text{kcal/m}^2\text{hr})$$

3. The total maximum heat flux

$$q_{\text{лоб}} = q_{\text{лоб}} + q^{\text{н}}_{\text{лоб}} = (0.73+0.127)\times 10^{6} = 0.857\times 10^{6} \quad (\text{kcal/m}^2\text{hr})$$

References

[1] Г. И. Шваб и П. Д. Дыгтядрев: *Проектирование корабельных главных котлов*, 1953.

[2] А. А. Никонов: *Оценка надежности работы испарительных поверхностей нагрева судовых котлов*, **Судостроение**, 1958. 7.

[3] Н. И. Пушкин: *Судовые паровые котлы*, 1965.

[4] А. М. 古尔维奇, Н. В.库兹聂佐夫: 锅炉机组热力计算标准方法, 北京水利电力出版社, 1960.

[5] Steinmüller: *Pocket book steam generation*, Vulkan-Verlag Essen, 1976.

Annual of the CSNAME, Vol. 1, 1982

DAMPING METHOD OF FITTING SILICONE FLUID DAMPERS TO TRANSMISSION SHAFTS

NIE DEYAO (聂德耀)

Changjiang Shipping Science Research Institute

SUMMARY

Owing to the fact that diesel engines on board ship neither have dampers nor can be modified for solving the torsional vibration of shaftings, the damping effort can hardly be implemented through conventional methods. The mechanism of fitting silicone fluid dampers to transmission shafts is, therefore, a new damping measure, which was obtained through both theoretical and experimental study.

Being affected by the mass of transmission shafts, the modes of the torsional vibration of shaftings may yield a rather high peak on transmission shafts[1][2]. It is quite evident that greater damping effects can be achieved through fitting silicone fluid dampers to the point on transmission shafts, where the relative amplitude is greater. Of late years, we have thereby attained the expected purpose through adopting the above means on long shaftings. As to short shaftings, investigations showed that greater relative amplitude can be obtained through proper selection of coupling flexibility while fitting silicone fluid dampers to transmission shafts. There have been proven through ship trials and marine practices. Because of the fact that room around transmission shafts is spacious, the temperature condition there is better than that in engines, and it is also convenient to carry out routine inspections and maintenances, it is really a simple feasible and proven out damping method.

In this paper, transmission shafts are first of all considered as levers of uniform mass, and we try to ascertain their effects on the torsional vibration characteristics of shaftings, the distribution of the vibration modes on transmission shafts, as well as the rules of peak occurences of the modes. Thereby, the mechanism of fitting silicone fluid dampers to transmission shafts, and that of improving the effects of transmission shaft dampers of short shaftings by properly selecting coupling flexibility are studied. The basic principles of the design of the above-mentioned damping method and preliminary ideas of its design procedures are further developed. Finally, examples for the damping method adopted by either long or short shaftings aboard are presented.

I. The Effects of the Mass of Transmission Shafts on Torsional Vibration Characteristics

For the shafting as shown in Fig. 1, let the inertia per engine cylinder be J_s, the flexibility of crankshaft element be e_s, the length of the transmisson shaft be L, and its mean diameter

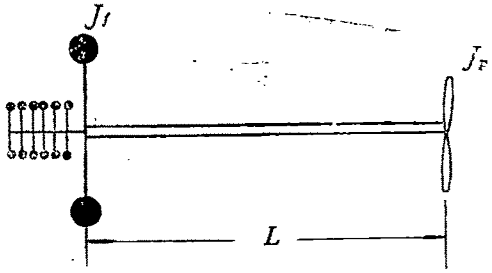

Fig. 1

be d, then the total flexibility of the transmission shaft is $e=\frac{32L}{\pi Gd^4}$, its total inertia $J=\frac{\pi\gamma d^4L}{32g}$, the frequency parameter of the shaft $\lambda=\frac{1}{\sqrt{Je}}$, corresponding dimensionless quantity

$$E=e/e_s,\ \nu=J/J_s \text{ and } \sqrt{\nu E}=\sqrt{\frac{Je}{J_se_s}}=\sqrt{\frac{\gamma}{Gg}}\frac{L}{\sqrt{J_se_s}} \tag{1.1}$$

In case of the vibration frequency of the shafting is ω, the dimensionless frequency is $\sqrt{\Delta}=\sqrt{J_se_s}\omega$, the frequency ratio of the transmission shaft is

$$V=\frac{\omega}{\lambda}=\sqrt{\nu E\Delta} \tag{1.2}$$

Then, for free vibration without damping, according to the classical theory[3], the torsional vibration of uniform lever is

$$\varphi=\phi(z)\sin\omega t=(a\cos V_z+b\sin V_z)\sin\omega t \tag{1.3}$$

where, $z=Y/L$, Y=the distance from the points on shaft to wheel. To make use of the boundary conditions at $z=0$ (wheel end), the relative amplitude and moment on the transmission shaft are

$$\phi=\alpha_f\cos V_z-\frac{E\delta_f}{V}\sin V_z=A\cos(V_z+\xi) \tag{1.4}$$

$$\delta=\delta_f\cos V_z+\frac{V\alpha_f}{E}\sin V_z=D\sin(V_z+\xi) \tag{1.5}$$

where α_f=the relative amplitude of the wheel

δ_f=the moment at the output end of the wheel

$$\left.\begin{aligned}A&=\sqrt{\alpha_f^2+(E\delta_f/V)^2}\\ D&=\sqrt{\delta_f^2+(V\alpha_f/E)^2}\end{aligned}\right\} \tag{1.6}$$

$$\operatorname{tg}\xi=E\delta_f/V\alpha_f \tag{1.7}$$

at $z=1$ (propeller)

$$\left.\begin{aligned}\phi_p&=\phi(1)=A\cos(V+\xi)\\ \delta_p&=\delta(1)+\gamma_p\Delta\dot{\varphi}(1)=D_p\sin(V+\xi+\eta)\end{aligned}\right\} \tag{1.8}$$

where

$$D_p=\sqrt{D^2+(\nu_p\Delta A)^2} \tag{1.9}$$

$$\mathrm{tg}\,\eta=V_p^2/V \tag{1.10}$$

$V_p=\sqrt{\nu_p E\Delta}$, ν_p=the dimensionless inertia of the propeller. From $\delta_p=0$, it is obtained that the frequency equation of the shafting is

$$V+\xi+\eta=n\pi \quad (n=1,2,3...) \tag{1.11}$$

Discussion:

1. In considering the mass of the transmission shaft, the vibration modes along the length of the shaft are distributed as cosine function. The effect of the mass is reflected by the frequency ratio V. From Eq. (1.1) the amplitude of the effect increases with the length of the shaft.

2. The resonance on the first mode of torsional vibration will occur, while $V+\xi+\eta=\pi$. In this case, at $z=0$, $V_z+\xi=\xi>0$; *at* $z=1$, $V_z+\xi=V+\xi<\pi$, then, on the transmission shaft, it emerges only one node $V_z+\xi=\frac{\pi}{2}$, without peak. The corresponding mode is similar to one, wherein the mass of the shaft is neglected. Calculation examples also show that the effect of the mass on the transmission shaft for the first mode of torsional vibration is insignificant.

The second mode of torsional vibration will occur while $V+\xi+\eta=2\pi$. For the system as shown in Fig. 1, there exists one node in engine crankshaft, then $\xi>\pi/2$. If $\xi\geqslant\pi$, the mode on the shaft, yields only one node $V_z+\xi=\frac{3\pi}{2}$, without peak. In this case, the effect of mass on shaft section is not significant,. If $\xi<\pi$, the mode on the shaft consists of one peak $V_z+\xi=\pi$ and one node $V_z+\xi=\frac{3\pi}{2}$. This mode is much more different from one, wherein the mass on transmission shafts is neglected.

For $\xi=\pi$, $\delta_f=0$, corresponding to the case of engine crankshaft system frequency Δ. Obviously if $V_e+\eta_e>\pi$, while frequency is Δ_e, the second mode of vibration frequency $\Delta_{II}<\Delta$, the mode on shaft consists of a peak, the effect of the mass on the transmission shaft becomes obvious gradually. Furthermore, since the inertia ν_p of ship propellers is graeter, the η_e value is less than, but approaching to $\frac{\pi}{2}$. As a result, it can be considered approximately that when $V_e>\frac{\pi}{2}$, i.e.

$$\omega_e L\geqslant\frac{\pi}{2}\sqrt{Gg/\gamma}=5100 \qquad (\mathrm{m/s})$$

the effect on the characteristics of the second mode of torsional vibration by the mass of the shaft section becomes obvious gradually. When $V_e\geqslant\frac{11}{18}\pi$ i. e.

$$\omega_e L\geqslant 6335 \qquad (\mathrm{m/s})$$

the effect on torsional frequency by the mass of the shaft section can reach as high as 3~5%.

Again it is the third mode of vibration while $V+\xi+\eta=\pi$. In general, the effect on the third mode of torsional vibration by the mass of transmission shafts is more obvious. Therefore, for short shaftings such as those on board stern-engine vessels, pushers etc., the high order wave of the third mode of the torsional vibration on transmission shafts is also to be measured easily.

3. The relative amplitude at peak is $A=\sqrt{\alpha_f^2+(E\delta_f/V)^2}$. Usually $E/V\gg1$, and $\delta_f=0$ while frequency is Δ_e, so the value of δ_f will augment while Δ deviates from the Δ_e. Therefore, when the frequency of the system deviates from the frequency Δ_e of the system of the single engine, the relative amplitude at peak is greater on transmission shafts.

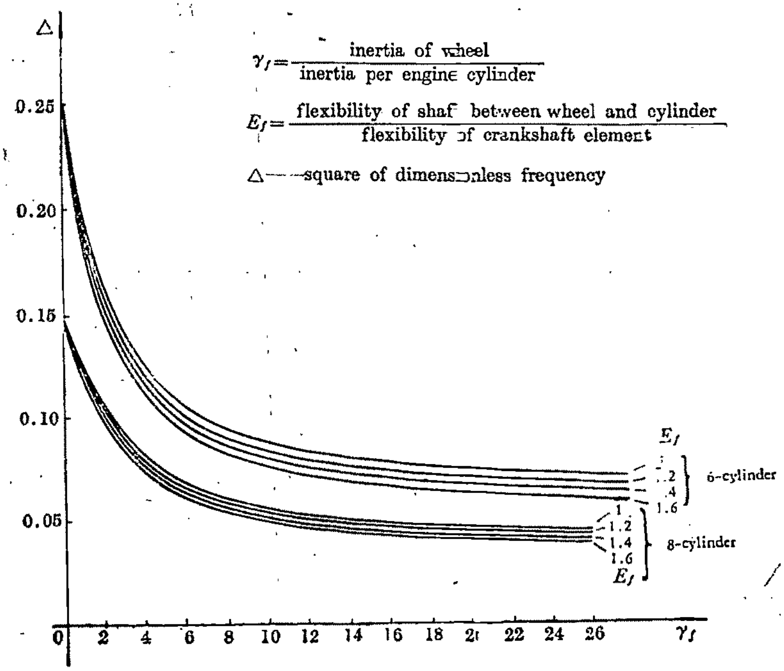

Fig. 2 Curves of dimensionless frequency of diesel engines

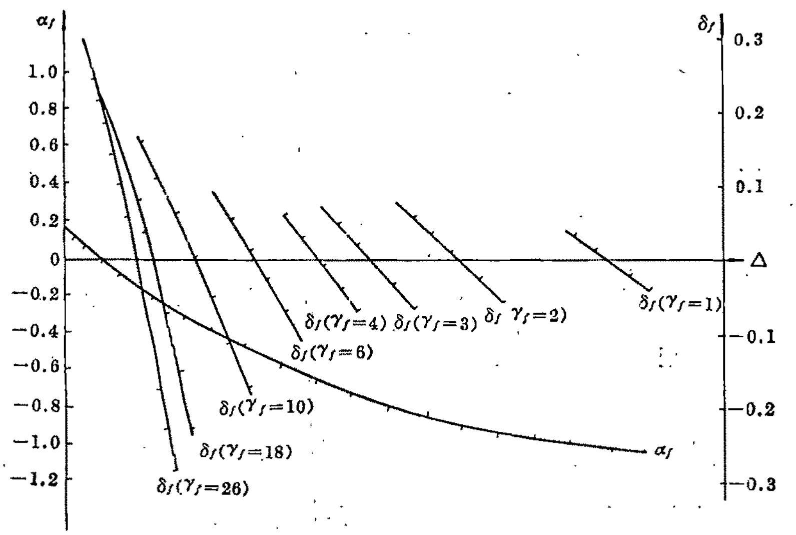

Fig. 3 Curves of δ_f, α_f 6-cylinder engines

As stated above, in addition to the length of shafts, the effect of the mass on the transmission shaft to the characteristics of torsional vibration of shaftings still relates to the characteristics of diesel engines very much. Fig. 2 shows the curves of frequency Δ_e of the diesel engine, of which the free end does not have any additional mass and the cylinders are distributed evenly. Fig. 3 indicates the examples of α_f, δ_f curves changed near by Δ_e.

II. The Mechanism of Fitting Silicone Fluid Dampers to Transmission Shafts

As shown in Fig. 4, a viscous damper of inertia J_d, is fitted on the transmission shaft, its distance from the wheel is l_d. Being calculated as free vibration, on the shaft section from wheel J_f to damper J_d $(z=0,\sim z=z_1=l_d/L)$, the relative amplitudes and moments remain the same as shown in E_q. (1.4), (1.5), i.e.

$$\phi=A\cos(V_z+\xi) \qquad (2.1)$$

$$\delta=D\sin(V_z+\xi) \qquad (2.2)$$

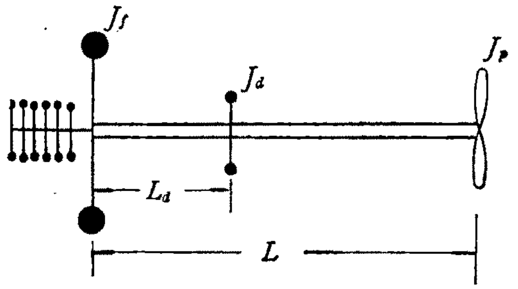

Fig. 4 Schematic diagram showing fitting dampers to transmission shafts

The relative amplitude and moment of the output end at the place, where the damper $(z_1=l_d/L)$ is J_d, are

$$\alpha_d=\phi(z_1)=A\cos(V_{z_1}+\xi) \qquad (2.3)$$

$$\delta_d=\delta(z_1)+\nu_d\Delta\alpha_d=D_d\sin(V_{z_1}+\xi+\theta_d) \qquad (2.4)$$

where

$$D_d=\sqrt{D^2+(\nu_d\Delta A)^2}=D\sqrt{1+\left(\frac{V_d{}^2}{V}\right)^2} \qquad (2.5)$$

$$\theta_d=\mathrm{tg}^{-1}\frac{V_d{}^2}{V} \qquad (2.6)$$

$$V_d^2=\nu_d\Delta E \qquad (2.7)$$

$$\nu_d=J_d/J_s \qquad (2.8)$$

on the shaft section from z_1 to 1, the relative amplitude is

$$\phi=\alpha_d\cos V(z-z_1)-\frac{E\delta_d}{V}\sin V(z-z_1)$$

substituting the relationship of α_d, δ_d into the above equation, then

$$\phi=A\cos(V_{z_1}+\xi)\cos V(z-z_1)-\frac{E}{V}[D\sin(V_{z_1}+\xi)+\nu_d\Delta A\cos(V_{z_1}+\xi)]\sin V(z-z_1)$$

considering $\frac{E}{V}D=A$, $V_d^2=\nu_d\Delta A$ and let $V_z+\xi=\beta$, then

$$\phi=A\cos(V_z+\xi)-\frac{V_d^2}{V}A\cos\beta\cdot\sin[(V_z+\xi)-\beta]$$

$$=A\left[1+\frac{V_d^2}{V}\sin\beta\cdot\cos\beta\right]\cos(V_z+\xi)-\frac{V_d^2}{V}A\cos^2\beta\cdot\sin(V_z+\xi)$$

We obtain at last:

$$\phi=KA\cos(V_z+\xi+\zeta) \tag{2.9}$$

where

$$K=\sqrt{\left(1+\frac{V_d^2}{V}\sin\beta\cos\beta\right)^2+\left(\frac{V_d^2}{V}\cos^2\beta\right)^2}$$

$$=\sqrt{1+\frac{V_d^2}{V}\sin 2\beta+\frac{V_d^4}{V^2}\cos^2\beta} \tag{2.10}$$

$$\zeta=\mathrm{tg}^{-1}\frac{\dfrac{V_d^2}{V}\cos^2\beta}{1+\dfrac{V_d^2}{2V}\sin 2\beta} \tag{2.11}$$

ditto, on the shaft section from z_1 to 1, the moment is

$$\delta=KD\sin(V_z+\xi+\zeta) \tag{2.12}$$

at propeller

$$\alpha_p=\phi(1)=KA\cos(V+\xi+\zeta) \tag{2.13}$$

$$\delta_p=\delta(1)+\nu_p\Delta\alpha_p=D_p\sin(V+\xi+\eta+\zeta) \tag{2.14}$$

where

$$D_p=KD\sqrt{1+\left(\frac{V_p^2}{V}\right)^2} \tag{2.15}$$

$$\eta=\mathrm{tg}^{-1}\frac{V_p^2}{V}$$

$$V_p^2=\nu_p\Delta E$$

ν_p = dimensionless inertia of propeller

Form residuary moment $\delta_p=0$, the frequency equation of shafting is

$$V+\xi+\eta+\zeta=n\pi \quad (n=1,2,3,\ldots) \tag{2.16}$$

Compared with Eq. (1.11) it has one more term ζ, i.e. the effect of damper is considered.

Discussion:

1. Through fitting a damper to the transmission shaft, a point of broken line is made to appear at the damper over the vibration mode of the shaft, a term ζ is added to the frequency equation, so as to render the frequency of the shafting to be lowered.

2. From $\zeta=\mathrm{tg}^{-1}\left[\frac{V_d^2}{V}\cos^2\beta\Big/\left(1+\frac{V_d^2}{2V}\sin 2\beta\right)\right]$, and the relative amplitude of the damper $\alpha_d=A\cos\beta$, one may easily find out that the effect of damper does not only relate with its inertia, but also with its place fitted. When $V_{z_1}+\xi=3\pi/2$, $5\pi/2$ etc. i.e. the damper is fitted where the node is $\cos\beta=0$, thus $\zeta=0$, $\alpha_d=0$, the damper is inoperative. And when $\beta=\pi$, 2π, ..., i.e. the damper is fitted at the peak, $\cos\beta=1$, thus $\zeta=\mathrm{tg}^{-1}\frac{V_d^2}{V}=\theta_d$, $\alpha_d=A$, the damper would be in its maximum operative state.

3. In order to enable the damper to play a sufficient role, we usually demand

$$\alpha_d=\sqrt{\alpha_f^2+\left(\frac{E\delta_f}{V}\right)^2}\cos\beta$$

to be greater or approaching to 1. For this reason, we must consider all-sidely the characteristics of diesel engines and shafting aspects to design and arrange the damper, so as to make the natural frequency Δ_{II} and Δ_{III} all deviating from Δ_e properly, then the value δ_f would be greater, reaching $\alpha_d \geqslant 1$. Thus, a satisfactory damping effect can be obtained.

It is well known that $\xi_e = \pi$ while $\Delta = \Delta_e$. Besides, since inertia of the propeller is greater, and value Δ_e is also greater, usually $\eta_e \to \pi/2$. Thus, if $V_e + \zeta_e = \pi$, $V_e + \xi_e + \eta_e + \zeta_e \to \frac{5\pi}{2}$; so, from Eq. (2.16), the Δ_{II} and Δ_{III} would be arranged symmetrically on both sides of Δ_e, and deviating from Δ_e a proper distance. Therefore, we shall regard $V_e + \zeta_e = \pi$ as primary selective value of the design while fitting silicone fluid dampers to transmission shafts.

For long shaftings, it is preferable that the inertia of dampers must be small to prevent the third mode frequency from approaching Δ_e too, while reducing the second mode frequency. Moreover, it is requested that the inertia should be reduced without sacrificing the friction area, thus it may be considered to make dampers with light mateirals.

For short shaftings, the inertia of dampers may be greater, to make the second mode frequency properly deviating from the diesel engine frequency Δ_e. If it is difficult to increase the inertia of the damper because of the restricted space and so on, we may select couplings with proper flexibility, so as to improve damping effect.

III. Effect of Elastic Coupling

For short shaftings when the relative amplitude at the damper-fitted place on the transmission shaft is smaller, the effect of the damper will be poorer. In this case, the damping effect can be improved through fitting couplings with proper flexibility.

The shafting with eleastic coupling is shown in Fig. 5. In this case, it is only needed to replace the α_f, δ_f in above-mentioned related formulas with the relative amplitude α_c and the moment δ_c of the output end of the coupling. Thus, the frequency equation is

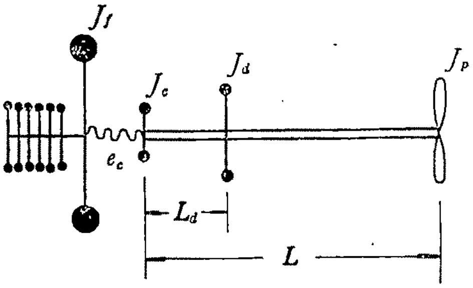

Fig. 5 Shaftings with elastic coupling

$$V + \xi_c + \eta + \zeta = n\pi \qquad (n=1,2,\ldots) \tag{3.1}$$

where

$$\xi_c = \mathrm{tg}^{-1}\left(\frac{E\,\delta_c}{V\alpha_c}\right) = \mathrm{tg}^{-1}\left[\frac{E\,\delta_f}{V(\alpha_f - E_c\delta_f)} + \frac{V_c^2}{V}\right] \tag{3.2}$$

$$\begin{aligned} \alpha_c &= \alpha_f - E_c\delta_f \\ \delta_c &= \delta_f + \nu_c\Delta\alpha_c \\ V_c^2 &= \nu_c E\Delta \end{aligned} \tag{3.3}$$

ν_c=the dimensionless inertia of the passive end of the coupling

E_c=the dimensionless flexibility of the coupling

The amplitude of the damper is

$$\alpha_d = A_c \cos(V_{z_1} + \xi_c) \tag{3.4}$$

where

$$A_c = \sqrt{\alpha_c^2 + \left(\frac{E\delta_c}{V}\right)^2} \tag{3.5}$$

Owing to the above-mentioned results it is obvious that the initial phase ξ_c of the coupling is greater than one ξ of wheel, so the frequency of the shafting will be reduced. Thus, for short shaftings, it will make the second mode freqeuncy Δ_{II} to deviate more from the diesel engine frequency Δ_e, then the relative amplitude at the damper is greater, the damping effect is, therefore, improved. But care must be taken that the third mode frequency must not be reduced too much. Thus, after selecting the damper inertia ν_d and its fitting place z_1 according to practical possibilities through several trial calculations from *Eq.* (3.1), it is possible to select parameters E_c, ν_c of the coupling preliminarily.

IV. The basic principle and procedures of the design

To sum up, the basic principle for designing the silicone fluid damper fitted to transmission shafts is as follows. The resonant frequencies which may take place, must deviate properly from the engine frequency Δ_e, in order to ensure that the relative amplitude on the point of a transmission shaft where a damper is fitted is great enough so that an ideal damping effect is obtained. To this end, we regard

$$\zeta_{c0} = \pi - V_e \tag{4.1}$$

as the primarily selected value of the damper parameter.

For the procedures of the design, preliminary ideas are proposed below:

1. According to parameters of inertia and flexibility of an engine, Δ_e is calculated or found from Fig. 2 (Δ_e is usually known). And the frequency ratio V_e of a transmission shaft is also calculated.

2. From *Eq.* (4.1) and Eq. (2.11), and according to the possible condition of shafting arrangement, the preliminary selection of damper ν_d and its fixed position z_1 are made. For short shaftings, if it is difficult to increase inertia ν_d, the ν_c, z_1 can be, therefore, selected in accordance with practical conditions. Then, the parameters ν_c and E_c of couplings are preliminarily selected through several trial calculations from Eqs. (3.1) and (3.4).

3. Δ_{II}, Δ_{III} the corresponding α_{dII}, α_{dIII} are evaluated for the free vibration calculation by Holzer method, with which a shafting is divided into sections. According to the above–

mentioned values necessary adjustment to ν_d, z_1 and ν_c, E_c are made.

4. The design of the damper drawing is made and its damping coefficient is calculated.
5. Calculation of forced vibration is made with the values of stress and amplitude near every resonant vibration range, ν_d, z_1, ν_c, E_c and the damping coefficient of the damper are finally adjusted and determined, and the drawings are revised accordingly.

V. Examples

Example 1, a passenger ship on the Changjiang River. Its shafting is shown in Fig. 6. The propulsion engine is 8350GZC diesel engine, rated speed is 350 rpm, rated horsepower is 1600 hp. Intertia per engine cylinder J_s=220 kg cm sec^2, flexibility of crankshaft element $e_s=2.735\cdot10^{-9}$kg^{-1}cm^{-1}. The dimensionless parameters of the shafting are

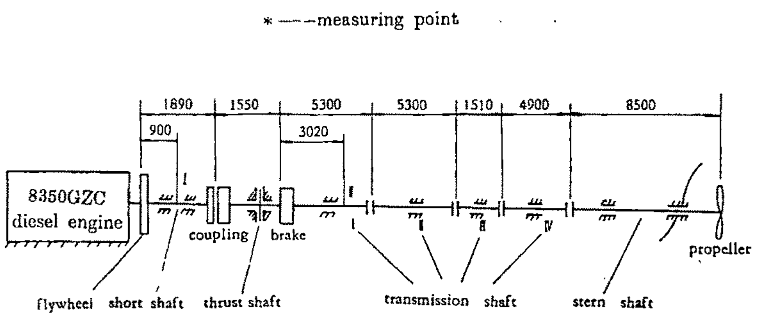

Fig. 6 Diagram of shafting arrangement for a passenger ship

$$\nu_1=\nu_2=\nu_8=1,\quad \nu_9=24.5832,\quad \nu_{10}=6.3932$$

$$E_{12}=E_{23}=\cdots=E_{78}=1,\quad E_{89}=1.3231,\quad E_{9,10}=85.2254=E$$

the length of the trasmission shaft L=32 m, from Eq. (1.1) $\sqrt{\nu E}=12.80924$.

Through tests and calculations it was shown that a torsional resonance of the second mode of the eighth order arised when at about 294 rpm, and the additional stress of the torsional vibration was over 440 kg/cm^2 for the shafting. A torsional resonance of the third mode of the eighth order arised when at about 334.5 rpm. The two resonant ranges were close to each other and within the operational speeds, so it is necessary to take measures to solve the problem.

Owing the fact that the main engine on the ship had no damper and the damping effect could hardly be performed through conventional methods either. In this case we took the measure of fitting a damper to the transmission shaft.

We read $\Delta_e=0.04$ from Fig. 2, so $V_e=\sqrt{\nu E\Delta}=2.561848$, and therefore $\zeta_{oe}=\pi-V_e$ $=0.5797446$ was preliminarily selected.

According to the possibility of the practical ship, and rendering the decreasing of the third mode smaller, for the damper-fitted place, we took z_1=0.155085, V_{z_1}=0.3973041. Substituting the values of ζ_{oe}, V_{z_1} into Eq. (2.11) yielded V_{do}^2=2.704, ν_{do}=0.8.

When designing the damper, we took J_d=268.57 kg cm sec^2, ν_d=1.22, which was greater than that we selected preliminarily. In view of the objective conditions and our lack of experiences at that time, we did not revise J_d further. Also the damping coefficient of the damper is $C=9596$ kg cm sec^2.

We distributed the mass of the transmission shaft according to the sections already divided by the flanges, and calculated the torsional vibration of the shafting taken as discrete system. The results were: the second mode frequency $f^{II}=2148$ cpm; the eighth order critical speed is 268.5 rpm; the additional torsional stress on the crankshaft is $\tau_8^{II}=20.18$ kg/cm^2.

The third mode frequency $f^{III}=2535$ cpm; the eighth order critical speed is 316.8 rpm; additional torsional stress is $\tau_8^{III}=138.46$ kg/cm^2.

The above-said damper worked most effectively for the second mode vibration, and also satisfactory for the third mode vibration. But if a smaller value had been taken further for ν_d of the damper, so it could approach the preliminarily selected one, more rational results would have been obtained. The means of fitting the silicone fluid damper to the transmission shaft is proved to be effective through ship trials and marine practices ever since 1977. We have thereby attained the purpose expected. Figure 7 shows the comparison between the measuring results obtained before and after fitting the damper to the transmission shaft.

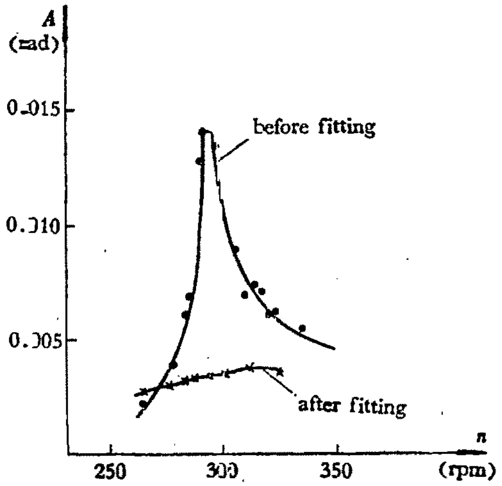

Fig. 7 Comparison between the measuring results obtained before and after fitting the damper to transmission shaft in example 1

Example 2, a push boat on the Changjiang River, its shafting as shown in Fig. 8. Its

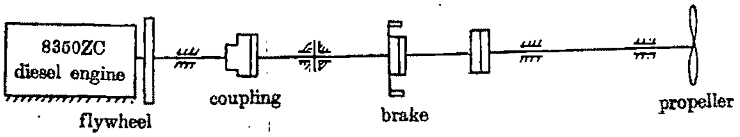

Fig. 8 Diagram of the shafting of a pusher

propulsion engine is 8350ZC diesel engine; rated speed is 350 rpm; rated horsepower is 1200 hp Inertia per engine cylinder $J_s=210$ kg cm sec^2, flexibility of crankshaft element $e_s=2.9\cdot 10^{-9}$ kg^{-1} cm^{-1}. The dimensionless parameters of the shafting are

$$\nu_1=\nu_2=\cdots=\nu_8=1,\quad \nu_9=26.9,\quad \nu_{10}=9.7857$$

$$E_{12}=E_{23}=\cdots=E_{78}=1,\quad E_{89}=1.3\quad E_{9,10}=E=35.1338$$

The total length of the transmission shaft $L=15$ m. From Eq. (1.1), $\sqrt{\nu E}=5.9682$.

Through tests and calculations it was shown that the torsional resonance of the second mode of the eighth order arised when at about 302 rpm, the additional stress on torsional vibration reached 632 kg/cm^2, causing frequent breakage to the pump gears at the free end of the engine and some other problems. So the forbidden range of rate speed, from 290~310 rpm was set, thus resulting in hindering the transporting ability of the vessel from being brought into full play.

We adopted the damping method of fitting silicone fluid dampers to transmission shafts, in order to tap the potential shipping ability of the vessel.

We read $\Delta_e=0.04$ from Fig. 2, so $V_e=\sqrt{\nu E\Delta_e}=1.19364$, and selected preliminarily $\zeta_{oe}=\pi\cdot V_e=1.9479526$. Due to the possibilities on board ship, we could only take $J_d=321.3088$kg cm sec^2, $z=0.33907$, tg $\zeta_e=0.92133127$, thus yielded $\zeta_e=0.7450102$, which was much smaller than the preliminarily selected value. For this reason it was necessary to select a proper flexibility for the coupling to increase the damping effect.

Dividing the mass of the transmission shaft according to the sections already divided by the flanges, we obtained, through calculation, the effective damping coefficient of the damper $C_d \simeq 47500$kg cm sec. Using iterative solving process[4], for the shafting with coupling flexibility $e_c=15.5\cdot 10^{-9}$, $19\cdot 10^{-9}$, $22\cdot 10^{-9}$, $24\cdot 10^{-9}$, $25.8\cdot 10^{-9}$ kg^{-1} cm^{-1}, forced vibration calculation was made respectively. The results shown in Fig. 9 indicated that the damping effect was better while $e_c=24\cdot 10^{-9}$kg^{-1} cm^{-1}.

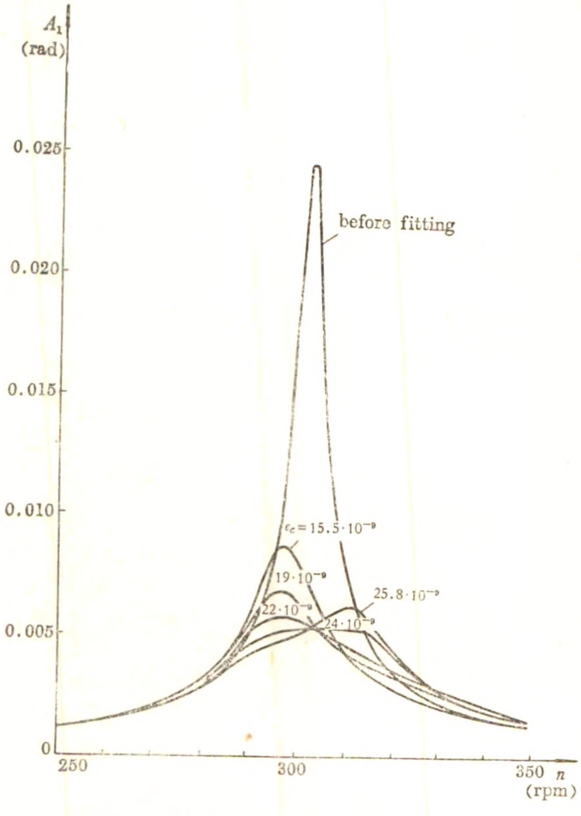

Fig. 9 Calculated amplitude for first mass point

In view of the above, we adjusted the hardness of the original rubber ring from Shore 70 into 55, i.e. adjusting e_c from $15.5\cdot 10^{-9}$ into $24\cdot 10^{-9}$ kg^{-1} cm^{-1}. The case of fitting the damper on the push boat is shown in Fig. 10 (a), (b).

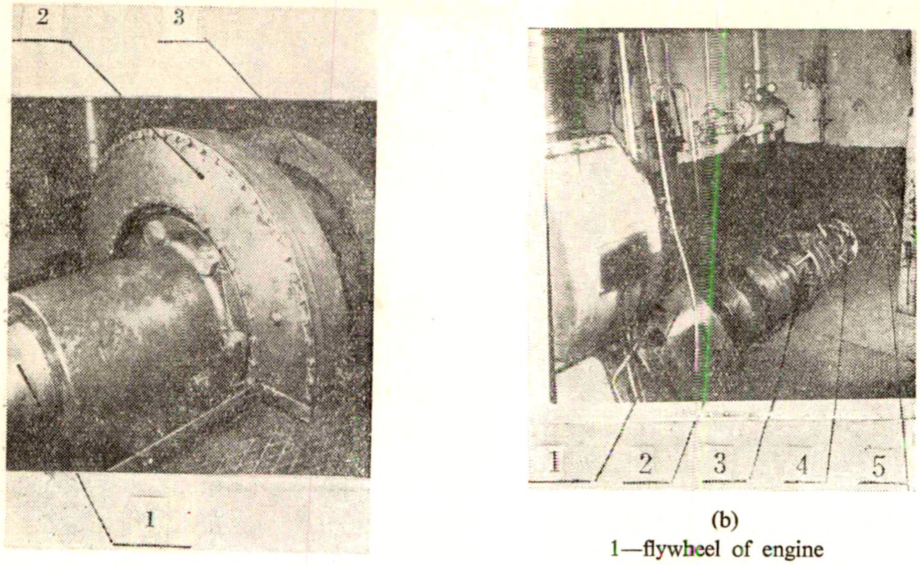

(a)

1—stern shaft
2—damper
3—brake

(b)

1—flywheel of engine
2—elastic coupling
3—axial bearing
4—brake
5—damper

Fig. 10 Pictures showing fitting dampers to transmission shafts

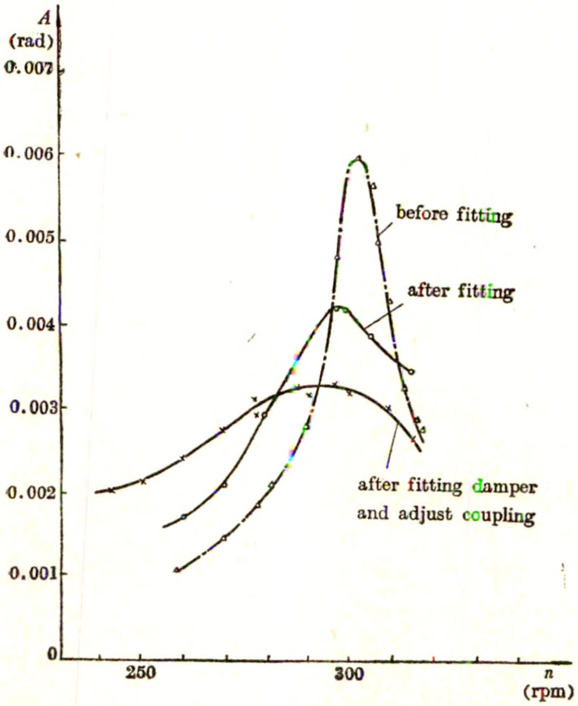

Fig. 11 Amplitude at measuring point in different cases

The comparison of the amplitudes of vibration at measuring points in different cases for ship trials are shown in Fig. 11. Finally the additional stress of the torsional vibration on the crankshaft was reduced to about 115 kg/cm^2, which indicates that the effect is good. With the forbidden range of speed removed, no breakage of the pump gears at the free end of the engine was seen during the long-period marine practices, the ship vibration was improved. When increasing the speed from 287 rpm to 305 rpm each engine generated 132 hp additionally. Also the speed of the ship was accordingly increased. Satisfactory results have been obtained.

References

[1] 越智重信: 軸係質量かわベり振動特性に及ぼす影響, «日立造船技報», Vol. 23, No. 4, 1962.

[2] Shanghai Office of Register of Shipping, Shanghai Shipping Science Research Institute: *The effect of inertia of shaftings to the characteristics of torsional vibration*, **The Material of Science and Technology of the Ship**, No. 5, pp.7–29, 1975.

[3] J. P. Den Hartog: Mechanical Vibrations, McGraw–Hill Book Co. New York, 1956.

[4] Nie Deyao: *Several Problems of Calculation & Damping in Torsional Vibration*, **Changjiang Shipping Science & Technology**, No. 31, pp.1–28, 1979.

Annual of the CSNAME, Vol. 1, 1982

EXPERIMENTAL INVESTIGATION ON CYLINDER HEAD OF E390V MARINE DIESEL ENGINE

JIANG RONGPEI (蒋荣培), ZHANG XIAOLING (张晓泠), LI CHANGHAN (李昌汉)

Shanghai Hudong Shipyard

LI FUXING (李福兴) AND WU JINYUAN (吴金源)

Shanghai Marine Diesel Engine Research Institute

SUMMARY

The thermal-loaded components of an engine are usually subjected to thermal load and mechanical load as well. For the cylinder head and exhaust valve, the key to successful designing lies in the sufficient rigidity of cylinder head, rational cooling of combustion plate and valve seat, better thermal conditions of valve and suitable materials.

The writers have worked out a plan of experimental investigation for some existing problems of early cylinder head and exhaust valve of E390V diesel engine, and described the designing concept of the cylinder head and exhaust valve of medium speed, large power diesel engine through the experimental investigation on thermal-loaded component wall temperature and stress measurement, static pressure measurement of cylinder cover sealing band, model test of cooling water passage, blowing test of exhaust duct static pressure, 3-dimensional isoparametric finite element calculation, analysis of suitable materials and endurance test for 600 hrs, etc.

I. Structural Characteristics of Early Cylinder Head and Exhaust Valve

E390V model engine is a two-stroke, purely exhaust-turbocharged with uniflow scavenging, and highly intensified marine diesel engine. It has a cylinder bore of 390 mm and a piston stroke of 470 mm, and develops 667 hp per cylinder at a speed of 480 rpm with a corresponding BMEP of 11.14 kg/cm^2.

The early design of the cylinder head adopted a combined cast and weld construction, i.e., the top deck was cast with molybdenum steel and the cylinder head was welded up with the top deck, exhaust ducts and bottom deck made of boiler steel. The four exhaust valves were made of heat-resisting steel. Without any seperate valve seats, the sealing cone of each valve was armoured with cobalt-based steel by pad welding. The fuel injector was fitted in the centre of the cylinder head. The cylinder head was secured with eight M42×2 studs and

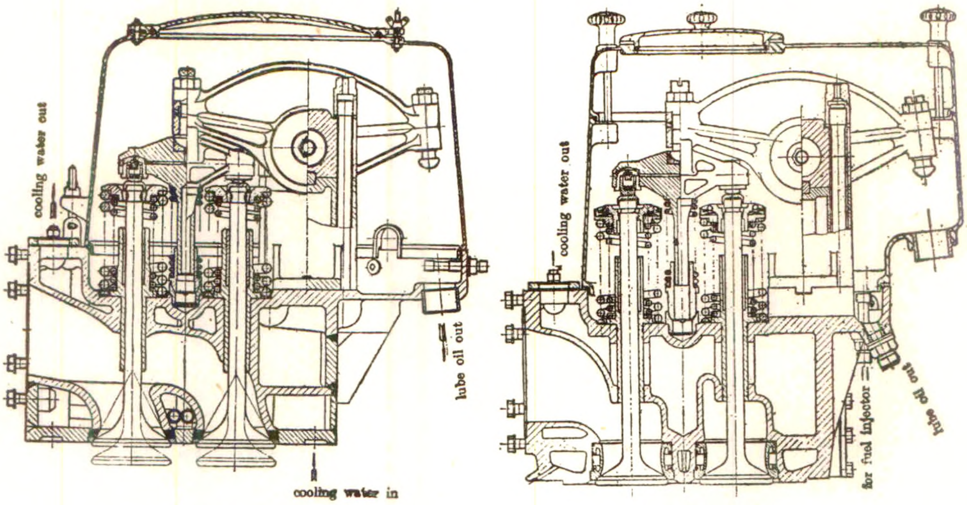

Early design Modified design

Fig. 1 Cylinder head cross sections

cooling water was admitted into it via cylinder liner collar. Copper gasket was used between the cylinder head and the cylinder liner to avoid gas leakage. Fig. 1 shows the cross section of the cylinder head.

II. Analysis of Main Problems of Early Cylinder Head and Exhaust Valve

After 2000 hours' running of E390V engine on board ship such problems were found as deformed cylinder head bottom plate, fractured exhaust duct, faulty sealing between cylinder head and cylinder liner, corroded water passage bottom (Fig. 2), burnt-through exhaust valve, cracked valve face and pitted sealing band (Fig. 3). It can be seen from the figures that the valve cracks originated from the surface of the pad welding and the propagation of the cracks

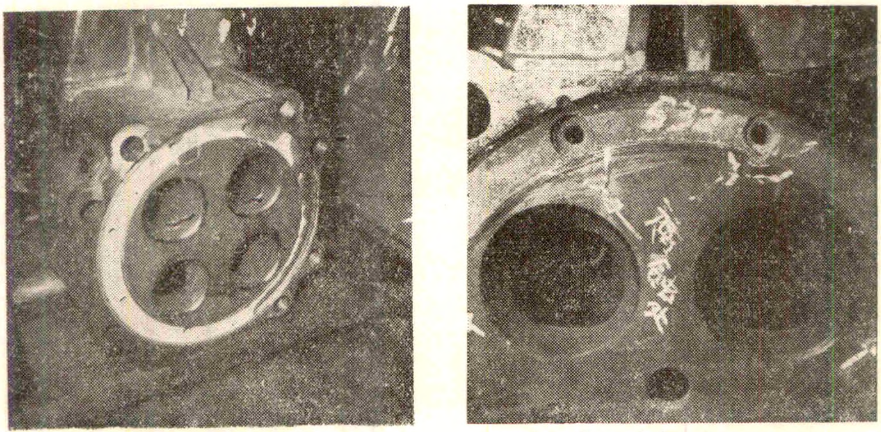

a. Fractured exhaust duct b. Corroded water passage

Fig. 2 Damages of early cylinder head

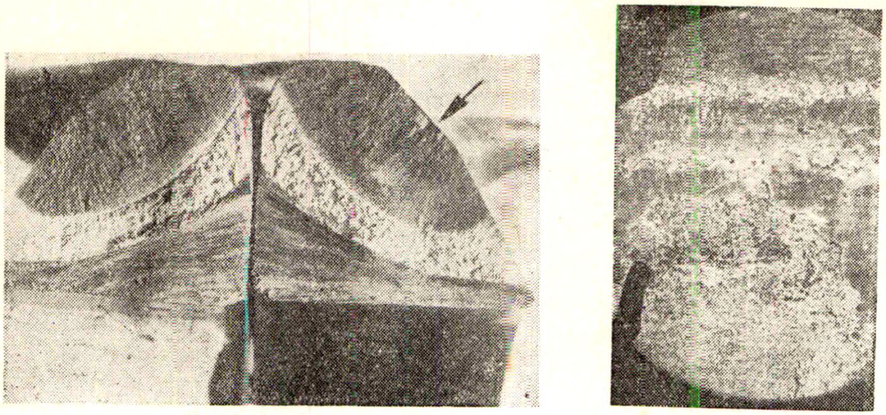

a. Cracked valve cone

b. Pitted sealing band

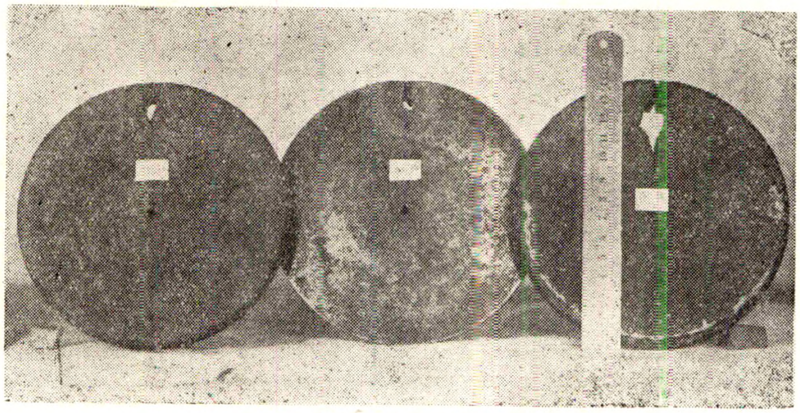

c. **Burnt-through valves**

Fig. 3 Damages of early exhaust valve

resulted in the burning-through of the exhaust valve. An example of some cracks passing through pits is shown in Fig. 4. It is evident on the fractured surface that the position of the crack coincides with that of the pit.

The causes were partly that the engine was highly intensified with its cylinder head being long exposed to cyclic impacts of 105 kg/cm² combustion pressure and over 420°C exhaust temperature. On the part of the cylinder head, insufficient local stiffness, inadequate cooling and uneven temperature distribution (of both the cylinder head and the exhaust valve) had also contributed to the above-mentioned failures. That was why investigations and various improvement were made on the cylinder head and exhaust valve of the engine.

The deformation of combustion plate was due to the structure of cylinder head as well as the thermal load acting on it. As the early cylinder head was originally not rigid enough, the combustion plate became distorted after mounting, causing the ground valve seats to be out of roundness. To prove it, a real cylinder head and cylinder liner assembly

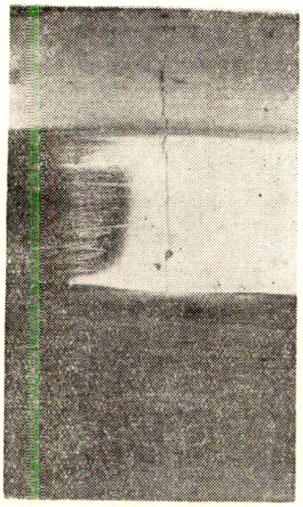

Fig. 4 Crack passing through pit

had been tested on a hydraulic rig to check the static contact pressure over the sealing band between the cylinder head and the gasket. It was shown that there existed a much uneven distribution of the peripheral contact pressure, the ratio between the maximum and the minimum values being 3.92 (Fig. 5). The weakest areas between the sealing band and the exhaust ports and between the sealing band and the push rod bore sides, because the pressure of the exhaust ports reduced the local rigidity and the ratio of the height of the cylinder head on the push rod bore side to the cylinder bore was only 0.72. The maximum pressure on the sealing band was found near the starting valve bore. The reason was that the bore wall of this valve served as a stiffener of this part of the cylinder head. This shows the necessity of stiffeners for increasing rigidity and diminishing deformation of the combustion plate.

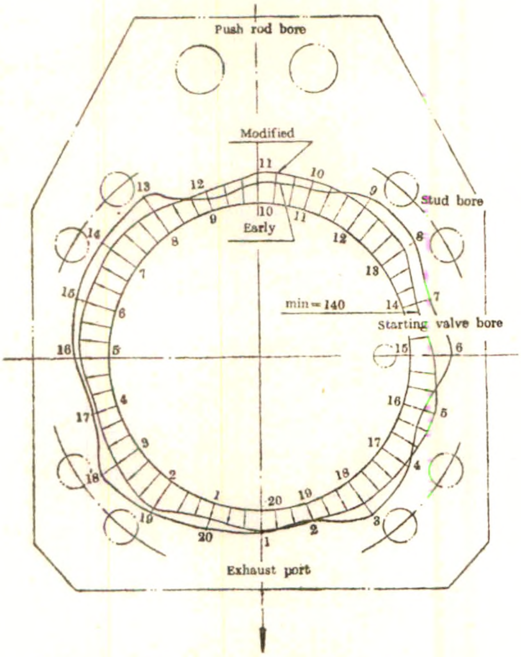

Fig. 5 Contact pressure distribution over cylinder head sealing band

Besides, the intermediate plate, outer walls and top deck were too thin. And by using the octagonal-shaped cylinder head, the maximum and the minimum distances between outer walls and the sealing band mean diameter were 90mm and 60mm respectively. As a result, when being mounted, the combustion plate got buckled under a large bending moment.

The thermal deformation of the cylinder head was caused by uneven cooling because of the improper layout of the water passages. As soon as thermal deformation occured, the sealing of the exhaust valves and the cylinder head became faulty leading to gas blow-by. On entering the water passages, the gas tended to bring about cavitation erosion of the water passages. The increased thermal stress was also one of the factors in developing exhaust duct fracture. Photographs showing water flow path were taken during the test (Fig. 6). It can be readily seen that there existed eddies between two rows of the exhaust valves and between the exhaust valves and the fuel injector, and moreover, there were dead water zones in the two water passages.

As regards the exhaust valve, Fig. 7 indicates that the cracks generally propagated along crystal boundary in the pad welding, while in the base metal, the crack almost went through the dendrite crystal. It was found under the scanning electron microscope that in the pad welding there were corroded grooves ranging inwardly from the surface in the same direction of the cracks. The grooves were covered with large amount of corrosion product, of which it was found, by means of Auger election spectroscope, containing sulphur, calcium and silicon, etc.

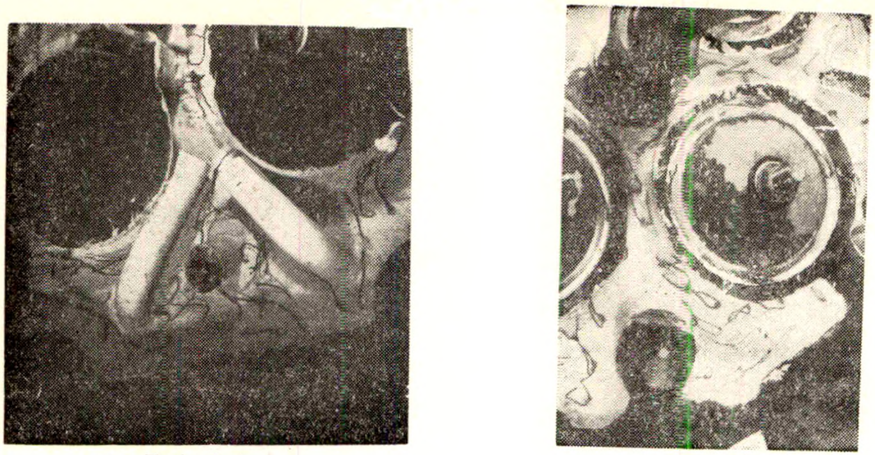

a. Early design b. Modified design

Fig. 6 Water passage test results

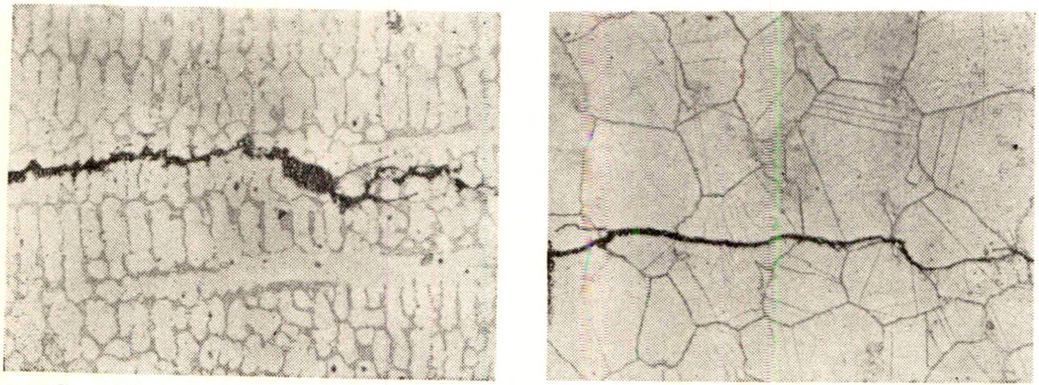

a. Crack along crystal boundary in pad welding b. Crack through crystal of base metal

Fig. 7 Cracks on exhaust valve

Moreover, on the exhaust valves deposited some dark grey combustion product. According to the result of X–ray analysis, its major constituents were calcium sulphate and barium sulphate. It was concluded that the deposit will result from the decomposition of lubricating oil additives.

Possible factors involved in the occurrence of exhaust valve cracks were: (1) local blow–by at valve cone due to the grave distortion of the valve and the valve seat; (2) pits over valve cone becoming a fatigue source; (3) failure of the sealing band of the valve due to the cumulated pits; (4) inadquate design strength or technological problems.

Thermocouples were employed to determine the thermal load on the exhaust valve (Fig. 8). The highest temperature measured was up to 802°C and the circumferential temperature difference was 169°C (at point 4), which proved the extremely high thermal load on the exhaust valve. On the other hand, there was a big difference between the linear expansion coefficient of the valve base metal and that of the hard pad welding on the valve cone. All this resulted in excessive thermal stress of the valve, which was considered one of the main factors in developing cracks, and the pitting might be another. Investigation[1] showed that on the exhaust valve face, due to local overheating, some salts within the corrosive combustion product deposited were melted. This molten matter etched all the way along crystal boundary and carbonide-metal interface deep into the metal, resulting in internal eroded cavities.

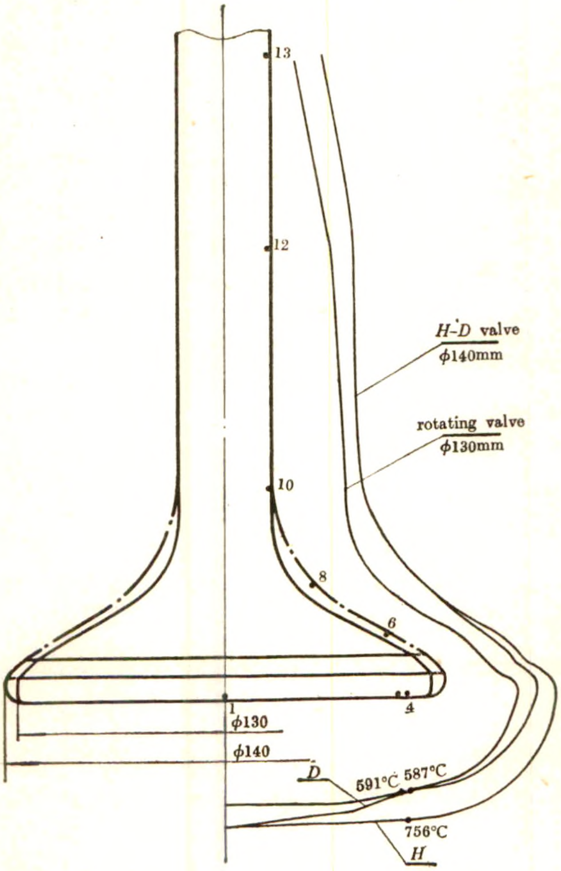

Fig. 8 Temperature curves of exhaust valve surface

It was discovered that before macro-cracks finally came into being under stress, either micro-cracks were formed along crystal boundary and crystalline grains collapsed leading to the erosion of the metal in the vicinity or alternatively, microetch pits happened to cover an area.

III. Modification of Cylinder Head and Exhaust Valve

It can be concluded through the above investigations that deformation and high temperature are the two main reasons for the failures of the early cylinder head and exhaust valve, and behind them are poor rigidity and inadequate cooling. Therefore, design modifications were carried out on these two components.

3.1. Improvement on structural characteristics of cylinder head and exhaust valve

Cast with high strength nodular cast iron, the modified cylinder head keeps the double bottom design but with thinner bottom deck and thicker intermediate plate. To cater for the fitting of flexible and water–cooled valve seats on the cylinder head, which are made of heat–resisting steel, exhaust valve deck diameter has been reduced from 140mm to 130mm. On the top of the valve outer spring is fitted a spring–loaded saucer type valve rotator (Fig. 1).

3.2 Details of modification

3.2.1. Increase rigidity

Monoblock casting is used for the cylinder head instead of a cast and welded construction. The thickness of the top deck, outer walls and intermediate plate is considerally increased. Of the outer walls, the former octagonal shape has been replaced by an upside–down conical shape. Furthermore, the mean diameter of the sealing face between the cylinder head and the water jacket has been shifted 39 mm outwardly, thus effectively diminishing the deformation of the combustion plate. The ratio of the height of the cylinder head on the side of the rocker arms to the cylinder bore is now 0.87 (against the former 0.72) with the result of stiffening the area near the rocker arms. The combustion plate is wedge–shaped, with the minimum and maximum thickness of 15 mm and 20 mm respectively. The combustion plate and the intermediate plate are connected by stiffening ribs.

The former thin cylinder head gasket made of T4 steel is now replaced with a thicker one of No. 20 steel coated with copper. The new gasket is more flexible and offers a better sealing property.

The modified cylinder head has also undergone a static contact pressure test. The result shows that a much better pressure distribution over the sealing band has been achieved. The ratio between the maximum and the minimum pressures is about 2.58. Static oil seepage test has been carried out on the modified design and exhaust valve arrangement to be fitted on a 6E390V test engine.

No oil seepage was found on the new design, whereas three oil droplets seeped out per minute on the early cylinder head. This proves the increased static rigidity of the modified cylinder head.

3.2.2. Intensify cooling

To solve the problems encountered on the early exhaust valve, measures have been taken to improve the design for a better cooling effect and more uniform temperature distribution. Water–cooling valve seat is used to intensively cool the exhaust valve. The new valve seat of flexible thin–wall type is so embedded in the cylinder head without interference that no additional stress is produced when the engine is running hot. Around the seat cooling chamber are arranged three heat–resistant and oil proof seal rings for both gas and water. The valve guide sleeve fitted on the modified cylinder head is also rationally cooled, yielding a better cooling of the valve rod.

Each valve rotator includes seven groups of steel balls loaded with springs. When the exhaust valve opens, it is made to rotate by thin rotator at a rate of 3 to 10 rpm. The exhaust valve is in this way evenly heated in operation.

Thanks to these measures, the thermal load on the modified valve has been markedly brought down. Thermocouples and a slip ring assembly are used for the measurement of the temperature of the exhaust valves. For measured temperature fluctuation curves, see Fig. 9.

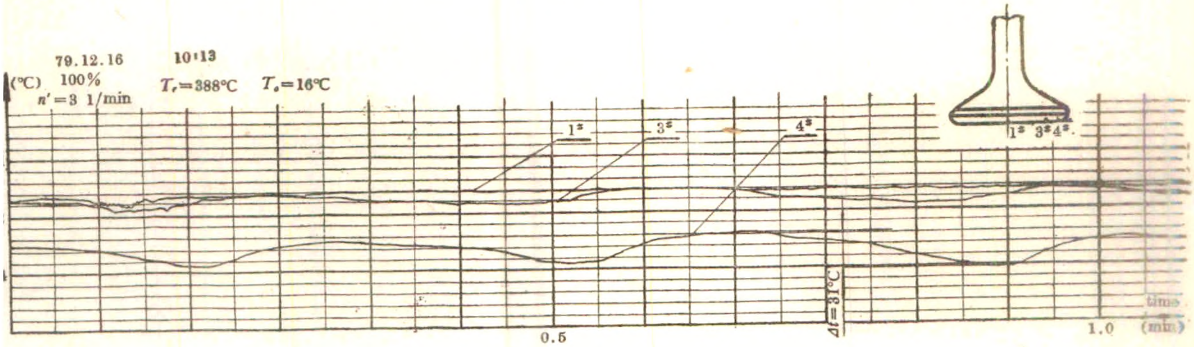

for valve ϕ130mm

Fig. 9 Temperature fluctuation curves of exhaust valve

After improving, a drop of 136°C can be seen in the maximum temperature on the new exhaust valve with a temperature variation of only 30°C (Fig. 9).

Finite-element analysis has been conducted to further investigate the temperature field and stress values of both old and new cylinder heads and exhaust valves. Considering the asymmetry of the thermal load and the required high accuracy of the results, a 3-dimensional twenty-node isoparametric cylindrical coordinates computer programme was used for the analysis. Fig. 10 shows the isothermal maps of both valves calculated with 3-dimensional method.

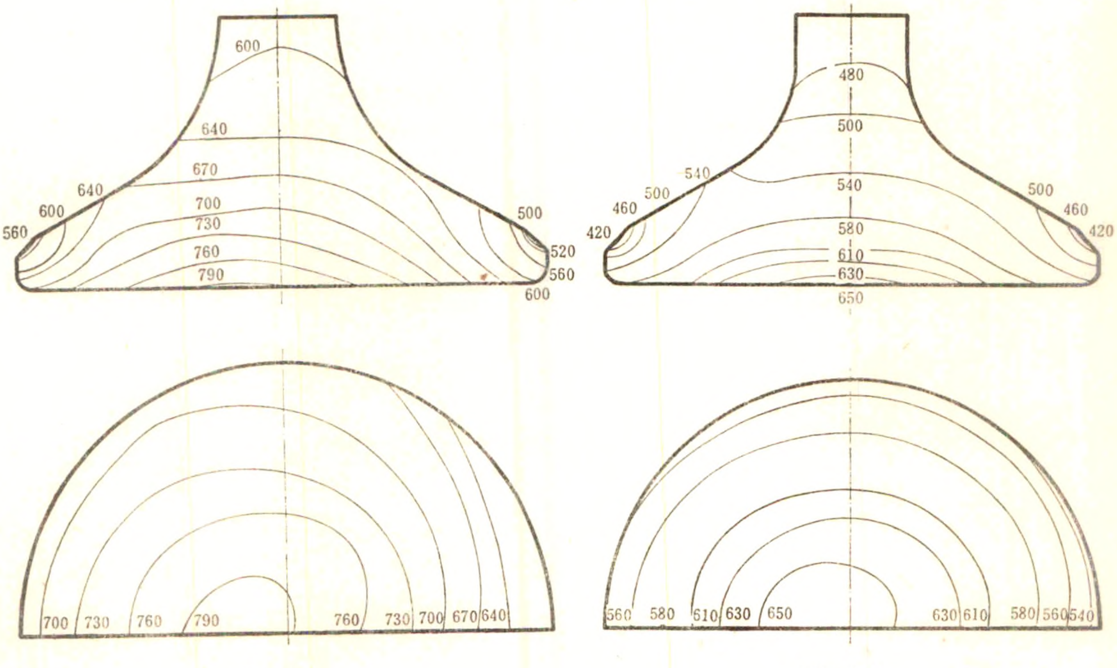

valve ϕ140

valve ϕ130

Fig. 10 Isothermal maps of both valves calculated with 3-dimensional method

Because of the improved thermal conditions, the thermal stress and the synthesis stress on the valve face are now ten percent lower than before.

In improving the cooling of the cylinder head, efforts were made mainly to modify the layout of the water passages. Fig. 11 shows the water passages connecting the cylinder liner and the cylinder head. It turned out after the flow test that the modified passage is more smooth without any dead water zones and eddies which appeared in the original design shown in Fig. 6. It is also shown through high speed photographic analysis that water flows much more quickly between two rows of the exhaust valves and between the exhaust valves and the fuel injector.

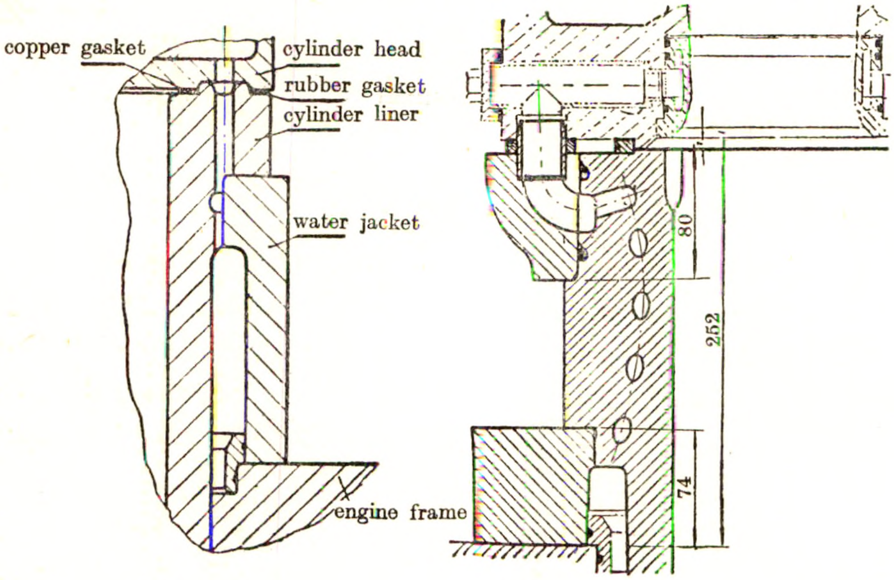

Early design Modified design

Fig. 11 Water passage between cylinder liner and cylinder head

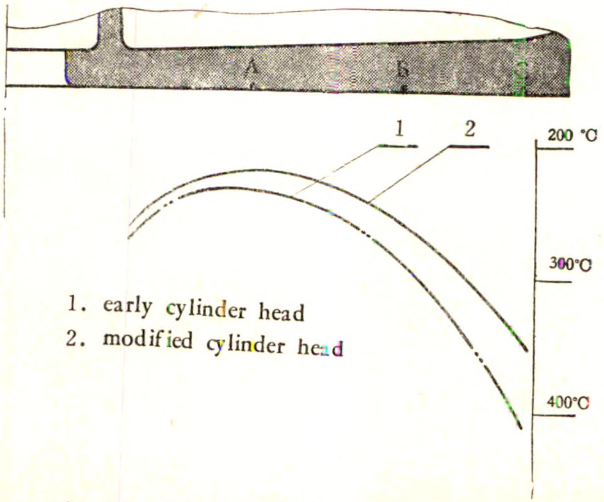

Fig. 12 Measured temperature curves of combustion plates of both cylinder heads

The measured and calculated temperatures on the combustion plate surfaces of both old and new cylinder heads are presented in Fig. 12 and Fig. 13 respectively.

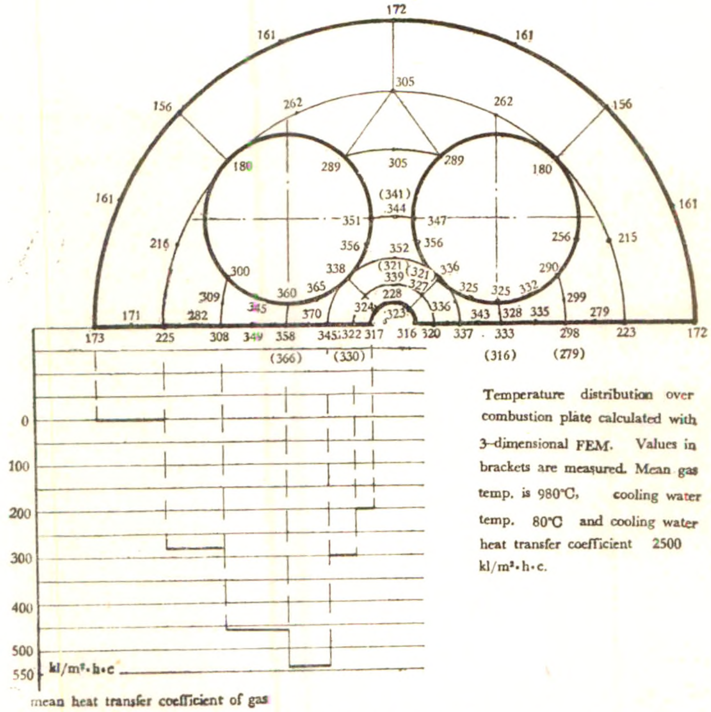

Temperature distribution over combustion plate calculated with 3-dimensional FEM. Values in brackets are measured. Mean gas temp. is 980°C, cooling water temp. 80°C and cooling water heat transfer coefficient 2500 kl/m²·h·c.

Fig. 13 Node temperatures calculated with 3-dimensional method and boundary conditions of combustion plate

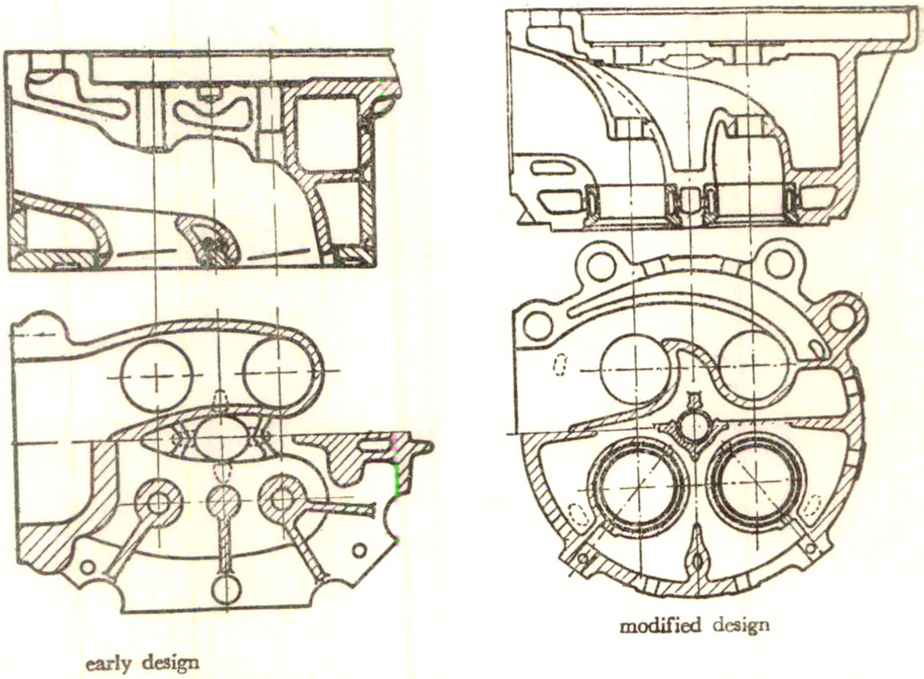

Early design Modified design

Fig. 14 Exhaust duct profiles of both cylinder heads

The newly designed exhaust duct with the reduced diameter of the valve disc is proved by the static pressure port blowing test to be up to the expected standard (Fig. 14 and Fig. 15). Although the throat cross section of the new exhaust valve is 6.8% smaller as compared with the old version, nevertheless, the flow is 15.7% higher and the flow characteristics are 13.5% better. The two valve rods near the exhaust port were shown to be kept from being flushed for the second time during each cycle of the engine. Real engine tests also showed that the new cylinder head with improved exhaust ducts is conducive to the engine performance.

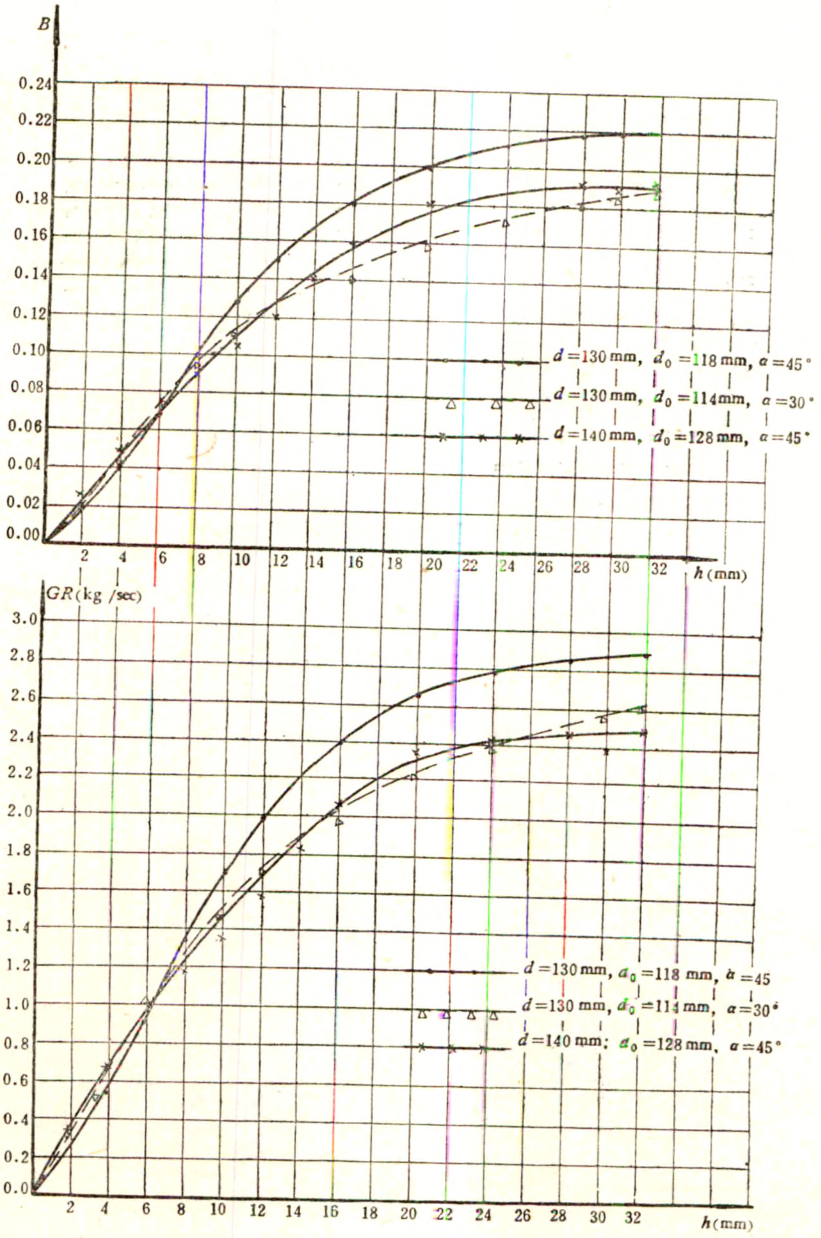

Fig. 15 Characteristics curves of both cylinder heads obtained in static pressure blowing test

3.2.3 Choose suitable material

The inherent complexity of the cylinder head requires cast iron or cast steel. On large low speed diesel engines, forged steel cylinder head of shaker cooling is becoming popular. Of late, there have been an increasing number of engine manufacturers using cylinder heads of nodular cast iron. Therefore, a series of investigations and tests were made to seek the possibility of choosing high strength nodular cast iron for cylinder heads.

Thermal intensity is normally adopted to characteristically evaluate the materials for thermal-loaded components.

$$\text{Thermal intensity} \propto \frac{\lambda \cdot \sigma}{\alpha \cdot E}$$

where λ=thermal conductivity

σ=high temperature strength

α=linear expansion coefficient

E=elastic modulus

It can be seen from Fig. 16 that the thermal intensity of high strength nodular cast iron is much higher than that of the other two materials for cylinder head. The material for exhaust valve has to have a good corrosion-resistance under high temperature, higher hot strength, better thermal conductivity and higher temperature hardness, and smaller linear expansion coefficient. Normally martensitic steel, austenitic steel or high temperature alloy can be used for this purpose.

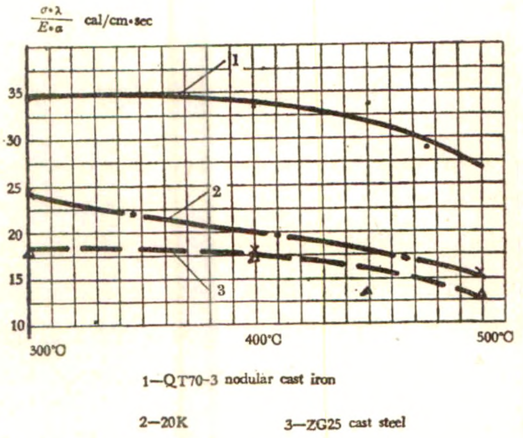

Fig. 16 Thermal intensity of various materials

Martensitic steel is rarely used for making exhaust valves subjected to higher thermal load. Austenitic steel has a higher hot strength, but a greater linear expansion coefficient, which can lead to large tangential stress of the valve, and has a poorer thermal conductivity, which will result in higher temperature of the valve. The high temperature alloy has ideal hot strength, high temperature hardness and linear expansion coefficient, it has also the ability to withstand corrosion under high temperature, except for its low thermal conductivity and higher cost.

The exhaust valve of the early design bore very high thermal load. If the valve had been made of the heat-resisting alloy (Nimonic 80A), which is hard and corrosion-resistant under high temperature, the valve cone would not have had to be treated with pad welding. This solution may be applied to the modified exhaust valve. But the fact is that satisfactory sealing and better cooling of the cylinder head and the exhaust valve have been achieved after modification. So the material used now will not be changed.

Fig. 17 shows the comparison between three valve materials based on the thermal intensity[2]. It is found that martensitic steel has a higher value below 500°C. The conditions for the exhaust valve tend to improve with the development of the engine performances. Consequently, it may be possible for the martensitic steel exhaust valve to be used on E390V engine burning diesel oil.

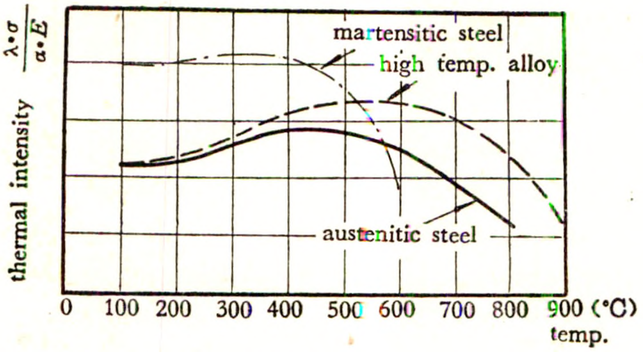

Fig. 17 Thermal intensity of various materials for exhaust valve

IV. Acceptance Test

Comparative test for acceptance was conducted on a 6V test engine for the early and the modified cylinder head arrangements according to the endurance test procedure shown in Fig. 18. During the whole test period of 600 hrs and more the exhaust gas temperature and the peak pressure were kept in excess of the rated values. Surface examination and flaw detection were made both before and after the test. The results showed that the previous problems were eliminated on the modified cylinder head and exhaust valve; whereas on the early designs the com-

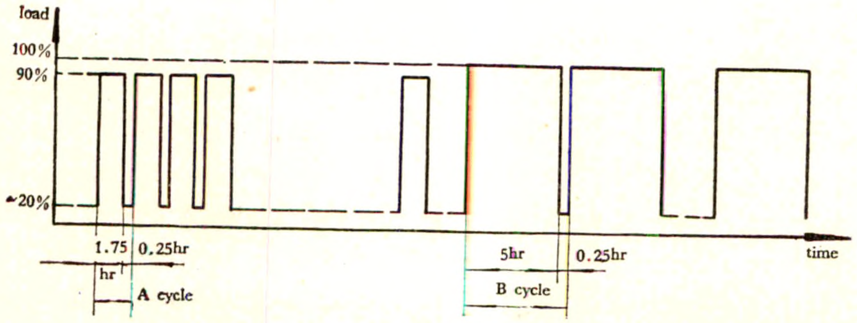

Fig. 18 Endurance test procedure

bustion plate became severely distorted after test (Fig. 19) and sealing band failure, corrosion, valve fracture were found on 25% of the early cylinder heads and exhaust valves under test (Fig. 20).

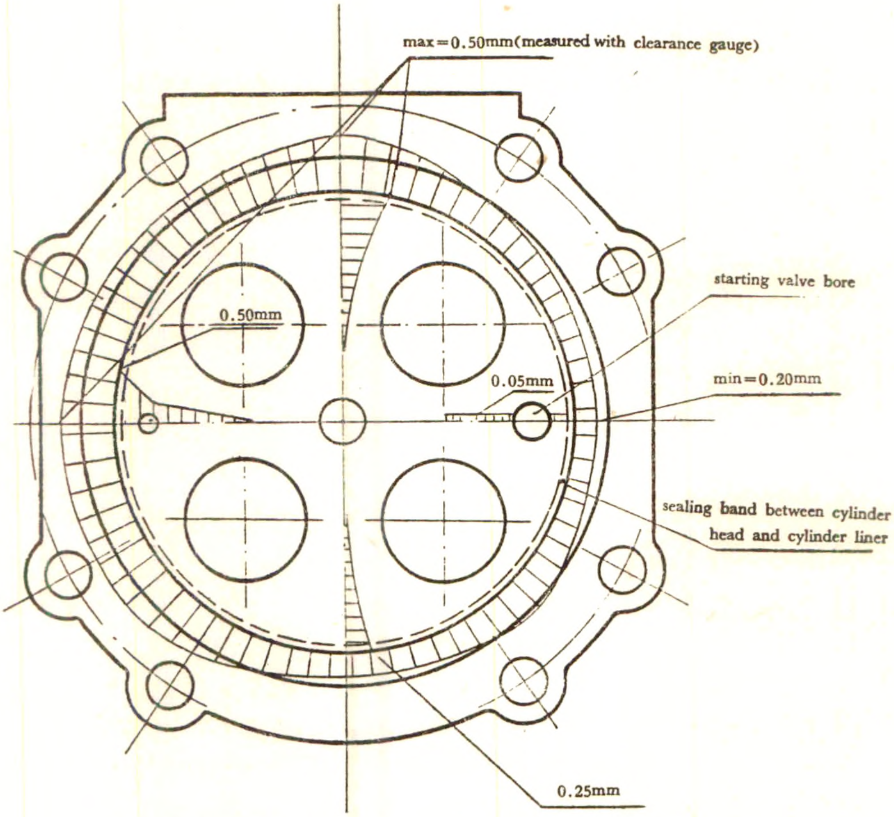
max=0.50mm(measured with clearance gauge)
starting valve bore
0.50mm
0.05mm
min=0.20mm
sealing band between cylinder head and cylinder liner
0.25mm

Fig. 19 Deformation of combustion plate of early cylinder head

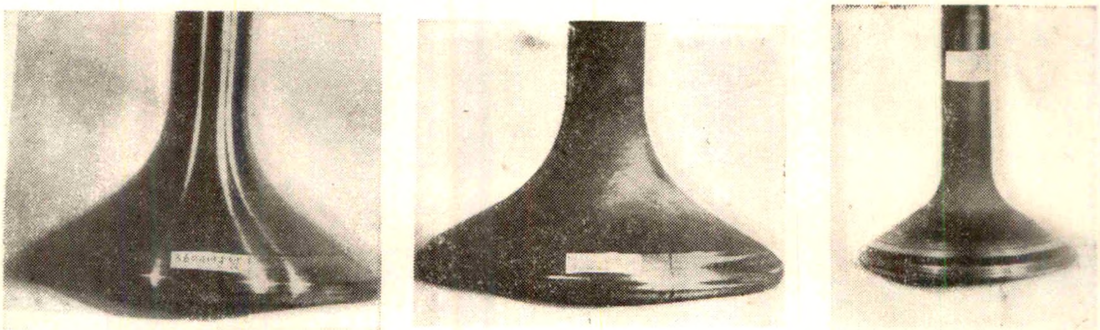

Cracks found on valve ϕ 140 mm after 360 hours

Cracks found on valve ϕ 140 mm after 540 hours

No cracks found on valve ϕ 130 mm after 600 hours

Fig. 20 600-hours test results

It was also shown that thanks to the modification of the water passages (Fig. 11) corrosion of cylinder head sealing band no longer existed.

V. Conclusion

1. With the continuous uprating of diesel engines, component test should be performed from time to time. Only by using electronic computer and other modern techniques can the development time be shortened and the quality of the components improved.

2. Compromise has to be sought between the strength, the rigidity and the cooling of the cylinder head and of the exhaust valve. Special attention has to be paid to the reduction of the thermal load.

3. The exhaust valve face pitting is a complex problem involving the effect of stress and high temperature corrosion. It cannot be effectively solved just by reducing the wall temperature and using water droplet seperator after the intercooler. The corrosion–resistant and wear–resistant coating on the valve cone may be a cure.

Acknowledgment

Our thanks go to Mr. Luo Xingbo, Mr. Xu Zhongliang, Mr. Qiang Qiaosong and Mr. Han Jinhong for their assistance in the whole work.

References

[1] *Investigation into the Thermal Corrosion of the I. C. Engine Valve Steel in China,* Published by Beijing Iron and Steel Research Academy under the Ministry of Metallurgical Industry, May 1979.

[2] Walter Vormstein: *Schwerölbetrieb mit Mittelschnellanfenden KHD–Dieselmotoren,* MTZ, No.1/2, 5–10, 1976.

Annual of the CSNAME, Vol. 1, 1982

THE RELIABILITY ANALYSIS OF THE SHIP'S NAVIGATION SYSTEM

LI ZIGANG (李滋刚)

Tianjin Navigating Instrument Works

SUMMARY

In designing ship's navigation system it is very important to assess the mean time to failure (MTTF) of various equipments which indicates the reliability characteristics and repair capabilities of these equipments. This paper discusses the reliability of various system configurations, and puts emphasis upon the analysis of the reliability and accuracy for different repairable navigation system configurations using Markov random process theory and mathematical statistic method and solves the computation of reliability and accuracy. The analysis in this paper shows that, when the accuracy, reliability and maintainability are much different from the specified performances of the navigation equipment. Using the triple modular redundancy (TMR) majority voting system configuration is a proper way; when the performances of the actual requirements approach the specified performances for the equipment and the error detection hardware and software are quite perfect, then the two-equipment parallel system is reasonable. But, the configuration of single navigation equipment is not adoptable.

I. Introduction

The ship's navigation system is an information processing system. The task of the ship's navigation system is to provide the precise instant location and heading and velocity data continuously, during the entire sailing period. Recently, with the technological development and the improvements in electronic technology and precision electromechanical instruments, the fabrication and design of self-contained navigation equipment have become practicable. In this paper, the reliability analysis of the self-contained navigation is discussed.

The reliability of ship's navigation equipment is described by the probability that an equipment will perform the intended function, in a given environment, for a predetermined period of time, without failure. The definition of reliability involves three parts: the length of time, the given environment and the intended function. The intended function of the navigation equipment means not only that a totally inoperative failure of the elements or units will not be allow, but also that all errors must be limited in a specified margin. Therefor, the navigation equipment must have performance monitor method, so that it can detect the system's performance degradation. This self-monitor technique can be hardware or software method, also, it can be at the unit or system level.

In the sea-going technique, the navigation data must be provided continuously by the ship's navigation system. The navigation data effectiveness can be performed by two methods. The first one is a costly "static configuration" adopting redundancy technique at the unit or equipment level, in which a quite high reliability level can be achieved in theory. The second one is a "dynamical configuration", where the system operates in a multiple equipments-parallel maintainable manner, so that the reliability of the system depends on the availability of a single navigation equipment. In addition, the independent observation data of the multiple-equipment system can be used to improve the accuracy of the ship's navigation system.

As such, reliability analysis of navigation system can be transformed into the analysis of configuration in which the system performance must be requried to meet some specified requirements.

II. The Reliability of a Single Navigation Equipment

To know whether the navigation equipment is in failure state or not, it depends on whether the data output accuracy of the equipment exceeds the specification limit or not. When there are not any failure machanism to be predominantly responsible for some failure, the failure distribution function is a negative exponential distribution. This distribution is called a "one-parameter distribution", once the failure rate is set, the reliability function is completely defined. When the failures due to wear-out or performance degradation beyond tolerance limits have a significant effect on the overall failure rate, the normal (or Gaussian) distribution is the applicable distribution. There are two principal applications of the normal distribution in navigation equipment reliability. The first is concerned with the relationship of variable characteristics of the equipment to the specifications. This involves the probability of the navigation data to meet performance requirements. The second relates to wear-out life of components and the distribution of components failure due to extended periods of operation. Actually, wear-out could be considered as another variable characteristic which effects the components reliability. In the navigation system, the main error sources are monitored by using the performance monitoring techniques. When the monitored error meets the specified performance requirements, it will be corrected promptly. Whereas, when the performance degrades beyond tolerance limits, the monitor system presents a failure warning information. As a result, the failure distribution of the navigation equipment is still described as the negative exponential function. The reliability with an exponential distribution failure rate is

$$R(t) = e^{-\frac{t}{T_{cp}}} \qquad (1)$$

where T_{cp} is the mean time to failure (MTTF) of navigation equipment.

When a ship performs a round-the-world cruise, it is necessary that the reliability of the navigation system provided by a single equipment is 90 percent during the 90-days continual cruise. From Eq. (1) the mean time to failure (MTTF) of the system is 20,000 hours. We can imagine how costly it must be to obtain such high MTTF as 20,000 hours for a single navigation equipment.

III. The Reliability of the Two-equipment Parallel System with Maintenance

1. The reliability description of single maintainable equipment

For a maintainable navigation equipment, it is not necessary that an equipment is as reliable as possible but rather that it be usable the maximum possible percent of the time. At first this statement may appear to be contradictory, but reflection will reveal that ease of maintenance, repair, or replacement might compensate for reliability. If we interpret the reliability as probability of adequate performance for a given period of time to mean for maintenance/repair, then we can evaluate as an alternative the total percent of time that a system will be operable when it is required. This measure of effectiveness is refered to as availability. We assume that the failure time and the repair time of an equipment are distributed exponentially with rate parameter λ and μ respectively. The availability of the maintainable equipment is

$$A(t)=\frac{\mu}{\mu+\lambda}+\frac{\lambda}{\mu+\lambda}e^{-(\mu+\lambda)t} \qquad (2)$$

The steady state value of the A(t) is

$$A=\frac{\mu}{\mu+\lambda} \qquad (3)$$

As mentioned above, the maintainence/repair action can change the reliability model of an equipment from "static configuration" into "dynamical configuration". But it can not change the mean time to failure of the navigation equipment. Therefore, the reliability of the navigation data outputs will not be improved. Only if the navigation system is a redundancy system, the repair action can increase the reliability of navigation data outputs.

2. The reliability of the two–equipment parallel system without maintenance

When a navigation system composed of two identical equipments in parallel operating, we assume that the system is failed only if the two equipments are being failure state. In terms of the reliability of the individual equipments, the overall reliability can be expressed as:

$$R(t)=2e^{-\frac{t}{T_{cp}}}-e^{-\frac{2t}{T_{cp}}} \qquad (4)$$

The mean time to failure (MTTF) for the two-equipment parallel configuration is found by integrating the reliability function. From Eq. (4), we have:

$$T_{cp_2}=\int_0^\infty R(t)\,dt=\frac{3}{2}T_{cp} \qquad (5)$$

The result shows that the reliability of the two-equipment parallel system is 50 percent higher than that of the single one.

3. The reliability of the two-equipment parallel system with maintenance

Consider a navigation system composed of two identical equipments which is described by Eq. (3). The navigation system has the following characteristics:

(1) The system has two-equipment. As soon as both equipments start, the system is put into operation. Only if the two equipments are under repair or failure simultaneously; the system is down.

(2) The equipments possess hardware and/or software error monitoring capabilities. Good/bad is a sufficient description of each equipment.

(3) The failure and repair processes are entirely independent. The failure time and repair time of each equipment are distributed exponentially with rate parameter λ and μ respectively.

(4) The failure in any equipment is detected at once and the repair is immediately begun. The repaired unit is like the new one.

In order to analyse the reliability behavior of a system, we assume that the system running state can be represented by state variables. These states represent different conditions under which the system can be. The transition from one state to another is a Markov process, i.e. the probability of being in a certain state at a certain time does not depend on its history. The sojourn time in each state is exponentially distributed, the state transition rates are constant in time.

To apply Markov processes for the system reliability analysis, we define the following three states.

State x_0—two equipments are operating;

State x_1—one equipment is operating and the other begins to get repaired;

State x_2—the two equipments are under repair or failure simultaneously; the system is down.

Using the relationship between Markov processes and signal flow graphs, the state transition diagram (i.e., the signal flow graph) for the configuration of the two-equipment system is shown in Fig. 1

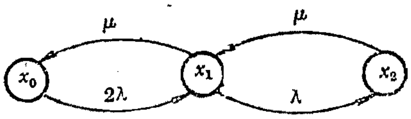

Fig. 1 State transition diagram of the two-equipment system

Thus the probability of the system's being in a certain state can be calculated by node equations of the Graph-theoretic techniques. We have:

$$\dot{P}(t)=AP(t) \tag{6}$$

where $P(t)$ is the probability of the system's being in a certain state as a function of time. The matrix A is a coefficient matrix

$$A=\begin{pmatrix} -2\lambda & \mu & 0 \\ 2\lambda & -(\lambda+\mu) & \mu \\ 0 & \lambda & -\mu \end{pmatrix}. \tag{7}$$

The initial condition is

$$P(0)=[1\ 0\ 0]^T \tag{8}$$

By using Eq. (6), we have following Laplace transformation expression:

$$P(s)=\phi(s)P(0)=[SI-A]^{-1}P(0) \tag{9}$$

Then the solution of the system states probability is

$$P(t)=\phi(t)P(0) \tag{10}$$

As described above, the probability of the system's being in a certain state is only a state transition of the initial condition. So the matrix $\phi(t)$ is also called the state transition matrix.

As stated above, the navigation system must provide the data outputs continuously. Once the running state of the two equipments system transform into the state x_2, the navigation system will loss the specified function. Therefore, the navigation system is required to operate in $\{x_0, x_1\}$ state which is called a set of operting state and noted by x_T, but the $\{x_2\}=\bar{x}_T$ is called a set of failure state. The set $\bar{x}_T$ is considered as a closed set if the state transition of system can not transform from $\bar{x}_T$ set to x_T set, it is called an absorbing state as well. Then we shall obtain state transition diagram shown in Fig. 2.

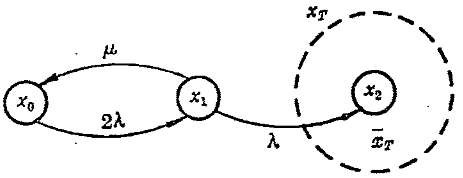

Fig. 2 State transition diagram with an absorbing state

Following Eq. (6), we have the coefficient matrix A

$$A=\begin{bmatrix} Q & 0 \\ R & I \end{bmatrix} \tag{11}$$

where

$$Q=\begin{bmatrix} -2\lambda & \mu \\ 2\lambda & -(\lambda+\mu) \end{bmatrix} \tag{12}$$

is a coefficient matrix which represents the transition law of states within set x_T. The unit matrix I is a coefficient matrix to represent the transition law within set $\bar{x}_T$, and matrix R represents the transition from states set x_T to an absorbing state set $\bar{x}_T$. The 0 is a zero matrix which represents that once the navigation system enters set $\bar{x}_T$, it can not make the transition out again.

The mean time to failure (MTTF) is often used as a reliability measure for system which must provide the data outputs at a random instant of time. We assume that the system starts in x_0 at $t=0$, the probability sum of the system's being in the set x_T can be obtained by solving Eq. (6), we have:

$$Px_T(s)=\sum_{x_n\in x_T} P_n(s)=[SI-Q]^{-1}\begin{bmatrix} 1 \\ 0 \end{bmatrix} \tag{13}$$

Thus, the mean time to failure, T_{scp} is given by the following equation:

$$T_{scp}=Px_T(s)\Big|_{s=0}=\frac{3}{2}T_{cp}+\frac{1}{2}\frac{T^2_{cp}}{T_r} \tag{14}$$

where the T_r is the mean repair time of a single equipment.

We assume that the ship's navigation system is required to provide continuously the data outputs with 90 percent reliability during three months, and the mean repair time of the equipment is three hours. From Eq. (14), the mean time to failure T_{cp} of an equipment is obtained.

$$T_{cp}=355\ \mathrm{h} \tag{15}$$

4. The contribution made by the improvement of an equipment reliability, T_{cp} and T_r, to that of the system reliability

As shown above, the reliability of the two-equipment parallel system with maintenance can be determined by the reliability parameter of the single equipment, T_r and T_{cp}. From Eq. (14), we have:

$$\Delta T_{scp}=\left(\frac{3}{2}+\frac{T_{cp}}{T_r}\right)\Delta T_{cp} \tag{16}$$

$$\Delta T_{scp}=-\frac{1}{2}\left(\frac{T_{cp}}{T_r}\right)^2\Delta T_r \tag{17}$$

These results show that the reliability of system rises with the MTTF of equipment in proportion as the factor T_{cp}/T_r, but it rises with the mean repair time of equipment in proportion as the factor $(T_{cp}/T_r)^2$. In general, T_{cp}/T_r is very large. Therefore, system designer must use various special techniques to decrease the mean repair time T_r of the equipment. The maintainability is an important technical requirement of an advanced ship's equipment.

We assume that the T_{cp} is 240 hours, the original value of the repair time is 10 hours, but its improved value is three hours, then the MTTF of system will increase by 6720 hours, thus, the corresponding MTTF of an equipment will increase by about 200 hours.

5. The data accuracy of the two-equipment parallel system

The states x_0 and x_1 are the operating states of two-equipment parallel system with maintenance. The state x_0 in which two equipments are all in operating indicates that the data accuracy of equipments meet the performance requirements which are detected by monitoring system. If the data outputs, x_A and x_B, of two equipments are independently and normally distribution variables with variance σ_A^2 and σ_B^2 respectively. Then the estimated value $\hat{x}$ of the system data outputs is obtained by the maximum likelihood estimating method. Then

$$\hat{x}=\frac{\sigma_B^2x_A+\sigma_A^2x_B}{\sigma_A^2+\sigma_B^2} \tag{18}$$

When the data outputs of two equipments are identical accuracy, we have $\sigma_A=\sigma_B=\sigma$. From Eq. (18), we can obtain:

$$\hat{x}=\frac{1}{2}(x_A+x_B) \tag{19}$$

And the standard deviation of the estimated value $\hat{x}$ is found.

$$\sigma_{\hat{x}}=\frac{1}{\sqrt{2}}\sigma \tag{20}$$

It is obvious from Eq. (20) that the accuracy of the system has been improved 30 percent as compared with one of a single equipment.

6. The operating probability of different system states

At any instant of time, the two-equipment system must be in one of the states, x_0 or x_1, the state probability of the system's being in the state x_0 or the state x_1 can be evaluated from Eq. (9). The mean time T_{x_0cp} of the system's being in the state x_0 can be found.

$$T_{x_0cp}=\frac{1}{2}T_{cp}+\frac{1}{2}\frac{T^2_{cp}}{T_r} \tag{21}$$

The probability $P_{x_0/s}$ with which two equipments are operating simultaneously can be determined from Eq. (13) and (21), that is

$$P_{x_0/s}=\frac{T_r+T_{cp}}{3T_r+T_{cp}} \tag{22}$$

We assume that T_r is three hours and T_{cp} is 355 hours, from Eq. (22), the probability $P_{x_0/s}$ is then

$$P_{x_0/s}=0.984 \tag{23}$$

Thus we have the following result that the probability with which the two-equipment system with maintenance is in two-equipment operating state is quite large. Thereby, the redundant information of the two-equipment system can be utilized fully to improve the accuracy of the navigation system.

In addition, the operating state provides the hardware condition under which the navigation system can monitor the data performance change of the equipment.

The probability $P_{x_1/s}$ of the system's being in the state x_1 can be calculated similarly.

$$P_{x1/s}=\frac{2T_r}{3T_r+T_{cp}} \tag{24}$$

As mentioned above, the T_r is three hours and the T_{cp} is 355 hours, then

$$P_{x_1/s}=0.016 \tag{25}$$

The calculations indicate that the two-equipment navigation system with maintenance is a very significant system.

IV. The Reliability of Triple Modular System with Maintenance

1. The triple modular redundant, majority voting (TMR) system

The TMR system has characteristics as follows:

(1) The three navigation equipments are operating simultaneously, but they provide the navigation data independently. The data accuracy of three navigation equipments are identical, and the data outputs are independently and normally distributed.

(2) The equipment does not contain perfect error detecting hardware; however, software error detection have been introduced whenever the performance of system has degraded in order to identify the faulty equipment.

(3) The majority voter is performed by software processing technique. It can detect and

isolate a faulty equipment. And the failed equipment is diagnosed and repaired immediately.

(4) As long as at least two of the three equipments are in good operating state, the data outputs of the system are available.

2. The majority voting processing and data accuracy of the system

The TMR majority voter is performed by the software processing technique. When an equipment in the system has degraded, the navigation data outputs of three equipments, x_A, x_B, and x_C, are inequality accuracy. The inequality accuracy data set is processed by weighting, the weighted estimated value of the system data $\hat{x}$ is obtained by the maximum likelihood estimating method. Then

$$\hat{x}=\frac{(x_B-x_C)^2x_A+(x_C-x_A)^2x_B+(x_A-x_B)^2x_C}{(x_A-x_B)^2+(x_B-x_C)^2+(x_C-x_A)^2} \tag{26}$$

The voting action is illustrated by following numerical example. We assume that the data 40, 5 and 4 are provided by the equipments A,B and C respectively. The estimated value of the system output $\hat{x}$ can be obtained, we have:

$$\hat{x}\doteq 4.528 \tag{27}$$

This implies that the data of equipment A, x_A, and the estimated value of system output $\hat{x}$ seriously disagree, but the data x_A make very small contribution to the estimated value of system, $\hat{x}$. As such, the equipment A whose performance has degraded can be isolated by the software detection. It is obvious that the processing has performed software voter function.

When the data of the three equipments exactly agree, the data outputs are identical accuracy. From Eq. (26), the estimated value of the system $\hat{x}$ can be obtained. The standard deviation of the estimated value $\hat{x}$, $\sigma_{\hat{x}}$ will become

$$\sigma_{\hat{x}}=0.577\sigma \tag{28}$$

The accuracy of the TMR system has been improved 42 percent as compared with one of a equipment.

3. The reliability of TMR system without maintenance

The TMR majority voting system requires that the system can still operate as long as at least two of the three equipments are operating. Utilizing the result of the static configuration reliability analysis, we can obtain the MTTF of system, T_{cp_3}.

$$T_{cp_3}=\int_0^{\infty}\left(3e^{-\frac{2T}{T_{cp}}}-2e^{-\frac{3T}{T_{cp}}}\right)dt=\frac{5}{6}T_{cp} \tag{29}$$

The expression means that the TMR system without maintenance is not competitive with the single equipment for the long-time reliability.

4. The reliability of TMR majority voting system with maintenance

Utilizing the approach outlined above, the states of TMR system with maintenance can be defined as following:

State x_0—three equipments are in operating state simultaneously;

State x_1—two equipments are under operating state and the other one is under failure and repair state;

State x_2—one equipment is under operating state and the other two equipments are under failure or repair states;

State x_3—three equipments are under failure or repair states.

We apply Markov processes as well as the relationship between Markov processes and signal flow graphs to analyse this model. The state transition diagram (i.e., the signal flow graph) for the model can be shown as Fig. 3.

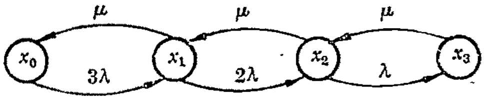

Fig. 3 State transition diagram of TMR system with maintenance

The probability of the system's being in a certain state can be calculated by following equations:

$$P(s)=[SI-A]^{-1}P(0) \tag{30}$$

where

$$P(0)=[\ 1\quad 0\quad 0\quad 0\ ]^T \tag{31}$$

the coefficient matrix

$$A=\begin{pmatrix} -3\lambda & \lambda & 0 & 0 \\ 3\lambda & -(2\lambda+\mu) & \mu & 0 \\ 0 & 2\lambda & -(\lambda+\mu) & \mu \\ 0 & 0 & \lambda & -\mu \end{pmatrix} \tag{32}$$

In figure 3 set $x_T=\{x_0, x_1\}$ means that the TMR majority voting system is under operating state, but set $\bar{x}_T=\{x_2, x_3\}$ means that the system is under failure state, viz. the system is down. The $\bar{x}_T$ is called closed set, or it can be called absorbing states. Thereby, the state transition diagram of TMR majority voting system is shown in Fig. 4.

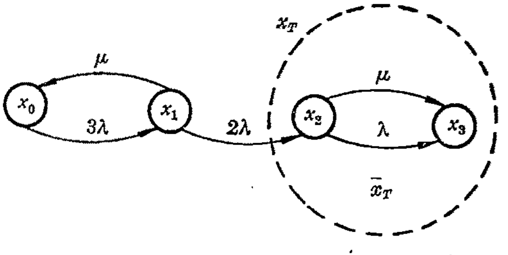

Fig. 4 State transition diagram of TMR majority voting system

The probability of the system's being in set x_T can be obtained from Eq. (30), where the coefficient matrix A will become

$$A=\begin{pmatrix} Q & 0 \\ R & I \end{pmatrix} \tag{33}$$

where

$$Q=\begin{pmatrix} -3\lambda & \mu \\ 3\lambda & -(2\lambda+\mu) \end{pmatrix} \tag{34}$$

From Eq. (31), the system starts in state x_0, then the sum of the probabilities of system's being in set x_T is

$$P_{x_T}(s)=\sum_{x_n\in x_T} P_n=[SI-Q]^{-1}\begin{pmatrix} 1 \\ 0 \end{pmatrix} \tag{35}$$

Then the MTTF T_{scp} of the system is

$$T_{scp}=\frac{5}{6}T_{cp}+\frac{2}{3}\frac{T_{cp}^2}{T_r}-\frac{1}{6}\frac{T_{cp}^3}{T_r^2} \tag{36}$$

We assume that the ship's navigation system is required to provide continuously the data outputs with 90 percent reliability during three months, and the mean repair time of the equipment is three hours. From Eq. (36), the MTTF T_{cp} of an equipment is obtained.

$$T_{cp}=102\ \mathrm{h} \tag{37}$$

If the repair time is 5 hours, then

$$T_{cp}=141\ \mathrm{h} \tag{38}$$

Obviously the TMR majority voting system configuration exceeds the parallel system configuration with the same reliability of an equipment. Especially when the error detecting hardware and the accuracy and the reliability of an equipment are not advanced, the configuration of the TMR system with maintenance will indicate more advantage.

5. The operating probability of different system states

From Eq. (35), we can evaluate the mean time T_{x_0cp} of the system's being in the state x_0, then

$$T_{x_0cp}=\frac{T_{cp}}{3}+\frac{T_{cp}^2}{6T_r}+\frac{T_{cp}^3}{6T_r^2} \tag{39}$$

but the mean sojourn time for the system in the state x_1 is

$$T_{x_1cp}=\frac{1}{2}T_{cp}+\frac{1}{2}\frac{T_{cp}^2}{T_r} \tag{40}$$

The probability $P_{x_0/s}$ with which three equipments are operating simultaneously can be determined from Eq. (39) and (40), that is

$$P_{x_0/s}=\frac{2T_r+T_{cp}-T_{cp}^2}{5T_r+4T_{cp}-T_{cp}^2} \tag{41}$$

We assume that T_r is three hours and T_{cp} is 102 hours, from Eq. (41), the probability $P_{x_0/s}$ is then

$$P_{x_0/s}=0.97 \tag{42}$$

As described above, the state x_0 is major operating state for the TMR majority voting system.

V. Conclusions

From the above discussion, the main system performance for the different configuration are illustrated in Table A.

Table A

performance / configuration			data accuracy	MTTF
Single equipment	without repair		σ	T_{cp}
	with repair		σ	T_{cp}
Two equipments	without repair		$0.707\ \sigma$	$\frac{3}{2}T_{cp}$
	with* repair	single	σ	T_{cp}
		dual	$0.707\ \sigma$	$\frac{1}{2}T_{cp}+\frac{1}{2}\frac{T^2{}_{cp}}{T_r}$
TMR majority voter	without repair		$0.577\ \sigma$	$\frac{5}{6}T_{cp}$
	with** repair	dual	$0.707\ \sigma$	$\frac{1}{2}\left(T_{cp}+\frac{T^2{}_{cp}}{T_r}\right)$
		triple	$0.577\ \sigma$	$\frac{1}{3}T_{cp}+\frac{T^2{}_{cp}}{6T_r}+\frac{T^3{}_{cp}}{6T_r^2}$

* The equipment has perfect performance monitoring technique.

** The equipment has not perfect performance monitoring technique.

The following conclusions are drawn from Table A:

(1) When the error detecting hardware, the accuracy and the reliability for the navigation equipment are not advanced, the system configuration of TMR majority voting system with maintenance will indicate more advantage.

(2) When the error detecting hardware and software, the accuracy and the reliability for the navigation equipment has achieved satisfactory level, the two-equipment parallel system with maintence is reasonable.

(3) The configuration of single navigation equipment is not adoptable, because the ship's navigation system is required to operate a long period of time without cease.

Acknowledgment

The author sincerely appreciates the many helpful discussions with Engineer Yan Shundi without which this paper could not have been written. The author also particularly grateful to Engineers Zhuang Liangjie, Teng Yun and Wang Shunting for their many helpful corrections and suggestions.

References

[1] L. R. Doyon: *Solving reliability models of nuclear systems*, Proc. **1977 Annu. Symp. Reliability and Maintainability**, pp. 322–331.

[2] F. Galetto: *System avialability and reliability analysis*, **Proc. 1977 Annu. Symp. Reliability and Maintainability**, pp. 95–99.

[3] J. A. Buzacott: *Markov approach to finding failure times of repairable systems*, **IEEE Trans. Reliability**, Vol. R–19, pp. 128–134, Nov. 1970.

[4] S. Osaki: *Reliability analysis of 2–unit standby redundant system with preventive maintenance*, **IEEE Trans, Reliability** Vol. R–21, pp. 24–28, Feb. 1972.

[5] 张世英，刘智敏：测量实践的数据处理，科学出版社，1977.

[6] И. Б. Шубинский и Е. Н. Пивень: Расчёт Надёжности ЭВМ. Техника, 1979.

[7] 高木昇：信頼性の基礎数学，東京電機大学出版局，1972.

Annual of the CSNAME, Vol. 1, 1982

SHIP END LAUNCHING WITHOUT FORE POPPET*

ZHU CHONGXIAN (朱崇贤) AND LU WEIDONG (陆伟东)

Shanghai Jiao Tong University

SUMMARY

The paper discusses the development of fore poppet with which a ship is launched from the building berth with two standing ways, and describes in detail a new launch technique called ship end launching without fore poppet. On the basis of full-scale measurements, necessary ayalysis is made, some experimental formulas are given, and the advantages of the new launch technique are illustrated.

I. Introduction

When a ship travels down the ways, forces acting on the ship will vary all the way. Launching is a very complex dynamic process. For convenience, the standard launching calculations regard the ship as being momentarily static on the ways, and divide the launching process into four stages, namely, sliding ashore, entering water, stern lifting and free floating.

While entering water, the ship is subjected to three forces, i.e. W, gravity of the ship at the centre G of gravity, γV, buoyancy of the water at the centre B of buoyancy, and P, reaction force of the ways at the centre R of pressure. The relationship between them is as follows:

$$W=\gamma V+P$$

$$W\times L_G=\gamma V\times L_B+P\times L_R$$

Where L_G, L_B and L_R are the distances from the fore end of fore poppet to the centres of gravity, buoyancy and reaction force respectively (Fig. 1 a).

When $\gamma V\times L_B=W\times L_G$, the afterbody of the ship begins to float (known as stern lifting). If the ship is regarded as a rigid body, then $L_R=0$ at this moment, and the reaction force would theoretically concentrate on the fore end A of the launching cradle. Therefore, the pressure which the fore poppet is subjected to would be $P=W-\gamma V$ (Fig. 1 b).

---

* This research was accomplished by Shanghai Jiao Tong University and Hu Dong Shipyard. The members of the research group are Zhu Chongxian, Lu Weidong, Wang Yonghua (王永华), Gao Xianzhi (高宪智), Wang Xingfei (王兴飞), Hong Zhanqiu (洪占秋), Wang Genlu (王根禄), (Shanghai Jiao Tong University), Yang Hongkang (杨洪康), and Lou Pengnian (楼彭年) (Hu Dong Shipyard).

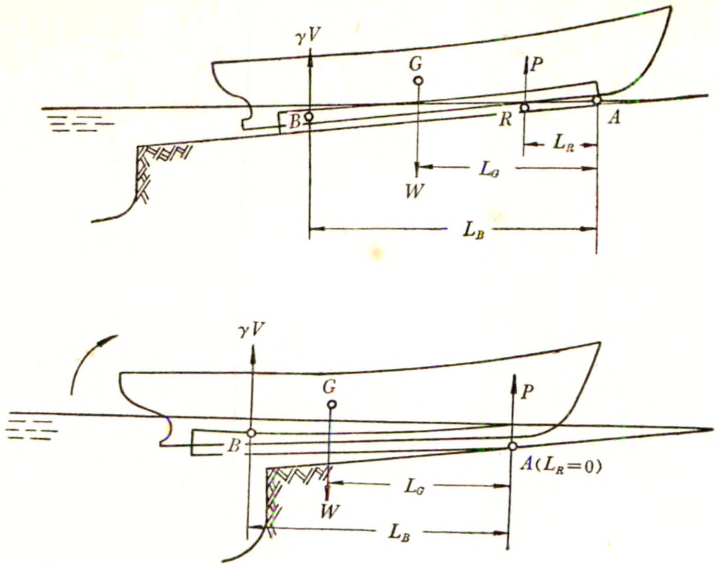

Fig. 1 Forces acting on the vessel while entering water and stern lifting

The standard launching calculations will show that the reaction force on A of the bow is enormous when the stern begins to lift, and that it would be 18～28% of the launching weight.

II. Application and Development of Fore Poppet

Because of such an enormous reaction force which occurs during stern lifting and such a sharp V-form the bow takes, it is a common way to mount fore poppet ensuring the safety of

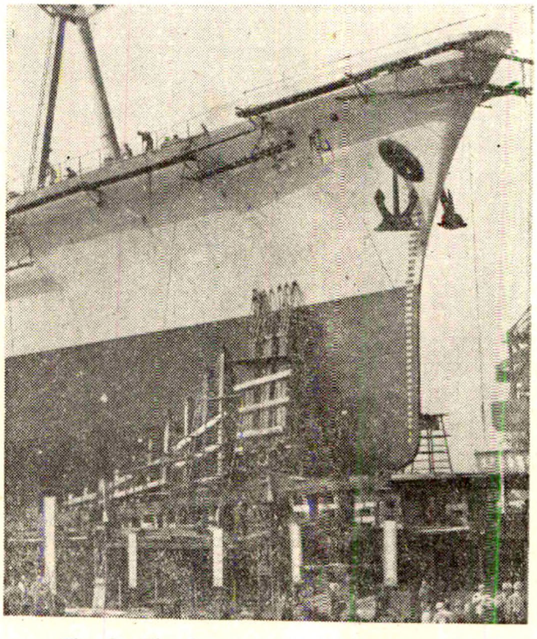

Fig. 2 The fore poppet of ship 'Dongfeng'

ship launch and preventing both ship and berth from damage. Precautions are made to mount the fore poppet under a transverse bulkhead of the ship, or to fit temporary pillars or fir shores inside the ship. At the same time, the fore poppet must be made strong enough to withstand the reaction force.

Fig. 2 shows the fore poppet of ship 'Dongfeng', a cargo ship of a tonnage of 10,000. The fore poppet consisted of several groups of timber poppets and under the foremost group there was a rotatable supporting cradle made of steel. A steel sling plate was set between the first group and the hull plate, the space between the hull plate and the sling plate was full of timber packing. These precautions were expected to prevent the hull structure from damage during stern lifting. Many keep plates were welded on the hull in way of poppets top to keep the timber poppets in position.

This kind of fore poppet was widely used in many countries. Before launch, fore poppet must be made to fit the lines of the hull. Obviously this was a time-consuming and material-wasting job and would raise many difficulties both in making and mounting. After launching the ship must be docked to have her fore poppet released and the keep plates cut. This was surely a disadvantage as far as the docking expenses were concerned.

Shipbuilders all over the world have been doing their best to improve the launching technique. And it is the following aspects which benefit the launching process a lot.

1. Change in fore poppet material

As a large number of timber poppets crashed during the process of launch, few timber poppets can be used to launch the ship of the same type repeatedly. So it is reasonable to have fore poppet made of steel instead.

2. Moderating the pressure distribution over fore poppet during stern lifting

Fixed fore poppet almost withstands a total reaction force during stern lifting and the pressure distribution might be triangular and the greatest loading would be on the fore-end of the poppet. Timber bar packing can be used to moderate the pressure distribution. Fig. 3 shows the fore poppet of a large icebreaker (Finland). In order to transfer the fore poppet loading on to the surface with an area of 20 sq m of standing ways, 5 rows of Norway fir

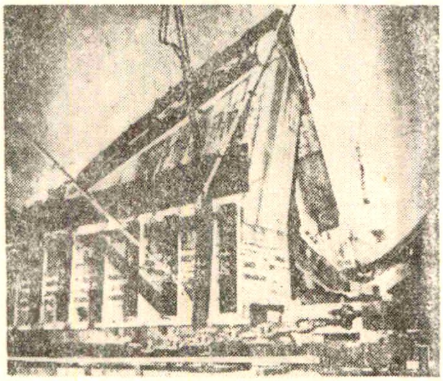

Fig. 3 The fore poppet of a large icebreaker (Finland)

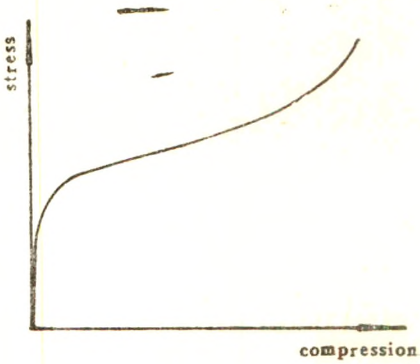

Fig. 4 Typical compression/stress curve of timber bar packing

packing measured 3 in by 3 in were used at the foremost end, and the pressure over fir packing was kept in the moderate zone of the compression / stress curve[1], as shown in Fig. 4.

Fig. 5 shows a rotatable fore poppet made of steel (China). The upper and lower parts were hinged together and the former hinged on the latter during stern lifting. So the reaction force on the hull or the pressure on the ways would present a more uniform distribution.

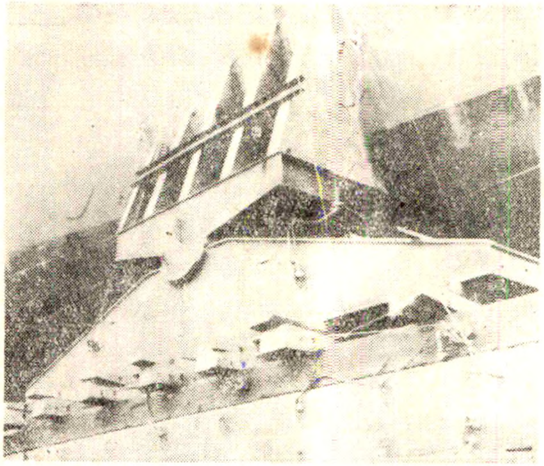

Fig. 5 Rotatable fore poppet of steelwork (China)

3. Simplifying the process of mounting and dismounting fore poppet

Fore poppet can be fixed to the hull indirectly, and the ship needs not docking after launch to have her fore poppet dismounted. Thus the launching process can be simplified.

Fig. 6 shows a new type of fore poppet in 70's (Soviet Union)[2]. It was said that such

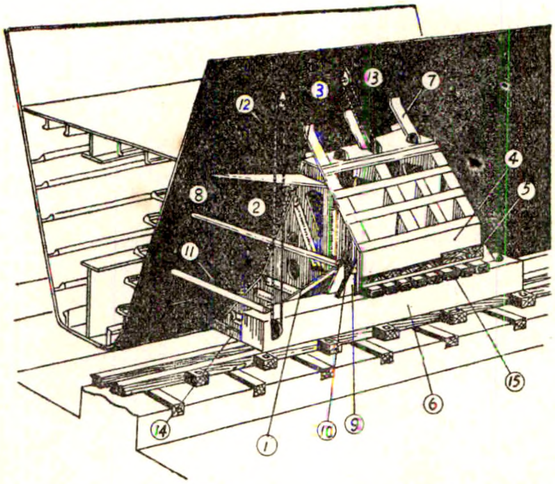

Fig. 6 A new type of fore poppet in 70's (Soviet Union)

1. web of fore poppet
2. face plate of fore poppet
3. oak packing
4. supporting cradle
5. timber bar packing
6. sliding way
7. flat steel
8. horizontal member
9. bracket
10. pin
11. steel bar
12.13. wire
14. pipe tie
15. pine slivers

a type of fore poppet was advanced and could be adopted to launch ships of various forms and displacements.

Much improvement has been made in ship launch with fore poppet, there still remains undertaking to replace or to cancel the fore poppet. Jiang Nan Shipyard first successed in replacing fore poppet with steelwork beams and launching a ship of a tonnage of 10,000. As shown Fig. 7, and achieved great saving on workhours and materials, at the same time, the launching preparation period was shortened[3].

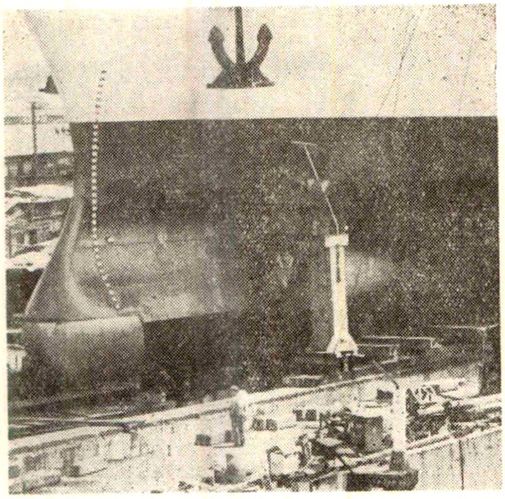

Fig. 7 Launching with steelwork beams and poppet

It is suitable for the ship, the bow of which takes a sharp V-form, to be launched this way on fixed standing ways. However, this launching technique requires some 7 beams to be mounted under the fore body of the ship and a steelwork poppet to be mounted on the beam near the bow (See Fig. 7). The steelwork poppet has a height of 4.7-metre, and sometimes it is difficult to be mounted. In order to insert the beams, the distance from standing way surface to ship bottom must be larger than 0.8 metre, and the distance from berth floor to standing way surface must be large enough as well. Because of this, it is not feasible for some building berths to adopt this launching technique. Moreover, the existence of launching beams would give rise to some difficulties while knocking down the keel blocks before launching the ship, and in case the standing way is not high enough, the beams would trip on the keel blocks during the launching and threaten the shipbuilders with unsafety.

III. Practice and Measurements of Ship End Launching without Fore Poppet

In 1978, Shanghai Jiao Tong University and Hu Dong Shipyard started a cooperation in research on canceling fore poppet and successed in the new launch technique—ship end launching without fore poppet. The new tehcnique requires neither fore poppet nor launching beams, just uses ordinary timber blocks and stopping. A lot of launching practice has proved the new method both simple and economical.

In the research, full scale measurements were made during the launches of different ships, deadweight ranged from 1,000 to 25,000 tons. The main items of measurements were:

1. Launching speed measurements

Two methods were introduced in measuring launching speed. Firstly, shore marks were erected at intervals of given distances, measuring the time intervals corresponding to the distances, a distance / time curve was obtained. Secondly, a speed–measuring device was made by ourselves, its sketch is shown in Fig. 8. The speed–measuring wheel has a cycle of 1 metre and can signal 5 impulses a cycle, one of which is a two–peak impulse. The high or low level of each impulse stands for 0.1–metre and can be recorded by a ultra–violet light recorder. During launching, the wheel was being turned by the wire, which was tied to the ship, and signaling impulses to the recorder, and together with the time scale impulses, an accurate distance / time curve was obtained. Then, speed / time curve, acceleration / time curve and dynamic friction coefficient / time curve could be drawn easily.

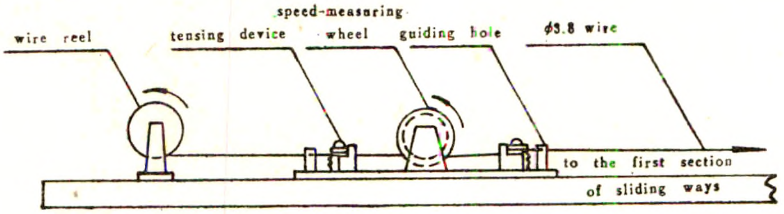

Fig. 8 Sketch of speed–measuring arrangements

2. Timber block loading measurements

In order to investigate the actual timber block loading and the way pressure distribution during the launch without fore poppet, pressure–measuring boxes (short for p.m.b.) were used in the full scale measurements. The size of a pressure–measuring box is the same as an ordinary timber block (Fig. 9). These boxes were put on the sliding ways in desired positions. Between a box and ship bottom plate were the stopping and the slivers. Before launching, the slivers on these boxes were hammered in a bit tighter than those on the timber blocks so that the boxes could measure the block loading a bit greater. Fig. 10 shows the actual launching cradle arrangement of ship B, a cargo ship of a tonnage of 25,000.

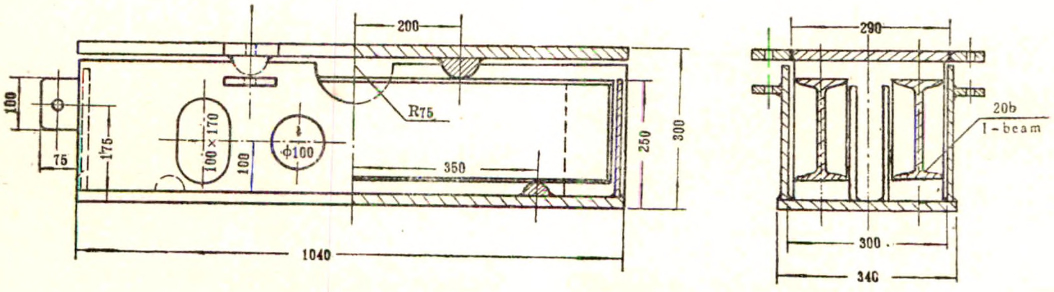

Fig. 9 Construction details of pressure–measuring box

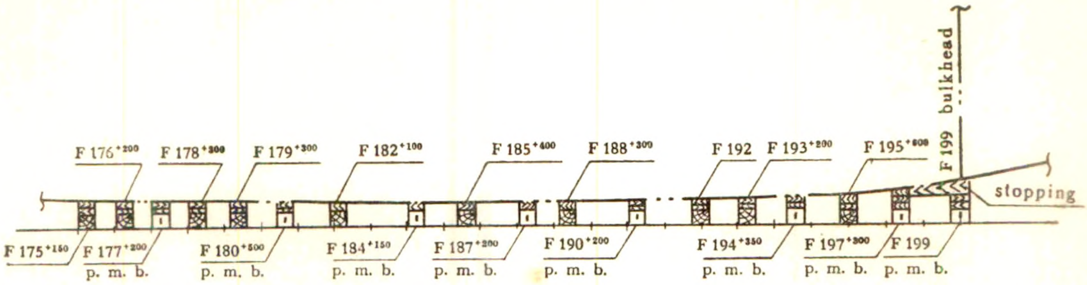

Fig. 10 Launching cradle arrangement of ship B (starboard)

During launching, local weight of the ship was transfered on to the cover plate of the box. There were two freely supported I-beams inside each box, the cover plate gave a couple of concentrated forces on to the I-beam and the I-beam then bent. A strain gauge had been sticked at the centre of the upper flange of the beam and connected to the instruments, so the dynamic strain could be recorded and the dynamic loading of the box could be calculated too.

Fig. 11 is a force graph of I-beam in the box. According to the mechanics theory, in the middle section of the beam the bending moment

$$M=P\times C$$

bending stress

$$\sigma=M/W=P\times C/W$$

and the strain

$$\varepsilon=\sigma/E$$

Therefore, $P=\varepsilon EW/C$.

As E, W, C are constants, P is a linear function of ε.

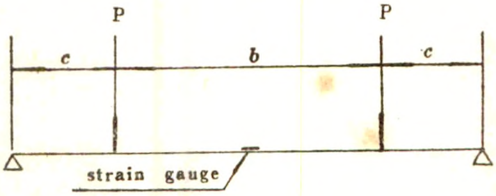

Fig. 11 Force graph of I-beam in pressure-measuring box

Fig. 12 shows the static loading of the I-beams on the testing machine. It can be found that the actual relationship between the loading and the strain appears linear, too.

Instruments which were used in the pressure-measuring work are multi-channel strain amplifiers and multi-channel ultra-violet light recorders. The power supply is storage batteries of 24 V.D.C. which must be converted into 220 V.A.C. by D.C.-A.C. converters. Connection of the instruments is shown in Fig. 13.

Fig. 14 shows the calculated loading / time curves of the pressure-measuring boxes of ship B during launching, and Fig. 15 shows the actual strain patterns which were recorded during the stern lifting of ship B.

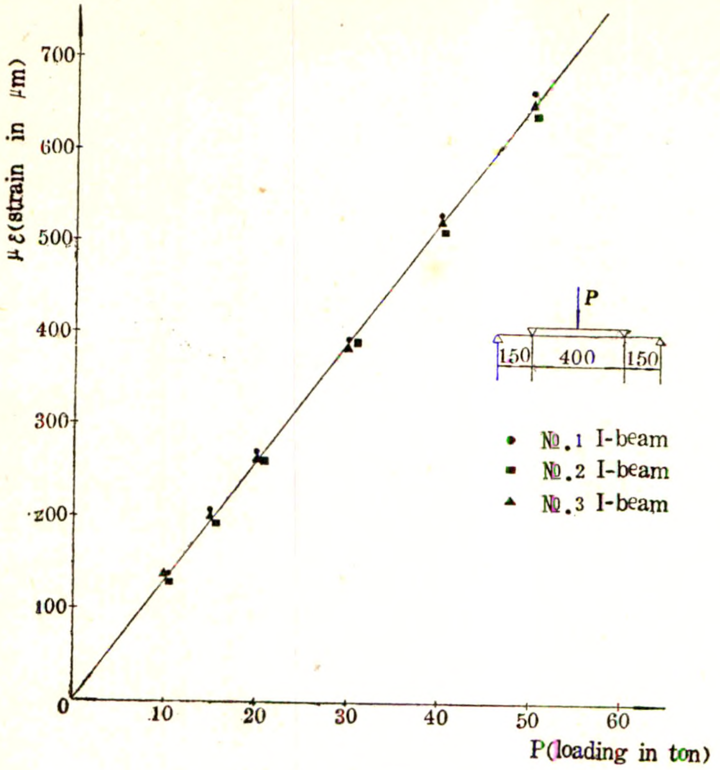

Fig. 12 Static loading curve of a single I-beam under test

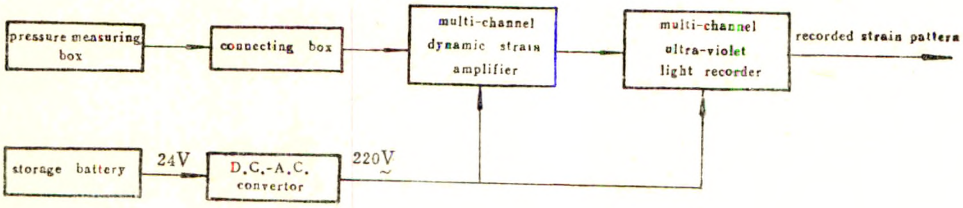

Fig. 13 Connection of the instruments

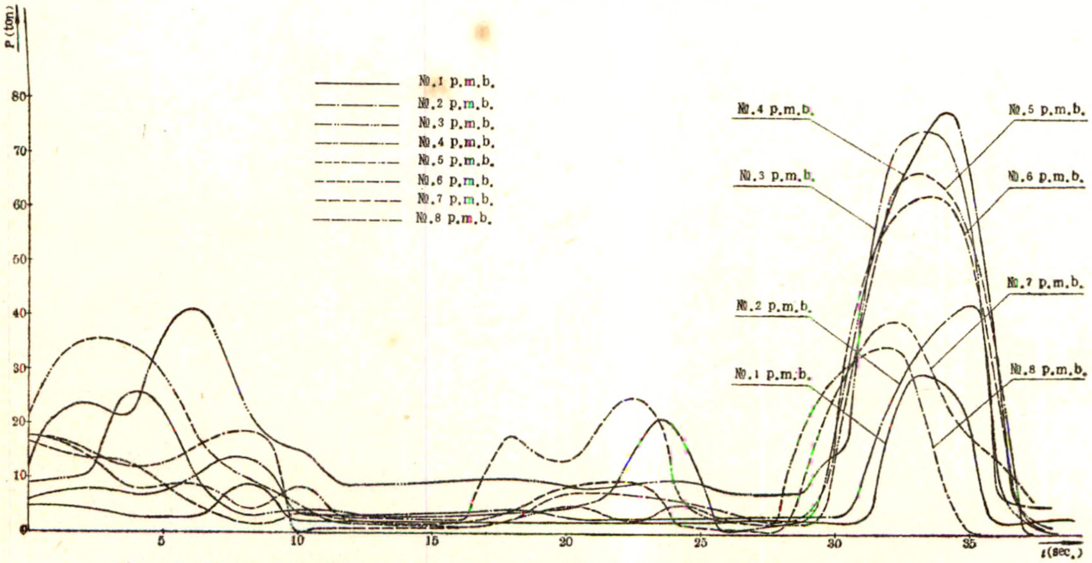

Fig. 14 Dynamic loading of pressure-measuring boxes of ship B during launching

Besides, film camera, gyroscope, inclinometer, etc. were also used in other items of full scale measurements.

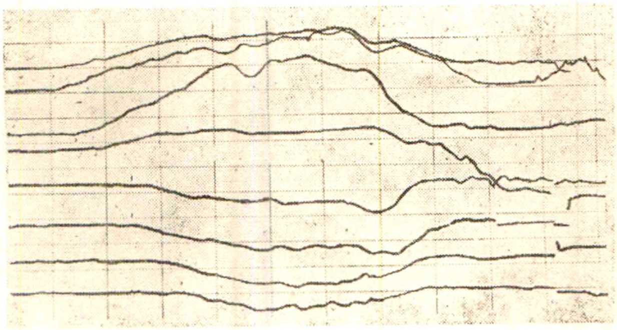

Fig. 15 Strain patterns recorded during the stern lifting of ship **B**

IV. Record Analysis

Many ships were measured during launching for a variety of purposes and the records obtained from these ships were analysed with an entirely new method. Now the general views on ship end launching could be given as follows.

(1) From the beginning to the end of stern lifting, reaction force on the bow region varies all the way. It is a new view different from the standard launching theory that the maximal reaction force on the bow region does not occur at the beginning of stern lifting, but in the process of stern lifting. Table 1 gives time T_{SL} which the process of stern lifting experiences, time T_{MR} at which the maximal reaction force occurs and the ratio of T_{MR}/T_{SL}.

Table 1

ship	A	B	C	D
T_{SL} (sec)	11	8	12	8
T_{MR} (sec)	5	4	5.5	3
T_{MR}/T_{SL}(%)	45.4	50	45.8	37.5

Note: Ship A, B are of the same type but were launched from different berth. Ship C is a passenger-cargo ship of a tonnage of 3,000. Ship D is a special cargo ship with a displacement of 3,000 ton.

(2) A ship is actually an elastic beam with varied section area and rigidity and is acted upon by non-uniform loads. Since the fore poppet has been canceled, timber blocks become an elastic foundation of the beam. When the stern lifts, the ship will actually bend and the fore bottom will still rest on the timber blocks spacing a certain distance, which is called "effective contacting length" (short for L_e). The enormous reaction force will distribute over such a length and the length can be measured from the unloading curve of the timber blocks (Fig. 16).

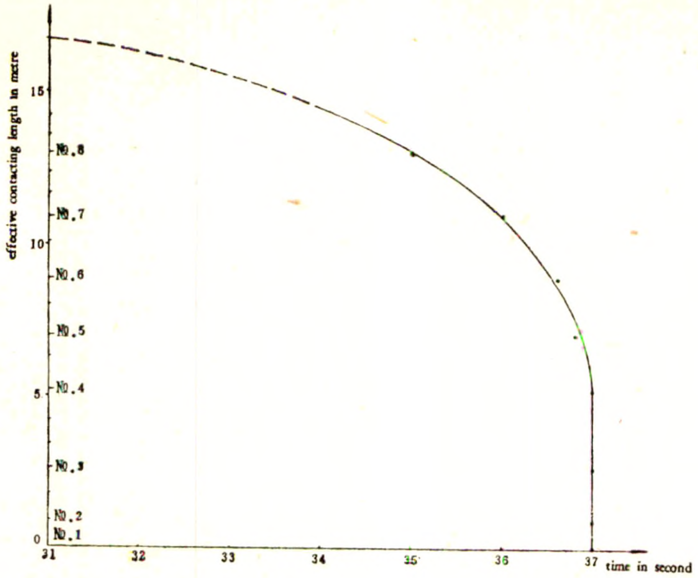

Fig. 16 Unloading curve of timber blocks of ship B during launching

From statistics, when launching without fore poppet,

$$L_e = K \times L_c$$

Where L_c is the total length of the sliding way, K is a contaction coefficient concerning the size and rigidity of the ship, the position of the first timber block and the space of the timber blocks. The value of K is suggested be 0.1~0.2 depending on the ship and launching arrangements.

Table 2 lists the values of L_c, L_e and K of launching ships mentioned before.

Table 2

ship	A	B	C	D
L_c(m)	162	162	73	90
L_e(m)	16.0	16.6	14	22
K	0.10	0.10	0.19	0.24

Note: Ship D is comparatively thin and there were less timber blocks at the bow, so its K appears a bit greater.

(3) Because both the ship and the timber blocks are not rigid bodies and the process of stern lifting will experience a definite while of time, it is not true that the ship will pivot about the fore end of the cradle. It is found that the reaction centre is mobile and coincides with the position of maximally loaded timber block. Generally speaking, the centre of reaction force moves forward during stern lifting. Fig. 17 shows the tendencies of reaction force and reaction centre during the stern lifting of ship B.

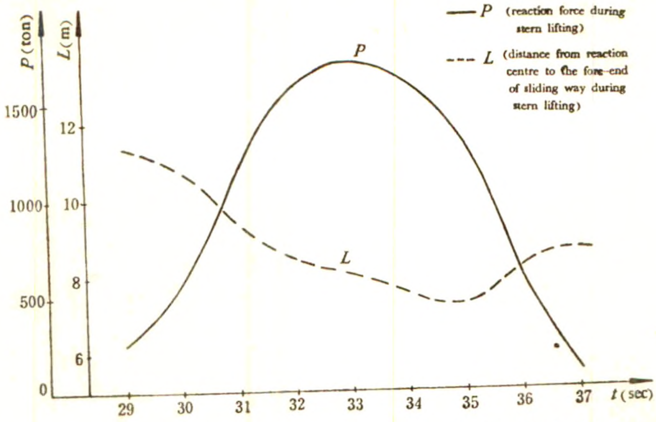

Fig. 17 Reaction force and reaction centre curves of ship B during stern lifting

(4) Canceling the fore poppet does not mean the non-existence of an enormous reaction force which will act on the bow region during stern lifting. Full scale measurements demonstrated that the total measured block loading Σ_p was close to the calculated reaction force P, as shown in Table 3, but the distribution patterns were quite different. Canceling the fore poppet resulted in a moderate distribution of the timber block loading.

Table 3 (in ton)

ship	A	B	C	D
P (cal.)	1660	1700	507.4	580
Σ_p (meas.)	1702	1680	528	510
Σ_p/P	1.02	0.99	1.04	0.9

Static loading tests on the timber block were also made. During the launching, if a timber block is compressed or even crashed, the blocks beside it will be loaded more and the loading range of the blocks will be adjusted automatically. The raise of curve L in Fig. 17 maybe is the case.

(5) Because the timber blocks on two sliding ways supported the ship with varying degrees and the surfaces of two standing ways were not extremely even, the ship rolled and the hull vibrated during her launch. And in addition, there were other dynamic factors which would affect the full scale measurements, so the measured loading of the box on port way differed from that on starboard way, and sometimes, the ratio of the two loading at the same frame might be 1:1.5.

(6) During stern lifting, if there are N timber blocks over the effective contacting length L_e, and the total mensured loading is Σp, then the average loading of each timber block can be calculated.

$$p=\Sigma p/2N \qquad \text{(ton)}$$

If the measured maximal loading of a timber block in this region is $p_{\max}$, then the coefficient of non-uniform distribution of the loading can be arrived.

$$U=p_{\max}/\bar{p}$$

In fact, U is an experimental coefficient which coordinates the unsymmetrical distribution of the loading on two ways and the non-uniform distribution of the loading on the same way. The value of U is suggested 1.5～2.25 depending on the launching conditions.

Owing to the closeness of the magnitudes of the total measured loading and the calculated reaction force, the average loading of each timber block can be calculated this way:

$$\bar{p}=P/2N$$

In practice, total measured loading is not available, and if the reaction force has not been calculated yet, then the average loading of each timber block can be calculated by the formula

$$\bar{p}=d\times W/2N$$

where W is the launching weight, d is a dynamic coefficient and its value is suggested 0.20～0.30.

Here $\bar{p}$ and $p_{\max}$ are important data in controlling the launch arrangement of timber blocks.

Table 4 gives the statistics of measured N, Σ_p, $p_{\max}$, $\bar{p}$, U and d during the launches of ship A,B,C,D.

Table 4

ship	A	B	C	D
N	19	19	14	15
Σp (ton)	1702	1680	528	510
$\bar{p}$ (ton)	44.8	44.2	18.8	17.0
$p_{\max}$ (ton)	80.7	77.9	/	38.3
$U=p_{\max}/\bar{p}$	1.8	1.76	/	1.80
$d=\Sigma p/W$	0.258	0.24	0.29	0.29

V. Significance and Advantages of the New Launch Technique

Ten ships of seven types were measured during their launches and more than 40 ships had been launched without fore poppet by the end of 1980. Now the new launch technique has won popularity in our country and that it is of value is a common opinion.

Firstly, new theory on ship end launching was examined. The standard launching calculations and traditional launching techniques are based upon[4-6]:

(1) The ship is a rigid body and it pivots about the fore end of the poppet when the stern lifts.

(2) The reaction force on the ship bow is maximal when the stern begins to lift and then becomes smaller and smaller.

(3) The enormous reaction force ought to be withstood by the fore poppet and the greatest loading is on the fore end of the poppet.

While the new launching technique is based upon:

(1) The ship is a non–uniform beam on an elastic foundation and it sags when the afterbody submerges more. The sagging curve varies all the way and the reaction centre moves forward gradually.

(2) When the stern begins to lift, a definite length (L_e) of the bow remains to make in contact with the ways, and afterwards the reaction force on the foremost region of the bow (say, 10–metre long) reaches the maximum. It was measured that the reaction centre moved forward at a rate (V_{RC}) about 2.5 m / sec, see Table 5.

Table 5

ship	A	B	C	D
V_{RC} (m/sec)	2.40	2.67	2.18	2.35

(3) During stern lifting, the pressure distribution is not triangular but is moderate and is over the effective contacting length which decreases as the stern lifts.

Fig. 18 shows a comparison of pressure distributions during stern lifting between launches with and without fore poppet. Ship E was launched with fore poppet[7] while ship B without. Launching particulars of the two ships are given in Table 6. Though the launching weight and the calculated reaction force during stern lifting of ship B are much larger than those of

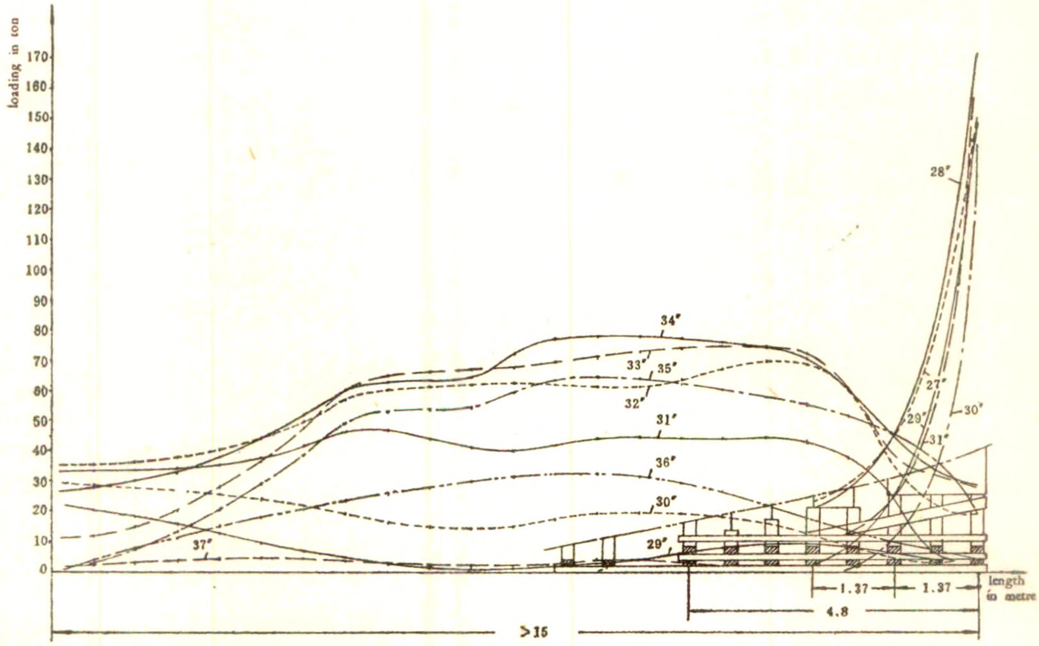

Fig. 18 A comparison of pressure distributions during stern lifting between launches with and without fore popp

ship E. Fig. 18 substantiates that the pressure distribution of ship B is much more favourable than that of ship E.

Table 6

ship	$L_{B.P.} \times B \times H$	Dead weight (ton)	launching weight (ton)	length of fore poppet (m)	calculated reaction force (ton)
E	12 × 18×11	10,600	3,060	4.8	863
B	172×23.2×14.2	25.000	6,653	/	1660

The fore poppet of ship E was 4.8 metre long. During stern lifting, the distribution of reaction force over the fore poppet was nearly a steep line and the maximum was at the fore end. It was measured that the maximal loading on the fore end was 177 ton and was about 40% of the total reaction force which was 431.5 ton each side by calculation. Nevertheless, ship B canceling the fore poppet, the distribution of the reaction force during stern lifting appeared a moderate spline curve and the loading of timber blocks over the effective contacting length was comparatively uniform. The maximal loading of the timber block was in the middle region of the length and was of a value of 77.9 ton which was 10% of the calculated reaction force, 830 ton each side. It is obvious that mounting the fore poppet artificially concentrates the reaction force on the bow when the stern lifts.

Secondly, as the new launch technique does not require fore poppet, beams, sling plate and keep plates any longer, great saving has been brought about on manpower, material resources and expenses of docking. The economic effect is rather considerable. For example, launching a ship of a deadweight of 25,000 ton without fore poppet, saved 20 cubic metre of wood, 1760 workhours and RMB 70,000 yuan of docking expenses, and a ship of 3,000 dw., saved 10 cubic metre of wood, 880 workhours and RMB 15,000 yuan of docking expenses.

Thirdly, the operation of ship end launching without fore poppet is surprisingly simple, meanwhile the launching process is rather safe as well. When launching with fore poppet, it can be often found that the timber poppets were crashed and some sections of the sliding ways were damaged after launch owing to some unforeseen factors. While launching without fore poppet, there is no restriction on the ways at the bow and the timber block loading is under allowance, so the sliding ways and timber blocks were seldom found damaged after launch. Observations on the berth and the ship were also taken after launch or while docking and no distortions were found in the standing ways or in the hull structure. So the safety of the new launch technique is reliable.

Finally, in case the fore poppet is used in launching a ship, the working load Q of the berth in the stern lifting region is calculated by the following formula:

$$Q = \frac{1.2 \times P}{2L_p} \quad \text{(ton/metre)}$$

Where P is the reaction force calculated by the standard launching calculations, L_p is the length of fore poppet. Now the fore poppet has been canceled, the calculated reaction force will distribute over the effective contacting length L_e. It was confirmed that $L_e \geqslant 2L_p$, therefore, the working load on the ways in the stern lift region will reduce a half or more. This means that the building berth in use can increase its capacity to launch larger ships when the new launch technique is employed, while the building berth in future can spend less in piling if the new method is considered.

VI. Conclusion

From the foregoing, a ship can be well launched without fore poppet from the building berth with two standing ways. The new launch technique has put forward a practical theory on ship end launching and has been proved both reliable and economical.

As there are so many building berths with two standing ways in our country, it is of great importance to introduce the new launch technique in national wide. As long as some necessary calculations are made and some proper measurements are taken, it is feasible for the ship, the block coefficient of which is $\geqslant 0.6$, to be launched without fore poppet.

In case the block coefficient of a ship is less than 0.6, or the distance between two standing ways is too large for a ship, launching can also be conducted without fore poppet. The ship can be launched with a few launching beams if the height of the standing ways is tolerable. Full scale measurements have identified that the basic theory of launching with beams is the same as that of launching without fore poppet.

References

[1] E. Enkvist and Helsingfors: *The Launching of a Large Icebreaker*, **European Shipbuiding**, No. 1, 1960.

[2] А. А. Малярчук, В. П. Суслов, Л. П. Суслова и В. Т. Третьякова: *Новая Констрункчия Баксового Устройства для Спуска Судов*, Судостроение, 1971. 4.

[3] 江南造船厂坞吊车间：万吨级船舶采用横梁下水，造船技术， Feb. 1975.

[4] 白神弘尚，寺岡伸行，野村次郎：進水時に船体船底に働く外力の調査研究，造船工業， Vol. 4, No. 6, Nov. 1972.

[5] K. V. Taylor and M. Williams: *Dynamic Loading on Launching Ways and Building Berths*, **The Institution of Engineers and Shipbuilders in Scotland**, Vol. 110, Part 5, 1966–1967.

[6] 宮田貞一，岡本治郎，友貞三郎，藤村洋，大島康弘，松浦利昌，西板豊：応幅15万トンタソカーの進水についこ，関西造船協会志， No. 157, 1975.

[7] 寺尾貞一，木藤正宏，横田健：進水時 *Fore Poppet* にかかる圧力測定の一方法についこ，造船協会論文集，第100号。

Annual of the CSNAME, Vol. 1, 1982

THE MECHANISM OF FISHEYE FORMATION IN WELDED SEAM AND ITS INFLUENCE ON THE FRACTURE PROCESS

CAI ZEGAO (蔡泽高), CHEN YAZHEN (陈雅珍), ZENG ZHENPENG (曾振鹏)

Shanghai Jiao Tong University

SHUI CHENG (水澄)

Zhong Hua Ship Building Factory

SUMMARY

Both the macro-and microscopic characteristics of the weld fisheye were studied in this paper. It is proved that fisheye is caused by hydrogen. Its influence on the properties of metal and on the processes of fracture was also studied. It is found that the weld fisheye is not an inherent defect of material. It is manifested with tension at the necking stage and at the stage between necking and fracture. In fatigue load it only forms when numbers of cycles are large enough. The weld fisheye is not considered to be the source of fatigue, so it has no conspicuous influence upon tensile strength and fatigue limit; it only affects the tensile ductility and the fatigue overload endurance value.

A lot of experiments were made to remove hydrogen in the welded seam. Specimens have been placed in the atmosphere for more than 8 years. It is found that if the defects of the welded seam and the amount of supersaturated hydrogen are lesser, no fisheye is manifested in tensile fracture surface after the specimens have been placed in the atmosphere for 160 days; if they are greater (unusual weld process), it is necessary to preserve more than 8 years for the fisheye to disappear.

The mechanism of fisheye formation in the welded seam was discussed and the authors presented their own viewpoint at the end of this paper.

I. Introduction

Hydrogen-induced cracking is a common phenomenon in engineering. The mainfested characteristics of hydrogen-induced cracking are different owing to the differences of the properties of materials, the technological processes, the environmental conditions and the types of mechanical loads[1].

1. In high-strength steels ($\sigma_B > 125$ kg/mm^2) containing hydrogen, particularly, the high-strength aero steels covered with cadmium and operating under high static stresses (especially

tension stresses in various directions) the crack will nucleate and propagate gradually until the material fractures, ever though the content of hydrogen is $C_a < 1$ cm^3/100g.

2. In general median-strength or low-strength steels, such as the quenched and tempered steel of $\sigma_B > 85$ kg/mm^2, the crack will uncleate and propagate gradually, until fracture takes place. This is so because when steel is placed in a corrosive environment (H_2S etc.) and bears a high mechanical load, it absorbs the atomic hydrogen from the environment, such as the petrochemical industry and the transport system of natural gas.

3. In median-strength and high-strength steels, as the content of hydrogen is high, hydrogen-induced crack will nucleate and propagate, and finally will cause fracture though no exterior mechanical load operates, such as some unreasonably treated steel component in electroplating.

4. In the cooling process of welding parts, because of the difference of the decomposition rate of austenite, hydrogen will be segregated in the austenite of posterior decomposition. Under the action of both the segregation and the transformation stress, cracking will take place, such as the crack under the bead etc.

The above mentioned aspects are the common ones of hydrogen-induced cracking. Sometimes many flakes may be manifested in these steels. The common white spots appearing on the fracture surface are called flake-type white spots.

The white spots surveyed in this article were manifested on the fracture surface of tensile test of deposited metal when the quality inspection on welding of low-alloy steel 14 MnVTi was carried out. They are named weld flakes or weld fisheyes as they resemble the eyes of fish.

Many investigations on fisheyes have been carried out, but many problems remain unsolved or are unsatisfiedly solved. In the past few years the authors have systematically surveyed the formation of fisheyes during the failure process and studied their influences on the properties of materials. Some results of theoretical value have been obtained and engineering significance is discussed in this paper.

II. The Macroscopic and Microscopic Characteristics of Weld Fisheyes

The weld fisheyes on fracture surface appear as silver-white spots (Fig. 1) with macroscopic defects such as blowholes and included slags as their nuclei inside the materials. The spots are mostly round or elliptical in outer appearance. The size of the weld fisheye is often in propor-

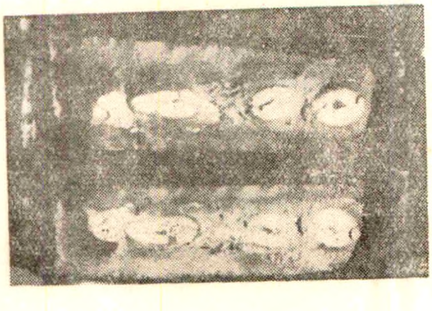

Fig. 1 The weld fisheyes manifested on the fracture surface of static tensile test

tion to that of the nucleus. In general, the larger the nucleus, the larger the fisheye. The practical diameters of fisheyes vary from less than 1 mm to more than 10 mm.

In macroscopical observations, the zone of the fisheye is found to be flat and slightly concave. The enlarged nucleus is shown in Fig. 2.

The electron micrographs of fisheye zone (Fig. 3) show cleavage and quasi-cleavage.

The fact that fisheyes are brittle fracture zones has been confirmed by the analysis of fracture in both macroscopic and microscopic examinations. The electron micrographs of the outside of fisheye zone show dimple expressed plasticity.

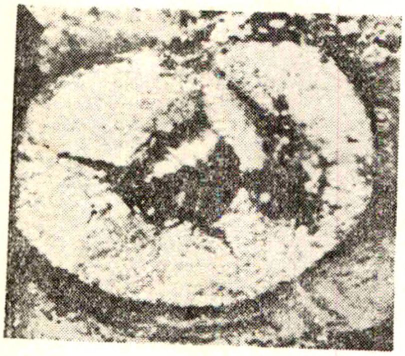

Fig. 2 The enlarged weld fisheye (15X)

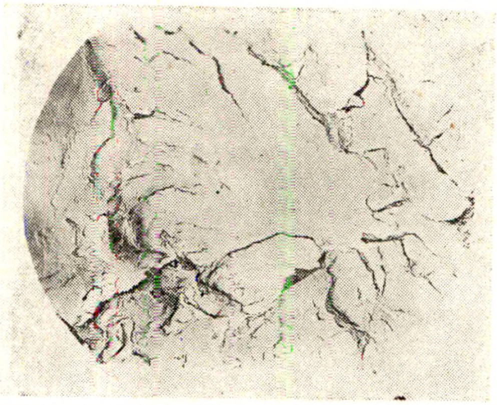

Fig. 3 The electron micrograph of fisheye zone (4000X)

In the weld parts of low-alloy steel 14 MnVTi, investigated fisheyes are mostly situated at the fusion line, the reason is that there are more blowholes and included slags in the lines, so that the material breaks easily and fisheyes appear. Also fisheyes have been manifested in welded seam but never in base metals.

Besides weld parts of steel 14MnVTi, fisheyes have been manifested in fatigue fracture of steel 18Cr2Ni4WA treated with gas soft nitriding. Fisheyes usually appear at the boundary between the soft nitriding layer and matrix (Fig. 4).

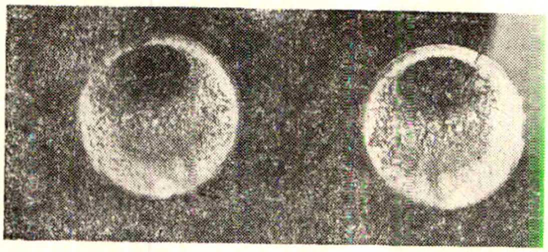

Fig. 4 Fisheyes manifested in fatigue fracture of steel 18Cr2Ni4WA treated with gas soft nitriding

Moreover, fisheyes have been manifested in the fracture surface of tensile specimen taken from a normalized 9-ton crankshaft made of cast steels No. 35. The nucleus of fisheyes was porosity.

So fisheyes appear not only in welded seam but also in heavy cast parts and some high alloy steels. It seems that fisheyes appear on the fracture surfaces of tensile and fatigue tests as there are some macroscopic hollow defects and a quantity of supersaturated hydrogen inside the meterials. Therefore the fisheye is a common and concealed defect in engineering.

III. The Effects of weld Fisheye on Failure and Properties of Materials

It is necessary to distinguish flake from fisheye mentioned in the introduction when the influences of weld fisheye on failure and properties of materials are to be discussed. The formation of the former is consequent on excess hydrogen contained in the materials for certain reasons. If some technological processes such as forging, casting, welding, heat treatment are performed, supersaturated hydrogen could not escape by means of diffusion (or the materials absorb excess hydrogen in hydrogen-bearing environment), flakes would form in the materials or components and white spots would appear in flakes after breaking off. Actually the flakes have already been formed during the technological process, which would greatly influence the properties afterwards, and make the materials and components useless.

The weld fisheye however surveyed by the authors, is formed and visible only in given conditions. In tensile test it is manifested only when the tensile rate is appropriate and a large quantity of plastic deformation appears. In fatigue load it forms when number of cycles are large enough. The fisheye appears only on the tensile surface in the fracture of cold bending test. And no fisheye exists on the fracture surfaces of press and impact failure.

For example, a number of specimens in which fisheye appeared in tensile fracture were examined with X-ray to find such defects as blowholes. The specimens were then forced to break with impact at the defect position. Another group of specimens treated with penetration of hydrogen were broken with impact. Only defects existed on the impact fracture surfaces in both these cases. There was no fisheye. Therefore the weld fisheye is not considered to be an inherent defect of the material, it forms only in certain conditions. The formation and influence of this kind of white spot in failure processes of tensile and fatigue tests will be discussed later.

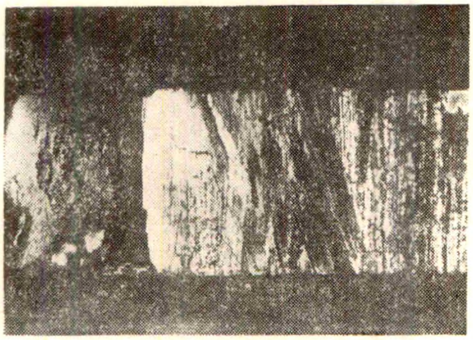

Fig. 5 Fracture surface broken with impact load, no fisheye appears

1. The formation of weld fisheye in static tensile test

The thickness of the specimen was 12～14 mm and width was 30 mm. To reveal sufficiently the aspects of fisheye, unbaked electrodes were used, the rust on groove surface was not cleaned, some slag was left between the layers. Thus a large amount of supersaturated hydrogen and a lot of defects in welded seam were intentionally given. Specimens were detected with X-rays in order to find the location and quantity of detects. Then a dangerous section in specimen was made. The specimens were compulsively broken with tensile in the position of defects. Two groups of specimen were prepared. One group was used for surveying the relationship between the tensile-plastic deformation and the fisheye formation. The other was used for investigating the action of hydrogen on fisheye formation.

In the tests surveying the relationship between tensile deformation and fisheye formation, the specimens were tensioned at different stages of deformation, such as yielding, between yielding and necking, near necking point, and between necking and fracture (Fig. 6, point 1,2,3,4 shown in tensile curve). Then the load was removed and the specimen was broken with impact, and the fracture was studied.

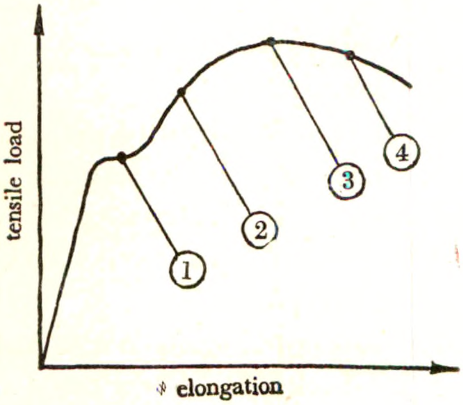

Fig. 6 The tensile curve of welded seam of steel 14 MnVTi

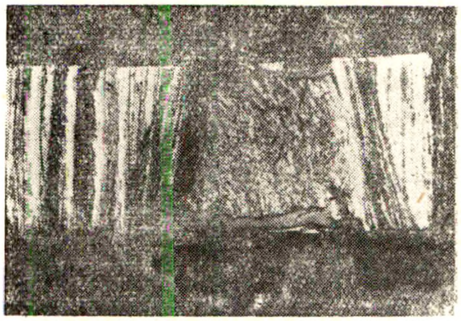

Fig. 7 Fracture surface tensioned at yield point and then broken with impact, no fisheye appears

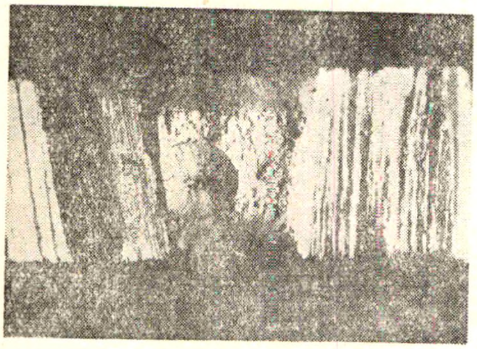

Fig. 8 Fracture surface tensioned at the stage between necking and fracture and then broken with impact, fisheye appears

The results of test show that the fisheye is not formed in tension at yielding stage and the stage between yielding and necking (Fig. 7), that fisheye is manifested with tension at necking stage, and a large quantity of fisheyes appears with a large amount of plastic deformation during the period from necking to fracture (Fig. 8). Therefore the fisheye will not form when the stress and plastic deformation are not great enough. When the stress is sufficient and a large amount of plastic deformation has been generated, the zones of microvoid aronud blowholes and other defects take place. Simultaneously the hydrogen is activated and diffuses into the microvoid zone, thus the brittle zone of fisheye around the blowhole is built up. This deduction will be discussed in detail in the description of mechanisms of fisheye formation.

The above mentioned fact shows that the weld fisheye which is not the inherent defect of material would be manifested in certain conditions and has no obvious effect on yield strength and tensile strength of welded seam. Also fisheye forms at the stage of the plastic deformation correlated with necking in tensile test, so that it hardly injures the forming technology such as bending plate.

Furthermore, to understand the relationship between hydrogen and the fisheye formation, a group of specimens of tensile fracture in which the fisheye should be manifested, was heated to various temperatures (65 °C~600 °C) to remove hydrogen and then was broken with tension.

It is found that fisheye disappears after heating the specimen at 250 °C for 8 hrs. It is believed that all supersaturated hydrogen in the welded seam has escaped by means of diffusion at this temperature, therefore no fisheye appears on the fracture surface of the welded seam.

Moreover, to confirm the action of hydrogen, the specimens in which hydrogen had been removed were penetrated with hydrogen again, and it was observed that fisheyes were manifested on the fracture surface again. This is shown in Fig. 9.

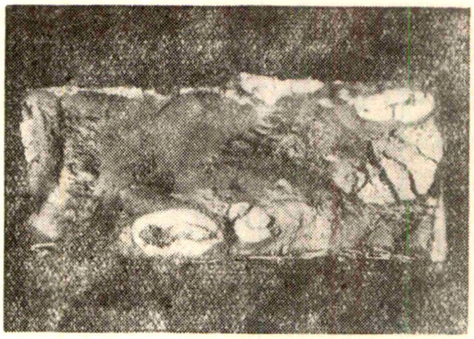

Fig. 9 Fracture surface of specimen in which hydrogen had been removed was penetrated with hydrogen again

Such repeated tests confirm that the investigated fisheye in welded seam is caused by hydrogen. The fisheye zone is the zone of local hydrogen induced cracking.

2. The fisheye formation and its influence on fatigue failure under cyclic load

(1) Specimen preparation and test conditions

Plate-shape fatigue specimens were taken from the welded steel plate which had been examined with X-ray to find the position of defects and to choose proper specimens. The specimens were planed and ground, and then were examined with X-ray again to direct the exact position, quantity, distribution and size of the defects. The weld bead was perpendicular to the tensile direction in taking the specimens.

To show fisheye characteristics, the tensile-tensile axial fatigue was adopted.

(2) The macroscopic and microscopic characteristics of fatigue fracture

(a) The macroscopic characteristics of fracture

To survey the fisheye on fracture surface under cyclic load, part of specimens was specially chosen to analyse fatigue fracture. The cyclic load σ_{max} applied to those specimens was gradually decreasing from 37.5 kg/mm^2 to 25 kg/mm^2, σ_{min} being equal to 5∼9 kg/mm^2. The test frequency was $f=860$ cpm. Every specimen was fractured by means of fatigue. The photos of fatigue fracture surface were shown in Fig. 10, 11.

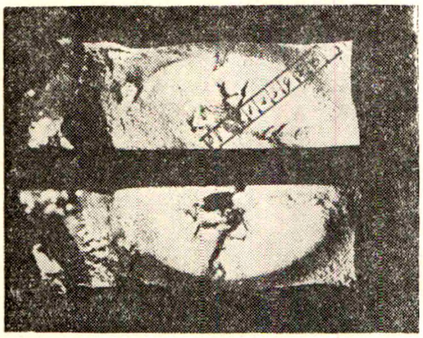

Fig. 10 Fatigue fracture ($\sigma_{max}=32$ kg/mm^2, $\sigma_{min}=8$ kg/mm^2, $N=6.33\times10^4$)

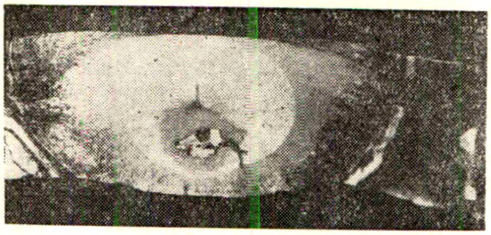

Fig. 11 Fatigue fracture ($\sigma_{max}=37.5$ kg/mm^2, $\sigma_{min}=8$ kg/mm^2, $N=4.478\times10^5$)

(b) The microanalysis of fracture surface

Three groups of typical fatigue fracture were selected and examined in an electron microscope in order to make a detailed survey of the failure process. The fracture surface shown in Fig. 13 is typical. Replicas were continuously made on the first dark zone, the fisheye zone, the second dark zone and the zone of instantaneous fracture. The positions of the replicas are shown as the straight line in Fig. 12. Fig. 13, 14, 15, 16 are the electron micrographs of replicas on zone 1, 2, 3, 4 respectively.

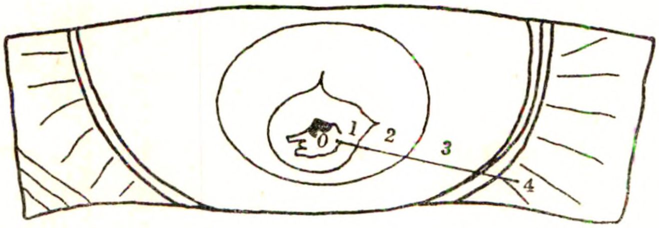

Fig. 12 Diagram of fracture shown in Fig. 11

0—zone of blowhole plus included slag (nucleus)
1—the first dark zone
2—the fisheye zone
3—the second dark zone
4—the zone of instantaneous fracture

In addition to this, replicas of the typical fracture surface of another group of specimen (Fig. 10) were made according to the marks in the diagram. The results examined with an electron microscope are that zone 0 (fisheye zone) is cleavage failure, zone 1 and zone 3, denoting the first dark zone and the second dark zone respectively, are clear fatigue striation. Therefore the results are in agreement with the above mentioned results[2].

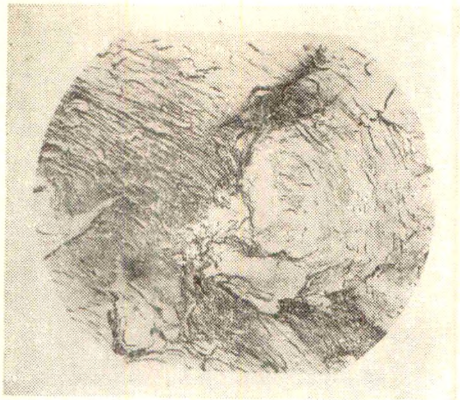

Fig. 13 Photo of replica on the first dark zone (mark 1) 5000X clear fatigue striation

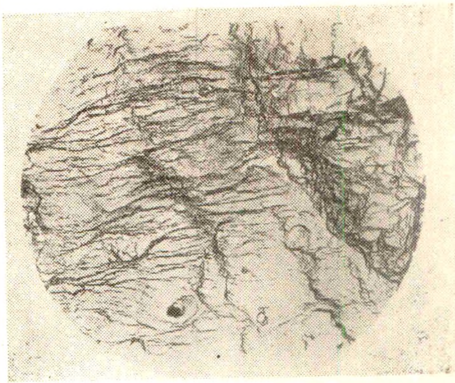

Fig. 15 Photo of replica on the second dark zone (mark 3) 5000X clear fatigue striation

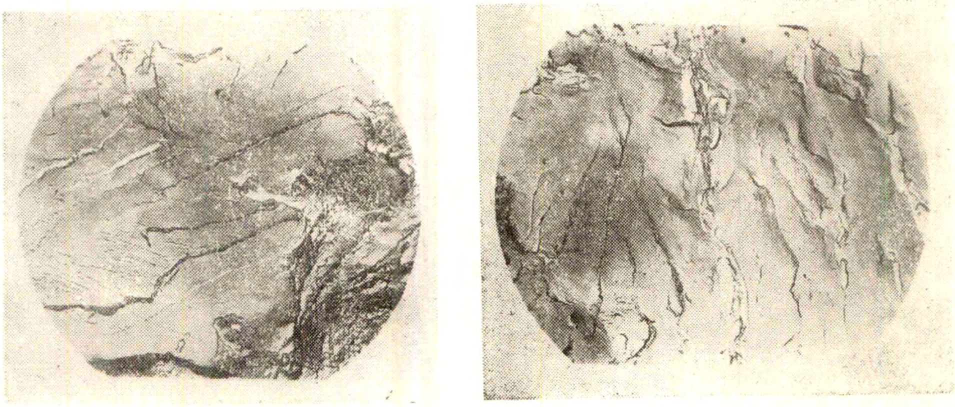

Fig. 14 Photo of replica on the fisheye zone (mark 2) 5000X cleavage and quasi-cleavage failure

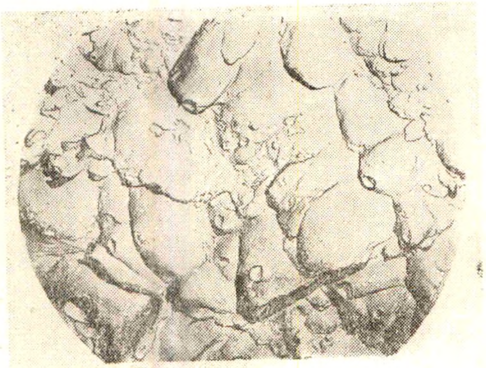

Fig. 16 Photo of replica on the zone of instantaneous fracture (mark 4) 5000X dimple

As shown in the macroscopic photographs, fisheyes appear in fatigue fracture in all specimens in which cyclic load is decreased from 37.5 kg/mm^2 to 25 kg/mm^2 gradually. The brightness of fisheye decreases with the decrease of load level. Comparing the fisheyes found in the fracture surface of fatigue specimen with those in the fracture surface of static tensile test, we find that in the center of fisheye there exist some kinds of microscopic visible defects (blowhole, included slag etc.) and no fisheye appears if these defects do not exist. However the fisheye disclosed in fatigue fracture is more coarse and less bright, the size of this fisheye is large than that disclosed in static tensile fracture and the size of some is so large that it covers almost the whole width of the specimen.

Special attention should be paid to the five clearly mainfested zones on the fatigue fracture surface (Fig. 11), i.e. the nucleus zone (blowhole, included slag etc.), the first fatigue failure zone (the first dark zone), the fisheye zone, the second fatigue failure zone (the second dark zone) and the zone of instantaneous fracture. It is obvious that the source of fatigue failure begins at the nucleus zone, not at fisheye. To be exact, the so-called first fatigue failure appears after the formation of the source of fatigue failure in blowhole or included slag. When fatigue crack grows to a certain extent, local hydrogen embrittlement emerges in the tip of fatigue crack, fisheye erupts, internal pressure of hydrogen releases, then the second fatigue failure begins until the crack growth reaches a maximum and whole fatigue fracture takes place. This process is completely proved in the above electron micrographs and is shown in Fig. 17: blowhole or included slag as nucleus (source of fatigue) → fatigue striation (the first fatigue failure) → brittle failure in character with cleavage and quasi-cleavage (the hydrogen embrittlement zone of fisheye) →fatigue striation (the second fatigue failure) →dimple (zone of instantaneous fracture).

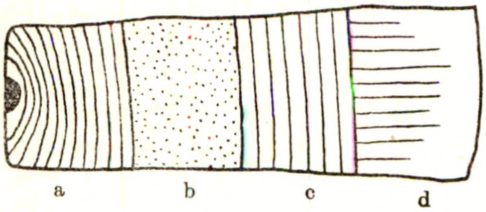

Fig. 17 Diagram of failure process on fatigue fracture surface
a—first fatigue failure zone
b—fisheye zone
c—second fatigue failure zone
d—zone of instantaneous fracture

From this, we come to an important conclusion: the source of fatigue is the defect such as blowhole etc. inside the specimen, not the weld fisheye itself. Fisheye forms at a definite stage of fatigue crack growth, so it has no conspicuous influence on the first stage of fatigue (nucleate stage), it only influences the second stage of fatigue (crack growth stage). On this account the weld fisheye affects conspicuously the fatigue overload endurance value (i.e. the incline part in fatigue curve) only. The effect on fatigue limit is negligible. This is the reason why the influence of the weld fisheye on fatigue limit of welded seam is rather small[1][3].

3. The influence of fisheye and defect on fatigue resistance

Besides the macroscopic and microscopic analysis of fatigue fracture surfaces, supplementary fatigue strength tests with another group of specimen were made. The preparation of specimen was the same as the above mentioned. The minimum cyclic stress was fixed at 5.3 kg/mm^2 and the maximum cyclic stress σ_{max} was changed. The number of cycles of fatigue limit was chosen to be $N=5\times 10^6$. The frequency of testing machine was 933 cpm.

These supplementary specimens were divided into three groups. One group showed no defects, while the other two showed small and large defects respectively, and fisheye appeared on the fracture surfaces of these two groups.

The results of the test show that the data of fatigue strength are considerably scattered owing to the differences of sizes and kinds of blowholes or included slags. To find the effect of fisheye alone on fatigue strength is difficult, because the weld fisheye are generally accompanied by macroscopic visible defects such as blowholes and included slags. The fatigue strength of the specimens in which no defects were disclosed by X-ray detection was compared with that of the specimens in which small defects were disclosed, the difference between them was not particularly great. That agrees with the results of microscopic analysis of the fatigue fracture surface.

IV. Discussion on the Mechanism of Weld Fisheye Formation

1. The states of hydrogen in the welded seam

Supersaturated hydrogen in the welded seam exists in three states. One is the molecular hydrogen (H_2) which is enclosed in internal macroscopic holes, such as blowholes, included slags and incomplete fusion during the solidification and cooling process of the deposited metal (here, the internal macroscopic visible defects are discussed). Another is atomic hydrogen (H) which "dissolves" in extended elastic lattice of iron and in the crystal defects such as dislocation, vacancy etc. The third type is ionic hydrogen (H^+) which really dissolves in iron lattice. The three states of hydrogen may transform into each other in certain conditions. Diffused and gathered in internal and external surfaces of the metal, the atomic hydrogen will combine into molecular hydrogen ($2H\rightarrow H_2$).

The reverse transformation of molecular hydrogen, i.e. $H_2\rightarrow 2H$, may proceed in defect positions inside the metal, such as on the surface of blowhole's wall. On the other hand, obtaining valence electron, the ionic hydrogen can change itself into atomic hydrogen, i.e., $H^+ + e\rightarrow H$. It follows that the ratio of H_2, H and H^+ in the deposited metal may change in different conditions[1][4][5][6].

The conditions which induce transformation are the preservation time after welding, temperature, stress and suitable strain rate. For instance, in preservation after welding, a part of atomic or ionic hydrogen, especially, the part of atomic hydrogen which has "dissolved" in the extended elastic lattice may escape by means of diffusion or diffuse into internal hole, and then gathers and becomes molecular hydrogen, i.e., the transformation of $2H\rightarrow H_2$ takes place. Furthermore, the molecular hydrogen which has been enclosed in internal macroscopic defects such as blowholes may be acted on by plastic deformation and its internal pressure. The molecular hydrogen situated on the blowhole's wall may be activated and changed into atomic hydrogen which may diffuse reversely into the metal adjoining the blowhole's wall. Thus the reverse transformation

$H_2 \rightarrow 2H$ takes place. Of course, this reverse transformation is more difficult than the former ($2H \rightarrow H_2$). But if the plastic deformation is sufficiently large and the stress level is sufficiently high, this reverse transformation would occur. It is because the hydrogen dissolved in the metal in the form of three states may diffuse, deposit and transform, that the formation of weld fisheye under a suitable condition is possible[7].

Another essential condition for the formation of the weld fisheye is that a certain amount of supersaturated hydrogen exists in the metal and internal holes (like blowholes) occupy some volume inside the metal. In common carbon steel and low-alloy steel in which a certain amount of supersaturated hydrogen exists, no fisheye is manifested in tensile or fatigue fracture if there are no macroscopic holes. However, when a certain amount of supersaturated hydrogen ($4 \sim 10$ $cm^3/100g$) and a definite volume of contained holes exist, not only will the fisheye often be manifested in tensile fracture, but also the capacity for dissolving hydrogen will be considerably changed. The experiment done by Gerwig Vibrans proved that for samples having 0.1% blowholes and low temperature (below 150°C), the capacity of dissolving hydrogen increased about 10 time compared with samples which have no blowholes. That is, the amount of hydrogen which is really dissolved and statistically distributed in the lattice is small and most of hydrogen is enclosed in blowholes[8][9].

2. The diffusion of hydrogen and its relation with fisheye formation

Owing to the existence of internal holes, not only is the capacity of dissolving hydrogen changed, but also the diffusing velocity will be greatly decreased in some content range.

Supposing *Ca* is the consistence of atomic hydrogen dissolved in the lattice. *Cm* is the consistence of molecular hydrogen enclosed in blowholes, *D* is the diffusion coefficient of hydrogen in the metal having no blowholes and *D** is that of metals having blowholes. It is found that when the temperature is 20°C, the blowhole volume is 0.2% and $Cm+Ca=10cm^3/100g$, $D^*/D=10^{-3}$. That is the diffusion coefficient of hydrogen decreases about 1000 times. At 300°C (or higher) and consistence $Ca+Cm$ is very low, D is nearly equal to D^*, i.e. the existence of blowholes has little effect on the diffusion of hydrogen. At 20°C and the hydrogen content is in the range $0.1 \sim 10cm^3/100g$, the existence of blowholes will evidently decrease the diffusion velocity of hydrogen. It is worth while noticing that the range $0.1 \sim 10$ $cm^3/100g$ of hydrogen content is the range in which the weld fisheye is usually manifested in engineering.

Having used preservation after welding, we performed a lot of experiments to survey the relation between the diffusion of hydrogen and the fisheye formation[10]. It is proved that the theoretical calculations mentioned above were in agreement with the results of our experiments. The experiments were divided into two groups. In one of them the normal welding process was adopted, that is, the electrodes were previously baked, the groove surface was cleaned, the slag between layers was obliterated. A large quantity of specimens were cut in such welded joint (section size of specimen is 12×100 mm). Having been detected with X-ray to decide the position of blowhole, the specimens were placed in the atmosphere of room temperature, then they were broken with tension by stages and in groups. It is evident that the fisheyes manifested on the fracture surfaces of specimens which were preserved for less than 64 days are the same as those in the specimens broken soon after welding in both size and clearness. The fisheyes manifested on the fracture surfaces of specimens which were preserved for 64～160 days become smaller and indistinct. Only blowholes appear after 160 days and the fisheye disappears in general.

In the second group of experiment the unusual welding process was intentionally adopted, i.e. the electrodes were unbaked, the slags between layers remained, the groove surfaces were uncleaned. The volume of blowholes was more than 1%. Also the amount of oversaturated hydrogen was greater than in the first group.

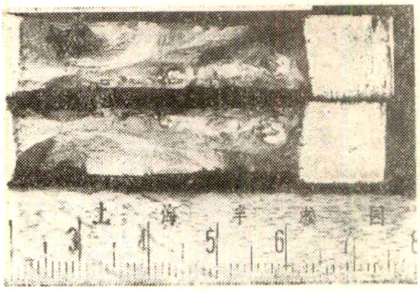

Fig. 18 Fracture surface of specimen preserved for 125 days (Fisheye disappears)

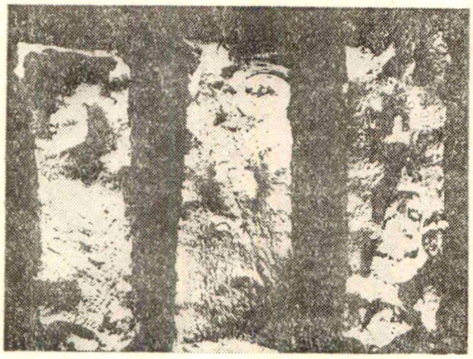

Fig. 19 Tensile fracture of specimen preserved for 4 years and 2 months (clear fisheye appear 1.5X)

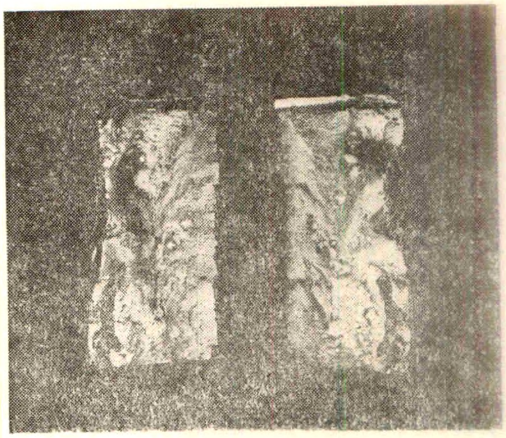

Fig. 20 Tensile fracture of specimen preserved for 8 years and 6 months (Fisheye disappears)

Clear fisheyes appeared after preservation for 6 years or more, but the fisheye disappeared after preservation for 8 years (Fig. 20).

It is well known that the hydrogen penetrated into the carbon steel and low-alloy steel in which no blowholes exist will escape after a preservation time of 4～5 days at room temperature by means of diffusion. However, in the tested weld pieces of steel 14 MnVTi in which blowholes exist, most of the supersaturated hydrogen will escape by means of diffusion at the end of 6～7 months of preservation. Moreover if the volume of blowholes and the amount of hydrogen (unusual welding process) are increased, it is necessary to preserve 8 years for the fisheye to disappear. All these are considered to be the results of existing blowholes which decrease the diffusion velocity rapidly.

3. The supposition on the mechanism of fisheye formation

The mechanism of the formation of weld fisheye has never been thoroughly understood. One point of view suggests that the formation of this kind of white spot may be explained as follows: having been diffused and deposited in blowholes, the hydrogen produces a great pressure which is added to the outward tension stress. When the sum exceeds the limit strength of the material, local brittle zones may be formed in the blowholes and the fisheyes with blowholes (or other defects) acting as nuclei are manifested on fracture surfaces. The other point of view is just the opposite. It says that fisheye formation is not due to the simple action of the pressure of hydrogen deposited in blowholes. It is the movement of molecular hydrogen in blowholes into slip planes to induce the local hydrogen embrittlement when the metal near the blowholes undergoes plastic deformation[9].

The authors beleive that these two proposals are not very satisfactory in explaining the objective phenomenon of fisheye formation. For instance, as discussed before, our experimental results as well as those of others show in general, the larger the nucleus of the blowholes, the larger the size of the fisheye. This experimental fact is inconsistent with the two above mentioned proposals, particulary the first proposal. The first point of view is true of μ-order size microvoid. However, the blowholes of our investigation is the macroscopic visible blowholes from several tenths mm to several mm in diameter. In these blowholes, the pressure caused by the hydrogen deposited is not great enough to induce brittle fracture. For example, based upon the second diffusion equation, the dependence of the deposited pressure on blowholes radius and time is deduced as[11]:

$$\frac{P}{P_0 C_0} = \frac{3Dt}{r_0^2} + \frac{6}{\sqrt{\pi}} \cdot \frac{\sqrt{Dt}}{r_0} \tag{1}$$

where

P=hydrogen pressure deposited in blowholes relative to time

P_0=relative pressure, in general, is 1 at.

C_0=hydrogen consistence in steel when $t=0$

D=the diffusion coefficient of hydrogen dissolved in steel

t=preservation time

r=radius of blowhole

In the same preservation time, equation (1) may be conceptualized as:

$$P \sim \frac{1}{r_0^2} \tag{2}$$

That is, the pressure of hydrogen deposited in blowholes is inversely proportional to the square of blowhole radius.

For example, the initial hydrogen consistence is $C_0=10\text{cm}^3/100\text{g}=0.795\ \text{cm}^3/\text{cm}^3$, the diffusion coefficient is $D=1.6\times10^{-7}\text{cm}^3/\text{sec}$, $P_0=1$ at, the approximate results calculated on equation (1) are listed in Table 1.

Table 1 Relationship between radius of blowholes and hydrogen pressure

radius of blowholes (mm)	preservation time (hrs)	hydrogen pressure in blowholes (kg/mm²)
0.5	0.5	0.0117
0.5	80	0.556
0.1	0.5	0.115
0.1	80	11.5
0.01	0.5	7.33
0.01	80	1110.0
0.001	0.5	691

As shown in Table 1, having been diffused for 80 hours, the hydrogen pressure in the blowhole of radius 0.5 mm is about 0.5 kg/mm^2 only. We may say that for many blowholes which act as nuclei of fisheyes with diameters being 0.5~5 mm, the pressure of deposited hydrogen is insignificant.

Therefore the authors suggest that the formation mechanism of this kind of white spots is as follows. The specimen which contains supersaturated hydrogen and defects like blowholes is loaded with tension stress. When the applied load is large enough, yield strain and microvoids (stacks of dislocation, accumulation of vacancy, original microvoid etc.) will be produced near blowholes. Thus the concealed brittle zone (microvoid zone) which may easily catch hydrogen forms. At the same time, the great outward stress and the deformation of the metal will make the hydrogen dissolved in the metal diffuse and fransform. On the one hand, the atomic and ionic hydrogen dissolved in the lattice diffuse to microvoid zone (three-dimensions tension stress zone) which may easily catch hydrogen. On the other hand, the molecular hydrogen which is enclosed in blowholes and is absorbed to the walls of blowholes may transform into atomic hydrogen which may diffuse into the microvoid zone connected with blowholes (the diagram is shown as Fig. 21). Having been diffused and deposited in the microvoids, the hydrogen may produce great pressure because the size of microvoids is in μ-order. Under the mutual effect of the pressure and the outward stress, the microvoid zone around blowholes may break and become local brittle zone, thus the weld fisheyes with blowholes as nuclei are manifested on the tensile fracture surface.

The above mentioned supposition on fisheye formation may explain the phenomena surveyed in the experiments. For example, the fisheye is only manifested near necking point, there must be a suitable deformation rate in static tensile test; the fisheye is not the source of fatigue failure; no fisheye appears under impact load, the outline of fisheye is the same as its nucleus; and the larger the blowhole, the larger the fisheye etc. The fact that the fisheye's size varies directly as that of the blowhole may be explained by the fact that the region where the microvoid zone may form may enlarge when loaded and when blowholes increase in size.

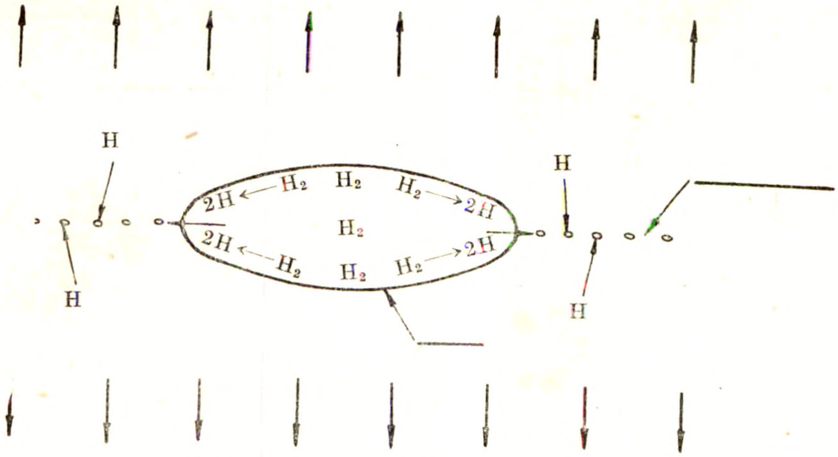

Fig. 21 Diagram of the formation of weld fisheye

V. Conclusion

A series of experiments and investigations on the problem of the weld fisheye in low-alloy steel 14 MnVTi brought us the following conclusion:

1. Weld fisheyes have the macroscopic defects as their nuclei such as blowholes, included slags, incomplete fusion flaws, porosities etc. which are enclosed in the steel. Fisheyes would not be manifested on tensile fracture surfaces if such defects do not exist.

2. Weld fisheye are different from flakes which usually appear in steel. The latter is the original defect in steel. The white spot will be manifested in the flake on fracture surfaces broken with any force (such as impact). The investigated weld fisheye is not the original defect. It forms only at a certain tension rate and in the stage scale plastic deformation near necking point, i.e. the stage near the limit strength of materials. It will not be manifested on the fracture surfaces of specimens which are broken with other loading such as impact. Therefore, it will not be detected by undamaged detection methods.

3. The weld fisheye is a local brittle fracture zone induced by hydrogen. The electron micrograph shows cleavage and quasi-cleavage.

4. The weld fisheyes have no distinct effect on the values of yield strength and tensile strength, because they form near the limit strength only. Also the weld fisheyes have no distinct effect on the process of bending steel plate into desired form. However the elongation and reduction ratio of the cross-sectional area are conspicuously reduced.

5. Under the tensile-tensile fatigue load, fisheyes are manifested on fatigue fracture surfaces of all specimens in which the fisheyes would appear no matter whether the fatigue stress loaded on specimen is high or low, and the fisheyes are much bigger than those in static tensile tests. The fisheye itself, however, is not the source of fatigue failure. It forms only when the fatigue

crack produced in blowholes or other defects propagates to a certain extent. As regards the fisheye itself, there is no visible influence on the germination of fatigue cracking, but fisheyes considerably accelerate the growth stage of fatigue cracking. Therefore the fatigue strength of specimens in which fisheye exists is not distinctly affected, but the overload fatigue life is considerably reduced.

6. After the welded parts have been placed in room temperature for 6～7 months, the supersaturated hydrogen contained in them welded with the normal welding process and having fisheyes will mostly escape by means of diffusion and no fisheye appears on tensile fracture surfaces. However, in the unusual welding process, i.e. both the amount of supersaturated hydrogen and the blowhole's volume increase, it takes more than eight years for the fisheye to disappear. These circumstances are explained by the fact that the existence of blowholes causes the obvious increase of the amount of hydrogen dissolved in steel and the great decrease of the diffusion velocity of the hydrogen in the steel.

In the case of the investigated weld parts of steel 14 MnVTi, specimens having been heated to 250°C for 6～8 hours (that is the regulation noted in the National Standard of Electrode), all hydrogen escapes by means of diffusion. No fisheye appears on tensile fracture surfaces.

7. In respect of the investigated weld fisheye with macroscopic blowholes (or defects) as nucleus, it seems that fisheye formation is not caused by the pressure of hydrogen deposited in blowholes. The actual mechanism is as follows: when specimen being loaded sufficiently, plastic deformation occurs in blowholes, a microvoid zone is produced in the neighboring metal around blowholes. Hydrogen deposits in these microvoids and produces a great hydrogen pressure. The mutual action of the pressure and the outward stress induces the weld fisheye which has blowholes as nucleus.

References

[1] V. Jurgere und J. Ruge: **Schweissen und Shneiden,** H. 3, S. 89, 1971.
[2] F. Erdman-Jesnitzer: **Schweisstechnik,** Vol. 6, H. 5, S. 133-139, 1956.
[3] W. Hofman und G. Vibrans: **Schweissen und Schneiden,** Vol. 12, H. 3, S. 95-101, 1960.
[4] H. G-Ellerbrack: **Schweissen und Schneiden,** H. 4, S. 139, 1973.
[5] A. L. Schaefflen, H. Thielsh und H. C. Campbell: **Wlg. J.** Vol. 31, S. 283-309, 1952.
[6] F. Erdman-Jesnitzer: **Archiv für das Eisenhüttenwesen,** Vol. 28, H. 5/6, S. 355, 1957.
[7] W. Hofman und W. Rauls: **Archiv für das Eisenhüttenwesen,** H, 3, S. 169-171, 1961.
[8] G. Vibrans: **Schweissen und Schneiden,** H. 1, S. 1-5, 1972.
[9] 上海交通大学、中华造船厂：焊接白点的试验研究，1977.
[10] Tetelman/McEvily: **Fracture of structural meterials,** p. 414, 1967.
[11] W. Schwang: **Archiv für das Eisenhüttenwesen,** Vol. 36, H. 5, S. 343-349, 1965.

中国造船工程学会年刊（英文）
第一卷　1982年

*　*　*

编辑者：《中国造船》编辑部
出版者：中国学术出版社
印刷者：上海市印刷三厂
国外总发行：中国国际书店
（北京399信箱）

1982年第一版

统一书号：W15262·002
编号：（英）15—E—1686D